

Broadband On-chip Terahertz Spectroscopy

Christopher Russell, BEng

*Submitted in accordance with the requirements
for the degree of Doctor of Philosophy*

University of Leeds

School of Electronic and Electrical Engineering

August 2013

The candidate confirms that the work submitted is his own, except where work which has formed part of jointly authored publications has been included.

The candidate confirms that the appropriate credit has been given within the thesis where reference has been made to the work of others.

This copy has been supplied on the understanding that it is copyright material and that no quotation from the thesis may be published without proper acknowledgement.

© 2013 The University of Leeds and Christopher Russell

Abstract

An enhancement of on-chip terahertz time domain spectroscopy (THz-TDS) systems for the analysis of polycrystalline materials has been made. An in depth review of planar Goubau lines is presented for which there are no analytically defined terms for transmission line parameters such as characteristic impedance and effective permittivity. Using a simulation package, Ansoft HFSS, the transmission line is optimised for spectroscopy applications and the bandwidth enhanced using a variety of methods. The theory for calculating the effective permittivity of the transmission line is derived based on a two dimensional interpretation of electromagnetic field patterns and cross-section transmission line geometry. The resulting formulae have a significant impact on both bandwidth and resonant filter designs.

The excitation of the planar Goubau line's quasi transverse magnetic mode, which is typically excited using coplanar to planar Goubau line transition, has been modified in favour of a novel all-planar Goubau line on-chip spectroscopy system utilising photoconductive generation and detection methodologies. In doing so, the frequency resolution of the system is heightened enabling a narrow line width system to be resolved.

The planar Goubau lines are fabricated on a quartz substrate with epitaxial transferred low-temperature-grown GaAs based photoconductive switches for both THz generation and detection. The bandwidth of the planar Goubau line is enhanced using a substrate thinning methodology to 2 THz for a 1-mm-long planar Goubau line. Using the enhanced bandwidth, THz-TDS spectroscopy using a planar Goubau line is demonstrated for the first time, where spectra of polycrystalline lactose monohydrate is obtained with a 3.75 GHz frequency-resolution over variable temperature range (4 – 298 K). The THz-TDS spectra are compared with spectra found using alternative THz spectroscopy systems to highlight the improved benefits of using this device.

The theoretical development of a narrow bandstop filter design is presented, with the analytical terms defined. This novel filter enables the dielectric sensing of overlaid materials at a multiple of predefined frequencies to be pushed away from the transmission lines, which would otherwise reduce the bandwidth of the system.

Results presented in this thesis present a strong candidacy for planar Goubau lines to be utilised in a broad range of applications which hold information in the THz regime.

Contents

Abstract.....	i
Contents	ii
Acknowledgements	vi
List of Figures	vii
List of tables.....	xxii
Chapter 1. The Latest Developments in THz Spectroscopy	1
1.1. Introduction to THz Radiation	2
1.2. Free Space Spectroscopy Systems	3
1.2.1. Fourier Transform Infrared Spectrometer	4
1.2.2. Free space THz-TDS	7
1.3. Free Space Coupled Waveguides	11
1.3.1. Attenuated Total Reflection	11
1.3.2. Parallel Plate.....	12
1.3.3. Sommerfeld, Goubau and Zenneck waveguides	14
1.4. On-chip THz-TDS Systems	16
1.4.1. Microstrip Lines	16
1.4.2. Coplanar Transmission Lines	19
1.4.3. Planar Goubau Lines.....	24
1.5. On-chip Generation and Detection of Picosecond Pulses.....	28
1.5.1. Electro Optic Detection.....	28
1.5.2. Electro Absorption Detection.....	34
1.5.3. Electro Optic Generation	36
1.5.4. Photoconductive Generation and Detection	38
1.5.4.1. Material Considerations	41
1.5.4.2. Switch Geometries	43

1.5.4.3.	Different Illumination and Bias Considerations for PC Switches	47
1.5.4.4.	External PC Detection of On-chip Systems	49
1.6.	Conclusion	50
Chapter 2.	Transmission Line Theory and Simulation Models	53
2.1.	Lumped Element Method	54
2.1.1.	Lumped element method for PGLs.....	59
2.2.	General Solutions from Maxwell's Equations	59
2.2.1.	Solving Maxwell's Equations for Radial Fields.....	61
2.3.	Introduction to Ansoft HFSS	63
2.4.	PGL Simulation Results	66
2.4.1.	PGL Field Patterns.....	67
2.4.2.	Substrate Permittivity	69
2.4.3.	PGL Transmission Line Width.....	70
2.4.4.	PGL Length.....	74
2.5.	Experimental Comparisons with HFSS Results.....	74
2.6.	Conclusion	75
Chapter 3.	The Fabrication and Measurements of THz On-chip Systems and the Bandwidth Enhancement of Planar Goubau Lines	76
3.1.	Design of Second Generation PGLs.....	77
3.2.	Fabrication of THz On-chip Device on Quartz.....	78
3.2.1.	The Growth and Annealing of LT-GaAs	79
3.2.2.	Van der Waals Bonding of LT-GaAs to Quartz and etching of LT-GaAs to define photoconductive switches	80
3.2.3.	Lithography and Metallization	83
3.2.4.	Mounting of On-chip Systems to PCBs.....	86
3.3.	System Setup and Measurement Scheme	88
3.4.	Initial Testing of On-chip Systems.....	93
3.4.1.	Initial PGL Device Characterization.....	93

3.4.2.	Electrical Chopping of the PC Switch	103
3.4.3.	Annealing Measurements.....	106
3.5.	Wafer Thinning Theory	109
3.6.	Chemical and Mechanical Thinning of Quartz Substrates.....	112
3.6.1.	Hand Lapping Process	112
3.6.2.	Mechanical lapping – Logitech PM5 Precision Lapping & Polishing System 113	
3.7.	Experimental Results for Substrate thinning of PGLs.....	115
3.7.1.	Device characterization.....	115
3.7.2.	Effects of Substrate Thinning.....	117
3.8.	Spectroscopy Application for PGLs.....	120
3.9.	Conclusion	122
Chapter 4.	Variable Temperature THz-TDS Measurements of Polycrystalline Materials using Planar Goubau Lines	124
4.1.	Initial Design Improvements to Enhance the Frequency Resolution of PGL devices 124	
4.1.1.	Sliding PC Switch Design.....	124
4.1.2.	Experimental Results	127
4.2.	Direct Excitation of the PGL Mode	129
4.2.1.	Optimization of the PC Switch Designs for Direct Excitation of PGL Modes 130	
4.2.2.	PGL Device Design for use in a Microstat	135
4.2.3.	Front Versus Backside Excitation of PC Switches	136
4.3.	PGL Device Characterization	137
4.4.	Low-temperature Characterization of PGLs on Quartz.....	139
4.5.	Spectroscopy of Polycrystalline Lactose Monohydrate using PGLs.....	141
4.5.1.	Theoretical Modelling of the Origins of the Spectral Features in Lactose Monohydrate	141
4.5.2.	HFSS Simulations to Model PGL Absorption Spectroscopy	142

4.5.3.	Sample Preparation.....	148
4.5.4.	PC Switch Bias Conditions Effect on Recorded Spectral Features	149
4.5.5.	Variable Temperature Measurements using PGLs	150
4.6.	Conclusion	157
Chapter 5.	PGL dielectric sensing	160
5.1.	Filter Designs	160
5.1.1.	Transmission Line and Series Filters	161
5.1.2.	Stub Filters	162
5.1.3.	Coupled Filters	166
5.1.3.1.	Filter Optimisation for an Improved Frequency Response	168
5.2.	PGL Geometry Changes	173
5.3.	Experimental Results for Dielectric Sensors on PGLs	174
5.4.	Conclusion	174
Chapter 6.	Conclusion	176
6.1.	Project Overview.....	176
6.2.	Potential Improvements to Further PGL Research.....	177
6.2.1.	Device Design and Fabrication	177
6.2.2.	Testing and Characterization of PGL	181
6.2.3.	Further Spectroscopy Work	182
6.3.	Direction of PGLs for Sensing Applications	183
6.4.	Publications.....	188
6.4.1.	Conference Proceedings.....	188
6.4.2.	Publication	188
References.....		189

Acknowledgements

I am grateful the guidance and support of my project supervisors Professor John. E. Cunningham, Professor Edmund H. Linfield and Professor A. Giles Davies who have, throughout my project, given me an insightful view of research. My thanks also go to the EPSRC who funded this project.

The introduction of planar Goubau lines was provided by my predecessor, Dr. Dazhang Li, to which I am thankful. Thanks go to Dr. Christopher D. Wood who provided the experience of on-chip THz research in all aspects which proved invaluable throughout the project. I must acknowledge Dr. Andrew D. Burnett has given so much of his time to the spectroscopy aspects of this project, providing comparable spectral results and ideas to what further purposes the transmission lines can be modified for. For work in the cleanroom, I must express my gratitude to Dr. Mark Rosamond for advice in cleanroom fabrication methodology, to Dr. Lianhe Li for growing the all-important LT-GaAs and to Nicholas Hunter who helped with the fabrication of the said devices.

I am forever grateful to all the students (in particular D. Mistry and J. Cooper to name a few) and staff in the School of Electronic and Electrical Engineering, who have moulded me into the person I am today in both a professional and social manner.

On the personal note, I must express my utmost thanks to my family who have supported me throughout my life and finally to my wife, Louise, who has provided me so much love and care.

List of Figures

Figure 1.1: Diagram highlighting the THz region of the electromagnetic spectrum. The photonics range of the spectrum lies right of the THz gap whereas the electronics lies to the left.....	2
Figure 1.2: A simplified schematic of the FTIR system. BS represents the beam splitter and SUT, the sample under test.	4
Figure 1.3: (a) Low (60 GHz) and (b) high (15 GHz) resolution FTIR scans of lactose monohydrate at room temperature (black) and 4 K (red) [15].	6
Figure 1.4: A simplified schematic of the (a) standard and (b) broadband free space THz-TDS systems used in the current work. The input near-infrared beam is split by the beam splitter (BS) in to the pump (red) and the probe (blue) beams. The pump is then focused onto the photoconductive switch (PC) to emit THz radiation (green) which is focused on to the sample under test (SUT). The transmitted THz is focused onto the electro optic (EO) crystal. The probe beam is subjected to an optical delay by the moving retroreflector (RR) before being focused onto the EO crystal. The beam is transmitted through the quarter wave plate ($\lambda/4$) before being split into its orthogonal components by the Wollaston prism (WP) and detected by the balance photodiodes (PD).	7
Figure 1.5: Standard system (a) refractive index and (c) absorption spectra for 100 % purity sample of lactose monohydrate. The equivalent (b) refractive index and (d) absorption measured using the broadband system.	9
Figure 1.6: Schematic of the ATR setup THz radiation (green) is coupled into the dove prism. The evanescent field (blue (exaggerated in the figure for clarity)) interacts with the overlaid material and the remaining radiation is reflected out of the prism. The angle of incidence (θ) is highlighted.	12
Figure 1.7: THz radiation (green) coupled into and from a PPWG using (a) silicon lenses and (b) tapered transitions.	12
Figure 1.8: cross-section views of the (a) Sommerfeld, (b) Goubau and (c) Zenneck waveguides where the direction of propagation is out of the page. The red and blue arrows are representative of the magnetic and electric fields, respectively. The electric field patterns for the (d) Sommerfeld (also representative of the Goubau line) and (e) Zenneck along the	

long axis. Magnetic field is coming out of the page and the direction of propagation is represented by the black arrow [36].	14
Figure 1.9: (a) MSL cross-section with the support substrate of an arbitrary permittivity (has no effect on transmission line characteristics), the ground plane metallization and the transmission line on top of the separating dielectric layer. (b) Electric (blue) and magnetic (red) field lines shown of the supported quasi-TEM mode.....	17
Figure 1.10: Aerial view of (a) CPW, (b) CPSlot and (c) CPS. Yellow represents the metallization and the grey represents the substrate material.	19
Figure 1.11: Cross section view of the CPW with the electric (blue) and magnetic (red) field lines for the (a) odd mode and the (b) even mode (also representative for field patterns supported by the CPS and CPSlot). The cross section view with geometry parameters for the (c) CPW and (d) CPS.....	20
Figure 1.12: (a) A simplified schematic of a CPW on a membrane substrate as demonstrated by references [74, 80, 81]. The waveguide (yellow) is defined on the membrane using standard cleanroom processing before the material beneath the waveguide is etched away using wet etching. (b) A simplified schematic of a coplanar-air transmission lines demonstrated by references [84, 85]. The waveguide is defined similarly to (a) except the material is etched top down from between the metal.	23
Figure 1.13: (a) Cross section view of a PGL showing both the electric (blue) and magnetic (red) field lines shown of the supported quasi-TM mode. (b) Cross section view along the propagation path to illustrate emerging and terminating electric field lines (magnetic field not shown).....	25
Figure 1.14: Different geometries of CPW – PGL transitions defined with a (a) single stage linear transition [91], (b) a double stage linear transition [92] and (c) the curved transition of the ground planes [91].	25
Figure 1.15: The cross-section view (PGL propagation out of the page) of a 5- μm -wide PGL's evanescent electric field measured using a positional external EO detection [96]. The orientation of the EO crystal is rotated 90 ° between (a) and (b) to reveal the nature of the PGL mode.	27
Figure 1.16: A simplified schematic of the EO detection scheme. The probing optical pulse (red) and THz pulse (green) have been vertically offset for clarity. Both the THz and optical pulse propagate collinearly through the electro-optic (EO) crystal. The optical pulse then	

propagates through the quarter wavelength plate ($\lambda/4$) before being split into its orthogonal components by the Wollaston prism (WP), which are then compared to one another by balanced photodiodes (PD).	29
Figure 1.17: (a) Schematic showing the x and y components of refractive index before (n) and an applied electric field (n'). (b) Schematic showing phase shift ($\Delta\Phi$) in x (out of the page) and y (upwards) components of light as it propagates through an EO crystal under an external electric field bias. Figure reproduced from reference [112].	30
Figure 1.18: Schematic of a Wollaston prism where two wedges, of angle θ , of birefringent material with their optical axis offset by 90° (vertical lines and dots (denoting axis into page)). The electric field of the incident optical beam is split into the two polarities; E_x and E_y . Figure reproduced [112].	32
Figure 1.19: External EO detection used for on-chip systems demonstrated by Meigien <i>et al</i> [120]. The ps pulse (black pulse on left) propagates along the CPW into the EO crystal (green) (ZnTe). 1.55- μm -wavelengths, 130-fs-FWHM laser pulse (red arrows) is manipulated by the THz pulse biased EO crystal.	33
Figure 1.20: Internal EO schematic diagram showing both transmitted (laser between the CPS metal) and reflected (off the substrate/metal interface) EO detection schemes. Red line shows the incident and transmitted laser and blue the reflected laser.	34
Figure 1.21: (a) Schematic diagram for PC switch generation and EA detection as demonstrated by Desplanque <i>et al</i> where the CPS (yellow) sits on the quartz substrate [121]. Red spots denote the excitation and probe lasers. (b) Schematic setup showing detection setup for reflective EA detection. Red line and arrow shows the incident laser path whereas the blue shows the reflected going through the mirror to the photodiode. The THz pulse is shown propagating along the transmission line (CPS).	35
Figure 1.22: Schematic diagram of EO generation with the EO material (green) as a (a) superstrate on an arbitrary substrate (grey) CPS and the (b) EO material substrate.	38
Figure 1.23: (a) An energy band diagram of semiconductor highlighting the photo-excitation of the electron from the valence band, VB to the conduction band CB. (b) Energy band diagram of semiconductor under a bias electric field $E_{Applied}$ with the resulting direction of drift the electrons and holes highlighted.	38
Figure 1.24: Schematic diagram of PC switch designs; (a) sliding contact, (b) sliding contact with defined PC material (above and below metallization) on substrate, (c) centre conductor	

gap and (d) defined switch. The grey areas are semi conducting material; yellow areas are the conducting material (usually Ti/Au) and the red highlights the illumination spots.	44
Figure 1.25: Schematic diagram of the PC switch with interdigitated electrodes used by (a) Griebel <i>et al</i> [70] and used by (b) Lee <i>et al</i> [69].	46
Figure 1.26: Schematic diagram of the material independent PC switch design for coplanar strip-line used by Holzman <i>et al</i> [149]. The green box highlights an optical delay of finite thickness, and the red spot highlights the area excited by the laser pulse.	46
Figure 1.27: Cross section diagram of switch regions for coplanar waveguides demonstrating (a) standard planar geometry, (b) recessed electrode geometry [150] and (c) annealed ohmic electrode geometry [151].	47
Figure 1.28: (a) Schematic of the external probe arm used for contact detection of electrical transients along a conductor. The red laser spot is hitting the PC material. (b) The THz pulse propagates along the transmission line with some of the signal going along the external probe arm to the PC switch. The rest continues along the transmission line.	49
Figure 1.29: Schematic of the external probe arm used for non-contact detection of electrical transients along and around a transmission line. The red laser spot is hitting the PC material. Two designs are presented; (a) and (b). (c) The THz pulse propagates along the transmission line with some of the signal being coupled onto the external probe arm to the PC switch. The remaining portion continues along the transmission line.	50
Figure 2.1: A two conductor transmission line supporting a TEM mode can be approximated by a lumped element method as shown. Reproduced from reference [30].	54
Figure 2.2: A two conductor transmission line terminated with a load, Z_L , at $z = 0$. Reproduced from reference [30].	58
Figure 2.3: A two conductor transmission line supporting the TM mode can be approximated by a lumped element method as shown.	59
Figure 2.4: (a) Cross section ($x - y$ axis) view and (b) longitudinal ($x - z$) view of the Sommerfeld line with the wave propagating along z	60
Figure 2.5: (a) Cross section ($x - y$ axis) view with the radial distance (p) and angular coordinate (φ) highlighted for a Sommerfeld line. (b) The longitudinal ($x - z$) view of the Sommerfeld line with the wave propagating along z	62

- Figure 2.6: Diagram of the HFSS model used to represent the studied PGL. The boundaries of the model are defined by a vacuum box (a) with the substrate highlighted (b). The excitation of the PGL is achieved by non-model planes (c, purple). The length and height of the substrate are highlighted as L and t , respectively. 67
- Figure 2.7: HFSS scalar plots for the (a) electric and (b) magnetic fields along the PGL. (c) Electric field plotted using vector plots to emphasise the direction of the electric field. All plots shown are for a 5- μm -wide PGL at 500 GHz. 68
- Figure 2.8: HFSS scalar plots for the (a,c) electric and (b,d) magnetic fields across the PGL. Vector plots are also shown to emphasise the direction of the field patterns. All plots shown are for a 5- μm -wide PGL at 500 GHz. 68
- Figure 2.9: The normalized exponential fits of the evanescent field strength as a function of perpendicular distance for a 5- μm -wide PGL on a 50- μm -thick quartz substrate for frequencies, $f = 100 \text{ GHz} - 1.8 \text{ THz}$ in 100 GHz increments. Insets: Scatter plots of the fitting parameters d_1 and d_2 from Equation 2-31. 69
- Figure 2.10: (a) S_{21} (solid lines) and S_{11} (dotted lines) parameters for an 800- μm -long, 5- μm -wide PGL on a 200- μm -thick substrate with a varying relative permittivity (1 – 30). (b) The simulated effective permittivity (ϵ_{eff}) plotted against the relative permittivity of the substrate (ϵ_r). The red line represents the theoretical effective permittivity given by Equation 2-32. .. 70
- Figure 2.11: (a) The exponentially fitted electric field strength plotted as a function of perpendicular extent from the centre of the PGL for a range of different widths of 800- μm -long PGLs on a 200- μm -thick quartz substrate. The inset shows the perpendicular distance (PD) of the electric field decay to a value of $e^{-1}E$ ($0.368E$, where E is the electric field strength on the PGL conductor) as a function of the PGL width (W). (b) Normalized exponentially fitted electric field strength as a function of perpendicular extent. This further emphasizes the dependence of the extent of evanescent field on the PGL width. The inset shows the fit parameter W_1 (black points) and W_2 (red points) for the exponential fits. A linear fit has been plotted for W_1 71
- Figure 2.12: The magnitude of the extent of the fields measured at the surface of the conductor as a function of the width of the PGL. The red line is a fit using Equation 2-35. .. 72
- Figure 2.13: (a) S_{21} parameters for different widths of an 800- μm -long PGLs on a 200- μm -thick quartz substrate. (b) Effective permittivity of the transmission line for the same simulation. 73

Figure 2.14: The characteristic impedance of the PGL as a function of the PGL width at 500 GHz. The data has an exponential fit (red line), extended to wider transmission line width.	73
Figure 2.15: S_{21} parameters for different lengths of 5 μm wide PGLs on a (a) 200 μm and (b) 50- μm -thick quartz substrate.	74
Figure 3.1: (a) A schematic of the device tested in this chapter with metallization shown in orange. (b) A magnification of the switch regions of the design for clarity with the grey LT-GaAs (rotated 90° with respect to (a)).	78
Figure 3.2: Simplified schematic of the step-by-step process used for epitaxial lift off, van der Waals bonding and for the LT-GaAs etch; (a) wax is deposited onto the LT-GaAs; (b) AlAs is removed in HF etch; (c) LT-GaAs and wax are transferred to the quartz substrate with water between the two; (d) water evaporates bonding the LT-GaAs to the quartz; (e) wax is removed in trichloroethylene and the device baked in a vacuum oven; (f) S1813 photoresist is patterned over the LT-GaAs defining the PC switches; (g) slow etching of the LT-GaAs defining a sloping profile of the LT-GaAs edge; (h) resist is removed in acetone revealing patterned LT-GaAs on quartz.	81
Figure 3.3: Micrograph of the LT-GaAs (lighter areas) on the quartz substrate after wax removal. The green and blue squares highlight a double layer of LT-GaAs and ripples in the transferred film, respectively. The film shown in (a) was transferred without the use of weights during van der Waals bonding, whereas weights were used in (b), demonstrating the micro-cracking which frequently appeared when weights were applied.	82
Figure 3.4: A comparison of (a) single layer resist pattern and (b) bilayer resist pattern.	83
Figure 3.5: Simplified schematic of the step by step of the processes for a bilayer resist, metallization and lift off (note; the same schematic is representative of both bilayer processes described in the text); (a) PMMA/LOR resist layer spun on and bake; (b) S1805/S1813 spun on and soft baked; (c) S1805/S1813 layer exposed and developed; (d) PMMA/LOR exposed and developed; (e) Ti: Au metallization of the device; (f) resists removed for metal lift off revealing the metalized device.	84
Figure 3.6: Micrograph of the S1805 – PMMA bilayer resists lifting off the substrate.	85
Figure 3.7: Photograph of the completed device used for substrate thinning measurements in this chapter.	86

- Figure 3.8: Schematic diagrams of (a) the original and (b) the modified PCB designs. The modified design has the “window” cut from the centre as well as the bottom half of the PCB to aid removal of the devices..... 87
- Figure 3.9: (a) Image of a PGL bond pad on a 50- μm -thick quartz substrate after attempting to bond the gold wire interconnects using the wedge bonder. Alternative method using (b) silver paint or (c) silver-loaded epoxy. 87
- Figure 3.10: (a) Schematic optical setup of the system setup where: (A) = solid state pump laser; (B) = Ti:Sapphire laser;(C) = 50:50 beam splitter; (D) = optical filter (10 mW unless specified); (E) = mirror; (F) = focussing lens; (G) = on-chip THz system; (H) = retroreflector; (I) = optical chopper. (b) Schematic electrical setup where black lines show electrical connections and blue is THz propagation between the PCSs (abbreviation: Gen. = generation; Det. = detection; PCS = photoconductive switch)..... 88
- Figure 3.11: Diagram demonstrating time domain spectroscopy with the transmitted electric pulse (blue), the optical pulse at five time intervals (red) and the mapped out pulse (green) with the corresponding data points in dark green. 90
- Figure 3.12: Simplified schematic diagram showing the electrical and optical bias conditions for generating and detecting (a) an input pulse and (b) an output pulse. The optical beams are represented by the red and blue lines. 91
- Figure 3.13: (a) Colour coded theoretical time domain traces for the (i) generated and (ii) transmitted pulses. Red traces represent the pulses propagating right to left and vice versa represented by blue. (b) Corresponding schematic of a transmission line with PC switches separated by PGL of length L 92
- Figure 3.14: Simplified schematic diagram showing the electrical and optical bias conditions for characterizing the PC switches. The optical beams are represented by the red and blue lines. The red line in this case is the optically chopped beam. (a) Shows the schematic for IV sweeps and (b) shows the schematics for photocurrent correlation measurements. 94
- Figure 3.15: IV sweeps for the PC switches at different laser powers for the two of the PC switches. (a) IV sweeps for the worst of the three PC switches with the more unstable photocurrent and (b) for the best of the three with the cleaner IV sweeps due to being a better switch quality. Insets: The resistance (linear fits of the respective main figures) plotted against the laser power..... 95

- Figure 3.16: (a) Photocurrent correlation measurements taken at 10 V, 20 V and 30 V for 10 mW pump and probe beams. (b) 10 V bias photocurrent correlation measurements with exponential fitting to both sides of the pulse. Inset: Electron lifetime (EL) obtained by exponential fit plotted against the bias voltage on both the rising and falling edges..... 96
- Figure 3.17: Bias voltage dependence of the switching times for LT-GaAs PC switches as calculated theoretically (solid line) and experimentally (scatter points) (taken from reference [177]). 97
- Figure 3.18: Normalised peak amplitude of input pulse measurements plotted for different positions of the half wave plate. Inset: Comparison of the relative amplitude (RA) as a function of the rotational angle of the half wave plate ($(\lambda/2)A$) fitted by sine function. 98
- Figure 3.19: TDS spectra of the measured input pulse as a function of the (a) applied average laser power (5 mW increments from 0 mW (black) to 25 mW (indigo)) and (b) the applied voltage bias (10 V increments from -30 V (black) to 30 V (purple)). Insets: the respective peak amplitudes (PA) of the TDS spectra plotted against the bias conditions. A line of best fit is shown. 99
- Figure 3.20: TDS spectra of the measured output pulse as a function of (a) the applied laser bias and (b) the applied voltage. Insets: the respective peak amplitudes (PA) of the TDS spectra plotted against the bias conditions. The line of best fit is shown. 100
- Figure 3.21: TDS spectra of the output pulse generated using slotline excitation, measured after propagation along a 1.5-mm-long featureless PGL. The pulse is measured from both sides of the CPW centre conductor..... 101
- Figure 3.22: TDS spectra of the coplanar (a, b) and slotline (c, d) modes measured after propagation along a 1.5-mm-long featureless PGL. Each plot shows the measurements from both PC switches on either side of the CPW centre conductor. 102
- Figure 3.23: (a) Comparison of the transmitted pulse generated by double switch and single switch excitation. (b) Collated TDS spectra of the individual modes (legend highlights the polarities of 30 V DC biases) measured from the same switch plotted against each other.. 103
- Figure 3.24: (a) Circuit diagram for testing the capacitance of the PC switch; the signal generator (sig. gen.), the PC switch (represented by the capacitor), the inductor and the oscilloscope (osc.) are all connected in parallel. (b) The impedance across the resonator against frequency (on a logarithmic scale)..... 104

- Figure 3.25: TDS spectra of an input pulse for different electrical chopping frequencies (a) without and (b) with the optical chop data (dotted line) for comparison. The amplitude of the (c) peak and (d) relative dark current of the TDS pulse are plotted as a function of the electrical chopping frequency. The inflection in the relative dark current measurement is the point where the sensitivity of the lock in amplifier is increased due to signal saturation. ... 106
- Figure 3.26: Micrographs of the PC switches following annealing at 500 °C. The LT-GaAs has been destroyed damaging the metallization surrounding the switches. 107
- Figure 3.27: TDS spectra of (a) the input and (b) the output pulse at different annealing temperatures. 108
- Figure 3.28: (a) Resistance of the PC switch for both dark (0 mW, black line) and illuminated (10 mW, red line) as a function of the anneal temperature. (b) Annealing temperature is against resistance and carrier lifetimes for free space emitters by Gregory *et al* [133]. I and II highlight the reported regions of the two stage increase in the resistivity of the LT-GaAs. 109
- Figure 3.29: Geometric diagram of the cross section of the PGL on a substrate of permittivity, ϵ_2 , in a superstrate of permittivity, ϵ_1 . The substrate thickness is denoted by h and the extent of the evanescent field by r 110
- Figure 3.30: (a) Plot of theoretical values for effective permittivity, calculated using Ansoft HFSS at 500 GHz (black) and Matlab using the derived formula (red) for a range of substrate thicknesses. (b) HFSS results showing S_{21} parameters for an 800- μm -long, 5- μm -wide PGL on a quartz substrate with a varying thickness (20 – 200 μm , in 20 μm increments). 111
- Figure 3.31: Photograph of the quartz after substrate thinning using HF wet etching. 112
- Figure 3.32: (a) Top view and (b) side view of the lapping chuck used. A = lapping chuck; B = sample holder; C = glass slide; D = sample to be thinned; E = sample holder levelling screws which alter the pitch of part B; F = sample holder securing screws. The difference between the top surface of A and the top surface of D is the distance to be removed by lapping. 113
- Figure 3.33: Simplified schematic of the step by step of the mechanical substrate thinning; (a) S1813 spun on and baked protecting the feature side of the device; (b) quartz edges are tapered for improved lapping; (steps not shown) device is mounted into the Logitech PP5 using the carrier disk and quartz wax; (c) quartz is removed by lapping; (d) wax is dissolved

in trichloroethylene releasing the device, the S1813 is removed in acetone to reveal the device.....	114
Figure 3.34: (a) Micrograph of the edge of a device substrate lapped by hand using BuehlerMet®II Abrasive discs, SiC grinding paper (P120). The micrograph shows the scratches (dark lines) caused by the rough grinding paper, which structurally weakens the substrate as well as the destroyed edge to the non-parallel mounting of the substrate to the chuck. (b) Micrograph of the edge of a device substrate (left hand side of image) lapped using the Logitech PM5 Precision Lapping & Polishing System with a consistent and even finish. The straight edges of the wafer have been maintained.	115
Figure 3.35: Time domain spectra of the transmitted pulse demonstrating the effect of increasing (a) the bias laser power for a fixed bias voltage and (b) the bias voltage for a fixed laser power (data taken from 85 μm substrate thickness device). The insets show their respective peak amplitudes (PA) with linear fits.....	116
Figure 3.36: IV sweeps one of the four PC switches of the PGL varying laser powers. The insets show the laser power against the switch resistance (with an exponential decay fit) obtained using linear fitting of the main figures.....	116
Figure 3.37: Normalised time domain spectra of (a) the input and (b) the transmitted pulses for five substrate thicknesses, vertically offset by 0.5 units for clarity. For (a), reflections of the input pulse off the back of the substrate have been marked on (i) 250 μm and (ii) 85 μm substrate thickness spectra.	117
Figure 3.38: (a) FWHM of the transmitted pulse against substrate thickness. (b) The time difference between the maxima of the transmitted and the reflected pulse.	118
Figure 3.39: (a) Scatter plot showing the time to reflection due to the back of the substrate with a linear fit. (b) Cross section view of the PC switch showing the propagation of the (blue) main input pulse from generating to detection PC switch and the (red) reflection off the back of the substrate.....	119
Figure 3.40: (a) Effective permittivity calculated using the time till reflection from the output data. (b) FFT of the normalised output pulse for varying substrate thickness.	120
Figure 3.41: (a) Time domain spectra of the transmitted pulse of overlaid lactose monohydrate with the truncation point highlighted (red line). (b) The frequency spectra of the (ii) raw data, (i) truncated and (iii) zero padded TDS spectra with the two spectral features labeled.....	122

Figure 4.1: (a) A schematic of the second generation PGL device with the metallization shown in orange. (b) A magnified region of the switch regions shown for clarity (rotated 90 ° with respect to (a)). (c) A schematic of the third generation PGL device, highlighting the reduction in the device size. (d) A magnification of the switch regions of the design for clarity, with grey regions indicating LT-GaAs of width W (rotated 90 ° with respect to (c)).	125
Figure 4.2: Simplified diagram demonstrating the use of LT-GaAs “rails” for defining the base material of the PC switches. The metallization position can be positioned anywhere along the LT-GaAs rails to select the best LT-GaAs (a) or the best graphene (green = good, red = bad) (b).	127
Figure 4.3: Simplified schematic diagram showing the electrical and optical bias conditions for generation and detection of an (a) input pulse and (b) an output pulse using the sliding switch geometry. The optical pump and probe beams are represented by the blue and red lines respectively.	128
Figure 4.4: Normalized (a) input and (b) output pulse measured for device geometry shown in Figure 4.1.	129
Figure 4.5: Schematic diagram of the overall LT-GaAs width, switch testing design with micrographs of the seven pairs of PC switches along the PGL for a range of LT-GaAs widths from 90 μm (i) to 5 μm (vii) (all rotated 90 ° with respect to the main figure).	131
Figure 4.6: (a) TDS of the input pulse for different widths of LT-GaAs. (b) FWHM of the input pulse plotted against the LT-GaAs width.	132
Figure 4.7: Schematic diagram of the overall metal width, switch testing design with micrographs of the seven pairs of PC switches along the PGL for the tapered tip (i) and a range of metal widths from 5 μm (ii) to 90 μm (vii).	133
Figure 4.8: (a) TDS of the input pulse for different widths of metallization. (b) FWHM of the input pulse plotted against the metal width as well as the tapered metal (red circle) and FWHM of the data obtained from Figure 4.6 from the same geometry (blue triangle).	134
Figure 4.9: Input pulse measurements for varying bias voltages (0 – 150 V, 10 V increments)	135
Figure 4.10: (a) A schematic of the device used for variable temperature spectroscopy measurements with the metallization in orange. (b) A magnification of one of the switch regions of the design for clarity with the grey LT-GaAs.	136

Figure 4.11: Image of the PGL mounted on the PCB used for microstat measurements. ...	136
Figure 4.12: (a) Comparison of input pulses generated by frontside and through-substrate optical excitation of the PC switches. (b) Same data as (a) but normalized for comparison of the pulse shape.	137
Figure 4.13: (a) Front and (b) through-substrate excitation of the PC switches. For (a) the gold metallization (yellow) screens the laser (red) from photo-generating carriers (green) in the LT-GaAs (grey). This screening is not observed in (b).	137
Figure 4.14: Time domain spectra of the transmitted pulse. The x -axis has been converted to distance in order to determine the origin of the reflections. Reflections are highlighted using arrows and lettering in both the spectra and schematic of the device (G represents the ps pulse generating PC switch).	138
Figure 4.15: Schematic of the MicrostatHe showing the continuous helium transfer from the dewar to the microstat. The vacuum control (VC), electrical contacts (EC) and temperature controller (TC) are highlighted. The device end of the microstat is shown showing the PGL mounted on the PCB (light green) which is mounted onto the cold finger (grey). The cold finger is connected to the heat exchanger which holds the helium, the thermometer and the heating elements.	139
Figure 4.16: Normalised TDS spectra of input (a) and output (b) pulses measured at different temperatures.	140
Figure 4.17: FWHM of the input pulse and output pulse plotted against temperature.	141
Figure 4.18: (a) The absorption and refractive index spectra of lactose monohydrate recorded using a free-space THz-TDS system (see Chapter 1). (b) The extracted permittivity and loss tangent of free space THz-TDS spectra of lactose monohydrate.	143
Figure 4.19: HFSS simulation determined (a) S_{21} parameters and (b) absorption spectra for a lactose monohydrate loaded PGL for varying interaction lengths.	145
Figure 4.20: HFSS simulation determined (a) S_{21} parameters and (b) absorption spectra for a lactose monohydrate loaded PGL for varying interaction thicknesses.	146
Figure 4.21: HFSS simulation determined (a) S_{21} parameters and (b) absorption spectra for a lactose monohydrate loaded PGL for varying interaction separation between the PGL and lactose surfaces.	147

Figure 4.22: Images of the lactose monohydrate held against the PGL using a heat reduction of S1813. (a) is illuminated from behind the substrate to more clearly emphasize that the PC switches are not obstructed by the sample under test.	149
Figure 4.23: (a) THz spectra of lactose monohydrate for different bias voltages. (b) THz spectra of lactose monohydrate for different laser powers.	150
Figure 4.24: Image of the PGL on the cold finger. The PCB is held in place by the PTFE tape and the thermal grease between the PCB and the cold finger. The lactose monohydrate (LM) can be seen attached to the PGL.	151
Figure 4.25: 292 K (a) and 4 K (b) FFT spectra of lactose monohydrate with standard deviation ($\times 3$) error bars (red) and TDS inset.	152
Figure 4.26: FFT spectra of lactose monohydrate for select temperatures (4, 50 – 250 (50 K increments) and 292 K). All spectra have been off-set vertically for clarity.	152
Figure 4.27: Frequency spectra of the truncated (black) and the non-truncated (red) TDS spectra for lactose monohydrate measured at 4 K. Spectra is off set for clarity. Inset: Same spectra with no offset.	153
Figure 4.28: (a) FWHM of a Gaussian fit of the 0.53 THz peak of lactose monohydrate against temperature with a linear fit. (b) The 0.53 THz peak's centre frequency as determined by Gaussian fit as a function of temperature.	154
Figure 4.29: (a) FWHM Gaussian fit of the 1.4 THz peak of lactose monohydrate against temperature with a linear fit. (b) The 1.4 THz peak's centre frequency as determined by Gaussian fit against temperature. Figure also includes a fit determined by Equation 4-6. ...	155
Figure 4.30: (a) Broadband THz-TDS absorption spectra of lactose monohydrate (5 % by mass dilution with PTFE) for 50 K increments from 4 K to 300 K. (b) The 1.4 THz peak's centre frequency as determined by Gaussian fit against temperature (error bars excluded for clarity as they exceed the limits of the figure). The figure also includes a fit determined by Equation 4-6 (red) as well as the fit for the PGL data for comparison (blue).	155
Figure 5.1: (a) Transmission line filter defined by corrugations in the PGL [101]. (b, c) Series filters defined in the centre conductor of CPWs used at microwave frequencies [196].	161
Figure 5.2: Stub filters using (a) quarter wavelength stub, (b) dual impedance quarter wavelength stub and (c) spiral rejecters.	162

Figure 5.3: (a) S_{21} parameters for unloaded QWS filters of varying lengths (200 μm – 40 μm) on a 5- μm -wide PGL. (b) The corresponding resonant frequencies plotted against the filter length with a formula fit (Equation 5-2, $n = 1$).	163
Figure 5.4: Cross section schematic for a loaded PGL. The load (red = ϵ_{load}), ϵ_L , has a finite thickness, h_L , with ϵ_F above the load determined by either free space or the permittivity of the fluidic material. The substrate (blue = ϵ_{sub}), ϵ_S , has a finite thickness, h_S , with ϵ_I below the substrate. The extent of the electric field is represented by r	164
Figure 5.5: Comparison between dual (impedance ratio = 3:1) and single impedance filters, highlighting the shift of the second harmonic to the third harmonic position in dual impedance filters.	166
Figure 5.6: Examples of (a) ring, (b) split ring and (c) metamaterial resonators on either side of a PGL. Images are reproductions from respective references.	167
Figure 5.7: (a) Schematic of the coupled U filter on the PGL. The width and length of the U filter are labelled w and l respectively with the coupling separation between the PGL and filter labelled s . (b) The corners have been experimentally tested with right angle (a) to a chamfer (b).	167
Figure 5.8: (a) S_{21} parameters for coupled U filters on PGL for varying total filter lengths, with the (b) corresponding plot highlighting the theoretical half wavelength and physical length values (Equation 5-8).	168
Figure 5.9: (a) S_{21} parameters for coupled U filters on PGL for varying coupling lengths, with (b) the corresponding scatter plot.	169
Figure 5.10: Comparison between the S_{21} parameters of a U filter and the same filter rotated 90° for a C filter.	170
Figure 5.11: (a) S_{21} parameters of multiple U filters of lengths; (i) = 300 μm , (ii) = 180 μm and (iii) = 120 μm . (a) S_{21} parameters of multiple U filters of lengths; (i) = 300 μm , (ii) = 120 μm and (iii) = 60 μm	171
Figure 5.12: (a) S_{21} parameters (10 GHz resolution error bars) of a 180- μm -long “U” filter loaded at position (i), (ii) and (iii) marked on (b). (b) The schematic of the filter and the position of the dielectric load (black box).	172
Figure 5.13: (a) S_{21} parameters for a loaded, 180- μm -long “U” filter coupled to a PGL for different load permittivity ($\epsilon_L = 1 - 10$, $\epsilon_L < 10$ omitted for clarity). (b) Resonant frequencies plotted against the load permittivity, fitted with Equation 5-9 ($n = 1$).	172

- Figure 5.14: (a) schematic of the PGL used for high resolution THz dielectric sensing. (b) Schematic of one of PC switches highlighting the LT-GaAs dimensions and the metallization..... 174
- Figure 6.1: An alternative method for epitaxial transfer of LT-GaAs to arbitrary substrates (quartz used here). (a) The as-grown LT-GaAs wetted with DI water and placed onto the quartz. (b) The water evaporates under ambient conditions. The growth substrate is then removed using either process I or II; for I, (c) the bulk SI-GaAs is removed using a selective etch or lapping, (d) followed by the removal of the AlAs etch stop layer. For process II, (c) the substrate is placed into a selective etch, removing the AlAs layer, releasing the bulk SI-GaAs, (d) which is subsequently removed..... 180
- Figure 6.2: A theoretical projection of the one-scan method TDS analysis method; the recorded TDS spectrum (a) is split into (b) the reference signal (blue) and the sample signal (red). The reference signal is extended to the same time domain as the sample signal with zero padding (dashed green). Both TDS spectra undergo a (c) FFT and compared to give an absorption spectrum..... 185
- Figure 6.3: Schematics of a multiport system using a straight length of PGL (a) and a split PGL (b) for simultaneous measurements of a unloaded transmission line and loaded (sample under test (SUT)). The pulse generated by the PC switch at G is recorded (c) after propagation in both directions (i and ii). The TDS spectra undergo a FFT (not shown) and compared with one another to reveal absorption spectra. 187

List of tables

Table 1-1: Table highlighting the EO materials used the THz detection with their corresponding Pockels coefficient (with measured optical wavelength in brackets), lowest TO phonon frequency and dielectric constant. Values are taken from [119] unless stated. ..	31
Table 1-2: Table from reference [134] (unless specified), comparing carrier lifetimes, band gap energies and TO phonon frequencies for selected PC materials.	42
Table 1-3: Table comparing the pros and cons of the three on-chip waveguides; microstrip line (MSL), coplanar waveguide (CPW) and the planar Goubau line (PGL).	51
Table 1-4: Table comparing the pros and cons of the three on-chip THz generation and detection schemes; Photoconductive switching (PCS), electro-optic (EO) and electro-absorption (EA).	52
Table 4-1: Table comparing the resolution (of the recorded data) and the bandwidth of systems used to investigate polycrystalline lactose monohydrate at room temperature. The table also specifies the recorded FWHM of the 0.53 and 1.36 THz peaks at room temperature where data is available. The values marked with “*”, represent values calculated from their respective publication figures using Origin image analysis tools and are indicative only of an approximation. Data which was not resolved due to bandwidth limits are marked as NR.	157

Chapter 1. The Latest Developments in THz Spectroscopy

In this chapter, a review of terahertz spectroscopy systems which have been used for absorption spectroscopy of materials is presented before focusing specifically on waveguides. Establishing a preferred choice of planar Goubau lines, different methodologies of generating and detecting of terahertz signal on on-chip systems are considered, with a conclusion that photoconductive switching will be used in this project.

Due to the limited theoretical modelling on planar Goubau lines, Chapter 2 covers transmission line theory for general transmission line terms, and simulations of different geometries of planar Goubau lines for transmission line specific design parameters. With an established understanding of the transmission line theory and the choice of terahertz generation and detection, Chapter 3 oversees the fabrication and initial testing of the proposed devices. In this chapter, the bandwidth enhancement of the transmission line through substrate thinning is presented, complete with a theoretical understanding. The first demonstration of terahertz time domain spectroscopy using a planar Goubau line is demonstrated in this chapter using overlaid lactose monohydrate.

Further development of the spectroscopy system is found with the introduction of a novel direct excitation and detection of the terahertz signal in the planar Goubau line is presented in Chapter 4. From these design modification a higher resolution and bandwidth spectra is obtained over varied temperature range to reveal temperature-dependant changes in the spectral feature widths and positions. Chapter 4 concludes with a comparison of this spectra with spectra obtained from free-space and other waveguide terahertz time domain spectroscopy systems to demonstrate the suitability of the waveguide to spectroscopy applications.

Dielectric sensing using a novel filter in the terahertz frequencies is proposed in Chapter 5, using simulations package HFSS to investigate different filter designs. The designs presented offer a competitive filter design with good sensitivity to overlaid material.

The thesis is summarised in Chapter 6 with several proposals for further development of terahertz spectroscopy systems, utilising the research covered in this project.

1.1. Introduction to THz Radiation

The “Terahertz” or THz frequency range is conventionally defined to cover frequencies from 300 GHz to 10 THz (Figure 1.1), bridging the gap between microwave and photonic engineering utilising techniques from both engineering methodologies. This frequency range has been referred to as T-rays, the THz gap, far infra-red, or sub-mm waves and THz radiation/waves in a vast range of literature. It is a region of the electromagnetic spectrum which over the past few decades has received considerable attention and research with advances in fabrication and experimental techniques to improve the bandwidth, power and resolution of the sources, waveguides and detectors of THz radiation. Furthermore, there is a rapidly expanding understanding of the theoretical and experimental knowledge of each of the applied applications.

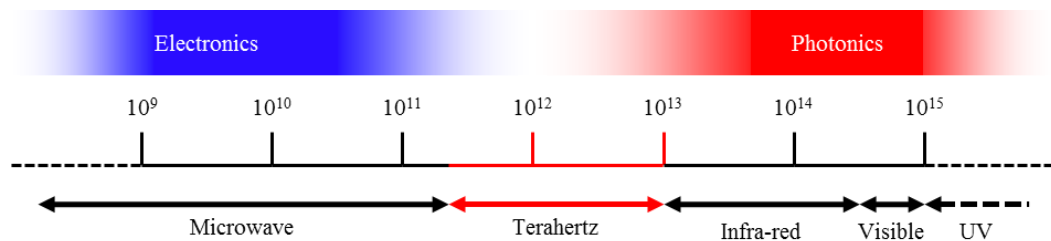


Figure 1.1: Diagram highlighting the THz region of the electromagnetic spectrum. The photonics range of the spectrum lies right of the THz gap whereas the electronics lies to the left.

THz research has been applied to a wide range of areas of research including communications [1, 2], astronomy [3], uses in medical imaging [3, 4] and pharmaceutical science [5], as well as material studies [3, 6], and many more such as environmental studies and security screening applications [6, 7]. In material studies, THz radiation has several advantages over other regions of the spectrum:

Non-ionising

Due to the low energy of THz radiation in comparison to the more commonly used x-rays; THz does not ionise molecules making THz more desirable for screening of biological samples and for security applications [4, 6].

Non-destructive

THz radiation freely propagates through a range of materials such as paper, plastic and clothes to interact with concealed

materials [8]. THz also penetrates through Si allowing packaged integrated circuits to be investigated [9].

Collective motion of atoms Like IR spectroscopy, THz radiation is used for spectroscopy of molecules at lower frequencies, but also interacts with the collective arrangements of several molecules within a crystal structure [5, 8].

meV energy THz energy lies between $100 \mu\text{eV} - 10 \text{ meV}$, so can be used in studies of condensed matter systems which have comparable energy scales (eg. the cyclotron energy in two dimensional electron systems (2DES)) [10].

Most THz time domain spectroscopy (TDS) is performed in a so-called free-space modality to analyse materials in the THz frequency range, though this setup suffers a range of disadvantages:

- The need for a purged environment to remove problematic atmospheric water vapour [11].
- A diffraction limited spatial resolution, therefore the free-space THz spectroscopy requires relatively large surface-area samples, with a greater quantity of sample being required when compared with guided-wave systems [6].
- The frequency resolution of spectra is typically low ($\sim 10\text{s GHz}$) due to in-system reflections at the emitter and detector crystal / free space interfaces.

1.2. Free Space Spectroscopy Systems

Free space spectroscopy refers to systems in which the THz radiation is guided through free space, while the beam path is defined through the use of parabolic and flat mirrors, as well as lenses. Unlike waveguide systems, the THz radiation is not confined to one or more conducting surfaces or wires potentially making the system lossy as well as difficult to setup with respect to the alignment of the flat and parabolic mirrors. Nevertheless, free space systems have been used extensively with modifications being made to several elements of the system; THz emitters, detectors, sample mounting methodology which itself can be

reviewed extensively. From a spectroscopy point-of-view, the free space system is advantageous in the sense of being able to quickly change the sample under test and to measure multiple samples within a single session, whereas waveguide systems require cleaning of the transmission line when used in contact spectroscopy to remove traces of the previous samples. It is possible to do non-contact spectroscopy using a waveguide system at cost of reduced absorption spectroscopy sensitivity [12].

For the purpose of this thesis, this section will only review both THz-TDS and Fourier transform infrared spectroscopy. Though THz quantum cascade lasers demonstrate higher power, and have potential future routes to tenability, they are currently too narrow-band (10 – 20 % of the centre frequency which can range from 1 – 5 THz [13]) for absorption spectroscopy to be practical for use in the analysis of liquids and solids.

1.2.1. Fourier Transform Infrared Spectrometer

The Fourier transform infrared spectrometer (FTIR) is a third generation infrared spectrometer which takes radiation from a broadband infrared source and passes it through a Michelson interferometer. In the Michelson interferometer (Figure 1.2), the incoming source beam is split 50:50 into two beams by the beam splitter which are reflected off two separate mirrors, one of which is on a translation stage. The beams are then recombined by the same beam splitter and passed through the sample under test. The transmitted radiation is detected by a detector such as a bolometer and converted to an electrical signal. By moving one of the mirrors, the optical path of the beam is changed and the interference between the two converging beams is altered. As a result an interferogram is produced; this is a function of time and can be converted to the frequency domain by performing a Fourier transform.

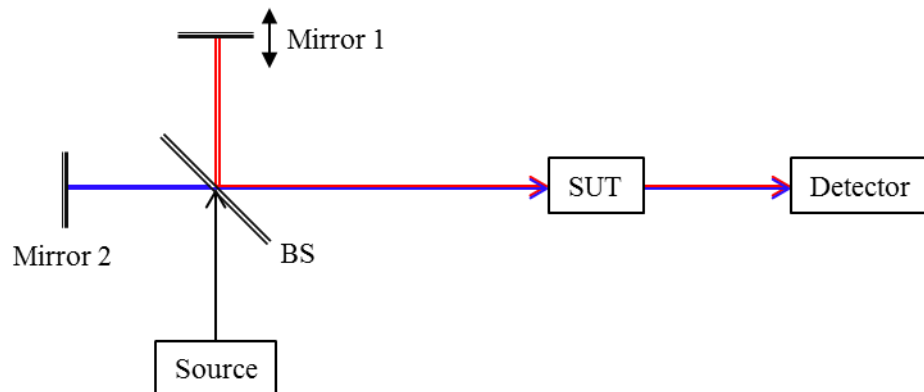


Figure 1.2: A simplified schematic of the FTIR system. BS represents the beam splitter and SUT, the sample under test.

When using a FTIR for spectroscopy applications, a reference signal is typically recorded of the background spectra before pressing a sample into a pellet and recording the sample spectra. The reference and sample spectra are then compared in order to obtain absorption spectra for the tested sample.

The resulting spectra can have a wide scan range (300 GHz – 30 THz) at a high resolution (0.15 – 3 GHz) and accuracy (± 300 MHz). However the sampling time is reported to be quite long and the pellet needs to be diluted for radiation to pass. Improvements can be made by substituting the source for a synchrotron source.

A synchrotron is a cyclic particle accelerator used to generate synchrotron radiation (also referred to as brilliant light and synchrotron light). Synchrotron radiation has a high brightness (also referred to as brilliance) which refers to the intensity of the beam per unit time per unit solid angle of the beam (units of brilliance: photons $\text{s}^{-1} \text{mm}^{-3} \text{mrad}^{-1}$). This high power enables spectroscopy samples to be prepared undiluted by matrix materials used to lower the bulk absorption of the sample under test in order to record the transmitted signal. Synchrotron radiation also has the advantages of improved SNR over other sources of radiation.

To generate synchrotron radiation in the third generation synchrotrons, an electron gun fires electrons into a booster synchrotron which accelerates the electrons using electromagnets, before releasing them into a storage ring. The storage ring is a large polygon made of linear sections angled together which keeps the electrons in a circular path using steering magnets. For third generation synchrotrons, the linear sections include an extra array of magnets called insertion devices which are used to provide a more intense and controllable light. At each of the turning magnets, the electron loses energy in the form of light, which is then channelled out of the storage ring into the beam lines. Here, the radiated light is passed through an optics hutch (silicon mirrors, slits and crystals) where the light is filtered to a specific frequency before being sent to an experimental setup where the FTIR and bolometer utilises the synchrotron radiation for THz transmission spectroscopy. To push the beam line wavelength to 2 mm (0.15 THz), the synchrotron is run in a low alpha mode in special beam conditions [14].

Whilst the brightness of synchrotron radiation is very attractive for spectroscopy applications, there remain several issues with the system itself. The brightness of the radiation decays over time as the electron propagate around the storage ring, thus requiring a periodic top up of accelerated electrons from the booster ring. As a result, the brightness over

time has a “saw tooth” profile, making it difficult to achieve scans over a long period of time. Additionally, the availability of such a system is limited to very few systems worldwide, with the low alpha mode in special beam conditions only being used infrequently. Therefore such a system is not yet commercially available for long term research.

Nevertheless, Figure 1.3 shows the low and high resolution FTIR spectra of lactose monohydrate (100 % purity, 40 mg pressed into a 550- μm -thick pellet with an 8 mm diameter) at room temperature and 4 K using a synchrotron radiation source (B22 beamline at Diamond Light Source Ltd, operating in the low alpha mode). Some of the spectral features appear to shift with temperature, whilst others remain fixed. From a resolution point of view, the advantages of high frequency resolution spectra is critical for accurately resolving narrow line width features; the peak in lactose monohydrate appears narrower and stronger with the improved frequency resolution. It is also interesting to note the single peak at 0.52 THz with a shoulder in the lower resolution spectra, has also been resolved into two peaks (at 0.44 and 0.54 THz) with the improved spectral resolution. This highlights the need for high-resolution systems for spectroscopy applications.

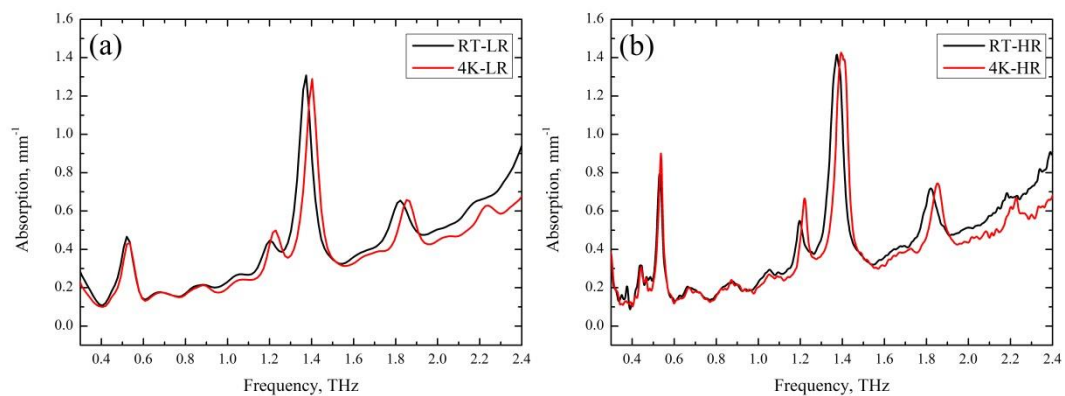


Figure 1.3: (a) Low (60 GHz) and (b) high (15 GHz) resolution FTIR scans of lactose monohydrate at room temperature (black) and 4 K (red) [15].

1.2.2. Free space THz-TDS

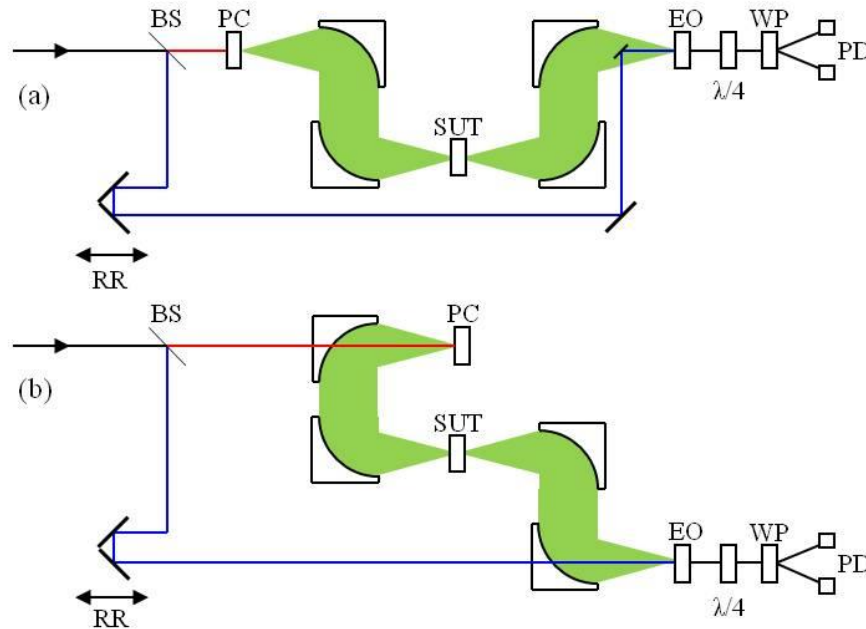


Figure 1.4: A simplified schematic of the (a) standard and (b) broadband free space THz-TDS systems used in the current work. The input near-infrared beam is split by the beam splitter (BS) into the pump (red) and the probe (blue) beams. The pump is then focused onto the photoconductive switch (PC) to emit THz radiation (green) which is focused onto the sample under test (SUT). The transmitted THz is focused onto the electro-optic (EO) crystal. The probe beam is subjected to an optical delay by the moving retroreflector (RR) before being focused onto the EO crystal. The beam is transmitted through the quarter wave plate ($\lambda/4$) before being split into its orthogonal components by the Wollaston prism (WP) and detected by the balance photodiodes (PD).

The standard transmission free space THz-TDS system setup is shown in Figure 1.4a. In this setup, a green diode solid state laser operating at 532 nm (Millennia Xs, Spectra Physics) pumps the Ti:Sapphire laser (Tsunami, Spectra Physics) to produce near-infrared (NIR) pulses (800 nm with a full width at half maximum (FWHM) of 8 nm and a pulse width of 110 fs) with a repetition rate of 80 MHz. The NIR beam is split into a pump and probe beam by the beam splitter. The pump beam (400 mW) is focused onto the PC switch via a lens to generate the THz radiation. The THz emitter is defined by a bowtie antenna with a 400- μm -wide gold electrode separation, on a 500- μm -thick, double sided polished semi insulating GaAs substrate. The electrodes are electrically biased to 50 V and chopped at 10 kHz for lock in detection.

Using the pseudo transmitted radiation (larger THz power amplitude than pseudo reflected) the THz radiation is collected and focused onto the sample under test using a series of parabolic mirrors. In a transmission spectroscopy setup, the transmitted radiation is collected from the other side of the sample under test by a second set of parabolic mirrors and is focussed onto an electro optic (EO) crystal (2-mm-thick ZnTe crystal) or photoconductive (PC) switch detector. The detector is “triggered” using the time delayed optical pulse (40 mW). This time delay is achieved with a change in the position of a retroreflector, which alters the propagation length of the probe beam. The standard system has a bandwidth of 0.1 – 2.8 THz, with a frequency resolution of 10 GHz.

The broadband system setup (Figure 1.4b) is very similar to the standard setup; the green diode solid state laser operating at 532 nm (Millennia Xs, Spectra Physics) pumps the Ti:Sapphire laser (Femtosource Compact, Femto Lasers) to produce a NIR pulse (800 nm with a FWHM of 110 nm and a pulse width of 12 fs) with a repetition rate of 80 MHz. The beam is split into the pump and probe beams; the pump beam is focused onto the emitter and optically delayed probe beam is focused onto the EO detector (150- μm -thick GaP). The emitter is defined on a 2- μm -thick low-temperature-grown GaAs (grown at $\sim 200^\circ\text{C}$, and *ex situ* annealed at 550°C) on a 500- μm -thick SI-GaAs substrate. The gold electrodes, separated by a 400- μm -wide gap are biased at 100 V and electrically chopped at 10 kHz.

To remove the bulk absorptions due to the PC switch material of the emitter, the pseudo reflected THz radiation is collected and focused through the sample under test using parabolic mirrors. The transmitted radiation is collected and focused onto the detector. The bandwidth of the broadband system is 0.3 – 8 THz though has been demonstrated with a bandwidth over 30 THz with the inclusion of the TO phonon absorption due to the detector (20- μm -thick ZnTe) and emitter [16]. In the 30 THz bandwidth system, there is reduced detection sensitivity due to the thickness of the EO detector therefore the thicker detector is used at a cost of reduced bandwidth. The frequency resolution of the resultant spectra is < 160 GHz, limited by the first etalon originating from the back surface of the EO crystal.

The absorption coefficient (Equation 1-1, Figure 1.5c, d) and the refractive index (Equation 1-2, Figure 1.5a, b) of the sample under test can be calculated following a fast Fourier transform (FFT) of the transmitted signals with and without the sample under test;

$$\alpha_{SUT} = \frac{-\ln\left(\frac{I}{I_0}\right)}{x} \quad 1-1$$

$$n(\nu) = \left[\frac{(\varphi - \varphi_0) \times c}{2\pi\nu x} \right] + 1 \quad 1-2$$

Where I and I_0 are the intensities of the sample under test and reference respectively, x is the sample under test thickness, and φ and φ_0 are the phases of the sample under test and the reference respectively.

The same lactose monohydrate pellets used to test the FTIR system were used to test the spectral resolutions of the standard and broadband systems (Figure 1.5). Similarly to the FTIR data, the peak at 0.53 THz can be used to highlight the spectral differences between the two setups; the 0.53 THz peak is significantly narrower, with greater amplitude for the standard system. The broadband system is unable to resolve the 1.2 THz peak seen in the standard system data.

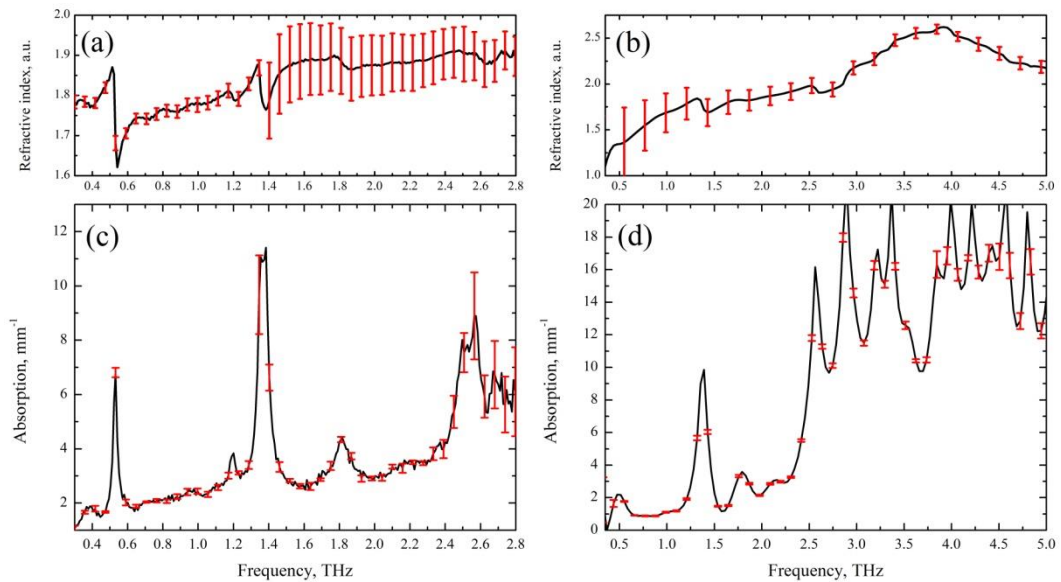


Figure 1.5: Standard system (a) refractive index and (c) absorption spectra for 100% purity sample of lactose monohydrate. The equivalent (b) refractive index and (d) absorption measured using the broadband system.

The complex permittivity of the sample under test can be calculated using the absorption coefficient and the refractive index. This proves beneficial when converting the data from a sample under test into permittivity and loss tangent as a function of frequency, which was

required in the theoretical simulation of transmission lines for spectroscopy application using simulation packages discussed in Chapter 4.

The system bandwidth is limited by the pulse width of the generated THz radiation whilst the resolution of the FFT data is determined by the scan length of the retro-reflector (as well as the practicality of the scan time). The frequency resolution of the FFT data is determined by the length of the etalon-free time window of the analysed TDS spectra [17]. The etalons which originate from the emitters and the detectors can be removed with modifications to their design, but etalons due to the finite sample thickness cannot be experimentally resolved and a sample too thick will attenuate the signal. However, there is research being done to mathematically resolve this issue [6, 17, 18].

Particularly in the transmission setup, the sample under test may need to be processed to be better suited to the system by drying and grinding it to a finer powder to reduce water absorption [11] and Mie [19] scattering respectively. The sample under test may also need to be diluted in THz transparent matrix material such as polytetrafluoroethylene (PTFE) to reduce the bulk absorption of the sample [20]. This treatment of the sample under test may alter the resulting THz spectra [15].

A free space system can also be used to create 2D images of the sample under test by placing the sample under test onto an X - Y stage, allowing the sample under test to be moved in the focus point of the parabolic mirrors. However the image suffers from the diffraction limited spatial resolution of the system from 100 μm to several mm's although the resolution can be enhanced with near field imaging [21]. This also suggests a larger volume of the sample under test is required for a reliable scan which in some cases, is difficult to achieve.

The sample under test in a free-space system can also be placed into a cryostat with THz-transparent polyethylene (PE) windows for variable temperature measurements. The PE windows ensured absorption free THz transmission from the free space setup, into the cryogenic environment within the microstat. However, the PE windows introduce further etalons into the TDS spectra reducing the resolution of the frequency spectra. This can be resolved by using a cryo-stream; a jet of cold air focused onto the sample under test, at a cost of increasing the minimum obtainable temperature to around 20 K.

In all free space setups, the THz path should be purged (with dry air or nitrogen), or evacuated of problematic water vapour resulting in a larger experimental setup [11].

1.3. Free Space Coupled Waveguides

Free space coupled systems use the same or a similar system setup as the free space THz-TDS systems, except the sample under test is replaced with a waveguide. By introducing a waveguide, the THz radiation becomes guided or confined within a controlled environment allowing the interaction length between the sample under test and the THz radiation to be increased to enhance any resulting spectral features. The following are short reviews looking at THz waveguides which have been used for spectroscopy applications. There are other types of waveguides omitted from these discussions which have been used for transmission applications but not absorption spectroscopy applications such as rectangular waveguides, dielectric waveguides and hollow core to name a few.

1.3.1. Attenuated Total Reflection

Attenuated total reflection (ATR) uses a dove prism (made from silicon or germanium [22]) to reflect THz radiation off a crystal-sample under test interface (Figure 1.6). At the interface, a THz evanescent field is created which interacts with the sample under test, which in turn alters the reflected THz signal. The reflected signal is collected and measured using either EO or PC detection. The perpendicular extent of the interacting evanescent field, d , is governed by Equation 1-3 where f is the frequency; θ is the angle of incident at the ATR – sample under test interface which is also governed by the ratio of the dielectric constant of the dove prism (n_1) and the sample under test (n_2) [23].

$$d = \frac{c}{2\pi f \sqrt{n_1^2 \sin^2 \theta - n_2^2}} \quad 1-3$$

Although this is not technically a waveguide system, it does demonstrate an interesting modification to the free space system. ATR has been applied successfully to the spectral analysis of solids (1 mg) and liquids (1 mL) in the 0.3 – 3.6 THz range with a detector limited resolution of 40 GHz [22]. The spectral sensitivity to the applied powdered samples is dependent on the amount of powder applied (more powder = stronger absorption peaks) as well as the amount of force used to press the powder onto the prism surface (more force = stronger absorption peaks since the sample contacts the prism better as well as increasing the density of the powder).

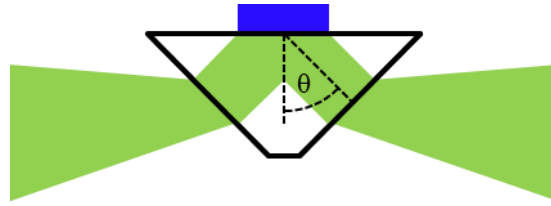


Figure 1.6: Schematic of the ATR setup THz radiation (green) is coupled into the dove prism. The evanescent field (blue (exaggerated in the figure for clarity)) interacts with the overlaid material and the remaining radiation is reflected out of the prism. The angle of incidence (θ) is highlighted.

1.3.2. Parallel Plate

Parallel plate waveguides, PPWG, as the name suggests consist of two polished metallic surfaces separated by an air gap or a dielectric. The waveguide supports all three modes (transverse magnetic (TM), transverse electric (TE) and the transverse electromagnetic (TEM)), which are coupled into and from the waveguide by the parabolic mirrors and plano-cylindrical high resistivity silicon lenses Figure 1.7a [24]. For an improved coupling efficiency into and from the PPWG, the separation between the plates at the open ends of the PPWG can be increased by tapering as shown in Figure 1.7b [25].

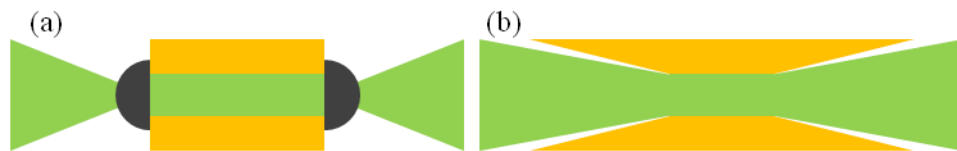


Figure 1.7: THz radiation (green) coupled into and from a PPWG using (a) silicon lenses and (b) tapered transitions.

The metal used for the PPWG is usually either polished aluminium [25-29], gold plated aluminium [26] or copper [24, 26], which are separated by dielectric supports. The attenuation of the waveguide for the TEM mode is defined by Equation 1-4 [30].

$$\alpha = \frac{R_s}{\eta d} \quad 1-4$$

Where η is the free-space impedance, d is the plate separation and R_s is the material specific, plate surface resistivity. Equation 1-4 can be expanded to find the frequency dependence of attenuation by redefining the resistivity to include the skin depth, δ_s , Equations 1-5 and 1-6 [30]. The skin depth is defined to be the depth at which the amplitude of the electric field decays to $1/e$ (i.e. 36.8 %), which becomes larger at lower frequencies. As a result, the skin

depth determines the low frequency cut-off losses and encourages thicker metals for broader bandwidths, or use of a metal with higher conductivity.

$$R_s = \frac{1}{\sigma \delta_s} \quad 1-5$$

$$\delta_s = \sqrt{\frac{2}{\omega \mu \sigma}} \quad 1-6$$

The magnitude of the attenuation coefficient will increase with frequency. In order to reduce the absorption in the PPWG, the plate separation needs to be reduced, and the plate surfaces made conductive.

As well as surface resistance losses, PPWGs also suffer coupling losses and reflections from the silicon lenses. Nevertheless, spectra with a resolution of 6.7 GHz (limited by the finite length of the waveguide and reflections from the silicon lens) of solid samples have been demonstrated up to 3.5 THz as well as variable temperature measurements achieved by cooling the plates [26, 31]. The sample under test is dissolved in an appropriate solution which is then drop-cast onto one of the plates. The waveguide is reassembled and the transmitted signal measured with a reference obtained by washing away the sample under test with a solvent. As a result, the method is currently limited to soluble samples. However, in direct comparison to free-space THz-TDS, Melinger *et al* had demonstrated that the PPWG spectroscopy results can produce narrower line widths with a greater sensitivity to temperature variation, crystal orientation and crystal morphology (itself is dependent on the metal plate and surface finish) of the sample under test than results produced using conventional free-space THz-TDS [28, 31].

PPWGs can also incorporate resonators in the form of a geometry with groove(s) in one of the plates [27]. The resonant frequency can be reduced to lower frequencies by making the groove(s) deeper or wider with the latter including higher-order cavity modes [27]. Alternatively, the resonance can be shifted to lower frequencies with an increase in plate separation [27]. The groove can be filled with sample under test materials whose refractive index will then shift the resonant frequency of the cavity, which is then detected. This technique has been successfully applied to liquid samples, and alkanes of different chain lengths distinguished, by a progressive increase in the resonance shift with chain length [29].

1.3.3. Sommerfeld, Goubau and Zenneck waveguides

Sommerfeld lines are single-wire transmission lines which can be used to guide THz radiation. The Sommerfeld line was later modified into a Goubau line with an addition of a dielectric coating to confine the radiation to the wire [32-34]. Both waveguides support a radial TM mode where the electric field is emitted towards and away from the conductor in radial nature with the magnetic field circulating the wire (see Figure 1.8a, b). The strength of the radial electric field has been proven both experimentally and theoretically to decay with increasing distance from the conductor surface as well as decaying as a function of the propagation length. The radial decay is reported to have an a/r dependence where the a is the radius of the waveguide and r is the radial distance from the waveguide surface [35]. This suggests that the greater the diameter of the wire, the greater the extent of the field.

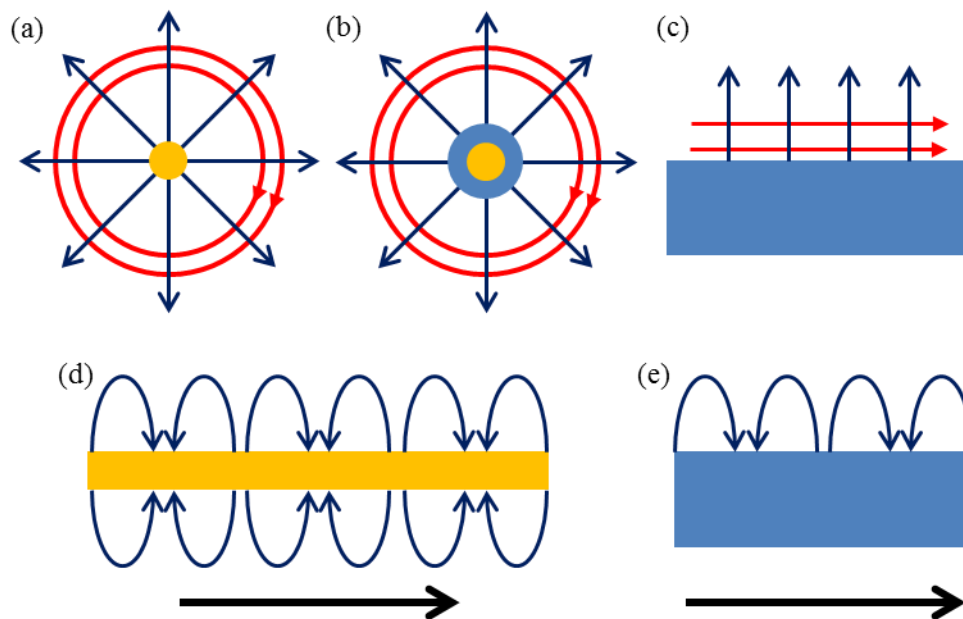


Figure 1.8: cross-section views of the (a) Sommerfeld, (b) Goubau and (c) Zenneck waveguides where the direction of propagation is out of the page. The red and blue arrows are representative of the magnetic and electric fields, respectively. The electric field patterns for the (d) Sommerfeld (also representative of the Goubau line) and (e) Zenneck along the long axis. Magnetic field is coming out of the page and the direction of propagation is represented by the black arrow [36].

For microwave measurements of the Goubau line, a coaxial line is fed into a horn antenna which launches the TM mode along the Goubau line. However the method is limited to the bandwidth of the coaxial line and the VNA used, which typically lies short of the THz regime. For THz measurements, where the Sommerfeld line is the preferred single wire

geometry over Zenneck waveguides and Goubau lines, THz radiation is coupled onto the suspended wire from a free space system either directly from the emitter [35, 37] or coupled onto the conductor from a free space emitter using a setup of parabolic mirrors and lenses [38, 39]. The radiation then propagates along the transmission line as a TM mode which is then detected using either EO [37] or PC [35, 40, 41] detection techniques. Sommerfeld lines which have been experimentally demonstrated have been defined using copper [35, 41-43], aluminium [42], and stainless steel [42] each supported by polystyrene disks.

The Sommerfeld line has undergone modifications to improve the coupling of incoming radiation. The coupling of radiation into the wire has been modified by introducing grooves into the wire. The number of grooves corresponds to the number oscillations in the measured time domain of the pulses which propagate along the wire, and the spacing between the grooves corresponds to the centre frequency of the spectra [39]. As a result, the wire can be designed to control the bandwidth and centre frequency of the pulse propagating along the wire. For enhancing the detection of the transmitted pulses, the wire should be made conical; by reducing the diameter of the wire, the electric field density is increased, improving the detected amplitude of the ps pulse [44].

The Sommerfeld line can be split into two transmission lines by coupling a second conductor from the main line [45]. The slitting of the Sommerfeld line allows for the potential of recording a reference signal and a sensing signal simultaneously. However, the radii of the corners when separating the wires need to be kept as large as possible; smaller radius results in larger attenuation of the signal [35, 45].

Sommerfeld lines have been successfully used for absorption spectroscopy of 1 mg of lactose monohydrate, deposited over a 55 mm length of the wire [37]. The setup as a result shows greater sensitivity than that of free-space by increasing the interaction length between the sample under test and the waveguide. However, the sample under test cannot be cooled for variable temperature measurements as done in free-space THz-TDS and PPWGs as there is nowhere to attach the appropriate heat exchanger.

The Zenneck waveguide is a single conductor transmission line similar to the Sommerfeld line, except it has a rectangular cross section as opposed to a circular cross section. The Zenneck waveguide has been successfully, though inefficiently excited using a free-space THz coupled silicon prisms onto and from the polished copper Zenneck waveguide [46]. This experimental setup was later improved by using free space THz coupled PPWG in which one of the plates is progressively removed to excite the remaining plate; the Zenneck

waveguide defined using a polished aluminium surface [47, 48]. There is very little research for this geometry, however, and no demonstration of practical applications as yet. However, the Zenneck waveguide, like the Sommerfeld and Goubau lines, does highlight potential similarities to the planar Goubau line.

1.4. On-chip THz-TDS Systems

In this section, we review three different types of planar transmission lines demonstrated at THz frequencies; microstrip lines, coplanar transmission lines and planar Goubau lines. Unlike the previous geometries discussed, here the THz radiation is both generated and detected by incorporating the PC switches or EO detectors into the waveguide. As a result, the emitter/detectors and parabolic mirrors required by free-space THz-TDS are not required. With the THz now confined to only the transmission line, there is no longer a necessity to purge the system of water vapour.

The on-chip waveguide also have further advantages over the previous designs with a more compact system, enabling the system to be fitted into smaller test environments such as microstats and fridges for low temperature measurements. The devices can also be designed and fabricated in the cleanroom, therefore allowing relatively more freedom in optimising the system parameters for specific applications.

1.4.1. Microstrip Lines

The microstrip line, MSL structure consists of a thin signal conductor and a ground plane separated by a low-loss dielectric material. The electric field pattern, shown in Figure 1.9, is mostly confined to the dielectric between the ground plane and the signal conductor with fringing evanescent fields along the signal conductor edge. As a result, the device can be fabricated on arbitrary substrates, as there is no electrical influence of the substrate which lies below the ground plane.

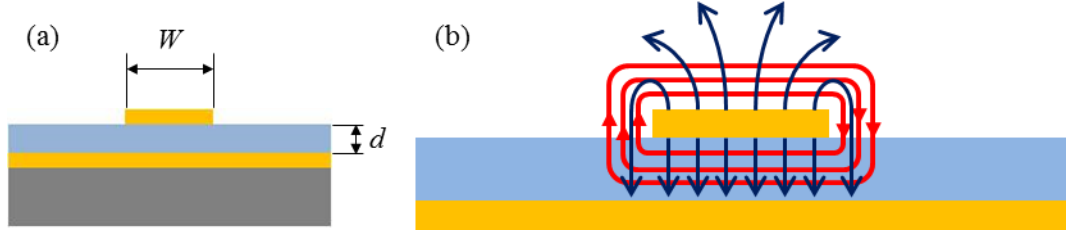


Figure 1.9: (a) MSL cross-section with the support substrate of an arbitrary permittivity (has no effect on transmission line characteristics), the ground plane metallization and the transmission line on top of the separating dielectric layer. (b) Electric (blue) and magnetic (red) field lines shown of the supported quasi-TEM mode.

The MSL has been used extensively in microwave engineering and has been pushed into the THz band. As a result, accurate terms describing the characteristic impedance and attenuation of this transmission line are readily available [30]. The characteristic impedance (Equations 1-7 and 1-8) is calculated from the geometry dimensions and the effective permittivity.

$$Z_0 = \frac{60}{\sqrt{\epsilon_{eff}}} \ln \left(\frac{8d}{W} + \frac{W}{4d} \right) \quad \text{for } W/d \leq 1 \quad 1-7$$

$$Z_0 = \frac{120\pi}{\sqrt{\epsilon_{eff} [W/d + 1.393 + 0.667 \ln(W/d + 1.444)]}} \quad \text{for } W/d \geq 1 \quad 1-8$$

Where W is the transmission line width, d is the dielectric thickness and ϵ_{eff} is the effective permittivity given by Equation 1-9.

$$\epsilon_{eff} = \frac{\epsilon_r + 1}{2} + \frac{\epsilon_r - 1}{2\sqrt{1 + 12d/W}} \quad 1-9$$

Where ϵ_r is the relative permittivity of the substrate. The attenuation of the transmission line is broken down into two contributing factors; the dielectric loss (α_d) and the conductor loss (α_c).

$$\alpha_d = \frac{k_0 \epsilon_r (\epsilon_{eff} - 1) \tan \delta}{2 \sqrt{\epsilon_{eff}} (\epsilon_r - 1)} \quad 1-10$$

$$\alpha_c = \frac{\sqrt{\frac{\pi f \mu_0}{\sigma}}}{Z_0 W} \quad 1-11$$

Where f is the frequency, μ_0 is the permeability of free space, σ is the metal conductivity, k_0 is the wave number and $\tan \delta$ is the loss tangent of the dielectric material. It is clear from these formulas for the attenuation of the MSL that the geometry and material choices need to be made with care. Initial MSLs measured with ps pulses used a silicon support substrate with a niobium transmission line and ground plane separated by a silicon oxide layer [49]. This was then substituted for more commonly used spin-on dielectric, benzocyclobutene (BCB) to separate the metals (aluminium, titanium: gold) [12, 50-60]. However, Peytavit *et al* suggested that the 250 °C curing temperature of the BCB was too high for some devices introducing a thermal stress as well as potential damage to the PC material [61]. As a result, Topas, which has a lower curing temperature (140 – 200 °C) was used [61]. Alternatively, polypropylene or kapton HN has been used for the dielectric separators, which are then attached to the ground planes using an adhesive layer [60].

To accommodate through-the-substrate optical excitation of the PC switches, the MSL can be fabricated on glass as opposed to Si, and the ground planes have two holes for the lasers. This introduces complications to the fabrication, however, such as the need to then align the PC material to the holes in the ground plane [57, 58]. These complications can be resolved by using an optically transparent, electrically conductive ground plane using a 1- μ m-thick indium tin oxide [62].

The MSL evanescent field has been used for THz-TDS absorption spectroscopy of polycrystalline materials up to 1.2 THz, demonstrating the spectroscopy with MSLs [12], but the majority of MSL spectroscopy has been focused on liquid samples; since the ground plane is electrically isolated by the dielectric substrate, it is very difficult for the liquid sample to short the transmission line. Therefore, by fabricating a crucible over the MSL to hold a small volume of liquid, a THz pulse can be transmitted through the sample and then detected to reveal any spectral information [54, 57]. As well as providing spectral information, the arrival time of the pulse also gives an insight into the refractive index of the

sample [54]. This technique has been utilised to distinguish between single strand and double stranded DNA, for example, as well as for the determination of the concentrations of dissolved material (such as proteins [63]) in water [54, 57, 64].

MSL dielectric sensing can be enhanced through the use of resonators; quarter wavelength stubs [51], ring resonators [65] and edge coupled resonators [56]. By observing the resonance shift, the dielectric constant of the overlaid samples (including dielectric material [66] and DNA [55]) can be determined. Whilst this method confines the sensing radiation to a smaller area thus increasing the sensitivity per volume of overlaid sample, it can only provide frequency specific dielectric information of the sample. Since the resonant frequency of the resonator is determined by the dielectric load, the substrate material and the filter geometry, it is not easy to tune the sensing frequency to an alternative sensing frequency.

The current bandwidth of MSLs stands at 2 THz for a 1-mm-long transmission line [67], limited by the finite permittivity of the substrate and the device geometry, although no absorption spectroscopy has been demonstrated beyond 1.2 THz.

1.4.2. Coplanar Transmission Lines

Coplanar transmission lines, CTLs, can be sub-categorised into three types: coplanar waveguides (CPW), coplanar slot-lines (CPSlot) and coplanar strip-lines (CPS). With all three, the signal conductor and reference conductor are on the same surface of the substrate material with the electric field distributed between them, which make them a very attractive design from a fabrication point of view; a working device can be achieved with a simple one-stage optical lithography and metallization process onto a suitable THz generating / detecting substrate such as LT-GaAs on GaAs [68, 69], ErAs:GaAs super-lattices on GaAs [70] and ion implanted silicon on sapphire [71-73].



Figure 1.10: Aerial view of (a) CPW, (b) CPSlot and (c) CPS. Yellow represents the metallization and the grey represents the substrate material.

In the three conductor CPWs it is possible to excite one of two quasi-TEM modes; the odd mode (also referred to as dipole and symmetrical modes; Figure 1.11a), or the even mode

(also referred to as quadrupole and asymmetric modes; Figure 1.11b). It is more common to excite the odd mode as the even mode has been found to be more dispersive and lossy [71, 74]. However, both modes can be found being generated in the same system which can introduce noise; therefore air bridges have been developed to suppress the even mode around the PC switches [69]. These typically consist of electrical connections between the two conductors on either side of the centre conductor. Alternatively, a CPS can be used where only a single mode is excited.

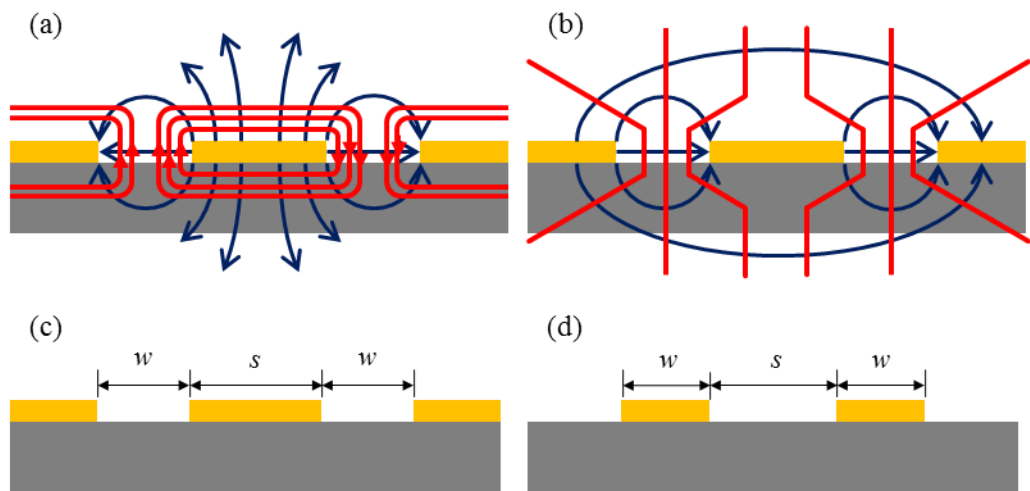


Figure 1.11: Cross section view of the CPW with the electric (blue) and magnetic (red) field lines for the (a) odd mode and the (b) even mode (also representative for field patterns supported by the CPS and CPSlot). The cross section view with geometry parameters for the (c) CPW and (d) CPS.

CTL theory is well established, particularly at microwave frequencies, defining terms for the characteristic impedance, relative permittivity and attenuation in terms of the material properties and the waveguide geometry. Here, the equations are presented for the CPS and the CPW; CPSlot is an uncommon geometry with very little literature defining theoretical terms for the transmission line properties.

Derived and experimentally reviewed by Frankel *et al*, terms for the characteristic impedance, Z , are given by Equations 1-12 and 1-13, where the subtext CPW and CPS denote the respective waveguide geometries [75, 76].

$$Z_{CPW} = \frac{120\pi}{\sqrt{\varepsilon_{eff}(f)}} \frac{K'(k)}{K(k)} \quad 1-12$$

$$Z_{CPS} = \frac{30\pi}{\sqrt{\varepsilon_{eff}(f)}} \frac{K(k)}{K'(k)} \quad 1-13$$

The effective permittivity is given by Equation 1-14 with the corresponding quasi-static effective permittivity and TE mode cut-off frequency given by Equations 1-15 and 1-16, respectively.

$$\sqrt{\varepsilon_{eff}(f)} = \sqrt{\varepsilon_q} + \frac{(\sqrt{\varepsilon_r} - \sqrt{\varepsilon_q})}{\left(1 + a \left(\frac{f}{f_{te}}\right)^{-b}\right)} \quad 1-14$$

$$\varepsilon_q = \frac{\varepsilon_r + 1}{2} \quad 1-15$$

$$f_{te} = \frac{c}{4d\sqrt{\varepsilon_r - 1}} \quad 1-16$$

Terms a and b are constants, and ε_r and d are the relative permittivity and thicknesses of the substrate, respectively. The metal geometry (Figure 1.11(c, d)) determined k is defined by Equation 1-17 and 1-18.

$$k = \frac{s}{s + 2w} \quad 1-17$$

$$K'(k) = K\left(\sqrt{1 - k^2}\right) \quad 1-18$$

It is clear from the breakdown of the initial formulae describing the characteristic impedance of both the CPW and the CPS, that their respective metal geometry and substrate material govern their characteristic impedance. As a result, to remove any potential reflections due to impedance mismatches (see Chapter 2), the substrate material and thickness need to remain constant and geometry of the waveguide kept consistent. This will prove problematic when

defining the THz generation and detection schemes such as probe arms and the introduction of electro-optic and photoconductive materials.

The attenuation coefficients are defined by Equations 1-19 and 1-20. A more in depth discussion of the origin of these equations can be found in reference [75]. There is a strong frequency dependence of the attenuation coefficient (f^3) suggesting a strong bandwidth limitation for CPW and CPS geometries due to attenuation with a sharp cut-off frequency. Nevertheless, there was a good agreement between the experimental results and theory.

$$\alpha_{CPW} = \left(\frac{\pi}{2}\right)^5 2 \left(\frac{\left(1 - \frac{\epsilon_{eff}(f)}{\epsilon_r}\right)^2}{\sqrt{\frac{\epsilon_{eff}(f)}{\epsilon_r}}} \right) \frac{(s + 2w)^2 \epsilon_r^{1.5}}{c^3 K'(k) K(k)} f^3 \quad 1-19$$

$$\alpha_{CPS} = \pi^5 \frac{(3 - \sqrt{8})}{2} \sqrt{\frac{\epsilon_{eff}(f)}{\epsilon_r}} \left(1 - \frac{\epsilon_{eff}(f)}{\epsilon_r}\right)^2 \frac{(s + 2w)^2 \epsilon_r^{1.5}}{c^3 K'(k) K(k)} f^3 \quad 1-20$$

The attenuation can be further expanded to break down the origin of the attenuation; conductor and dielectric losses. Another loss mechanism of the transmission line is the Cherenkov shockwave; this occurs when the charge moves faster than the phase velocity of the electromagnetic radiation in a material. Griscowsky *et al* showed that this occurs in ultra-short pulses propagating along multi-conductor transmission lines such as CTLs, since the substrate has a non-unity dielectric constant, the group velocity will be greater than the phase velocity in the dielectric resulting in the Cherenkov shockwave [73]. This radiation loss is shown to be significant; at 800 GHz, after 1 mm transmission along a CPS on an ion doped silicon-on-sapphire (SOS) substrate, the power was attenuated to 1/e of the original magnitude.

There are two ways to reduce the attenuation of the transmission line, particularly at the higher frequencies. The first is to change the metallization geometry, and the second is to reduce the effective permittivity. The latter can be achieved by using alternative lower permittivity substrate materials such as low permittivity plastics (Tsurupica, $\epsilon_r = 2.3$) [64, 77, 78], BCB [79] and quartz [78], where the pulses are generated using a van der Waals bonded LT-GaAs PC switch and detected using either a second PC switch or positional EO detection.

Alternatively, the presence of the material around the transmission line can be reduced by either thinning the substrate or removing the material from between the conductors. In the substrate thinning approach (Figure 1.12a), a membrane substrate and transmission line are fabricated on a sacrificial substrate which is later removed in a wet etch. This was initially demonstrated using a GaAs quantum well fabricated on a 1.97- μm -thick etch stop layer of AlGaAs on top of the sacrificial GaAs [80], but was then modified for a more robust membrane consisting of a 300-nm-thick silicon layer trapped between a 700-nm-thick and 400-nm-thick silicon nitride layers, grown on a sacrificial silicon wafer [74, 81]. This results in a transmission line supported by a thin membrane with an effective permittivity approximately that of free space. The membrane's structural integrity limits its applications, but bandwidth greater than 1 THz has been reported (with no maximum stated). As well as increasing the bandwidth, the dispersion differences between the odd and even modes has been significantly reduced [74]. The membrane's structural integrity can be improved upon, by mounting the membrane onto an aerogel substrate [82]. Aerogel improves the structure without loading the effective permittivity of the transmission line; however, it is very porous and will trap water moisture and organic material, limiting the spectral applications of the CPTs to dry testing, though the preparation of the aerogel can be modified to make the silica hydrophobic [83].



Figure 1.12: (a) A simplified schematic of a CPW on a membrane substrate as demonstrated by references [74, 80, 81]. The waveguide (yellow) is defined on the membrane using standard cleanroom processing before the material beneath the waveguide is etched away using wet etching. (b) A simplified schematic of a coplanar-air transmission lines demonstrated by references [84, 85]. The waveguide is defined similarly to (a) except the material is etched top down from between the metal.

An alternative approach removes the substrate material from between the conductors by chemical etching, relying then on the structural strength of the metallization on silicon dioxide to hold its shape (Figure 1.12b) [84, 85]. These are known as coplanar-air transmission lines (CAT). The downside of this design for spectroscopy applications is the

difficulty of placing samples on the transmission line without damaging the metallization and the presence of previously measured samples clogging the etched channel.

The evanescent field of the CPS has been utilised for spectroscopy of solid polycrystalline materials however no liquid samples have been tested [64, 72, 78]. This is likely to be due to complications arising from the sample under test electrically shorting the conductors. For the analysis of polycrystalline samples, the powdered material is placed over the transmission line between the THz generator and detector, or over a terminated length of transmission line. In the latter case, the generated pulse propagates along the transmission line and is reflected off the terminated line (see Chapter 2) back to the generating switch: the TDS spectra of the input pulse will then reveal a transmitted pulse after some period of time, which contains the information of the overlaid material. This method is particularly effective in doubling the effective sensitivity length of the transmission line, as the pulse will interact with the same sample twice.

As well as investigating overlaid materials, two dimensional electron systems (2DES) have also been studied, utilising the ability of the chip to be fabricated with waveguides on either side of a nano-scale geometry, as well as the ability to grow multi-layer systems which can be investigated with a lithographically defined waveguide [86, 87]. In this process, the 2DES is grown using molecular beam epitaxy with an incorporation of an LT-GaAs layer. The waveguide is then defined on the top (electric field coupling) or a section channel of the 2DES is etched to define a small transmission line (electric field injection) to review the THz interaction properties with the 2DES. The system is cooled to low temperatures (~ 8 mK) and ps pulse generation and detection is achieved using fibre coupled optical excitation of PC switches.

1.4.3. Planar Goubau Lines

The planar Goubau line, PGL structure consists of a single electrical conductor on a supporting substrate with no ground planes. Supporting a single quasi-TM mode, the structure has been studied using a range of modelling packages to determine the electric field properties. A simplified representation of the cross section across and along the PGL is shown in Figure 1.13. However, within all the theoretical modelling and practical testing of PGLs, a lot of the theory behind the waveguide remains undefined, unlike CPWs and MSLS, such as terms for characteristic impedance and cut-off frequencies. As a result, the PGL

geometries have been arbitrary, but a 5- μm -width has become the norm since Debuissou's optimisation of S parameters in 100 – 300 GHz frequency range [88].

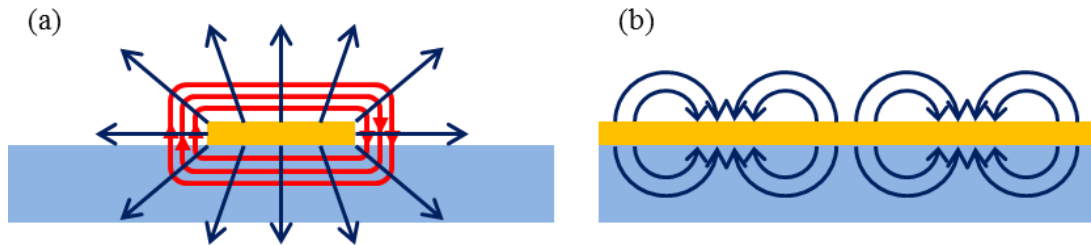


Figure 1.13: (a) Cross section view of a PGL showing both the electric (blue) and magnetic (red) field lines shown of the supported quasi-TM mode. (b) Cross section view along the propagation path to illustrate emerging and terminating electric field lines (magnetic field not shown).

The PGL is excited by a planar horn antenna fed from a CPW structure. This method of exciting the PGL on a planar surface was developed by Treizebré by taking a two dimensional interpretation of Goubau's horn antenna for launching the PGL's TM mode along a free standing wire from the TEM mode supported by the CPW [89]. Treizebré's work however was limited to frequencies up to 220 GHz due to the use of a vector network analyser (VNA). This has since been increased to 45 GHz – 325 GHz range using separate VNAs to build up the analyzed spectral range; 45 – 110 GHz, 140 – 220 GHz and 220 – 325 GHz [90]. Nevertheless, the PGL – CPW transition was optimised to improve the energy efficiency of the transition by substituting the linear tapering away of the ground plane for a curved geometry taken from inspiration of Vivaldi antennas (although no details were given regarding the nature of the curve such as radius size or polynomial geometry terms) as shown in Figure 1.14 [91, 92]. The latest coupling efficiency quoted for the PGL – CPW transition is 80 % [93].



Figure 1.14: Different geometries of CPW – PGL transitions defined with (a) single stage linear transition [91], (b) a double stage linear transition [92] and (c) the curved transition of the ground planes [91].

Due to the CPW – PGL excitation through the use of a horn antenna, it has been reported that as well as the PGL modes, substrate modes are also excited [90]. By exciting multiple

modes in the transmission line, there is an increase in the loss of the transmission line. Nevertheless, the excitation of the substrate modes has been compared with a dielectric waveguide where the cut off frequency is given by Equation 1-21.

$$f_c = \frac{c}{2\sqrt{\mu\epsilon_r}} \sqrt{\left(\frac{m}{a}\right)^2 + \left(\frac{n}{h}\right)^2} \quad 1-21$$

Where a is the PGL excitation width (defined by the horn dimensions), h is the substrate thickness, and m and n are the mode numbers [90]. It is clear from the term; the cut off frequency is dependent on the PGL horn geometry, the substrate material and the substrate thickness. Therefore to suppress the substrate modes to improve the clarity of the detection of the PGL mode substrate permittivity needs to be increased or the substrate thickness made thicker. However the implication of these modifications has a negative impact on the bandwidth of the PGL (see Chapter 2).

Whilst VNA measurements are well established, they are bandwidth-limited by the VNA (PGL systems utilising VNAs have been tested up to 325 GHz, whilst the highest frequency of commercially available VNA is 1.1 THz [94], setting the current bandwidth limits). To enhance the bandwidth of the PGL to 800 GHz for 0.7 mm transmission line, LT-GaAs PC switches and TDS operation was introduced [95]. Using PC switches for both generation and detection of ps pulses in the CPW regions of the VNA device design, pulses are generated, transmitted along the PGL and detected in the detecting CPW PC switch. An FFT is performed on the ps pulse to reveal the frequency spectra. This method currently lacks the frequency resolution of the VNA measurements but has significantly improved the bandwidth over the VNA. This method has since been used by Gacemi *et al*, but with an ion irradiated $\text{In}_{0.53}\text{Ga}_{0.47}\text{As}$ PC switch for THz generation and EO (ZnTe) detection [96]. The bandwidth was not recorded, but theoretical interpretations of the PGL mode were confirmed using the freely positional EO detector; the amplitude and polarity of the electric field across the cross section of the superstrate above the PGL are plotted in Figure 1.15. The attenuation and dispersion of the transient pulse as a function of the propagation distance are also presented within the paper, showing the both the pulse amplitude and width degrading with propagation length.

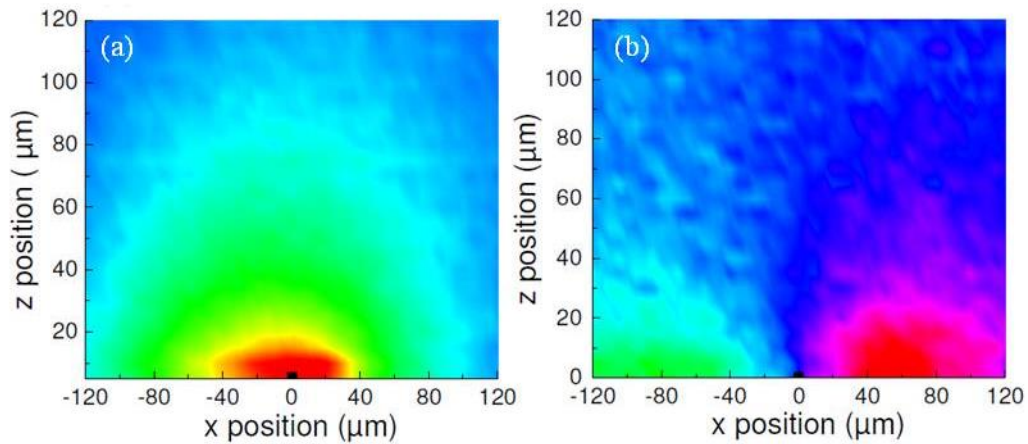


Figure 1.15: The cross-section view (PGL propagation out of the page) of a 5- μm -wide PGL's evanescent electric field measured using a positional external EO detection [96]. The orientation of the EO crystal is rotated 90° between (a) and (b) to reveal the nature of the PGL mode.

With the generation and detection of the PGL mode established for both VNA and ps pulse measurements, the field of focus has turned onto the PGL itself. The electric field can be manipulated for specific applications by changing the metallization geometry of the PGL; changing the width of the PGL has been shown to theoretically alter the extent of evanescent field [88, 97] while corrugations introduced into the PGL can reduce the propagation velocity (the deeper the corrugation, the slower the pulse propagates) and increase the extent of the evanescent field [98]. The introduction of corrugations is a 2D interpretation of a method used in single wire experiments [99, 100].

PGLs have also been utilised for dielectric sensing with the incorporation of resonators. These have been achieved with periodic corrugations in the PGL [101], spiral resonators [102], quarter wavelength stubs [95] and split-ring resonators [103]. For each, a frequency specific resonance can be altered by loading the filter with a sample under test. This method of sensing (with VNA excitation) has been used for liquid sensing of different concentrations of lysozyme in solutions [104]. However the preferred choice for microfluidics sensing using PGL has been to measure the change in the transmission parameters using a VNA up to 110 GHz [105-108].

As well as resonators, power dividers have been both theoretically and experimentally demonstrated as a potential method to realise multiport systems by splitting the PGL into two or more lines [90]. Similarly to power dividers, a Mach-Zehnder interferometer has been theoretically modelled at 1 THz, but experimentally tested only for the 40 – 110 GHz

frequency range, by breaking the PGL into two and recombining them again after a length of PGL [109]. By making the two separate PGLs different lengths, destructive interference occurs at fixed frequencies resulting in a rejection band in the frequency spectra. This rejection band can be shifted by a dielectric loading of one of the PGLs. This device configuration allows sensitive measurements of overlaid materials.

The bandwidth of PGLs have been practically limited to 800 GHz which has discouraged its use for THz spectroscopy applications as it falls short of the interesting frequency range where spectral features are more commonly found. The bandwidth could potentially be increased by using membrane devices, but has never been practically implemented for PGLs [103, 110]. As well as having an upper frequency limit determined by the dispersion and attenuation of the transmission line, the PGL is unable to support the lower frequencies (a characteristic of the supported TM mode) which can be supported by CPWs and MSLs (both supporting TEM modes) which may discourage designers from opting to use these geometries.

1.5. On-chip Generation and Detection of Picosecond Pulses

This section presents a review of ps pulse generation and detection methods used for on-chip systems, concentrating particularly on electro optic (EO) and electro absorption (EA) detection, before giving a more in depth review of photoconductive (PC) generation and detection since this is the method used in the work presented here.

1.5.1. Electro Optic Detection

Electro optic (EO) detection utilises the change in the refractive index of an EO material as a function of the applied electric field. The electric field applied can therefore be used to modulate the optical properties of the crystal. Figure 1.16 shows a schematic setup which is used to practically implement the EO detection scheme. Here, the probing optical pulse which has been split from the pulsed laser used to generate the THz radiation (see Figure 1.4), is focused onto the same spot on the EO crystal which the THz radiation is striking. An interaction between the co-propagating beams, caused by the birefringent properties of the EO crystal causes an optical change in the probe beam which is then detected using a quarter wave plate and Wollaston prism to elliptically polarise and split the orthogonal parts, respectively. The orthogonal components are then compared with one another to reveal the change in the electric field amplitude. To understand the advantages and limitations of this

method for EO detection for on-chip systems, the individual components of the detection scheme should be studied individually.

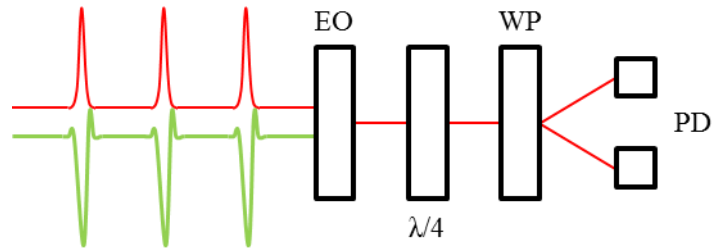


Figure 1.16: A simplified schematic of the EO detection scheme. The probing optical pulse (red) and THz pulse (green) have been vertically offset for clarity. Both the THz and optical pulse propagate collinearly through the electro-optic (EO) crystal. The optical pulse then propagates through the quarter wavelength plate ($\lambda/4$) before being split into its orthogonal components by the Wollaston prism (WP), which are then compared to one another by balanced photodiodes (PD).

The refractive index (n) of the EO detector as a function of the applied electric field is given by;

$$n = n(E) \quad 1-22$$

Which can be expanded as a Taylor series to;

$$n = n + a_1 E + a_2 E^2 \quad 1-23$$

Where a_1 and a_2 are the linear and the second order EO coefficient, respectively. The change in the refractive index due to the linear term is known as the Pockels effect and the non-linear change due to second order term is known as the Kerrs effect. All materials exhibit the Kerrs effect but only non-centro-symmetric materials exhibit the Pockels effect [111].

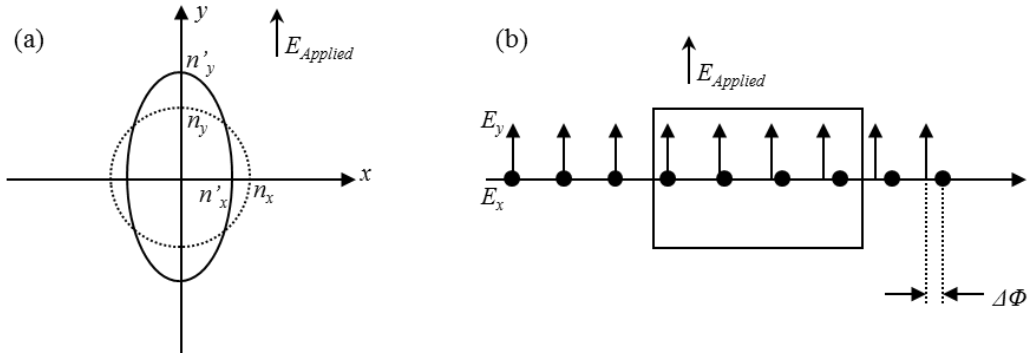


Figure 1.17: (a) Schematic showing the x and y components of refractive index before (n) and an applied electric field (n'). (b) Schematic showing phase shift ($\Delta\Phi$) in x (out of the page) and y (upwards) components of light as it propagates through an EO crystal under an external electric field bias. Figure reproduced from reference [112].

The change in the refractive index due to the applied electric field, shown in

Figure 1.17 can be expressed as the change in the refractive index of the x and y components as the wave propagate along the z axis;

$$n'_x = n_x + \frac{1}{2}n_x^3 r E_{applied} \quad 1-24$$

$$n'_y = n_y + \frac{1}{2}n_y^3 r E_{applied} \quad 1-25$$

Where r is the material dependent Pockels coefficient. Therefore if the optical beam travelling through an EO crystal of length L under a bias of $E_{applied}$, is considered in terms of phase change, Φ_x and Φ_y , then the change in phase, $\Delta\Phi$ can be calculated as the difference between the two components [112];

$$\Delta\phi = \phi_x - \phi_y = \frac{2\pi L n_0^3 r E_{applied}}{\lambda} \quad 1-26$$

Equation 1-26 suggests that to increase the phase shift between the two components for fixed electric field strength, an EO material should be chosen with as large as possible refractive index or Pockels coefficient, or with large interaction length used. Alternatively, a shorter wavelength optical field could be used. As the EO crystal is being used to detect a travelling THz pulse as opposed to a uniform static electric field, further considerations need to be made with regards to the phase matching of the THz propagation and optical propagation through the EO crystal (though this can be counteracted through thinning the EO crystal at a cost of reducing the sensitivity [6]). The material needs to be chosen with considerations to

the potential phonon modes being in the desired frequency spectrum. Table 1-1 highlights some of the more commonly used EO materials with the corresponding material parameters. Whilst 4-dimethylamino-N-4-stilbazolium-tosylate (DAST) has the largest Pockels coefficient, and a reasonably low dielectric constant, it has a TO phonon absorption at 1.1 THz, whereas the other materials have larger dielectric constants, but a broader phonon-free bandwidth. As well as choosing the material according to its sensitivity properties, consideration must also be made with regard to the system operating-wavelength of light.

Material	Dielectric constant (a.u)	Pockels coefficient (pm/V)	TO phonons (THz)
ZnTe	10.1	4.04 (633 nm)	5.3 [113]
GaP	-	1 [114]	11 [113]
InP	-	1.4 [115]	10.4 [113]
LiTaO ₃	41	30.5 (633 nm)	6 [116]
LiNbO ₃	43	30.9 (633 nm)	7.5 [117]
DAST	8	160 (820 nm)	1.1 [118]
GaAs	13	1.43 (1150 nm)	8 [16]

Table 1-1: Table highlighting the EO materials used the THz detection with their corresponding Pockels coefficient (with measured optical wavelength in brackets), lowest TO phonon frequency and dielectric constant. Values are taken from [119] unless stated.

The phase shift is detected by splitting the x and y components of the optical beam using a Wollaston prism. Wollaston prisms are made from optically anisotropic (birefringent) materials where the two orthogonal components of the incident light experience different refractive indices. By placing two pieces of birefringent materials offset 90° from one another along the optical axis, the prism wedge angle can be engineered to design the divergence angle of the two beams (Figure 1.18). The intensities of the two beams are compared with one-another using balanced photodiodes in order to determine change in the phase shift of the beam incident on the Wollaston prism.

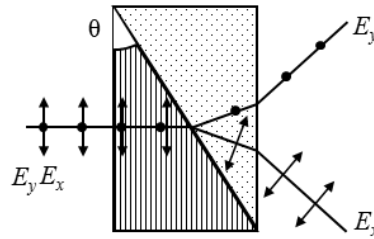


Figure 1.18: Schematic of a Wollaston prism where two wedges, of angle θ , of birefringent material with their optical axis offset by 90° (vertical lines and dots (denoting axis into page)). The electric field of the incident optical beam is split into the two polarities; E_x and E_y . Figure reproduced [112].

There are two reported types of EO detection systems for on-chip systems: internal EO, where the EO material is fabricated onto the transmission line. And external EO, where the EO crystal is on a probe head placed over the transmission line to detect the evanescent field.

External EO (Figure 1.19), though not strictly an on-chip method, has been used to detect THz pulses on CPW [120], MSL [60] and PGL [96] with the EO crystal placed onto an arbitrary point along the transmission line. The probe beam (1.55- μm -wavelength for ZnTe EO crystal [120], 750-780 nm for LiTaO₃ [59, 60]) is fed into and from the crystal via total internal reflection in prisms. The THz pulse then co-propagates through the crystal with the probe beam where the pulse interferes with the probe beam via the EO crystal. The laser pulse is then received and subjected to polarization detection.

External EO detection has proven useful for determining the extent, polarity and magnitude of the evanescent field as well as being able to plot the pulse shape at arbitrary points around the transmission line, but due to the relatively high permittivity of the EO crystal (Table 1-1), the external EO method is considered invasive [121]. This invasiveness has since been reduced by the use of organic materials (DAST) with a lower permittivity and good EO properties [122], however Desplanque *et al* had highlighted that the organic material produces high losses in the THz region [121].

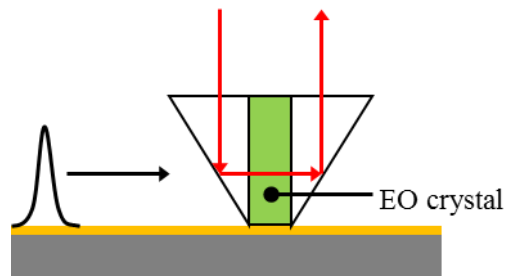


Figure 1.19: External EO detection used for on-chip systems demonstrated by Meigien *et al* [120]. The ps pulse (black pulse on left) propagates along the CPW into the EO crystal (green) (ZnTe). 1.55- μm -wavelengths, 130-fs-FWHM laser pulse (red arrows) is manipulated by the THz pulse biased EO crystal.

Internal EO detection (Figure 1.20) can be achieved by one of two methods. The first is to use a transmission setup where the probe beam is focused onto the EO material and with the transmitted beam collected on the other side; the chip is made by either gluing a PC material (Cr:GaAs) next to an EO material (LiTaO₃) with the transmission line running across both [123] or by using a substrate material with both PC and EO properties (LT-GaAs). The first chip design suffers impedance mismatch at the material boundary resulting in a THz pulse reflection along the transmission line. Using the same substrate for PC detection and EO detection removes this discontinuity, but usually requires two separate wavelengths for different photon energies (greater than the substrate band gap for pulse generation and less than for EO detection) which can be achieved by frequency doubling [124], although the same wavelength generation and detection has been demonstrated with photon energies (optimised to ~ 900 nm for LT-GaAs) just below the band gap energy where the PC generation is achieved by exciting band tail states [125].

An alternative internal EO method collects the reflected signal; the beam is focused into the substrate material for EO detection, but is then reflected off the substrate/transmission line metallization boundary to the detector [124, 126]. As with the transmission EO detection method, the substrate needs to have EO properties.

EO detection for on-chip systems has proven useful for characterizing devices, detecting pulse shapes and amplitude as well as the polarity of the pulse at arbitrary points along and around the transmission line, but does suffer drawbacks including the high permittivity of the EO crystal causing impedance mismatch. When thinned to combat the impedance mismatch, the EO detection sensitivity is reduced. EO materials also suffer phonon absorptions but these currently exceed the bandwidth of the transmission lines and therefore not considered an issue for on-chip devices with the exception of DAST.

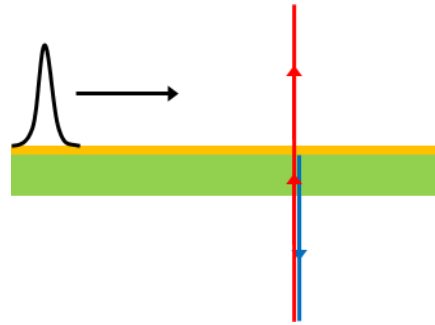


Figure 1.20: Internal EO schematic diagram showing both transmitted (laser between the CPS metal) and reflected (off the substrate/metal interface) EO detection schemes. Red line shows the incident and transmitted laser and blue the reflected laser.

1.5.2. Electro Absorption Detection

Electro absorption (EA) uses the intrinsic Franz-Keldysh effect in semiconductors for detection of THz pulses propagating along transmission lines, removing the need for modifications to the geometry of the device to include a PC switch or EO detectors. The Franz-Keldysh effect is the change in optical absorption due to a change in the applied electric field. By using the strength of absorption due to the EA material under influence of the THz pulse, the absorption of the reflected laser pulse (with an energy below the band gap of the EA material) at a specified point along a transmission line can be used to determine the magnitude and shape of the transient THz pulse, using a photodiode to detect the reflected light intensity (Figure 1.21). The sensitivity of the detection is increased with a larger static field (i.e a larger DC bias on the PC switch) thus simultaneously increasing the generated pulse amplitude and detector sensitivity [127].

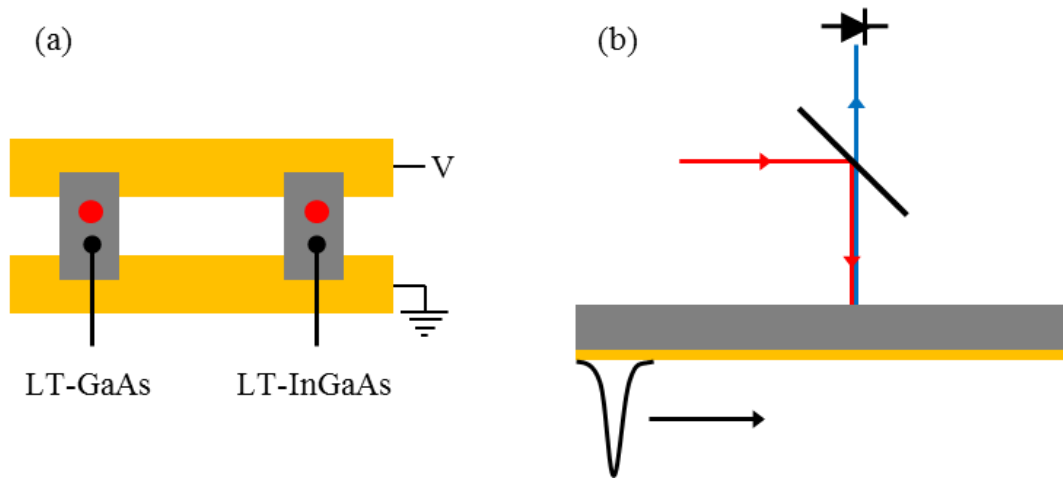


Figure 1.21: (a) Schematic diagram for PC switch generation and EA detection as demonstrated by Desplanque *et al* where the CPS (yellow) sits on the quartz substrate [121]. Red spots denote the excitation and probe lasers. (b) Schematic setup showing detection setup for reflective EA detection. Red line and arrow shows the incident laser path whereas the blue shows the reflected going through the mirror to the photodiode. The THz pulse is shown propagating along the transmission line (CPS).

Lampin *et al* [127] used EA for detecting ps pulses propagating along a CPS on a GaAs substrate but found the FWHM of the transmitted pulse to be wide due to the high permittivity of the GaAs substrate causing severe dispersion in the pulse, leading to an alternative design on a quartz substrate (EA material – LT-AlGaAs van der Waals bonded to define detection regions and PC material – LT-GaAs bonded to define the ps pulse generation regions) reducing the dispersion in the transmission leading to an improvement in the bandwidth to 2.5 THz [121]. However two separate materials were required; one for THz generation via PC switch (LT-GaAs) and one for THz detection (LT-AlGaAs) as seen in Figure 1.21, thus increasing the complexity of the fabrication process.

Though EA has been proven to be useful for minimally invasive detection of THz pulses providing the base material is suitable and reducing the need for discontinuities in transmission lines to accommodate detector needs, there are several drawbacks to the method; EA is not polarity sensitive and therefore unsuited for mode detection, the choice of substrate material is limited unless van der Waals bonding is used, the method is limited to parallel tracks and therefore unsuitable for PGLs.

1.5.3. Electro Optic Generation

To understand electro optic (EO) generation, there must first be an understanding of second harmonic generation (SHG) which uses the non-linear optical effects of non-centro-symmetric dielectric materials. A high energy laser with optical electric field, E is focused onto the material causing an induced localised polarisation, P . The applied field and the polarization are related by [111];

$$P = \varepsilon_0 \chi E \quad 1-27$$

Where χ is the electric susceptibility of the material. Equation 1-27 can be expanded using a Taylor series;

$$P = \varepsilon_0 \chi_1 E + \varepsilon_0 \chi_2 E^2 + \varepsilon_0 \chi_3 E^3 + \dots \quad 1-28$$

Where only the first, second and third orders are shown with further terms being of negligible value. All materials have a finite χ_3 term whereas only non-centro-symmetric material have a χ_2 value, thus for SHG operation, the third harmonic term becomes negligible. Rewriting Equation 1-28 to get a term defining the exciting oscillating optical electric field:

$$E = E_0 \sin(\omega t) \quad 1-29$$

The induced localised polarization can be written as;

$$P = \varepsilon_0 \chi_1 E_0 \sin(\omega t) - \frac{1}{2} \varepsilon_0 \chi_2 E_0 \cos(2\omega t) + \frac{1}{2} \varepsilon_0 \chi_2 E_0 \quad 1-30$$

Equation 1-30 demonstrates the induced permanent polarization (no harmonic) and the first and second harmonic polarization terms. The harmonic oscillations of the polarized atoms can be considered as oscillating dipoles which produce an electric field of the same frequency. Therefore electric waves of frequencies ω and 2ω are emitted where ω is the frequency of the applied optical electric field of magnitude E .

Difference frequency mixing, DFM uses these same materials but with two optical biases of different wavelengths where the difference between the two is that of the desired wavelength. The sum of the two electric fields incident on the EO material is given by;

$$E_{total} = E_1 \sin(\omega_1 t) + E_2 \sin(\omega_2 t) \quad 1-31$$

Where the subscripts denote bias wavelength 1 and 2. The instantaneous power is given by;

$$P \propto (E_{total})^2 \quad 1-32$$

Thus substituting Equation 1-31 into Equation 1-32, we obtain:

$$P = \frac{E_1^2}{2}(1 - \cos(2\omega_1 t)) + \frac{E_2^2}{2}(1 - \cos(2\omega_2 t)) + \frac{2E_1 E_2}{2}(\cos((\omega_1 - \omega_2)t) - \cos((\omega_1 + \omega_2)t)) \quad 1-33$$

Equation 1-33 shows the four emitted frequencies; $2\omega_1$, $2\omega_2$, $\omega_1 + \omega_2$ and $\omega_1 - \omega_2$. For continuous wave (CW) THz generation, the applied optical electric field wavelengths are those around 800 nm emitted from Ti:sapphire lasers. The sum and doubling of frequencies produce wavelengths in the optical regions of the spectrum whereas the difference of frequencies lies in the electrical region. Therefore only the difference frequency was coupled in to electrical waveguides. Verghese *et al* used continuous wave DFM as a source for a CPW (0 – 22 GHz measured using VNA) [128] where the EO material was excited using free space lasers and fibers.

Alternatively EO generation can also be used to generate a THz pulse which contains a broad range of frequency elements in a method known as optical rectification (OR). This is achieved, similarly to photoconductive switching, using a single femtosecond pulse to excite the EO material. The DFM occurs within the frequency spectrum of the pulse thus removing the need for two lasers. The narrower the bias pulse, the greater the frequency spectrum, therefore a broader bandwidth device, however there are still discrete frequencies within the spectrum separated by the repetition rate of the laser [6]. This method has been used for generation of THz pulse on CPS where the EO material used as the substrate material (an embedded copolymer material) [129] or superstrate material (LiTaO₃) [130] with an arbitrary substrate (with respect to pulse generation).

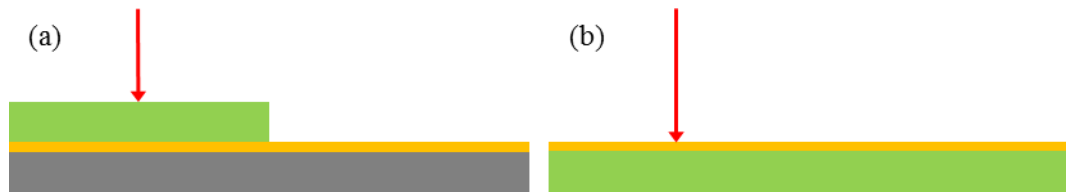


Figure 1.22: Schematic diagram of EO generation with the EO material (green) as a (a) superstrate on an arbitrary substrate (grey) CPS and the (b) EO material substrate.

1.5.4. Photoconductive Generation and Detection

Photoconductive (PC) switches can be used for both ps pulse generation and detection for on-chip systems by exploiting the photo-conductivity of semiconductor materials. When a photon with energy greater than the band gap of the material interacts with an electron in the valence band, the electron is excited to the conduction band leaving a hole behind. Both the electron and the hole contribute to the conductivity of the material, which is obtained by introducing an external bias field (Figure 1.23). During PC generation of pulses, the DC or chopped bias provides the external electric bias whereas in detection; the detected THz electric field pulse is the external bias.

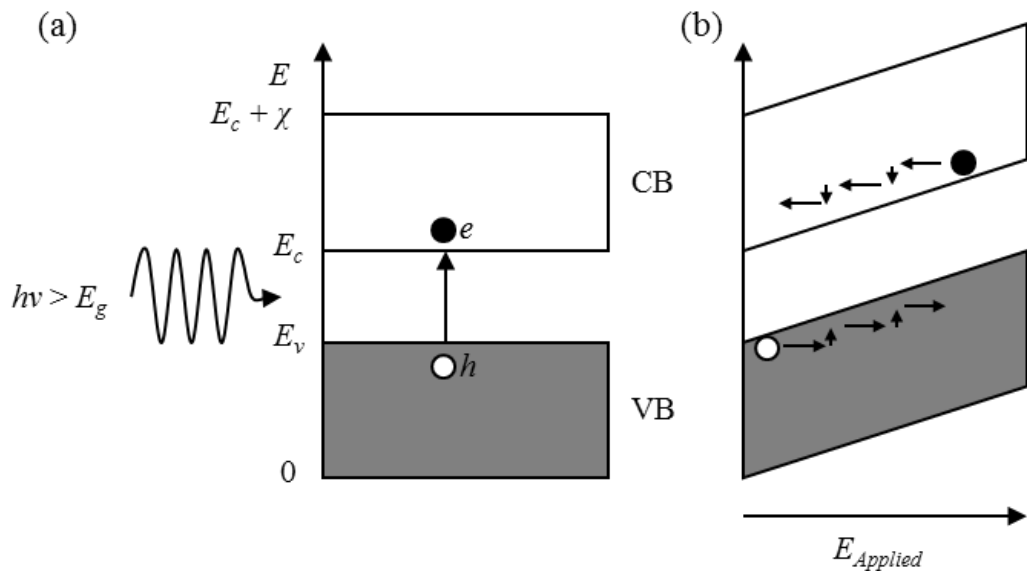


Figure 1.23: (a) An energy band diagram of semiconductor highlighting the photo-excitation of the electron from the valence band, VB to the conduction band CB. (b) Energy band diagram of semiconductor under a bias electric field $E_{Applied}$ with the resulting direction of drift the electrons and holes highlighted.

To further understand the THz generation and detection using a PC material, the formulae describing the behaviour of the PC base material under photoconductive operation needs to be understood. Though the following formulae have been derived for free space emitters, the resulting concepts can be carried through to on-chip systems. The emitted electric field, E_{THz} radiated from the PC switch is proportional to the change in the transient photocurrent density, J :

$$E_{THz} \propto \frac{\partial J}{\partial t} \quad 1-34$$

Where the current density can be defined as:

$$J = e[n_e v_{de} + n_h v_{dh}] \quad 1-35$$

Where n_e and n_h denote the electron and hole densities respectively, e the electron charge and v_{de} and v_{dh} denote the drift velocities of the electrons and holes. Therefore with the combinations of the two formulae, it can be determined that the emitted THz radiation can be defined by:

$$E_{THz} \propto e \left[n \frac{\partial v_{de}}{\partial t} + p \frac{\partial v_{dh}}{\partial t} + v_{de} \frac{\partial n_e}{\partial t} + v_{dh} \frac{\partial n_h}{\partial t} \right] \quad 1-36$$

The formula suggests that the THz electric field amplitude is determined by the rate of change in the carrier densities and the rate of change in the drift velocities. During photo excitation of the PC switches, the rate of change in carrier densities is determined by the rise time of the laser pulse used to excite the material [131]:

$$\frac{\partial n}{\partial t} = -\frac{n}{\tau_t} + G(t) \quad 1-37$$

Where τ_t denotes the carrier lifetimes of the material, n is the carrier density and $G(t)$ is the generation rate due to the laser which is given by [131]:

$$G(t) = n_0 e^{\left(\frac{t}{\Delta t}\right)^2} \quad 1-38$$

Where n_0 is the initial carrier density, and Δt is the pulse width of the exciting laser beam. Based on the formula, a shorter excitation pulse will yield a greater electric field amplitude. It has also been shown that as the laser power increases, the pulse amplitude increases as well (Chapter 3).

The rate of change in the drift velocities is determined by both the applied local electric field and the material's drift mobility [132]. The rate of change in the drift velocities can be given by:

$$\frac{\partial v}{\partial t} = -\frac{v}{\tau_{rel}} + \frac{eE_{Local}}{m_{eff}} \quad 1-39$$

Where v is the drift velocity, τ_{rel} is the momentum relaxation time for the carriers, m_{eff} is the effective mass of the carriers and E_{Local} is the local electric field strength, which is related to the applied electric field, $E_{Applied}$ by:

$$E_{Local} = E_{Applied} - \frac{P}{3\epsilon_r} \quad 1-40$$

The local field is dependent on the applied field, relative permittivity of the PC material, ϵ_r and the polarization induced by the separation of the electrons and holes, P :

$$\frac{\partial P}{\partial t} = -\frac{P}{\tau_{rec}} + J \quad 1-41$$

Where τ_{rec} is the recombination time of the electron hole pair. The relationship between the applied field and the drift velocity is defined by the drift mobility [111]:

$$v_{de} = \mu_e E \quad 1-42$$

$$v_{dh} = \mu_h E \quad 1-43$$

Where μ_e and μ_h are the electron and hole motilities, respectively. To produce high THz amplitude emission, the mobilities need to be large when considering the PC materials to be used.

For a THz bandwidth system, the generated pulse must also have a narrow FWHM (since the narrower the pulse, the greater the potential bandwidth). Therefore a fast rise and fall time is required in the transient pulse; the fast rise time is ensured by using a laser pulse with a narrower pulse width, hence faster rise time, which is provided by Ti:Sapphire lasers (100 fs) in this project. The fast fall time of the THz pulse is determined primarily by the material carrier lifetimes. Therefore material considerations are critical for the successful operation of a THz PC switch.

1.5.4.1. Material Considerations

Low-temperature-grown gallium arsenide, LT-GaAs is the most commonly chosen material for PC switches designed to operate at THz frequencies owing to its characteristic properties which can be altered based on growth temperatures and post growth anneal temperatures; band gap energy, short carrier lifetimes, high resistivity, high electron mobility and high electric field breakdown [133], though other materials (listed in reference [134]) such as silicon on sapphire (SOS), indium phosphide (InP), semi insulating (SI)-GaAs, graphene [135] and LT-indium aluminium arsenide (LT-InAlAs) have been tested. The first clear comparison comes from the carrier lifetimes of the materials, which can be seen in Table 1-2, where LT-GaAs is shown to have the shortest carrier lifetime. Another comparison made by the same group, was the PC switch response which demonstrates a significant amplitude difference between LT-GaAs, LT-InAlAs and SOS with LT-GaAs being 4.6 times larger than the other materials [134]. This magnitude difference was seen to be five times difference by reference [136].

Material	Carrier lifetime (ps)	Band gap at 300 K (eV)	TO phonon (THz)
Cr: doped GaAs	50 – 100	-	-
Ion-implanted InP	2 – 4	1.29 [137]	9 [114]
Ion-damaged SOS	0.6	-	-
Amorphous Si	0.8 – 20	1.55 [138]	-
MOCVD CdTe	0.45	1.606 [137]	4.3 [139]
LT-GaAs (MBE @ 200 °C)	0.3	1.41 [137]	8 [16]
In _{0.52} Al _{0.48} As (MBE @ 150 °C)	0.4	1.439 – 1.558 [140]	-
Irradiated In _{0.53} Ga _{0.47} As	0.2 [141]	0.75 [141]	6.8 & 7.6 [142]

Table 1-2: Table from reference [134] (unless specified), comparing carrier lifetimes, band gap energies and TO phonon frequencies for selected PC materials.

Additionally, Table 1-2 also shows the lowest TO phonon mode for some of the materials. This is problematic if the bandwidth of the system exceeds the phonon modes as the sensitivity to additional spectral features around this frequency becomes limited. For the recorded values, all materials appear to exceed the bandwidth of current on-chip systems. Similarly to EO materials, the dielectric constants of the materials may limit the transmission line characteristics as well as the band gap energy (highlighted in Table 1-2) restricting the choice of lasers used in the project. LT-GaAs has a band gap of 1.41 eV, corresponding to a wavelength of 880 nm, therefore in order to achieve photoconductive emission, a laser with a wavelength of 880 nm or less is required.

For un-annealed LT-GaAs, the carrier lifetimes can be as short as 90 fs, but this increases as the material is annealed after growth to orders of ps [133]. The short carrier lifetimes allows faster response times to changes in biases, but also allows faster repetition of switching operations. The high resistivity and electric breakdown field of the LT-GaAs allows a large external bias to be applied to the PC switch for generation to maximise the radiation amplitude, but the high resistivity also suppresses dark currents during detection operation of the PC switches. The resistivity of the LT-GaAs is improved during annealing. High electron

mobility allows faster movement of the electrons under an applied electric field. Thus a higher mobility in the material will result in a higher transient photocurrent, improving the amplitude of the emitted radiation.

1.5.4.2. Switch Geometries

Whilst it is clear that the material choice has a critical role in PC switching, several different switch geometries have been defined for the CTLs (see Figure 1.24). Each design holds different advantages and disadvantages from each other, determining the applications which they are used for. However, to date there has been no systematic study comparing one design to the next making it difficult to determine which is the best suited design. As a result, this section reviews the different designs based in the literature, without giving direct comparisons based on using the same laser powers, optical wavelength, material choice, etc.

Ketchen *et al* demonstrated the sliding contact approach using a coplanar waveguide geometry on an undoped SOS substrate to obtain a 0.6-ps-long electrical pulse [143]. This meant that the photoconductive switch was defined in the area in which the exciting beam is focused, allowing the switch to “slide” along the transmission line by changing the position of the focus spot of the laser. However, such a geometry require that the entire transmission line has to be constructed on a substrate which can generate photocurrent when illuminated, which may then have a larger relative permittivity than required, or other undesirable optical properties such as phonon absorptions (see Table 1-2). Another disadvantage to be considered is noise created by ambient lighting which may create a photocurrent in the transmission line, causing the length of transmission line to become, in effect, a large weak PC switch. However, sliding contacts do allow propagation tests to be performed at arbitrary points along the transmission line such as observing the pulse at different lengths of transmission to observe the gradual decay of the pulse as the device does not require any special lithographically defined features, ensuring continuity of the transmission line geometry, which also prevents reflections due to geometry discontinuity from occurring.

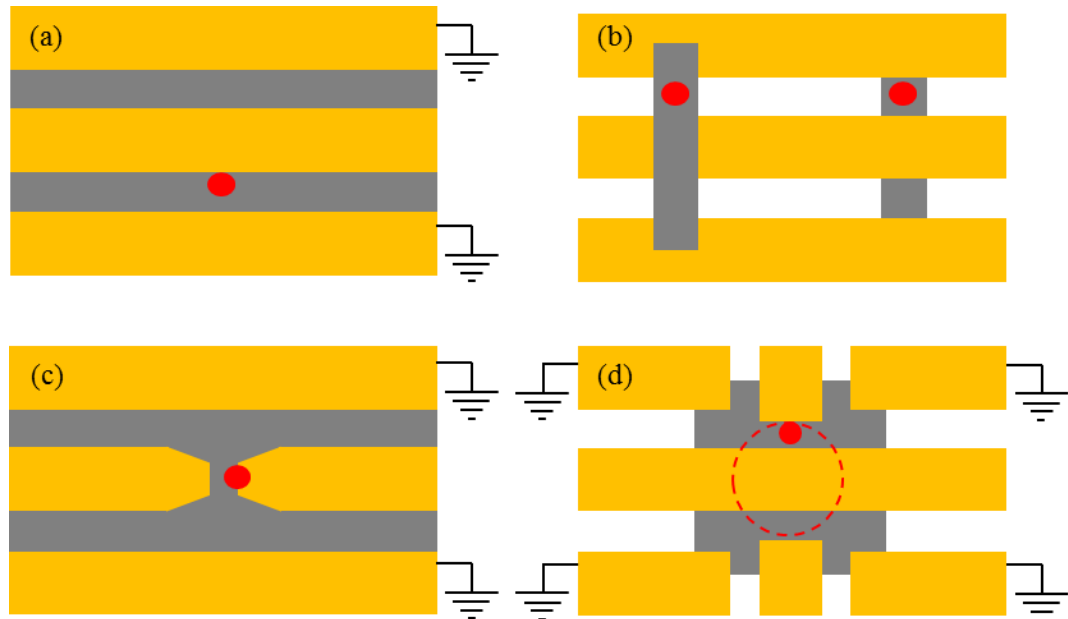


Figure 1.24: Schematic diagram of PC switch designs; (a) sliding contact, (b) sliding contact with defined PC material (above and below metallization) on substrate, (c) centre conductor gap and (d) defined switch. The grey areas are semi conducting material; yellow areas are the conducting material (usually Ti/Au) and the red highlights the illumination spots.

To overcome the problems encountered by the sliding switch geometry, Zheng *et al* demonstrated a sliding switch contact with the PC material defined to a small strip either above or below the CPS metallization [144]. This method does remove the ability to slide the switch along the transmission line to investigate changing pulse shape with propagation distance, but does allow a lower permittivity substrate to be used, lowering the propagation loss and dispersion. There was no found difference found between having the PC material above or below the metallization.

An alternative method of exciting the CPW is to have a gap in the centre conductor, as demonstrated by Alexandrou *et al* [145]. The device was defined lithographically on an undoped GaAs substrate and excited using a Ti:sapphire laser via a fibre, with a bias applied to one side of the centre conductor with the other centre conductor used as the transmission line. The resulting electric pulse propagates down the CPW with an odd mode, but this also suggests that only an odd mode can be biased using this design. The design parameters of this switch design has been further investigated by Tissafi *et al* using 3D modelling to find how the width of the gap between the ground and the centre conductor, W and the size of the gap for the switch affects the pulse shape and amplitude; the amplitude of the pulse is greater when W is greater than the length of the gap in the centre conductor [146]. However, with a shorter gap, the pulse amplitude is lower but the potential band width is increased [146]. This

design also suffers strong reflections, however, due to the break in the centre conductor used to define the PC switch, which will discourage this choice of design for high frequency resolution applications.

The design used by Li *et al* uses excitation probes which are biased with the centre conductor grounded was at the outset of this project the only design used for generation of ps pulses in a PGL systems [95]. The switching region is lithographically defined on the epitaxial transferred LT-GaAs, with the rest of the device being defined on a quartz substrate to reduce the permittivity of the transmission line whilst still being able to generate and detect ps pulses. The switches can be biased accordingly to produce the even or odd mode depending on which is required for the transmission line in use. There is very little work on optimizing the switch designs as the research is focused on the transmission line elements.

With the four main geometries defined, it is not necessary to choose one design for both the detecting and generating PC switches, as demonstrated by Griebel *et al*, as they had used the gap in the centre conductor for the generating switch and two PC switches similar to that of Li's for the detecting PC switch [70]. This device geometry allows the mode generated by the gap in the centre conductor to be distinguished (odd mode is to be expected due to generating switch design).

All the switch designs considered so far have used straight edge switches with large gaps. An alternative method is to mesh the two probes of the switch with interdigitated electrodes as shown in Figure 1.25. These designs have been favoured by on-chip devices operating within cryostats with the excitation pulse coming from fibres [70, 147]. However there has been no reason stated with experimental proof for the preference of interdigitated electrodes over the simpler designs, though Tissafi *et al* has made a comparison using 3D modelling finding that the interdigitated design improves the amplitude of the emitted pulse but also increases the FWHM when compared to the straight edge design when illuminated with the same intensity of light and bias voltage [148]. Based on this reasoning, it can only be assumed that interdigitated electrodes are used to reduce required optical power without lowering of the signal to noise ratio of the system. The lowering of the optical power will reduce the heating of the substrate which could potentially interfere with the experiments. It is noted however that such a design requires a higher resolution lithographic method than the non-interdigitated designs for either the whole device or just the switching regions.

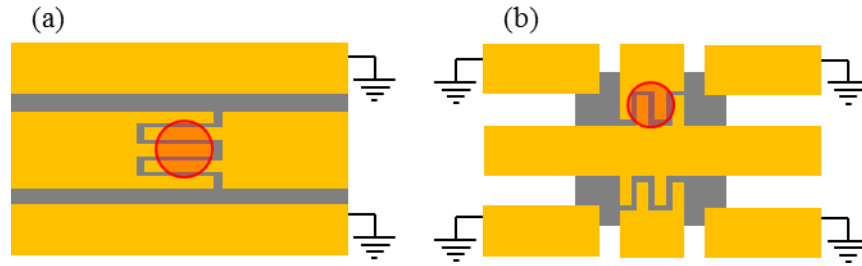


Figure 1.25: Schematic diagram of the PC switch with interdigitated electrodes used by (a) Griebel *et al* [70] and used by (b) Lee *et al* [69].

As previously stated, PC switching characteristics depend on the semiconductor material properties which may be considered a limiting factor. Holzman *et al* had opted for a “material-independent” (carrier lifetime independent) approach which uses the fast rising edge of the optical pulse to turn on and off the PC switch [149]. Using a coplanar strip line setup shown in Figure 1.26, the PC switch is defined as a gap in one of the conductors where the laser excites the gap as with normal PC switching, but due to the optical delay in half the pulse, the area exciting the PC switch between the signal line and the ground experiences a delay in reaching the substrate surface. Therefore photocarriers in the grounding switch are generated a short time after. Thus, a transient pulse is formed and then shorted out after a time delay, which depends on the thickness of the optical delay material. However, such a design requires precise thickness control of the length of the optical delay, which cannot be easily varied as well as having the same disadvantages as the sliding contact design. Additionally, the optical delay material may introduce dielectric loading of the transmission line as well as permittivity mismatches at the material edge.

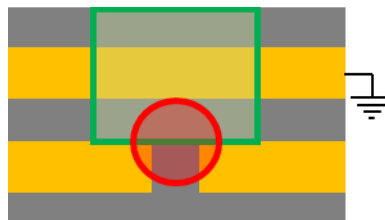


Figure 1.26: Schematic diagram of the material independent PC switch design for coplanar strip-line used by Holzman *et al* [149]. The green box highlights an optical delay of finite thickness, and the red spot highlights the area excited by the laser pulse.

As well as determining the switch geometry, the metallisation on top of the PC material should also be considered with three options shown in Figure 1.27. The more common method is to directly apply the metal to the surface of the LT-GaAs forming Schottky type contacts. However there are two alternative methods which have been demonstrated with

comparisons to the surface contact method. The first is to recess the electrodes into the LT-GaAs by etching channels for the metal (Figure 1.27b). This results in LT-GaAs between electrodes and therefore a stronger electric field in the LT-GaAs. This enhancement in the field strength in the LT-GaAs causes more efficient photocarrier collection. The method when compared to the surface contacts produced $> 40\%$ improved amplitude response and a reduction in the FWHM from 2.7 ps to 1 ps [150].

The second method is to bury the contacts into the PC material using AuGeNi metallisation and a successive annealing step (Figure 1.27c). This causes ohmic contacts to form with regions of higher conductivity buried beneath the surface of the LT-GaAs to improve the field strength through the PC material. As a result, in free space systems, the bandwidth of the generated increased from 4.5 THz to 6.5 THz, and the pulse amplitude increased, improving the SNR [151]. However, it is not known what this geometry is like as a detector, nor how effective AuGeNi is as a transmission line conductor.



Figure 1.27: Cross section diagram of switch regions for coplanar waveguides demonstrating (a) standard planar geometry, (b) recessed electrode geometry [150] and (c) annealed ohmic electrode geometry [151].

1.5.4.3. Different Illumination and Bias Considerations for PC Switches

There are two main forms of illumination which can be used for exciting the photocurrent; uniform and non-uniform illumination. Uniform illumination (filled gap) describes the situation where the PC switch is completely excited with the same light source. Non-uniform (asymmetric excitation, edge illumination) illumination describes the situation where the laser is focused to a spot smaller than the PC switch gap causing only a fraction of the PC switch to be illuminated. This can be easily achieved in larger geometries, however with small designs, better focusing lenses are required.

Alexandrou *et al* found when exciting the CPW using the sliding contact geometry with a 50 μm switch gap and a 5 μm beam size, that the electric pulses were strongly dependent on the location of the pump beam, with the larger amplitude being found when the beam was focused at the anode edge [145]. As the beam is moved to the centre of the PC switch the amplitude drops, but then slowly increases towards the cathode, but not to the same

magnitude as seen at the anode. Upadhyya *et al*, reporting on free space antennas, attributed this to there being a higher effective mobility of the electron population induced at the anode, compared with the mobility of the hole population at the cathode, which leads to a greater carrier acceleration at the anode [132]. Upadhyya also reported that by reducing the size of the focus spot, there is an increase in the pulse amplitude and a decrease in the pulse width due to the resulting increase in the rate of change in photocurrent. As a result, the bandwidth of the switch increased. However, such efforts in increasing the bandwidth may be wasted as the structure of the transmission line usually limits the bandwidth; therefore it is only an improvement in the amplitude of the THz pulse afforded. The increase in amplitude may allow longer devices to be tested however, since the length of the transmission line required to fully attenuate the pulse will increase.

When illuminating the coplanar structure, the spot size of the laser can be focused between the centre conductor and the outer conductor, or brought out of focus to illuminate both sides of the centre conductor. When focusing the beam in one slot, a coplanar waveguide, CPW mode and a coupled slot-line, CPS mode are formed, whereas illuminating both slots with the same beam produces only the CPW mode [69]. However, by bringing the beam out of focus, there will be a lower power density, therefore a lower magnitude of emitted radiation. An alternative method is to suppress the CPS mode by introducing air bridges over the centre conductor therefore allowing the PC switch to be excited in one slot rather than both [69].

As defined by the equation for the photocurrent, increasing the bias voltage across the PC switch will increase the magnitude of the emitted radiation due to the increase in the electric field strength causing the electron hole pairs to accelerate. However, the voltage cannot be increased indefinitely without breaking the PC switch. For non-uniform illumination of the PC switch, there is a non-linear relationship between the pulse amplitude and the bias voltage [152].

In different geometries, the polarity of the bias can determine which propagating mode is induced in the transmission line. This is best explained using CPWs; if the centre conductor is biased with the side planes grounded, an odd mode is produced whereas if the centre conductor is grounded with the side planes biased at equal but opposite bias, an even mode is produced.

1.5.4.4. External PC Detection of On-chip Systems

Similarly to external EO detection, PC switches can be used for mapping of the transient pulse at arbitrary positions along and around the transmission line. There are two configurations of external PC detection; one using capacitive coupling and the other making electrical contact with the test waveguide.

The electrical contact external PC detection uses a PC switch on a separate substrate with one electrical contact connected to the lock-in detection (or voltage supply for pulse injection) and the other connected to the transmission line under test via a titanium (or conductive epoxy) tip to complete the circuit [153-155]. The electrical pulse propagates along the transmission line under test, into the probe tip to the PC switch for detection. This method can be used for resolving the peak shape at different points along the electrical conductor, but cannot provide evanescent field measurements. Nevertheless, using external probes for ps pulse generation and detection allows devices with no ps pulse generators or detectors to be investigated in the THz regime [154].

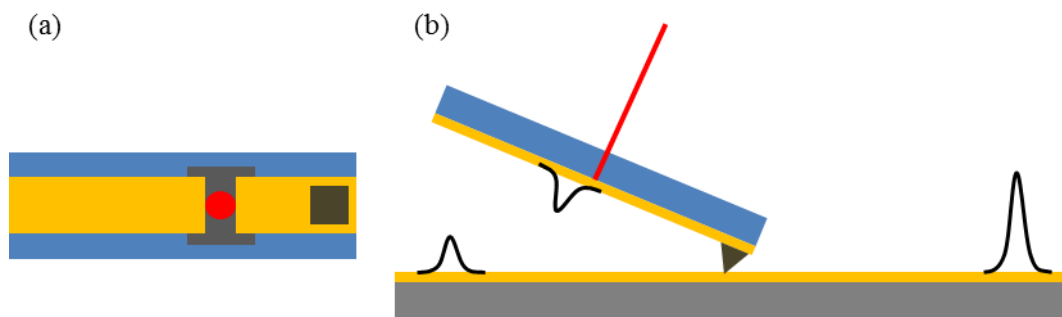


Figure 1.28: (a) Schematic of the external probe arm used for contact detection of electrical transients along a conductor. The red laser spot is hitting the PC material. (b) The THz pulse propagates along the transmission line with some of the signal going along the external probe arm to the PC switch. The rest continues along the transmission line.

For capacitive coupled detectors, the detector is fabricated on a separate substrate which then acts as a probe tip with the sensing region defined by the metallization. The PC switch can be defined at the probe tip by two gold tips [156, 157], or the PC can be moved further away from the tip, with the radiation being coupled to the PC switch by a PGL [158, 159]. This type of sensing geometry has been used to resolve peak shapes as well as produce a 2D representation of the evanescent field.

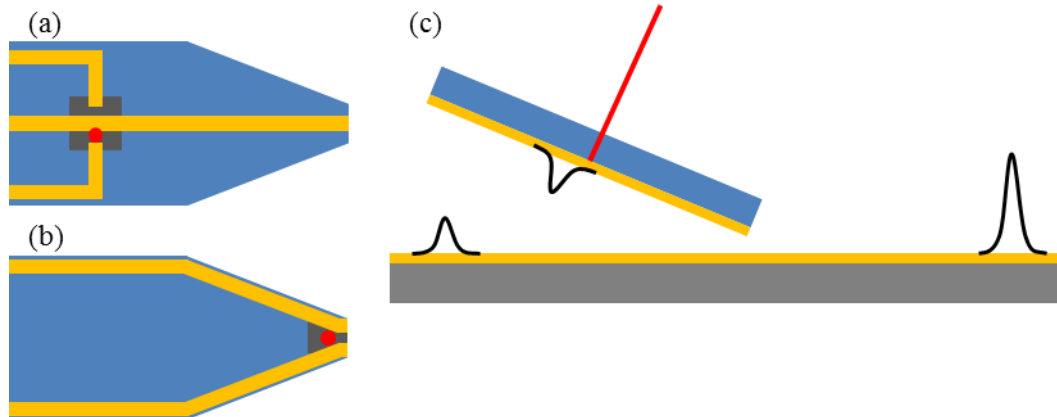


Figure 1.29: Schematic of the external probe arm used for non-contact detection of electrical transients along and around a transmission line. The red laser spot is hitting the PC material. Two designs are presented; (a) and (b). (c) The THz pulse propagates along the transmission line with some of the signal being coupled onto the external probe arm to the PC switch. The remaining portion continues along the transmission line.

However, as with the external EO detection, the external PC detection is invasive and has been shown to interfere with the transmission of the transient pulse along the transmission line under test [154]. In comparison to external EO detection, a higher spatial resolution can be achieved, however the time resolution of the PC detection scheme is considered to be worse [154, 156]. Whilst this method can be a powerful tool for rapidly testing different transmission line properties, removing any speculation of differences in the THz generators and detector, it removes one of the main advantages of the on-chip systems: their compact size.

1.6. Conclusion

THz technology has been introduced with a review of free-space systems. Due to their diffraction limited spatial resolution and short interaction length; there is a reduced sensitivity in comparison to setups which utilise waveguides. Free-space coupled waveguide methodologies still suffer the need for purging the system in order to remove the problematic water vapour. As a result, on-chip systems using MSL, CPW and PGLs have been researched with PGLs being chosen as the better option for spectroscopy options due to the greater extent of evanescent fields, single conductor systems (suitable for liquid samples as there will be no risk of electrically shorting the waveguide) and their potential broad bandwidth (see Table 1-3).

	Pro	Con
MSL	<p>Dielectric coated ground plane allowing fluidic spectroscopy.</p> <p>Established theoretical understanding and formulas.</p> <p>Can be fabricated onto arbitrary host substrates.</p> <p>Supports TEM mode – has no low cut-off frequency</p>	<p>Small evanescent field – field mostly confined to the substrate.</p> <p>More complex fabrication procedure.</p>
CPW	<p>Established theoretical understanding and formulas.</p> <p>One-step lithography fabrication procedure.</p> <p>Established waveguide choice in THz spectroscopy with several design options.</p> <p>Supports TEM mode – has no low cut-off frequency.</p>	<p>Multi-conductor system unsuitable for fluidic spectroscopy.</p> <p>Supports multiple modes.</p>
PGL	<p>Single conductor allowing fluidic spectroscopy.</p> <p>One-step lithography fabrication procedure.</p> <p>Greater extent of evanescent field.</p> <p>Potentially broader bandwidth</p>	<p>Limited available formulas.</p> <p>Relatively new waveguide therefore limited number of tested designs.</p> <p>Does not support lower frequencies (< 100 GHz).</p>

Table 1-3: Table comparing the pros and cons of the three on-chip waveguides; microstrip line (MSL), coplanar waveguide (CPW) and the planar Goubau line (PGL).

With the choice of waveguide established, the generation and detection method of THz ps pulses were reviewed; electro optic, electro absorption and photoconductive. Of the three methods, photoconductive detection is chosen for the generation and detection of the transient ps pulses, as it only requires the incident beam reducing the complexity of the alignment of the switches in comparison to EO and EA detections schemes which collect the reflected or transmitted optical signals. This proves critical when the devices are cooled using the microstat as the switches will move due to the cold finger contracting (see Chapter 4). Additionally, for EO detection, the crystal needs to be of a certain thickness and usually has a comparatively large dielectric constant making the designing of a reflection free high bandwidth system difficult.

	Pro	Con
PCS	<p>Polarity sensitive.</p> <p>THz pulse generation and detection is achieved with single wavelength optical influence.</p> <p>Established on-chip technique with numerous variations.</p> <p>Does not require optical detection scheme.</p>	<p>PC material generally has a high relative permittivity.</p> <p>Fixed generation and detection locations</p>
EO	<p>Polarity sensitive.</p> <p>Established on-chip technique.</p> <p>Freely positional THz detection scheme.</p>	<p>EO material generally has a high relative permittivity.</p> <p>Requires collecting and detecting the THz influenced optical signal.</p>
EA	<p>Freely positional detection scheme (between two conductors).</p>	<p>EA material generally has a high relative permittivity.</p> <p>Not polarity sensitive.</p> <p>Requires collecting the THz influenced optical signal.</p>

Table 1-4: Table comparing the pros and cons of the three on-chip THz generation and detection schemes; Photoconductive switching (PCS), electro-optic (EO) and electro-absorption (EA).

PC generation and detection is a broad field with respect to crystal choices, metal geometry designs and optical illumination options. In this project, LT-GaAs will be used as it is compatible with the laser wavelengths used (800 nm), transferable to quartz substrates and can be optimized to increase the electrical resistances and reduce carrier lifetimes. The switch geometry however has not been finalized and will be discussed in Chapter 4. The PC switches are built onto the same substrate as the PGL oppose to external probing in order to reduce the system size and etalons, but it should be a method to be considered for future work to characterize the operations of PGL systems.

Chapter 2. Transmission Line Theory and Simulation Models

There are many, well established theoretical treatments of the properties of the majority of commonly used transmission lines available in the literature. However, commonly defined parameters, such as the characteristic impedance, attenuation coefficient, cut off frequency, to name a few, are lacking for PGLs, partly since they are relatively young design geometry with the first published experimental studies published in 2005 [89].

For the more commonly used transmission lines, the transverse electromagnetic, TEM mode is supported, where neither the electric nor magnetic field is in the direction of propagation, and therefore is calculated as a 2D problem over the cross-section of the transmission line, perpendicular to the direction of propagation. For PGLs however, only the transverse magnetic, TM mode is supported, where the electric field is in the direction of propagation, introducing some complexity to the problem. Furthermore, the electric field is not confined between two conductors, but loosely confined to a single wire surrounded by free space and a host substrate.

As a result, this chapter will build the transmission line theory from a two conductor system supporting a TEM mode, where the derivations of formulae are well established and understood. From these formulae, key transmission line concepts such as reflection coefficient and propagation constants are extrapolated for the understanding of PGLs.

There are two approaches for calculating transmission line characteristics based on the geometry and material information; the classical lumped element method (where the transmission line is represented by per-unit-length discrete components such as capacitors, resistors and inductors) and by solving Maxwell's equations (where the geometry of the devices is analysed with respect to the electric field lines). Here, we use the lumped element method to provide insight into generic transmission line properties (such as reflection coefficients and propagations constants) [30, 160], whereas Maxwell's equations are presented to find a method for finding the characteristic impedance based on the geometry and materials used [30]. Ultimately, the required transmission line parameters are obtained using simulation package, Ansoft HFSS, which uses the finite element method to solve Maxwell's equations. Here, several transmission line parameters such as substrate permittivity and PGL conductor width are systematically changed, reviewing the change in

the response of the transmission line. For some design parameters, the responses are fitted with mathematical models to further the understanding of the transmission line's dependence on the design parameters.

As a result of the theoretical modelling presented in this chapter, an improved understanding of the PGL has allowed the PGL to be optimized for specific applications presented in this thesis.

2.1. Lumped Element Method

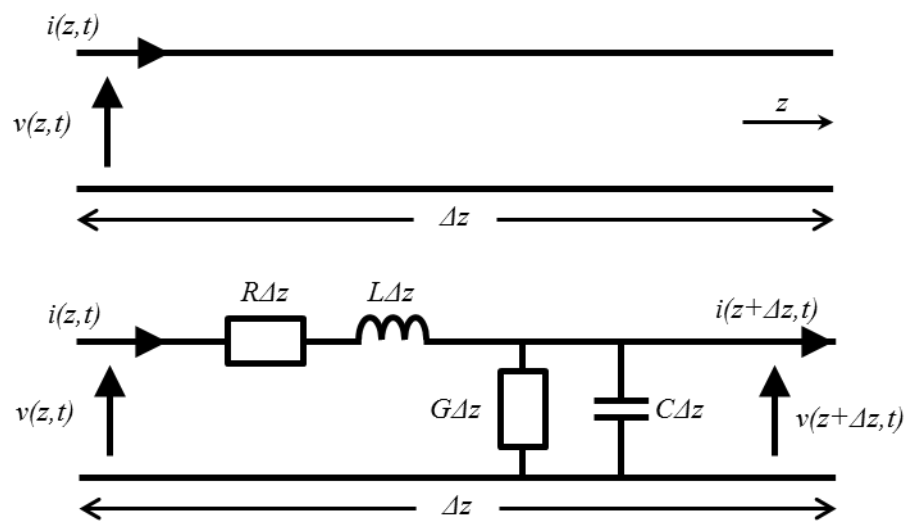


Figure 2.1: A two conductor transmission line supporting a TEM mode can be approximated by a lumped element method as shown. Reproduced from reference [30].

The lumped element method models the transmission line as discrete electrical components representing “per unit length” (Δz) electrical properties (Figure 2.1). As this is a transmission line methodology, it is limited to systems with two or more electrical conductors to support the propagating signal. The wire resistance and inductance are represented by a series resistance ($R\Delta z$) and inductance ($L\Delta z$) whilst the capacitance and resistance between the conductors is determined by a capacitor ($C\Delta z$) and conductance ($G\Delta z$), respectively.

Using Kirchhoff's voltage and current laws, the respective formulae for a transmission line supporting the TEM mode can be derived from the lumped element circuit equivalent (Figure 2.1):

$$v(z, t) = R\Delta z i(z, t) + L\Delta z \frac{\partial i(z, t)}{\partial t} + v(z + \Delta z, t) \quad 2-1$$

$$i(z, t) = G\Delta z v(z + \Delta z, t) + C\Delta z \frac{\partial v(z + \Delta z, t)}{\partial t} + i(z + \Delta z, t) \quad 2-2$$

The formulae are then divided by Δz , and the limit of Δz taken to 0:

$$\frac{\partial v(z, t)}{\partial z} = -Ri(z, t) - L \frac{\partial i(z, t)}{\partial t} \quad 2-3$$

$$\frac{\partial i(z, t)}{\partial z} = -Gv(z, t) - C \frac{\partial v(z, t)}{\partial t} \quad 2-4$$

In phasor form, the formulae can be rewritten:

$$\frac{\partial V(z)}{\partial z} = -[R + j\omega L]I(z) \quad 2-5$$

$$\frac{\partial I(z)}{\partial z} = -[G + j\omega C]V(z) \quad 2-6$$

Differentiated with respect to z :

$$\frac{\partial^2 V(z)}{\partial z^2} = -[R + j\omega L] \frac{\partial I(z)}{\partial z} \quad 2-7$$

$$\frac{\partial^2 I(z)}{\partial z^2} = -[G + j\omega C] \frac{\partial V(z)}{\partial z} \quad 2-8$$

Following substitution with Equations 2-5 and 2-6, the wave equations for the transmission lines can be found:

$$\frac{\partial^2 V(z)}{\partial z^2} = [R + j\omega L][G + j\omega C]V(z) = \gamma^2 V(z) \quad 2-9$$

$$\frac{\partial^2 I(z)}{\partial z^2} = [R + j\omega L][G + j\omega C]I(z) = \gamma^2 I(z) \quad 2-10$$

Where γ is the complex propagation constant:

$$\gamma = \alpha + j\beta = \sqrt{(R + j\omega L)(G + j\omega C)} \quad 2-11$$

Where α is the attenuation constant and β is the phase constant of the transmission line. The attenuation of the transmission line can be attributed to several parameters, such as conductor losses (which will include the skin depth; see Chapter 1), substrate losses and radiative losses. The phase constant can be used to find the frequency specific phase velocity of the transmission line (Equation 2-13). The transmission lines in this thesis are used to support the propagation of pulses which comprise a wide band of frequency elements, each with a different phase velocity. The differences in the phase velocities will lead to dispersion of the pulse, causing the pulse to broaden in the time domain as a function of propagation distance. For narrow bandwidth signals, or for transmission lines with a small dispersion, the group velocity (i.e. the velocity (v_g) of the pulse envelope along the transmission line) can be described as [160]:

$$v_g = \frac{\partial \omega}{\partial \beta} \quad 2-12$$

Whereas the frequency-dependent phase velocity is defined as:

$$v_p = \frac{\omega}{\beta} \quad 2-13$$

To find the characteristic impedance of the transmission line, solutions to Equations 2-9 and 2-10 can be found:

$$V(z) = V_0^+ e^{-\gamma z} + V_0^- e^{\gamma z} \quad 2-14$$

$$I(z) = I_0^+ e^{-\gamma z} + I_0^- e^{\gamma z} \quad 2-15$$

where $e^{-\gamma z}$ represents the wave propagating along the z direction, and $e^{\gamma z}$ represents the wave propagating along $-z$ direction. Differentiating Equation 2-14 with respect to z and equating to Equation 2-5, the current wave can be written as:

$$I(z) = \frac{\gamma}{R + j\omega L} [V_0^+ e^{-\gamma z} - V_0^- e^{\gamma z}] \quad 2-16$$

The characteristic impedance, Z_0 of the transmission line is defined by:

$$Z_0 = \sqrt{\frac{R + j\omega L}{G + j\omega C}} \quad 2-17$$

Equations describing the characteristic impedance have been defined for the most commonly used transmission lines, such as microstrip and coplanar transmission lines, allowing their geometries to be designed to achieve a specific value of characteristic impedances. The characteristic impedance is usually tuned to the microwave standard of 50 Ω , preventing impedance mismatching during measurements when using commercially available equipment, such as coaxial lines and vector network analysers (VNAs). However, as the generated frequency range begins to exceed the bandwidth of VNAs, and other schemes such as photoconductive detectors and electro-optic sampling, the 50- Ω -characteristic impedance is no longer a necessity. There is therefore more freedom to optimise the geometry for specific applications, or to achieve particular characteristics, such as increasing the evanescent field for spectroscopy applications. Within the device geometry however, the characteristic impedance of the transmission line still remains of particular importance when reviewing terminated transmission lines and changes in the geometry.

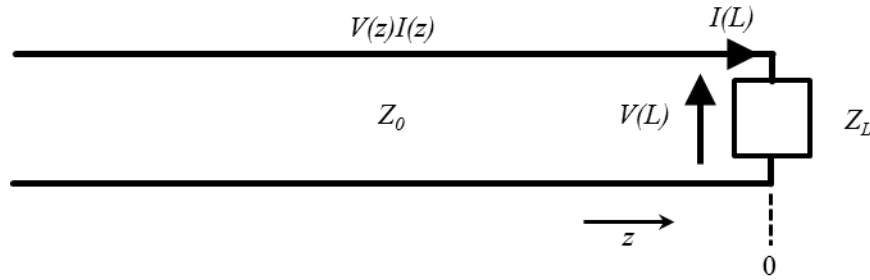


Figure 2.2: A two conductor transmission line terminated with a load, Z_L , at $z = 0$. Reproduced from reference [30].

When considering a terminated transmission line, Equation 2-15 is modified with the inclusion of the characteristic impedance, to remove I_0^+ and I_0^- . As a result, the current and voltage are calculated for $z = 0$ (Figure 2.2). The load impedance, as seen by the transmission line can be found and solved:

$$Z_L = \frac{V(0)}{I(0)} = \left(\frac{V_0^+ + V_0^-}{V_0^+ - V_0^-} \right) Z_0 \quad 2-18$$

Equation 2-18 can be rearranged to a ratio of the forward and backward propagating waves, which is known as the reflection coefficient, Γ .

$$\Gamma = \frac{V_0^-}{V_0^+} = \left(\frac{Z_L - Z_0}{Z_L + Z_0} \right) \quad 2-19$$

The reflection coefficient is powerful tool for analysing signals in both the time and frequency domains. The polarity of a reflected signal gives insight into whether it has reflected off an open circuit (e.g. a break in the transmission line or the ends of the transmission lines) for which $Z_L = \infty$ and $\Gamma = 1$ or from a short circuit (e.g. a low-resistance conductive path between the two conductors) for which $Z_L = 0$ and $\Gamma = -1$. For intermediate load impedances, the reflection coefficient will lie between -1 and 1, representing a point in the transmission line where a portion of the incoming signal has been reflected and the rest has been transmitted. For an etalon free THz-TDS spectra, which will ultimately improve the frequency resolution of the FFT spectra, the reflection coefficient needs to be as small as possible at all discontinuities in the transmission line. This encourages all transitions in the transmission line to be progressive rather than abrupt. This is achieved when the load

impedance is same as the transmission line impedance and all the power is transmitted; $Z_L = Z_0$ and $\Gamma = 0$.

2.1.1. Lumped element method for PGLs

The lumped element model can be modified to support the TM mode as opposed to the TEM mode demonstrated in Figure 2.1, with the inclusion of a series capacitance (Figure 2.3) [161]. However, as stated earlier, the lumped element method is limited to modelling transmission lines with two or more conductors, and therefore cannot be used to derive terms for the characteristic impedance of the PGL. Nevertheless, the terms derived for terminated transmission lines should remain a valid concept, and will prove beneficial for reviewing experimental time domain spectra with respect to the polarities of the reflected signals and allowing determination of the origins of etalons in the measured signal.

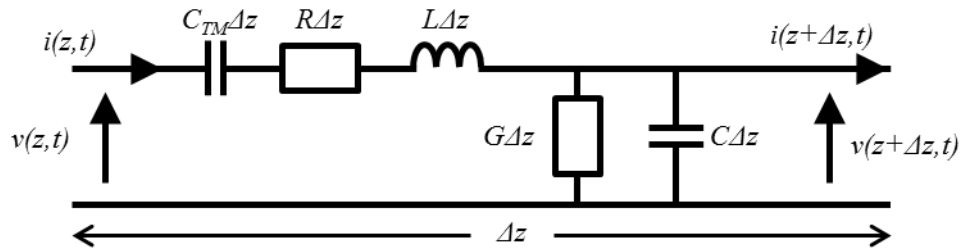


Figure 2.3: A two conductor transmission line supporting the TM mode can be approximated by a lumped element method as shown.

2.2. General Solutions from Maxwell's Equations

Solutions for all electrical transmission line structures begin by solving Maxwell's equations for a simplified structure, to produce an analytical term for the characteristic impedance based on geometric parameters such as conductor width and substrate thickness. For a PGL, which can be compared to a Sommerfeld line (see Figure 2.4), it can be determined that the electric field is in the same direction as the propagation path (z) whereas the longitudinal magnetic field is zero; $E_z \neq 0$, $H_z = 0$. These conditions imply that the wave propagates along the transmission line as a TM mode (also referred to as E-waves). This result also has further implications on the transmission line limits; the propagation constant and the characteristic impedances are both a function of frequency, and the PGL has a cut-off frequency (below which attenuation increases; $k_c \neq 0$).

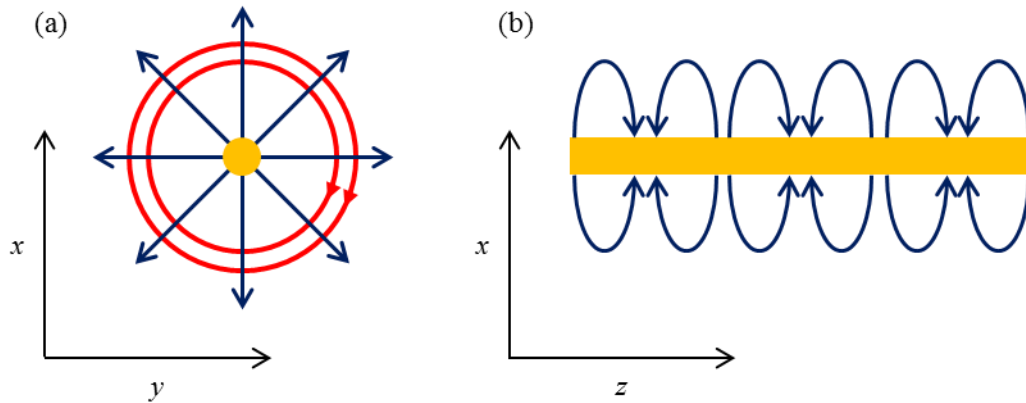


Figure 2.4: (a) Cross section ($x - y$ axis) view and (b) longitudinal ($x - z$) view of the Sommerfeld line with the wave propagating along z .

The electric and magnetic fields propagating along transmission line in the z direction are given by;

$$E(x, y, z) = [e(x, y) + ze_z(x, y)]e^{-j\beta z} \quad 2-20$$

$$H(x, y, z) = [h(x, y) + zh_z(x, y)]e^{-j\beta z} \quad 2-21$$

Equations 2-20 and 2-21 can be expanded and solved to reveal terms for the x and y components of the magnetic (Equations 2-22, 2-23) and electric fields (Equations 2-24, 2-25). The Helmholtz equation for the TM wave propagation is then solved for the given waveguide geometry with the boundary conditions defined the point at which the fields terminate. This in turn is used to find the characteristic impedance of the transmission line, Z_{TM} (Equation 2-26).

$$H_x = \frac{j\omega\varepsilon}{k_c^2} \frac{\partial E_z}{\partial y} \qquad H_y = \frac{-j\omega\varepsilon}{k_c^2} \frac{\partial E_z}{\partial x} \qquad 2-22, 2-23$$

$$E_x = \frac{-j\beta}{k_c^2} \frac{\partial E_z}{\partial x} \qquad E_y = \frac{-j\beta}{k_c^2} \frac{\partial E_z}{\partial y} \qquad 2-24, 2-25$$

$$Z_{TM} = \frac{E_x}{H_y} = -\frac{E_y}{H_x} \qquad 2-26$$

Where k_c is the cutoff wavenumber ($= k - \beta$) and k is the wavenumber ($= 2\pi/\lambda$). However, it is very difficult to define terms in order to calculate the electric and magnetic fields since the field is radial along the long axis of the transmission line with no physical boundary conditions, such as those usually determined by a second conductor in the analysis of other transmission line geometries.

2.2.1. Solving Maxwell's Equations for Radial Fields

PGLs have experimentally been demonstrated as supporting radial fields [96]. It is therefore helpful to assume a circular waveguide cross section (similar to the Goubau line and the Sommerfeld line) as opposed to the physical reality of the rectangular cross section, as it will greatly simplify the derivations of the equations. Indeed, it has been recently stated by Gacemi *et al* that the rectangular cross section of the geometry does not permit any analytical terms to be derived [162]. The initial equations have been derived previously for the analysis of other circular transmission lines such as coaxial and circular waveguides.

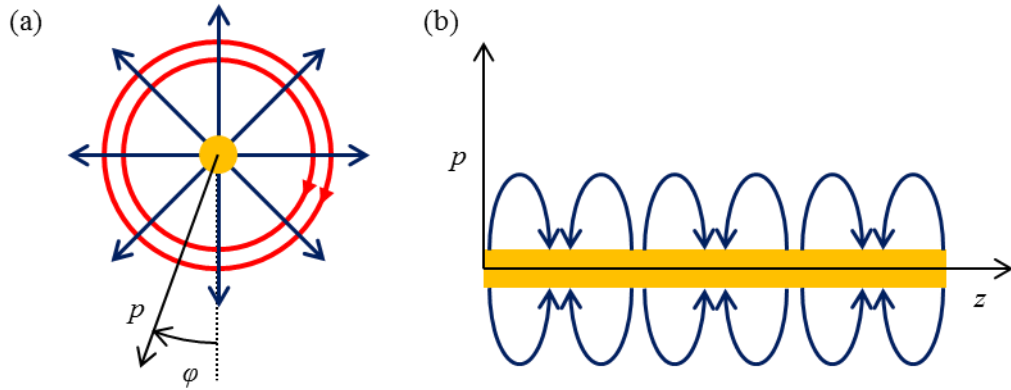


Figure 2.5: (a) Cross section ($x - y$ axis) view with the radial distance (p) and angular coordinate (φ) highlighted for a Sommerfeld line. (b) The longitudinal ($x - z$) view of the Sommerfeld line with the wave propagating along z .

Equations 2-20 and 2-21 are modified to express the electric and magnetic fields as a radial model (see Figure 2.5) around the long axis of the transmission line, propagating along z . x and y are substituted for angular co-ordinate, φ , and the radius, p ;

$$E(p, \varphi, z) = [e(p, \varphi) + ze_z(p, \varphi)]e^{-j\beta z} \quad 2-27$$

$$H(p, \varphi, z) = [h(p, \varphi) + zh_z(p, \varphi)]e^{-j\beta z} \quad 2-28$$

The characteristic impedance of the transmission line is then calculated using;

$$Z_0 = \frac{E_p}{H_\varphi} = -\frac{E_\varphi}{H_p} \quad 2-29$$

However, with radial coaxial cables and circular waveguides, there are clear boundaries which terminate the electric fields, allowing the equations to be solved; PGLs do not have this clear boundary condition with the electric field decaying with distance from the conductor. Due to the nature of the field patterns in the bounded waveguides, the equations cannot be taken to an extreme to equate a PGL. Should the electric field pattern be similar to that of a PGL TM mode, the coaxial line in the coaxial line equations, one could take the separation between the centre and outer conductor to an infinite value, thus resembling a single conductor system.

Terms for the magnetic field and both the radial and longitudinal electric fields have been defined in numerous publications [32-34, 163, 164], all following similar principles for

developing the formulae. These publications stem from Sommerfeld's initial evaluation of an uncoated electrical wire, which was then developed upon by Goubau (the transmission line namesake) with the inclusion of a dielectric coating [32, 33]. Despite there being terms defined for the electric and magnetic fields, they cannot be further simplified to define the characteristic impedance being a function of material and geometric parameters.

As a result of no definitive analytical formulas for characteristic impedance being defined for single wire transmission lines, simulation packages are used to draw equivalent models and to find the optimum design parameters [43, 92, 96, 102, 104, 165-167]. This has been accepted within the field's research community, and provides good comparison to experimental research. Further, frequency dependant parameters, such as characteristic impedance, can be quickly modelled over a defined frequency range for different geometries. The simulations are verified as being theoretically correct by reviewing the produced electric field patterns against published theory. Further, the results can be compared to those which are experimentally obtained.

2.3. Introduction to Ansoft HFSS

Several simulation packages have been used for the analysis of PGLs, including Microwave studio Computer Simulation Technology (CST) [92, 96, 102, 166], Comsol Multiphysics [89, 104] and Ansoft HFSS [95, 165]. Each of these simulation packages are used to simulate the electromagnetic field of the PGLs. Ansoft HFSS is used in this thesis.

Ansoft HFSS (version 12) is the 'High Frequency Structural Simulator' used for theoretical work in this project. It uses the finite element method (FEM) to solve electric and magnetic field patterns over desired frequency ranges. Several methods of showing the results can be obtained, such as viewing the scalar and vector field patterns on the design, plotting S-, Y- and Z-parameters and characteristic port impedance, etc. The program uses a catalogue of materials with predefined parameters or properties, such as the permittivity and conductivity of the material.

The model is defined to a set purpose (such as finding the effect of substrate permittivity on S parameters) to minimise the size of the simulation and therefore reduce computation time. The model is then kept within a radiation boundary which defines the limits of the simulation. Excitation of the model is defined by creating 2D planes at the input and outputs of the model. Electric field vectors are drawn on the ports defining the electric field pattern

used to excite the model; the even and odd modes can be defined where possible. By default, the incident port power is set to 1 W. Assume this value for all models unless specified.

Using the FEM, an initial tetrahedral elemental mesh is created based only on the 3D model drawn, and not on the electrical characteristics of the device (such as the S parameters). A solution frequency, and corresponding wavelength is defined by the user, and the mesh element sizes are approximately one quarter of this wavelength for air, and one third in dielectrics. A solution frequency 50 GHz greater than the highest frequency in the simulation was chosen, and is valid for all lower frequencies. This initial mesh is then solved, producing the initial results.

Adaptive meshing then automatically tunes this mesh to give a more accurate and efficient mesh design. The meshing algorithm searches for the largest gradients in the electric field strengths and sub divides the mesh in those regions, as well as targeting singularities (such as conductor edges) to add extra elements to the mesh. The mesh is then solved at the solution frequency, and the new S parameters compared to those of the previous mesh (Equation 2-30). If the difference is less than or equal to a convergence value specified by the user (delta S), then the mesh is accepted for use in the frequency sweep. If delta S is still larger than specified, the mesh is redefined by increasing the number of elements by a set percentage, and re-simulated. This process is iterative until either delta S (or better) is obtained, or the maximum number of adaptive frequency sweeps has been performed. Of the two meshes which were compared, either one can be used as the converged mesh since they have the same response as one another; by default HFSS uses the mesh with the fewest number of elements which was used to calculate the convergence value.

The convergence value does not decrease indefinitely and has been known to fluctuate. Therefore, to ensure that the first mesh to achieve the desired convergence parameters is not an anomaly, a condition is set which forces the mesh to redefine two further times to achieve three consecutive meshes with a convergence less than the defined value. However, this results in an increased number of elements and therefore more simulation time, and should only be done when absolutely necessary.

$$\Delta S \geq S_{ij}^N - S_{ij}^{(N-1)} \quad 2-30$$

Where ΔS is the defined maximum delta S and N is the adaptive sweep number. Since S is a vector quantity, delta S can range from 0 – 2. However, setting the value of delta S too low

will increase the simulation time to provide a higher accuracy, but the real world manufacturing still contains errors. Ansoft recommends values of 0.02 (default setting) to 0.01. The default value of 0.02 will be used in this project.

The material catalogue can be expanded with the inclusion of new materials or modified to better suit the frequency range under test. Although the predefined materials are independent of frequency, it is possible to make them frequency dependant to improve accuracy and for simulating absorption spectroscopy. This can be achieved by manually setting the individual frequency values (which are linearly interpolated for interim values), or by importing listed data from calculated experimental measurements (Chapter 4) or theoretical values.

HFSS can produce results in a range of formats depending on the information required. The data recorded in this project include; permittivity, wavelength, S parameters and characteristic impedance.

To calculate the extent of the evanescent field, the electric field (as well as the magnetic field) can be plotted as a 3D cloud model, with a colour coded contour surface of equal field magnitude. This is useful for a visual inspection of the evanescent field which can be simulated to observe reflections, but only the outer field (smallest value of the range) and the magnitude of the field can be seen. Alternatively, a 2D planar representation can be seen by plotting the colour coded field magnitude on the surface or by plotting vector arrows, giving more information about the direction of the field lines.

To obtain a graphical representation of the evanescent field, a non-model line (a feature which is not included in the simulations) is included into the design. The non-model line is perpendicular to the transmission line, and the magnitudes of the field along the line for a set number of data points are obtained. The values are plotted against the line length in a 2D plot to show the magnitude of the electric field with distance along the line. It is accepted that the results from these plots have very discrete lines; this is due to the data being plotted across the elements with a linear change. If smoother data is required, the number of mesh element needs to be increased by either increasing the solution frequency (thus reducing the wavelength) or by predefining the number of elements used to define the model.

The simulations presented in this project have been obtained for frequency domain work, as opposed to the time domain which is experimentally obtained. This is primarily due to the software limitations of HFSS version 12 - though the most recent versions have since been upgraded to version 14, introducing the ability to perform time domain simulations.

However, modelling the input pulses generated using PC switches using HFSS requires using a solution frequency of 50 THz (for a pulse with a 50 fs rise time; calculated using HFSS modelling), making it an extremely memory-intensive simulation. The frequency domain simulations may cause contradictions between results testing the same structures, especially where S parameters are experimentally unobtainable (see section 2.5.). Nevertheless, spectral features such as resonances due to filters will still be comparable.

2.4. PGL Simulation Results

PGLs have undergone significant levels theoretical modelling in order to gain a better understanding of the transmission line characteristics. However, there are currently no numerical solutions of the transmission line properties to be found in the literature. As a result, this section will use Ansoft HFSS to aid in building a purely theoretical understanding of the transmission line characteristics, by observing changes in the operational characteristics with systematic changes in the design parameters. The effect of substrate thickness is reviewed in Chapter 3, with experimental results supporting the simulated results.

The simulations presented have all involved direct excitation of the PGL mode with the CPW – PGL transition (as discussed in Chapter 1 and 4) removed. Unless specified, the substrate used in the simulations is quartz, using HFSS library parameters ($\epsilon_r = 3.78$) and the conductor is gold. The model is shown in Figure 2.6.

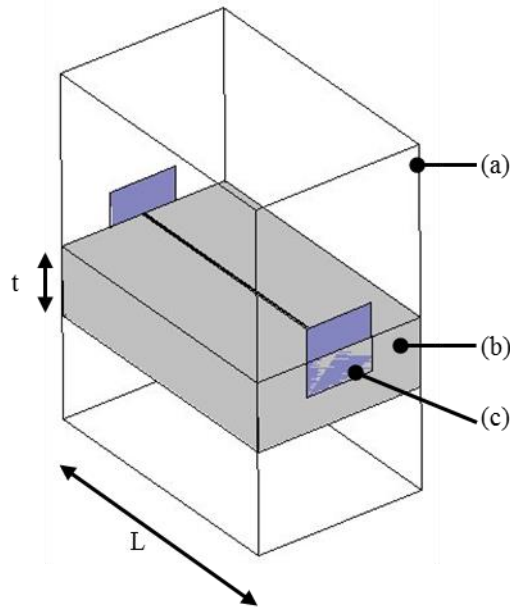


Figure 2.6: Diagram of the HFSS model used to represent the studied PGL. The boundaries of the model are defined by a vacuum box (a) with the substrate highlighted (b). The excitation of the PGL is achieved by non-model planes (c, purple). The length and height of the substrate are highlighted as L and t , respectively.

2.4.1. PGL Field Patterns

To validate whether the simulation is producing a PGL mode propagating along the transmission line, the electric and magnetic field are plotted using both scalar and vector representations. The electric field is seen to be propagating along the PGL with the electric field emerging and terminating along the conductor (Figure 2.7a, c). This is further confirmed by the cross sectional view of the electric field in Figure 2.8a and c, which shows a radial pattern evenly distributed around the conductor with the electric field emerging perpendicularly from the conductor surface into both the substrate and superstrate. A transmission distance of half a wavelength reveals the electric field directed towards the conductor. From this we can confirm that $E_z \neq 0$.

The magnetic field shows a similar magnitude plots to the electric field in both views (across and along the PGL, Figure 2.7b and Figure 2.8b, d respectively). However, the vector plots show the magnetic field to be circulating the centre conductor rather than propagating along its length; $H_z = 0$. From these conditions, it is confirmed that there is only a TM mode propagating along the PGL.

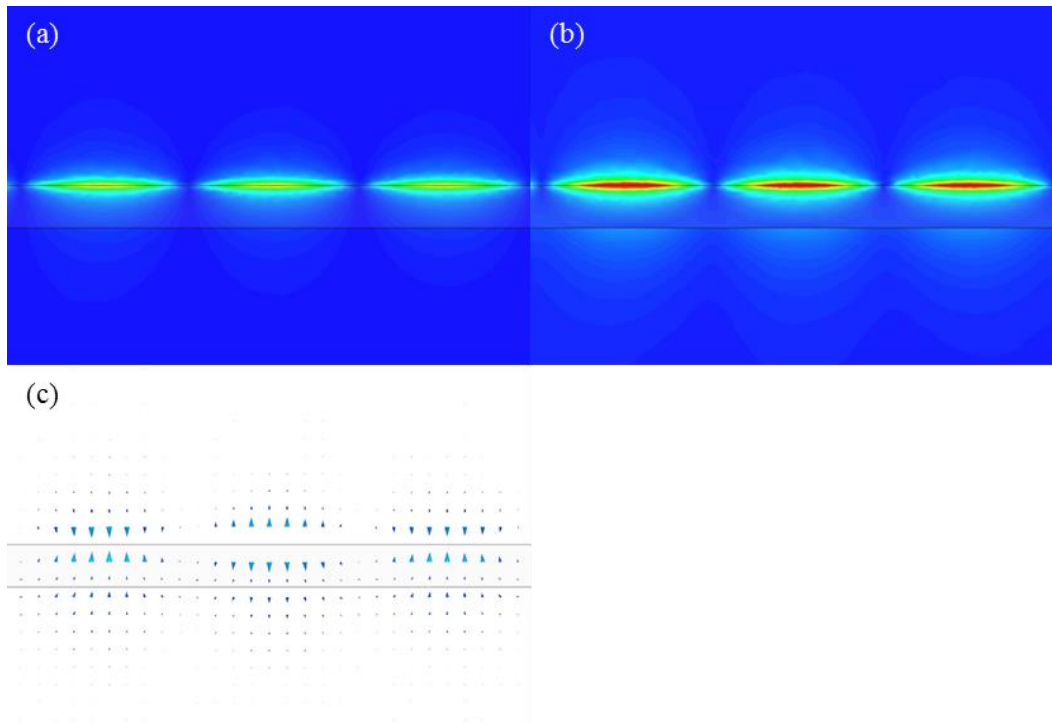


Figure 2.7: HFSS scalar plots for the (a) electric and (b) magnetic fields along the PGL. (c) Electric field plotted using vector plots to emphasise the direction of the electric field. All plots shown are for a 5- μm -wide PGL at 500 GHz.

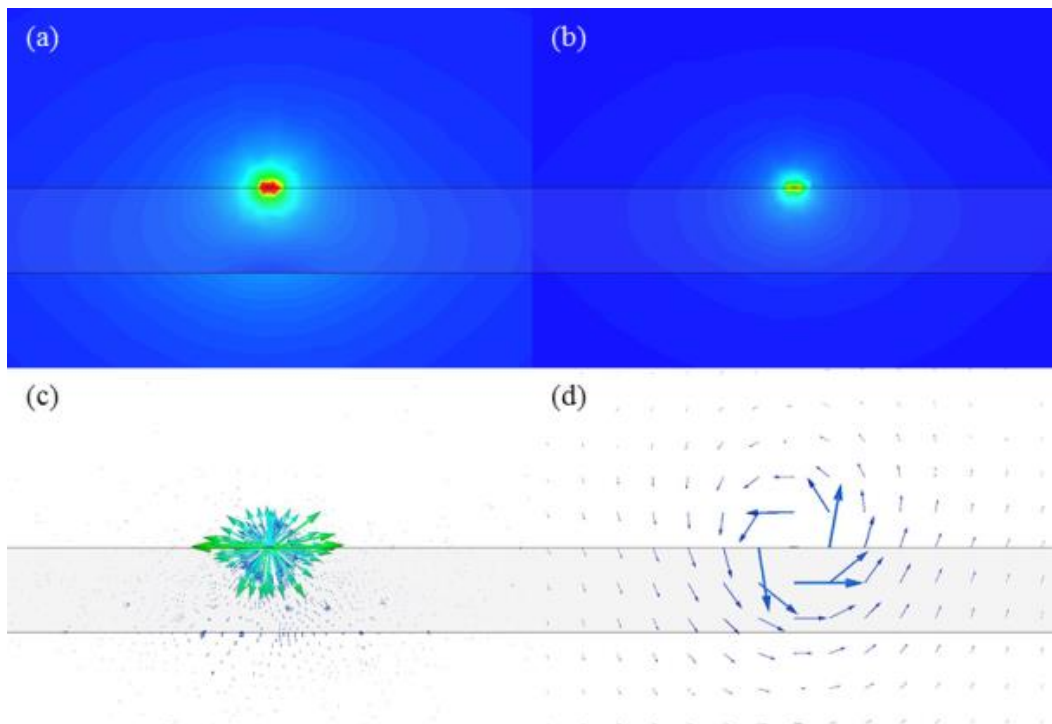


Figure 2.8: HFSS scalar plots for the (a,c) electric and (b,d) magnetic fields across the PGL. Vector plots are also shown to emphasise the direction of the field patterns. All plots shown are for a 5- μm -wide PGL at 500 GHz.

The scalar and vector plots of the PGL field patterns give a good understanding of the general shape and direction of the fields, but give unclear representation of the scales of the fields as a function of distance. Therefore, a 2D magnitude plot along a non-model line (a line which has no influence on the simulation) is used to show the exponential decay of the magnitude of the electric field strength as a function of distance (Figure 2.9).

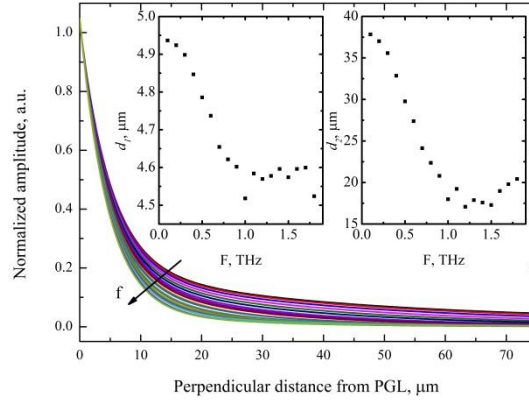


Figure 2.9: The normalized exponential fits of the evanescent field strength as a function of perpendicular distance for a 5- μm -wide PGL on a 50- μm -thick quartz substrate for frequencies, $f = 100 \text{ GHz} - 1.8 \text{ THz}$ in 100 GHz increments. Insets: Scatter plots of the fitting parameters d_1 and d_2 from Equation 2-31.

The extent of field was fitted to Equation 2-31, where E_1 and E_2 are scaling constants and d_1 and d_2 are the corresponding decay constants. It is clear from the insets of Figure 2.9 that, as the frequency increases, the extent of the evanescent field decreases and becomes more confined to the PGL. As a result, this will increase the necessity of ensuring good contact between an overlaid sample under test for broadband spectroscopy applications to ensure that higher frequency spectral features are detected.

$$E = E_1 e^{-x/d_1} + E_2 e^{-x/d_2} \quad 2-31$$

2.4.2. Substrate Permittivity

For all transmission lines, it is accepted that lowering the relative permittivity of the dielectric will lower the dielectric losses of the transmission line [92]. Using an 800- μm -long, 5- μm -wide PGL on a 200- μm -thick substrate in which we can vary its relative permittivity, allows the effect of the relative permittivity on the PGL's transmission line properties to be studied. The thickness of the substrate is assumed to be greater than the extent of the evanescent field, preventing the finite thickness of the substrate influencing the

change in effective permittivity. Figure 2.10a shows the resulting S_{21} and S_{11} parameters, which give clear indication that lowering the relative permittivity of the substrate, will increase the bandwidth of the PGL. The loss tangent is fixed at 1.

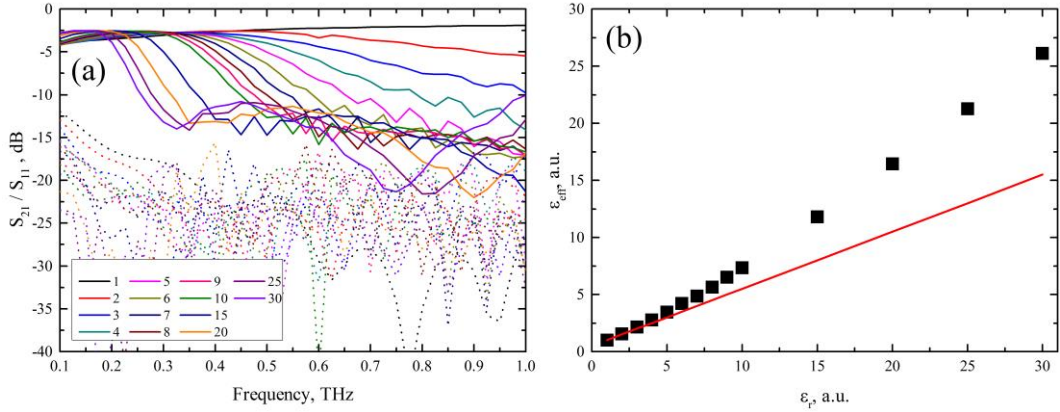


Figure 2.10: (a) S_{21} (solid lines) and S_{11} (dotted lines) parameters for an 800- μm -long, 5- μm -wide PGL on a 200- μm -thick substrate with a varying relative permittivity (1 – 30). (b) The simulated effective permittivity (ϵ_{eff}) plotted against the relative permittivity of the substrate (ϵ_r). The red line represents the theoretical effective permittivity given by Equation 2-32.

The increase in bandwidth is attributed directly to the reduction in the effective permittivity. Figure 2.10b shows simulated values for the effective permittivity at 500 GHz as determined by the relative permittivity of the substrate, alongside solutions to Equation 2-32, which is the accepted relationship for the effective permittivity (ϵ_{eff}) of the transmission line, as determined by the relative permittivity of the substrate (ϵ_r) [102]. It is clear that there is discrepancy between the simulated and mathematical values, which suggests that there non-symmetric distribution of the electric field with the field becoming more confined to the substrate for larger substrate permittivity.

$$\epsilon_{eff} = \frac{\epsilon_r + 1}{2} \quad 2-32$$

This study has demonstrated the need to reduce the relative permittivity of the substrate in order to enhance the bandwidth of the transmission line.

2.4.3. PGL Transmission Line Width

The width of the PGL has been demonstrated theoretically elsewhere to have an impact on the extent of the evanescent field [97]. For a clearer representation, the simulation has been

retested with the electric field strength plotted as a function of perpendicular extent from the centre of the PGL (Figure 2.11). The dependence of the extent of the evanescent field upon the PGL width is further emphasized by normalizing the data (data value divided by maximum data value) removing the field dependency upon the strength of the excitation of the transmission line. An exponential fit using Equation 2-33, is applied to each of the spectra with decay constants W_1 and W_2 shown in the inset of Figure 2.11b.

$$E = E_1 e^{-x/W_1} + E_2 e^{-x/W_2} \quad 2-33$$

It is interesting to note that there appears to be a linear correlation (see inset of Figure 2.11b) between W_1 and the width of the PGL with a fit of,

$$W_1 = 0.91w \quad 2-34$$

where w is the width of the PGL. This fit is consistent for the first term of Equation 2-33 throughout the tested range ($w = 5 \mu\text{m}$ to $50 \mu\text{m}$). However the fit does not hold for W_2 , as there appears to be steeper trend for PGL widths narrower than $25 \mu\text{m}$. The extent of field can be approximated by a single exponential term for PGL widths greater than $25 \mu\text{m}$. This change in trend may be attributed to the field moving from a circular field to a surface wave.

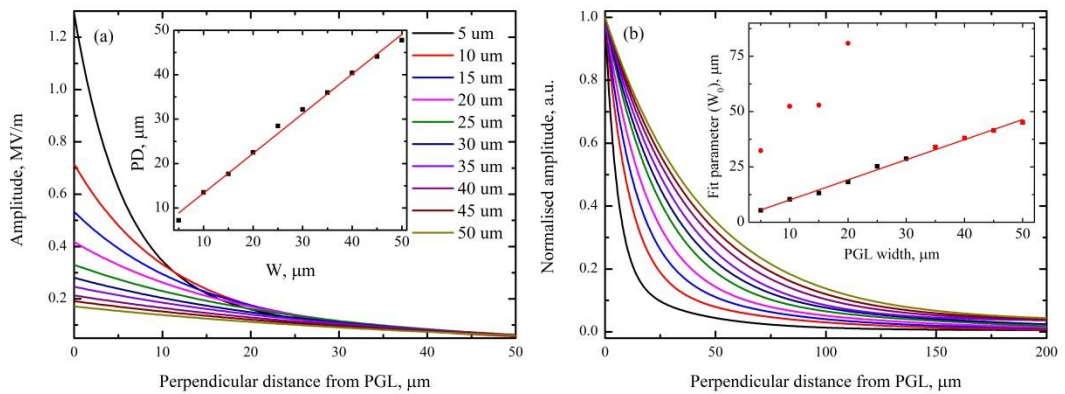


Figure 2.11: (a) The exponentially fitted electric field strength plotted as a function of perpendicular extent from the centre of the PGL for a range of different widths of 800- μm -long PGLs on a 200- μm -thick quartz substrate. The inset shows the perpendicular distance (PD) of the electric field decay to a value of $e^{-1}E$ ($0.368E$, where E is the electric field strength on the PGL conductor) as a function of the PGL width (W). (b) Normalized exponentially fitted electric field strength as a function of perpendicular extent. This further emphasizes the dependence of the extent of evanescent field on the PGL width. The inset shows the fit parameter W_1 (black points) and W_2 (red points) for the exponential fits. A linear fit has been plotted for W_1 .

As the width of the PGL is progressively increased, the extent of the evanescent field increases at a cost of lowering the electric field strength. This reduction in the electric field strength has been attributed to the increase in the cross-sectional perimeter of the PGL; the electric field strength at the PGL surface is determined by spread of the electric charge about the PGL cross sectional perimeter fitting Equation 2-35 which has been plotted in Figure 2.12. As a result, in order to recover the same field strength at the surface of the PGL as found with narrower PGLs, the system needs to be excited with more power. By exciting the system with more power the field magnitude changes, but the extent of the field does not. This suggests that when using the transmission line for sensing applications, increasing the optical or electrical bias of the PC switches should only be used to improve the signal to noise ratio and not to improve the physical sensing range of the device.

$$E = \frac{E_0}{2w} \quad 2-35$$

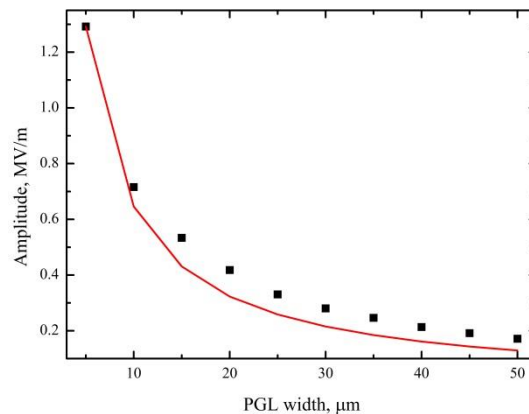


Figure 2.12: The magnitude of the extent of the fields measured at the surface of the conductor as a function of the width of the PGL. The red line is a fit using Equation 2-35.

It should also be noted that as the width of the transmission line affects the extent of the field, there is also a change in the S parameters of the transmission line (Figure 2.13). The bandwidth of the PGL appears to remain constant, but the pass band is shifted to higher frequencies as the width of the PGL is progressively increased. This suggests that the cut-off frequency for the PGL is a function of its width.

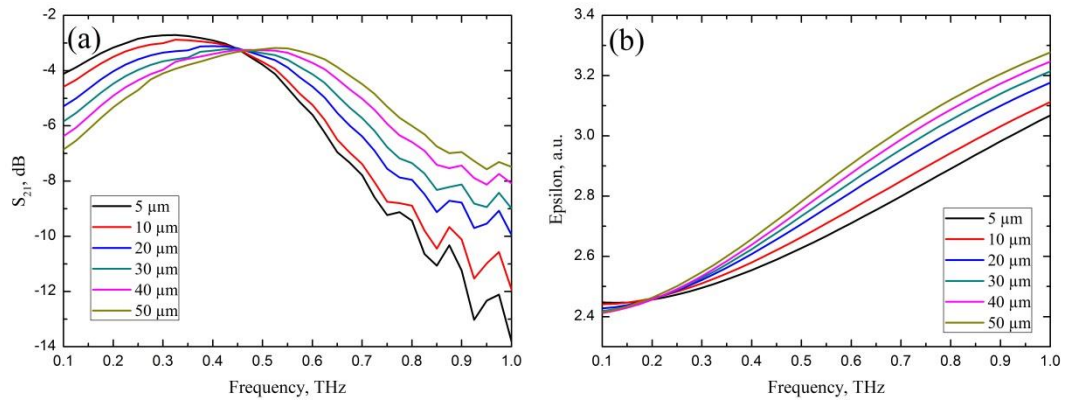


Figure 2.13: (a) S_{21} parameters for different widths of an 800- μm -long PGLs on a 200- μm -thick quartz substrate. (b) Effective permittivity of the transmission line for the same simulation.

The characteristic impedance of the PGL can be controlled by the width of the PGL (Figure 2.14) [168]. The trend of the data fits an exponential decay, which has been extended for PGL filter analysis (see Chapter 5). The results further emphasise that the transmission line needs to be kept at a constant width to remove impedance mismatches leading to potential reflections.

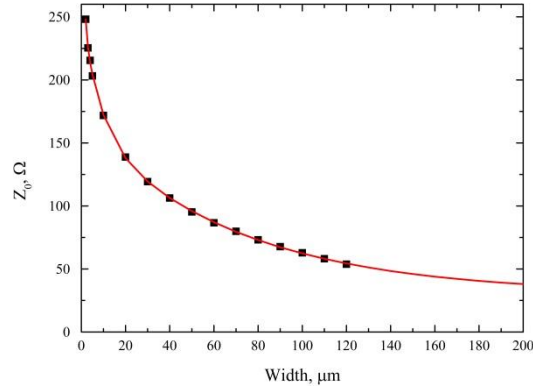


Figure 2.14: The characteristic impedance of the PGL as a function of the PGL width at 500 GHz. The data has an exponential fit (red line), extended to wider transmission line width.

It is clear from these simulation results, that the PGL width must be chosen according to the application; for applications where a thick sample is used, wider transmission lines are more appropriate for probing deeper into the material. For applications where a thin film of material is being analysed (direct contact with the material required) a narrower PGL is more appropriate.

2.4.4. PGL Length

It is widely accepted that as the length of the transmission line is increased, the bandwidth of the system is progressively reduced (Figure 2.15). By reducing the substrate thickness, the effective permittivity of the transmission line can be reduced, thereby improving the bandwidth (this is studied extensively in Chapter 3). Therefore, by re-simulating the effect of PGL length with a reduced substrate thickness (50 μm) in the 100 GHz – 1 THz frequency window, we find a progressive increase in the attenuation of the signal with length, but very little change in bandwidth. Therefore a PGL designed for spectroscopy purposes can be “designed” with an increase in length to improve the interaction length between the PGL and the overlaid sample, potentially enhancing weak spectral features in the frequency domain. For longer lines however, the input bias will need to be increased to compensate for the greater transmission line loss.

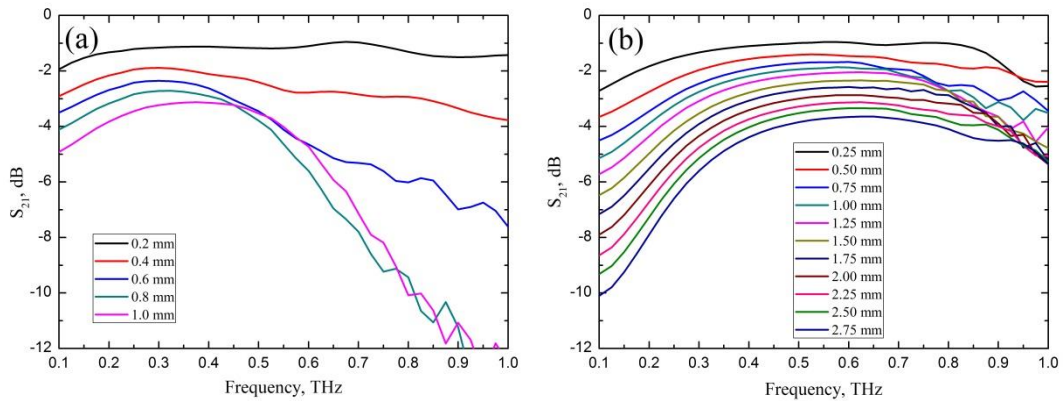


Figure 2.15: S_{21} parameters for different lengths of 5 μm wide PGLs on a (a) 200 μm and (b) 50- μm -thick quartz substrate.

2.5. Experimental Comparisons with HFSS Results

To compare the simulations with experimental results, the experimental TDS spectra need to be converted to the frequency domain, and then the S-parameters extracted. Both the input and transmitted pulse are Fourier transformed to the frequency domain using the same number of data points, with the same time spacing to ensure the same frequency resolution is obtained. Using Equation 2-36, S_{21} can be found and compared with the theoretical S parameters. However, for accurate results, the operation characteristics of the PC switches used to generate and detect the recorded TDS spectra need to be the same.

$$S_{21} = 20 \log \left(\frac{F_{Input}}{F_{Output}} \right) \quad 2-36$$

For comparisons of the field patterns, the evanescent electric field can be probed using external EO or PC detections. For the PGL, this has been obtained with EO detection to reveal the radial nature of the electric field as well as the polarities of the electric field (see Chapter 1). The evanescent field along the long axis of the conductor, however, has not been obtained due to the measurements being pulsed rather than continuous wave.

2.6. Conclusion

Whilst there have been no terms defined for the characteristic impedance of the PGL, it is not critical for the transmission line to have a 50- Ω -impedance since PC switching will be used in this project rather than VNAs (which have inadequate bandwidth). Equations for the impedance would, however, be beneficial for calculating the geometry of filters (Chapter 5). The width of the PGL should therefore be determined based on the extent of the evanescent electric patterns.

Ansoft HFSS has been proven to be a very powerful tool in the analysis of PGLs. The electric and magnetic field patterns have been studied, focussing primarily on the extent of the electric field. The extent of the electric field exponentially decays with increasing distance away from the PGL conductor with the rate of the decay dependent on the operating frequency and conductor width. As a result, it is wise to use a wider PGL for broadband spectroscopy applications as this increases the extent of the evanescent field at the cost of lowering the field strength, though this can be countered (within reason) by increasing the input power. However, wider PGLs also exhibit a higher cut-off frequency, losing the lower frequency components of the PGL.

HFSS will be used in the following chapters to study the PGL in the specific conditions determined by the content of the chapters; substrate thickness in Chapter 3, spectroscopy applications in Chapter 4 and resonators in Chapter 5.

Chapter 3. The Fabrication and Measurements of THz On-chip Systems and the Bandwidth Enhancement of Planar Goubau Lines

Planar Goubau lines, PGLs, have been used at microwave frequencies where a $\sim 500\text{-}\mu\text{m}$ -thick substrate has been the preferred choice of substrate material, as it does not limit the bandwidth capabilities within the measured VNA frequency range (up to 325 GHz) [89, 98, 101]. However, as the bandwidth is pushed to the THz frequency range with the introduction of photoconductive switches [95, 96] and EO detection [96], the bandwidth limitations of the transmission line are observed, which theoretical work suggests can be rectified by using lower permittivity substrates or substrate thinning [92, 110]. Though it is accepted that over the last eight years, the thicknesses of the substrates have been getting thinner (thinnest to date = $250\ \mu\text{m}$ [96]) to reduce the effective permittivity of the transmission line, they are still bandwidth limited by a finite thickness. Chemical etching has previously been used to achieve substrate thinning with coplanar devices made on silicon, with the etching made from the substrate side of the device to leave a freestanding $1.4\text{-}\mu\text{m}$ -thick membrane structure [74, 81]. Though this could in principle be replicated for PGL devices on LT-GaAs, the LT-GaAs would be too brittle for many practical applications. Therefore it is an attractive proposition to introduce a fabrication procedure which can be readily transferred to arbitrary substrate materials.

In this chapter, the fabrication procedure and experimental setup for measuring on-chip THz-TDS systems are discussed, alongside investigations into optimisation of the measurement procedure. Investigations are discussed into the use of alternative chopping techniques, PC switch characterization techniques, and the range of information about the transmission line and the PC switch operations which can be extracted from pulse measurements are detailed. The effects of substrate thickness on the PGL transmission properties are reviewed both theoretically and experimentally, and the concept of mechanical substrate thinning is introduced; substrate thinning is shown to lower the effective permittivity of the transmission line, allowing PGL devices with bandwidths extending beyond 1 THz to be formed for the

first time. The enhanced bandwidth of the PGL is then used to demonstrate the applicability of the PGL for spectroscopy applications.

3.1. Design of Second Generation PGLs

The PGL geometry used in this chapter is the 2nd generation design developed by the current Leeds research group, as discussed in reference [95]. The design uses a CPW device developed elsewhere for THz spectroscopy, with PC switches for both THz generation and detection [169, 170] later used to feed the CPW – PGL transitions at each end of the PGL. The CPW – PGL to CPW transition geometry used was initially designed and optimised by Akalin *et al* for frequencies up to 220 GHz [91].

The CPW to PGL transition, shown in Figure 3.1b was achieved by a progressive narrowing of the centre conductor from 30 μm to the width of the PGL, 5 μm whilst keeping the gaps at a constant separation of 10 μm . The gaps between the ground planes and centre conductor of the CPW were then gradually expanded to increase the characteristic impedance of the CPW to match the high impedance of the PGL. This design of a curved geometry is reported to be the more efficient transition method for launching the PGL mode than a linear transition (see Chapter 1) [91].

The PC switch is defined by 30- μm -wide probe arms separated from the centre conductor by a 6.5- μm -wide gap (Figure 3.1b). This metal geometry overlays the 70 $\mu\text{m} \times 70 \mu\text{m}$ square of LT-GaAs to complete the PC switch. This is a tested design configuration used in several devices [169, 170] whilst the metallization geometry has similarities to references [69, 70].

The CPW regions have a 30- μm -wide centre conductor separated from the ground planes on either side by 10- μm -wide gaps. This corresponds to a CPW waveguide characteristic impedance of 50 Ω when fabricated on quartz. In contrast to the first generation devices, the length of the waveguides in the CPW regions were extended to lengths of 28 mm to delay potential etalons from the external interconnects and the PC switches to enhance the etalon free time window of the resulting TDS spectra, which in turn enhanced the frequency resolution of the system.

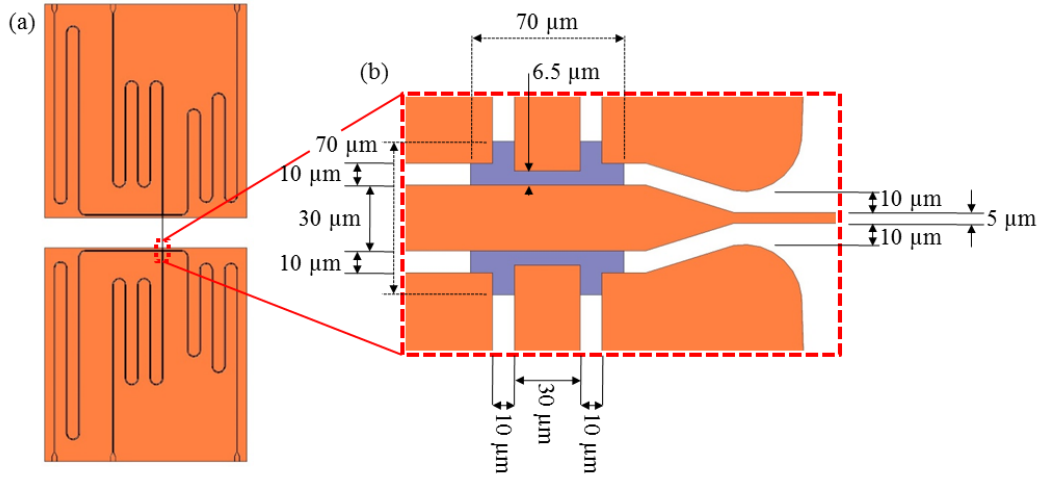


Figure 3.1: (a) A schematic of the device tested in this chapter with metallization shown in orange. (b) A magnification of the switch regions of the design for clarity with the grey LT-GaAs (rotated 90° with respect to (a)).

3.2. Fabrication of THz On-chip Device on Quartz

The method of device fabrication discussed in this section is specific to epitaxially grown LT-GaAs transferred onto quartz. However the processes are readily transferable to alternative substrate materials, and have been tested elsewhere with slight variations in methodology [53, 77]. Quartz was chosen for this project for several reasons: Firstly, it is optically transparent enabling the possibility of performing through-substrate excitation of the PC switches; secondly, it is structurally strong, allowing substrate thinning a few tens of microns without shattering, and finally, it has a low relative permittivity (3.78) at THz frequencies when compared to silicon and GaAs. Quartz is also found to have no absorption features in the frequency range of interest; 300 GHz – 3 THz.

The fabrication processes were taken from reference [170], but then improved upon to enhance the reliability and yield of the processes as well as improve the operational performances. These improvements to the existing procedure are made to the epitaxial transfer of the LT-GaAs to the quartz surface and the bilayer resist is altered for defining the metallization pattern before bandwidth enhancing modifications are made to the substrate by reducing its thickness. From preparing the LT-GaAs to completing metallization lift off, a PGL device on quartz takes approximately 2 weeks to fabricate.

3.2.1. The Growth and Annealing of LT-GaAs

A 350-nm-thick layer of LT-GaAs was grown on a 100-nm-thick sacrificial layer of AlAs, itself grown on a 500- μm -thick, 2-inch-diameter wafer of SI-GaAs using molecular beam epitaxy (MBE). The MBE method holds the wafer in an ultra-high vacuum (typically 10^{-11} – 10^{-10} Torr) where the wafer is heated and rotated to aid growth uniformity during the crystal growth. The substrate is initially heated to 630 – 640 °C for 10 minutes to remove surface oxides (which typically desorb at around 580 °C) before being cooled to the initial growth temperature [136]. The elemental materials which make up the crystal to be grown are then vaporised in dedicated ovens called effusion cells. Shutters on the effusion cells are opened and closed to control the atomic layer required during growth of the crystal accordingly.

First a 100-nm-thick layer of AlAs was grown at 580 – 590 °C, to be used as a sacrificial release layer for the epitaxial lift off. Then a 350-nm-thick layer of LT-GaAs was grown at 205 °C. The low temperature of this growth ensures an increase in concentration of As atoms incorporated into the zincblende GaAs crystal structure. The excess As atoms act as point defects within the crystal which are considered to be the dominant electron traps, trapping electrons from the conduction band into the mid gap states, resulting in the short carrier lifetime of the crystal. However, the growth temperature cannot be lowered indefinitely as the higher concentration of As atoms induces excess strain on the crystal lattice resulting in crystal defects such as stacking faults and pyramidal defects, thus limiting the thickness of the growth [171, 172]. The carrier lifetime starts to rise with lower temperature growth, an effect attributed to the defects introduced.

The as-grown LT-GaAs material has carrier lifetimes as short as 90 fs [133], but the low resistivity makes the material poor for photoconductive detection where a high dark resistance is desirable [173]. The material is therefore subjected to *ex-situ* rapid thermal annealing in a nitrogen atmosphere. Here, the whole wafer is heated to 500 °C for 15 minutes, which is long enough for an equilibrium state in the defect concentration to be met in the crystal [133], and the wafer is then allowed to cool. By annealing the wafer, As precipitates are formed which lowers the concentration of point defects in the crystal and increases the carrier lifetime [133, 172]. At the same time however, the resistivity of the material is increased through the formation of buried Schottky barriers [174]. The 500 °C anneal temperature was chosen as a result of previous research where a compromise between carrier lifetime and resistivity was met [133].

3.2.2. Van der Waals Bonding of LT-GaAs to Quartz and etching of LT-GaAs to define photoconductive switches

The complete working device can be directly fabricated onto the LT-GaAs surface in a simple one step lithography and metallization, but the waveguide characteristics are limited by the properties of the of the substrate material; ie the high relative permittivity of the SI-GaAs. To take advantage of the more desirable substrate materials which are available, a thin film of LT-GaAs for PC switching can be bonded to another substrate material through van der Waals bonding (Figure 3.2). This process is well studied (with several variations of the method [175, 176]) and widely used in on-chip THz devices [12, 53, 95]. In this process, an area of LT-GaAs which can cover both switch regions of the device design is diced from the growth wafer. The LT-GaAs is cleaned (acetone and isopropanol (IPA) wash) before having a layer of wax deposited onto the surface (120 °C, for 2 hours) (Figure 3.2a). The wax is then removed from the edges of the chip, using a trichloroethylene soaked swab, to expose the top edge of the wafer. The chip is then placed into a fast sulphuric acid etch ($\text{H}_2\text{SO}_4:\text{H}_2\text{O}_2:\text{H}_2\text{O}$, 1:40:80 by volume) for 1 minute, which non-selectively etches all layers of the wafer, with the wax protecting the LT-GaAs surface. The chip is then placed into a slow, selective hydrofluoric acid etch ($\text{HF}:\text{H}_2\text{O}$, 1:9 by volume) for 24 hours at 4 °C. The AlAs layer is removed, releasing the 350-nm-thick LT-GaAs film, supported by the wax, from the GaAs substrate (Figure 3.2b). Excess etchant is cleaned from the LT-GaAs by diluting the etch solution with DI water, before lifting the LT-GaAs out and transferring it onto the clean, polished surface of the chosen substrate material (quartz in this case) using a vacuum tool holding the wax support (Figure 3.2c). The substrate and LT-GaAs are left to rest for 1 week, allowing van der Waals bonding to take place (Figure 3.2d). Previous methods involved placing a weight on top of the wax to enhance the bond between the LT-GaAs and the substrate, but this has been found to introduce problematic micro-cracking (Figure 3.3), therefore no weight was used here. The wax was removed in trichloroethylene and the sample cleaned before being placed into a vacuum oven (250 °C, 20 mBar, for 15 hours) to further enhance the LT-GaAs adhesion (Figure 3.2e).

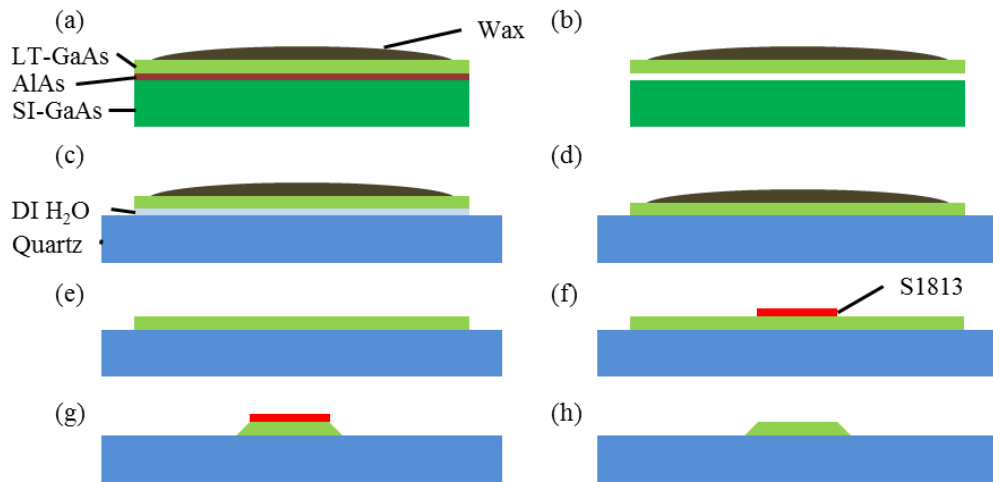


Figure 3.2: Simplified schematic of the step-by-step process used for epitaxial lift off, van der Waals bonding and for the LT-GaAs etch; (a) wax is deposited onto the LT-GaAs; (b) AlAs is removed in HF etch; (c) LT-GaAs and wax are transferred to the quartz substrate with water between the two; (d) water evaporates bonding the LT-GaAs to the quartz; (e) wax is removed in trichloroethylene and the device baked in a vacuum oven; (f) S1813 photoresist is patterned over the LT-GaAs defining the PC switches; (g) slow etching of the LT-GaAs defining a sloping profile of the LT-GaAs edge; (h) resist is removed in acetone revealing patterned LT-GaAs on quartz.

The surface of the substrate is cleaned before spin coating (5000 rpm for 30 s) a 1- μm -thick layer of S1813 photoresist followed by a soft bake (115 $^{\circ}\text{C}$, for 1 minute). The LT-GaAs switch pattern is then defined with UV exposure and a subsequent development in MF 319. The resist now protects the LT-GaAs in areas where LT-GaAs is required (Figure 3.2f). The exposed LT-GaAs is removed in a very slow sulphuric etch solution ($\text{H}_2\text{SO}_4:\text{H}_2\text{O}_2:\text{H}_2\text{O}$, 1:8:950 by volume, for 10 minutes) (Figure 3.2g). The slow etch ensures a slow rising edge (7 $^{\circ}$ incline) from the substrate surface to the LT-GaAs top to ensure continuation of the overlaid metal.

However not all the unwanted LT-GaAs is removed in the etch (particularly with the bilayer LT-GaAs) which can cause complications in the electrical operation of the device (shorting ground planes to the centre conductor, introducing permittivity mismatches) as well making further potential fabrication procedures difficult (graphene transfers require very clean surfaces, for example – see Chapter 4). There are two options; further etching or mechanical means. The first method would allow the etch solution to further undercut the resist pattern and desired LT-GaAs would lose its shape and quality. This can be overcome by using a second resist pattern larger than that used for the LT-GaAs switches in order to protect the side walls of the LT-GaAs squares, however the alignment would prove difficult and it

assumes that the un-etched material will be removed by further etching. The second option (used in this project) takes advantage of the hardness of the quartz substrate; the wafer is placed under a microscope and, using a scalpel blade, the unwanted LT-GaAs is scratched off. During this procedure, IPA is pipetted onto the substrate to trap, in suspension, the LT-GaAs which is scratched off. This method is effective, but cannot be used for accurately defining the shape of LT-GaAs, and is therefore limited to removing isolated areas of unwanted LT-GaAs. Under the microscope, there appears to be no damage to the surface of the quartz due to the scalpel blade. Finally, the S1813 resist mask is removed with acetone and IPA (Figure 3.2h).

The success of the transferring of the LT-GaAs film to the quartz substrate varied somewhat between samples, owing to the fragility of the 350-nm-thick LT-GaAs film, since several different types of defect could be introduced into the transferred film (Figure 3.3a). Ripples can form in the film, areas of LT-GaAs can break off (along the crystal axis of the LT-GaAs as suggested by the perpendicular crack lines), and some areas of LT-GaAs which have broken off can become trapped between the substrate and the LT-GaAs film, resulting in a bi-layer. These areas are avoided when aligning the photolithography mask used for definition of the PC switches.

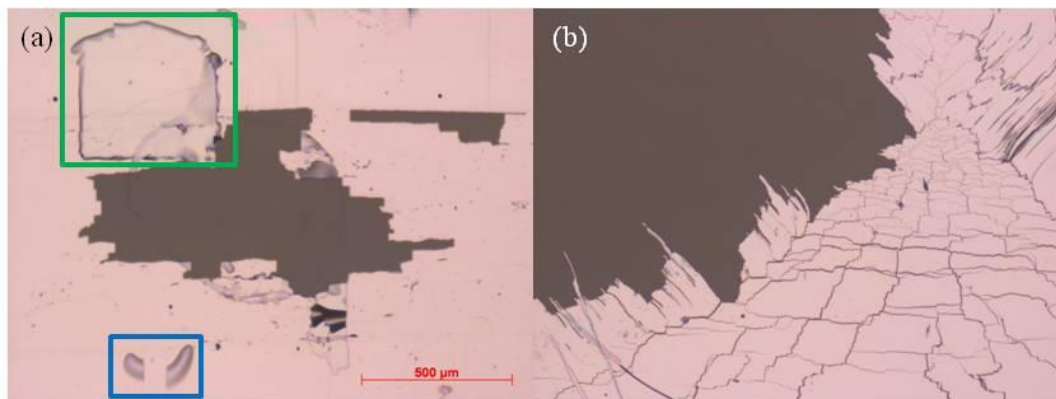


Figure 3.3: Micrograph of the LT-GaAs (lighter areas) on the quartz substrate after wax removal. The green and blue squares highlight a double layer of LT-GaAs and ripples in the transferred film, respectively. The film shown in (a) was transferred without the use of weights during van der Waals bonding, whereas weights were used in (b), demonstrating the micro-cracking which frequently appeared when weights were applied.

3.2.3. Lithography and Metallization

The resist pattern used to define the metallization is required to have an undercut to ensure a clean lift-off of the subsequently overlaid metallization. For silicon and GaAs substrates, this can be achieved using a single layer resist pattern (Figure 3.4a); the spun on S1813 is treated with chlorobenzene after UV exposure, prior to development, hardening the top surface of the resist. The hardened S1813 takes longer to develop in MF 319 than the untreated buried S1813, resulting in a developed undercut. However, due to adhesion problems between the S1813 and the quartz substrate, the bilayer process (Figure 3.4b) is chosen for this lift-off, which uses two different resists as opposed to a single resist, despite it requiring a longer processing time.

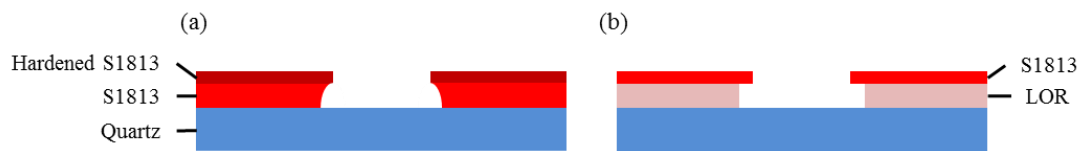


Figure 3.4: A comparison of (a) single layer resist pattern and (b) bilayer resist pattern.

Two metallization bilayer resist patterns are presented in this section (Figure 3.5). The first, involving a polymethyl-methacrylate (PMMA) – S1805 bilayer, was used for earlier devices, but was found to be overly time consuming and was not always reliable. The PMMA bilayer was ultimately replaced with the lift off resist (LOR 3A) – S1813 bilayer process, which proves to be faster and more reliable.

The metallization used for both lithography methods was a 20-nm-thick titanium metal adhesion layer followed by a 150 – 200-nm-thick gold metal layer, evaporated using either a thermal evaporator or an electron beam evaporator. The thickness of the gold is greater than the skin depth for the frequency range of interest as well as being thinner than the resist pattern to ensure a clean lift off. The final device is revealed following lift off. Due to the defined undercut in the resist, the metal on the resist and that on the quartz are isolated from one another owing to the directional evaporation of the metal (Figure 3.5e), ensuring a clean lift-off (Figure 3.5f).

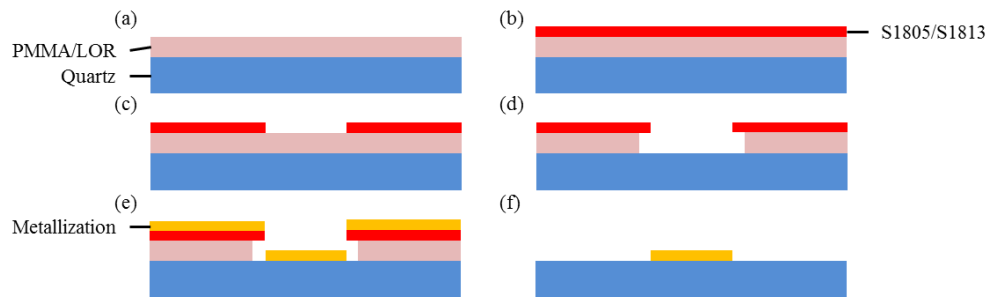


Figure 3.5: Simplified schematic of the step by step of the processes for a bilayer resist, metallization and lift off (note; the same schematic is representative of both bilayer processes described in the text); (a) PMMA/LOR resist layer spun on and bake; (b) S1805/S1813 spun on and soft baked; (c) S1805/S1813 layer exposed and developed; (d) PMMA/LOR exposed and developed; (e) Ti:Au metallization of the device; (f) resists removed for metal lift off revealing the metalized device.

3.2.3.1. PMMA Bilayer Process

In this bi-layer process, the cleaned substrate is coated in an adhesion promoter, hexamethyldisilazane, HMDS, which changes the surface chemistry of the quartz surface; the surface becomes more hydrophobic which prevents residual water from interfering with the following resist layers. After a 20 s wait, excess HMDS is removed by spinning the substrate (4500 rpm for 30 s). The HMDS improves the adhesion between the quartz and the subsequently spun on (4500 rpm for 30 s) 500-nm-thick layer of PMMA (495 – A8) (Figure 3.5a). The PMMA is then baked (170 °C, for 2 hours) before spin coating (2000 rpm for 30 s) a 650-nm-thick layer of S1805 (Figure 3.5b). The resist is soft baked (115 °C, for 1 minute) and the metal pattern exposed using the LT-GaAs and the switch designs as alignment markers. The S1805 is then developed in MF 319 and washed in DI water (Figure 3.5c). The pattern in the S1805 then acts as a mask for the subsequent PMMA layer exposure to deep UV. The exposure time was found to be 6 – 7 minutes compared to 16 minutes used for silicon and GaAs substrate devices. The significant time difference was attributed to back-scattering through the optically transparent quartz. The PMMA layer is then developed (methyl-isobutyl-ketone, MIBK:IPA, 1:3 by volume for 40 s) and cleaned in IPA (for 30 s) (Figure 3.5d) to produce a clean undercut.

To remove the resist during lift off, the sample is submerged in acetone and rinsed in IPA to remove any remaining residue.

Whilst the exposure and development of the S1805 proved repeatable, with reliable results each time, the PMMA proved troublesome when using quartz. Without HMDS, the PMMA

had poor adhesion to the substrate causing the resist pattern to lift and move during the development stages and a uniform result across the device was rarely obtained (Figure 3.6). The other issue was the consistency of the times required for exposing and developing the PMMA layer; the UVO exposure times need to be calibrated using practice patterns before defining the lift off pattern on the device. This timing typically changed by 30 seconds over 3 days, significantly affecting the patterning of the resist. This may be due to the inability to measure the UVO power with the current system, which would otherwise have allowed calibration of the process, as well as ensuring consistency in exposures on a day-to-day basis.

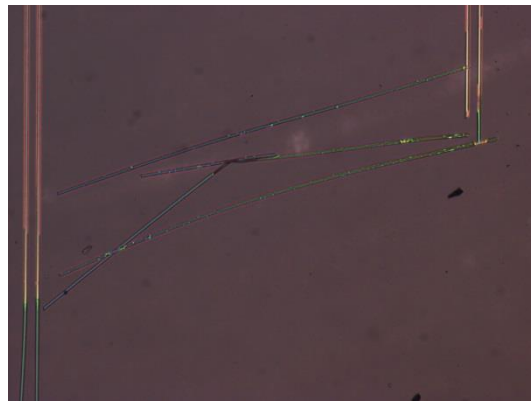


Figure 3.6: Micrograph of the S1805 – PMMA bilayer resists lifting off the substrate.

3.2.3.2. LOR 3A Bilayer Process

MicroChem LOR 3A, which does not require a deep UV exposure step, was eventually substituted for the PMMA layer. The cleaned substrate is placed on a hotplate at 200 °C for 30 minutes to desorb any water moisture. The substrate is treated with HMDS, baked for 1 minute at 200 °C and then rinsed with IPA and dried with N₂. A 400-nm-thick layer (2000 rpm, for 30 s) of LOR 3A was then spun-on and baked for 3 minutes at 170 °C (Figure 3.5a). A 1- μ m-thick layer of S1813 (substituted for the S1805) was then spun on and soft-baked (110 °C for 1 minute) (Figure 3.5b). The waveguide metal pattern was then exposed under UV light, using the PC switches as alignment markers. The resist was then given a post exposure bake (110 °C for 30 s) to reduce the rippling effects of the resist walls caused by the standing wave caused by the high reflectivity of the quartz substrate by diffusing the exposed and unexposed resist before development. The exposed S1813 layer was then developed in MF 319 for 1 minute and rinsed in DI water (Figure 3.5c). The sample was

baked for 1 minute at 200 °C to prevent further development of the S1813 layer, before being returned to the MF 319 for a further 1 minute to develop the LOR 3A layer and create the desired undercut (Figure 3.5d). The finished lithography was cleaned using DI water.

To remove the resist during lift off, the sample was submerged in Microposit remover 1165 and heated to 75 °C to dissolve the LOR 3A layer. The sample is cleaned in DI water.

This method was preferred over the PMMA bilayer process due the removal of the second problematic exposure.

3.2.4. Mounting of On-chip Systems to PCBs

The finished device was mounted onto a PCB using wax (Figure 3.7). By using wax, the device under test can be removed by dissolving the wax in trichloroethylene so that it can be modified, remounted and retested. The wax is also stable in the temperature range required for the variable temperature measurements (4K – 292K) which are presented in Chapter 4.

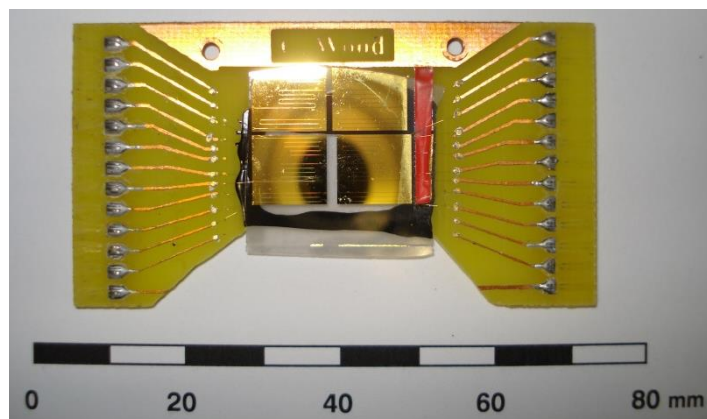


Figure 3.7: Photograph of the completed device used for substrate thinning measurements in this chapter.

The PCB was modified from previous designs with the introduction of a window and removal of PCB material along the bottom edge as seen in Figure 3.8. The “window” in the PCB ensures that the PCB has no influence as a substrate in the active region of the chip as well as providing optical access to the PC switches for rear-side laser excitation. Furthermore, the removal of the PCB bottom aids in removal of the device between modifications. The PCB had gold discs glued to the copper tracks using electrically conductive silver-loaded epoxy. The gold discs act as bond pads for connecting the chip’s gold wire interconnects made using a wedge bonder. Wedge bonding is preferred over ball

bonding as the wedge bond is more easily removed with little damage to both the chip and the gold disk, allowing for repeat bonding to the same pads.

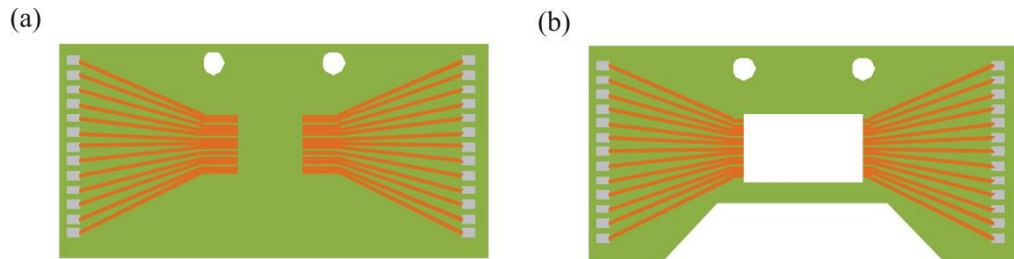


Figure 3.8: Schematic diagrams of (a) the original and (b) the modified PCB designs. The modified design has the “window” cut from the centre as well as the bottom half of the PCB to aid removal of the devices.

However, as the substrate thickness approaches $75\ \mu\text{m}$, the force involved in forming wire bonds is sufficient to break the substrate. To avoid this, the first bond was made on the gold discs, and the bond wire cut to an appropriate length to allow it to rest on the device bond pad. Using silver-loaded epoxy, the gold wire was then fixed into place onto the bond pads of the device. This method of sticking down the electrical interconnects allows thinner substrate devices to be electrically connected to the PCB, but it is a permanent fixture which is not suited for the “remount and modify” methodology.

Alternatively silver paint can be used but this was found troublesome to control, and not as effective as the epoxy. Silver paint is easily removed in acetone, however, allowing the bonds to be removed with minimal damage to the device contacts.

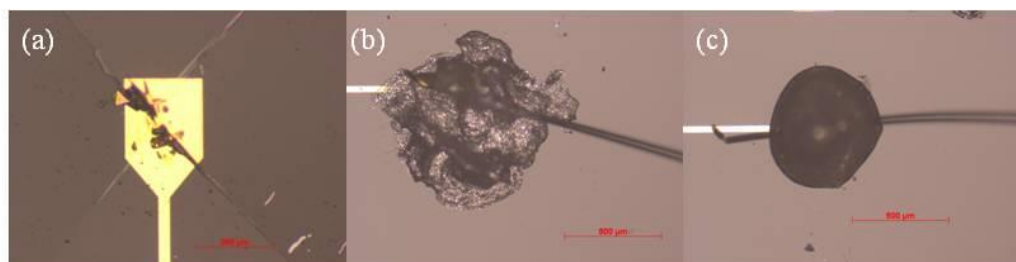


Figure 3.9: (a) Image of a PGL bond pad on a $50\text{-}\mu\text{m}$ -thick quartz substrate after attempting to bond the gold wire interconnects using the wedge bonder. Alternative method using (b) silver paint or (c) silver-loaded epoxy.

3.3. System Setup and Measurement Scheme

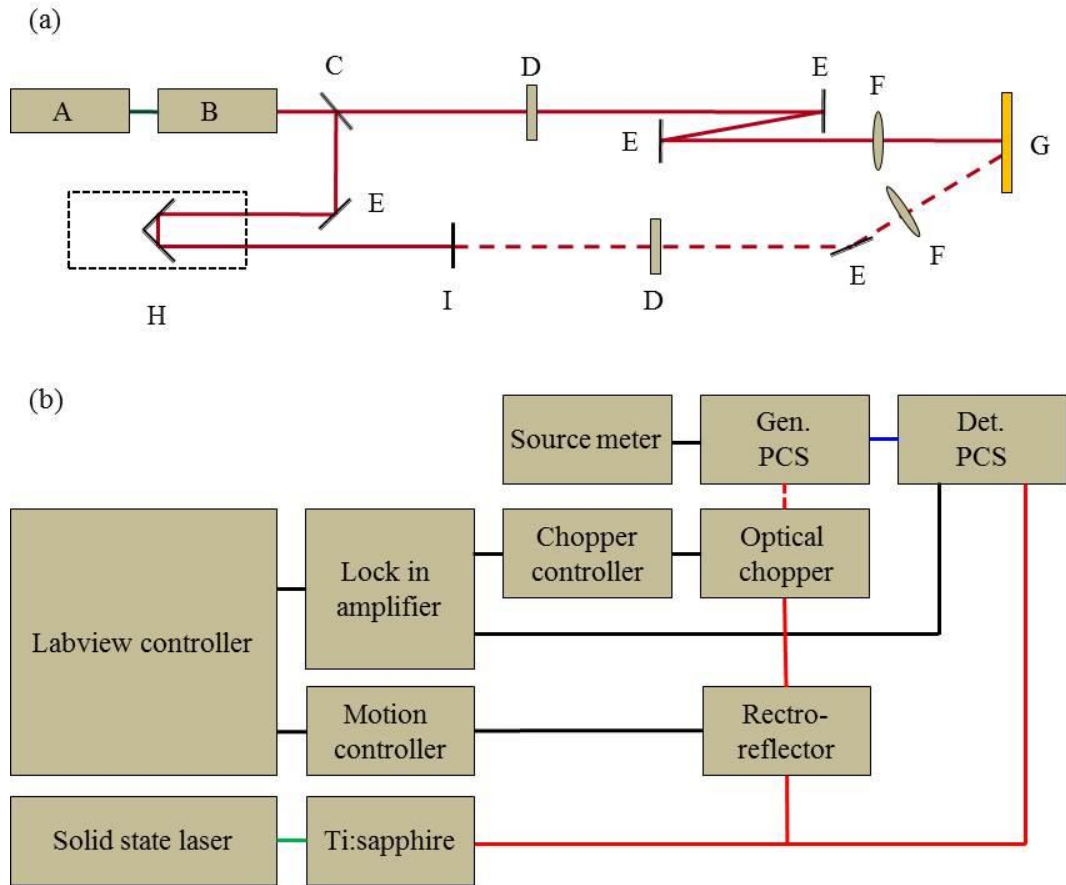


Figure 3.10: (a) Schematic optical setup of the system setup where: (A) = solid state pump laser; (B) = Ti:Sapphire laser; (C) = 50:50 beam splitter; (D) = optical filter (10 mW unless specified); (E) = mirror; (F) = focussing lens; (G) = on-chip THz system; (H) = rectroreflector; (I) = optical chopper. (b) Schematic electrical setup where black lines show electrical connections and blue is THz propagation between the PCSs (abbreviation: Gen. = generation; Det. = detection; PCS = photoconductive switch)

The on-chip systems are measured using the optical setup shown in Figure 3.10a, set on a suspended optical bench. The electrical connections between the controllers and the devices are highlighted in Figure 3.10b. The system has strong similarities to that of the free space TDS systems discussed in to Chapter 1 but does not require a purge box to remove water vapour.

The green diode solid state laser operating at 532 nm (Millennia Xs, Spectra Physics) pumps the Ti:sapphire laser (Tsunami, Spectra Physics) to produce a near infrared pulse (800 nm, 110 fs pulse width) with a repetition rate of 80 MHz. The beam is then split equally into a

pump and probe beam by the beam splitter. The pump beam was attenuated to 10 mW laser power (unless specified later) and focused onto a 30 V DC biased (unless specified) PC switch using a focusing lens (100 mm focal length). The probe beam was fed through a retro-reflector for time domain spectroscopy before being optically chopped (~ 2880 Hz) for lock-in detection, attenuated (laser power of 10 mW unless specified) and focused onto a second PC switch connected to a lock-in detector.

Using this system, the pulse at the detection switch can be mapped out by systematically probing the THz pulse at set time-intervals. By changing the propagation length of the probe pulse, the arrival time of the optical pulse to the PC switch in comparison to the arrival time of the electrical pulse could be varied, thus allowing the electrical pulse to be measured at discrete time intervals (Figure 3.11). Therefore, by increasing the number of data points and reducing the optical pulse width, a more accurate representation of the electrical pulse can be found at a cost of increasing the scan time. The cleanliness of the pulse representation is dependent on the limitation of the noise in the setup; the PC switch quality, the laser stability, and the probing time of each data point.

The position of the retro-reflector, x (m), is related to the time delay introduced to the time-of-flight of the probe pulse, t (s), by:

$$t = \frac{2x}{c} \quad 3-1$$

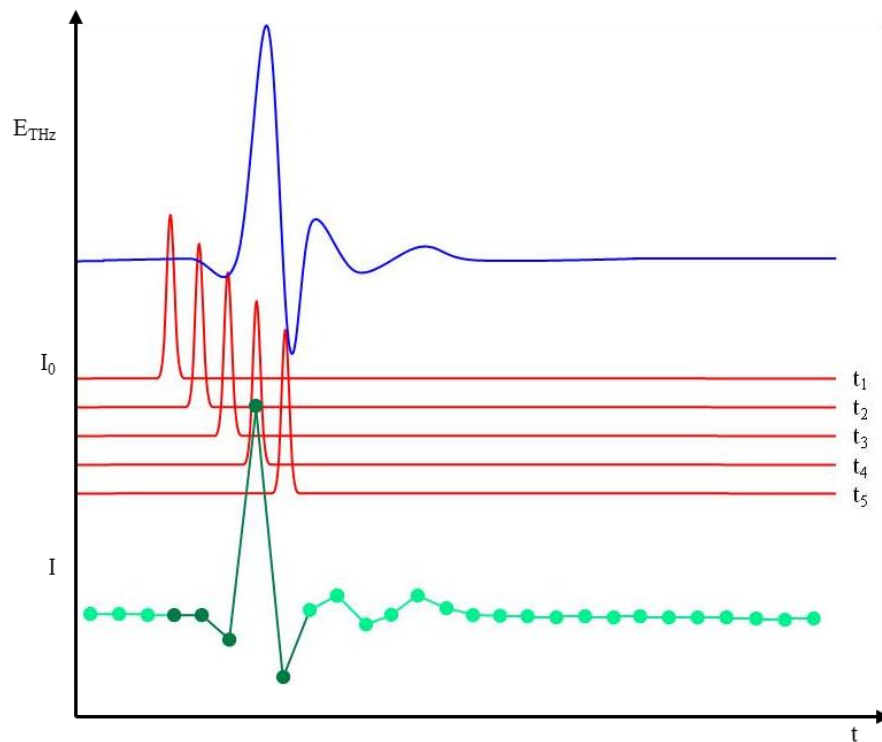


Figure 3.11: Diagram demonstrating time domain spectroscopy with the transmitted electric pulse (blue), the optical pulse at five time intervals (red) and the mapped out pulse (green) with the corresponding data points in dark green.

Using a four-switch design of on-chip system, generating and detecting at different PC switches allows a range of device characteristics to be obtained (Figure 3.12). By biasing and detecting pulses at the same end of the transmission line, the “input” pulse can be detected, which can be compared with the transmitted or “output” pulse to find the attenuation and dispersion of the transmission line. It is also useful to find the maximum bandwidth obtainable from the output pulse, since the bandwidth of the input pulse cannot be greater than that of the output; i.e. a passive transmission line can only reduce the bandwidth of a transmitted pulse. By generating and detecting pulses at opposite ends of the transmission line, the transmitted pulse is recorded, revealing transmission line properties and, in the case of spectroscopy measurements, information of the overlaid samples.

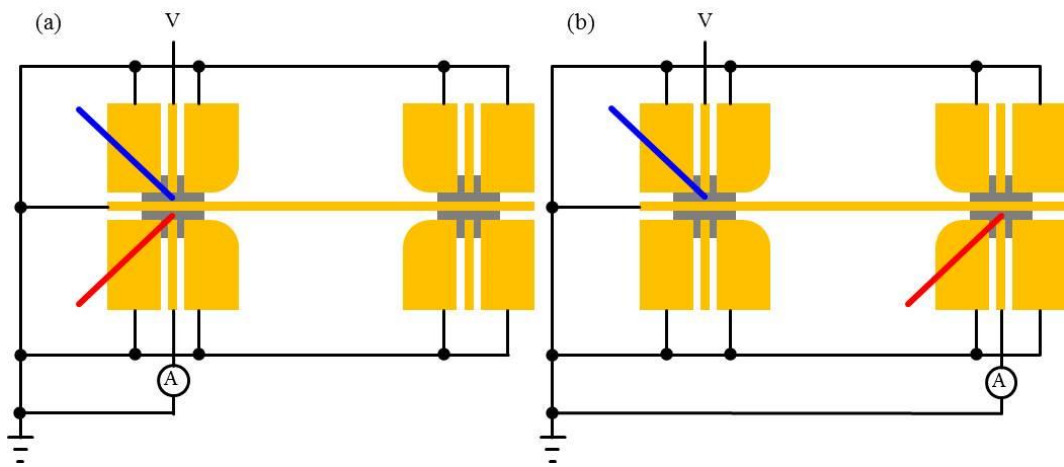


Figure 3.12: Simplified schematic diagram showing the electrical and optical bias conditions for generating and detecting (a) an input pulse and (b) an output pulse. The optical beams are represented by the red and blue lines.

The propagation velocity was calculated using one of two methods. The first method compared the position of reflections in the time domain spectra with respect to the transmitted pulse, against the device geometry. This single TDS scan spectral analysis required a certain degree of confidence for allocating the reflections to certain points of discontinuity in the transmission line based on the polarity of the pulse determining an increase or decrease in characteristic impedance (see Chapter 2), and in the case of multiple reflections, the relative time differences corresponding to relative distances. However, as the on-chip devices are developed, the amplitude of the reflections will be reduced in order to obtain clean frequency spectra making this method of calculating the propagation velocity increasingly difficult.

The second method uses a comparison of two TDS scans, measured in the same time window (Figure 3.13). The transmitted pulse is measured from one end of the transmission line to the other, and is then measured propagating in the opposite direction, by swapping the generating PC switch with the detecting PC switch; this is done by swapping the electrical connections with no change to the optical alignment. The propagation velocity, v_G , of the transmitted pulse is calculated using Equation 3-2, where t_1 and t_2 are the time positions of the forward and backward propagating transmitted pulses and L is the length of the transmission line.

$$v_G = \frac{2L}{t_2 - t_1} \quad 3-2$$

To further the understanding of this methodology, Figure 3.13a incorporates the experimentally unobserved (ie. within this time window) input pulses. The input pulses are measured and detected after a zero propagation distance and therefore have their maxima at the same position. Therefore the positions of the forward and backward transmitted pulses (see Figure 3.13a(i)) demonstrate the pulses propagating away from the point of origin, and hence the time difference between the transmitted pulses correspond to two propagation lengths.

This method is preferred over the single scan methods, since it removes any uncertainty in the origin of the reflections, as well as being applicable to reflection-free systems. There are alternative methods for measuring pulse velocities, but these require accurate measurements of the optical path lengths between the mirrors and the PC switches, which increases the error in the calculated velocity [169].

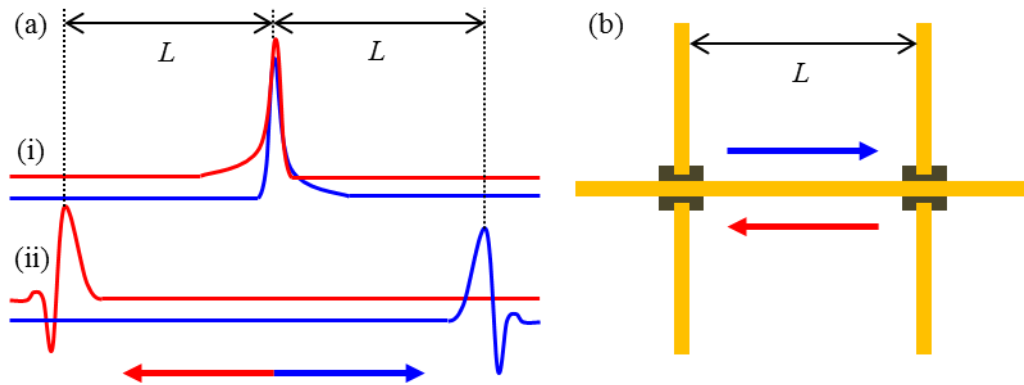


Figure 3.13: (a) Colour coded theoretical time domain traces for the (i) generated and (ii) transmitted pulses. Red traces represent the pulses propagating right to left and vice versa represented by blue. (b) Corresponding schematic of a transmission line with PC switches separated by PGL of length L .

Individual switch characteristics can be obtained by optically and electrically biasing a single switch, whilst recording the drawn photocurrent. The dark and light photocurrents (obtained for different laser powers) can provide insight into the sensitivity of the PC switches and the potential amplitude of generated pulses.

3.4. Initial Testing of On-chip Systems

To gain a better understanding of the system set-up and the characteristics of the tested device, an initial device was fabricated using optical mask designs from Li's work [95, 170]. The system was fabricated on a 350- μm -thick quartz substrate, and tested to gain an experimental understanding of previous work in this area, as well as to test some of the system limitations such as the ability to electrically chop the bias voltage as opposed to optical chopping for lock-in detection.

Owing to complications during fabrication, only 3 of the 4 PC switches were found to be operational, with the 4th switch found to have a high dark current. Nevertheless, several experiments can be done with 3 working PC switches to find the operating characteristics of the system, as discussed below.

3.4.1. Initial PGL Device Characterization

The initial device characterization involves determination of the operating characteristics of the different elements of the device: the individual PC switches, the input and output pulse characteristics.

3.4.1.1. Switch Characterization

The individual PC switches were characterized by taking IV sweeps as a function of illuminating laser power, and by taking photocurrent correlation measurements. The set-up for each of the two experiments is shown in Figure 3.14.

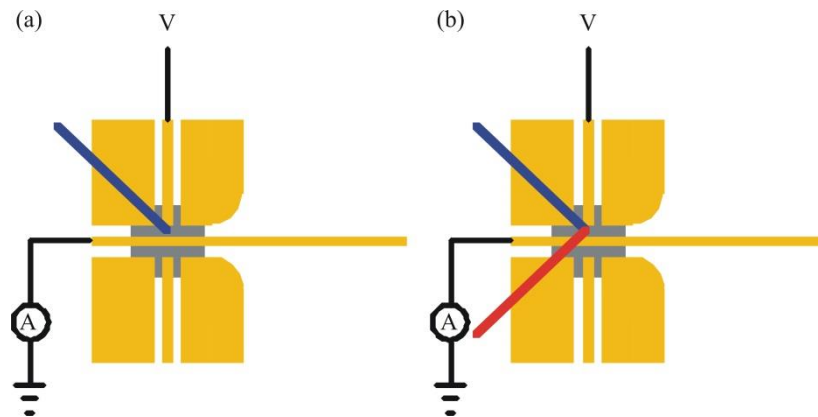


Figure 3.14: Simplified schematic diagram showing the electrical and optical bias conditions for characterizing the PC switches. The optical beams are represented by the red and blue lines. The red line in this case is the optically chopped beam. (a) Shows the schematic for IV sweeps and (b) shows the schematics for photocurrent correlation measurements.

3.4.1.1.1. IV Sweeps

IV measurements are obtained for each of the three working PC switches. In this test, the source meter is connected across the PC switch onto which a measured laser power is focused. The voltage is ramped from 0 V to the initial sweep value (-30 V), and then swept (in 0.1 V increments) to the final value (30 V), recording the drawn photocurrent at each set bias. The voltage was then ramped back to 0 V. By ramping the applied bias voltage before and after the scans, there is less electrical strain on the PC switches, reducing the likelihood of breaking the PC switch.

The IV sweeps show ohmic behaviour in the scanned range with the linear fits corresponding to the conductance of the switches (Figure 3.15). The resistance of the switches is found from the reciprocal of the conductance, which is then plotted against the laser power (insets of Figure 3.15).

Despite being made from the same LT-GaAs and subjected to the same fabrication conditions, no two PC switches were found to be precisely the same. Even reviewing the dark resistance, since it does not depend on laser power or the quality of the focus, shows variations in resistance from 345 M Ω to 394 M Ω . As a result, an accurate measurement of the S parameters will not be possible for these devices (Chapter 2). The differences in IV characterization may be due to the quality of the electrical contact between the LT-GaAs and

the Ti/Au metallization, or alternatively due to the uneven epitaxial transfer of the LT-GaAs film to the quartz.

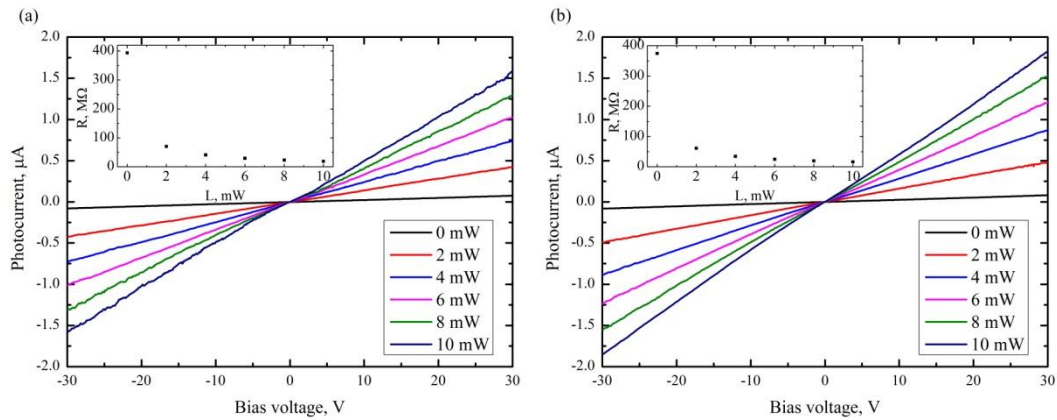


Figure 3.15: IV sweeps for the PC switches at different laser powers for the two of the PC switches. (a) IV sweeps for the worst of the three PC switches with the more unstable photocurrent and (b) for the best of the three with the cleaner IV sweeps due to being a better switch quality. Insets: The resistance (linear fits of the respective main figures) plotted against the laser power.

3.4.1.1.2. Photocurrent Correlation Measurements

For photocurrent correlation measurements (Figure 3.14b), the lock in amplifier was connected to the transmission line conductor, with the source-meter applied across the PC switch under test. Both the pump and probe beams were then focused onto same spot on the PC switch. A TDS measurement of the switch was then made. Due to the poor signal to noise ratio, 20 scans of each measurement were made and averaged to improve the SNR for analysis of the signal. The spectra are still relatively noisy, but clean enough to apply lines of best fit (Figure 3.16).

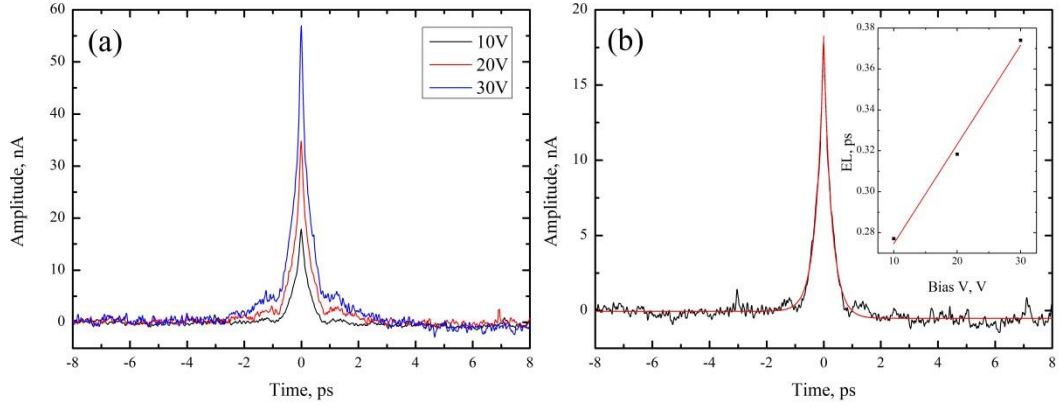


Figure 3.16: (a) Photocurrent correlation measurements taken at 10 V, 20 V and 30 V for 10 mW pump and probe beams. (b) 10 V bias photocurrent correlation measurements with exponential fitting to both sides of the pulse. Inset: Electron lifetime (EL) obtained by exponential fit plotted against the bias voltage on both the rising and falling edges.

The photocurrent correlation measurements exhibit large background amplitude, which is due to the current contribution from the source meter as well as the increase in the carrier density due to the additional optical influence. The lock-in detector is connected in series with the source meter, and therefore needs to provide a larger DC offset than that used for ps pulse measurements to prevent saturation in the recorded pulse.

The photocurrent correlation pulses shown in Figure 3.16 were all fitted with an exponential decay to each side of the pulse. The fit was chosen to match the Equation 3-3 derived by Deng *et al* [177] where t is the real time, τ_c is the carrier capturing time, δ is a ratio coefficient and T_G ($= 110$ fs) is the FWHM of the optical laser pulse used to excite the PC switch. However as the coherent interaction of the laser beams are not present in the photocurrent correlation spectra, the second term is neglected.

$$J(t) = \delta e^{(-t/\tau_c)} + (1 - \delta) e^{(-t^2 \ln 2 / T_G^2)} \quad 3-3$$

The measured carrier lifetime was found to be bias dependant (see inset of Figure 3.16b), increasing linearly from 277 fs (10 V bias) to 374 fs (30 V). A similar observation was made by Deng *et al* for high biased PC switches (Figure 3.17). Through theoretical analysis, the increase in the carrier lifetimes with bias voltage is attributed to the Frankel-Poole effect and enhanced thermal ionization due to the electric field. The Frankel-Poole effect is the lowering of the amount of energy required to excite electrons into the conduction band by increasing the electric field strength. The field enhanced thermal ionization which increases

the impact ionisation; the electrons have more momentum due to the increased electric field which is then transferred to exciting more electrons into the conduction band. This will increase the carrier concentration and ultimately increase the carrier lifetime of the PC switch.

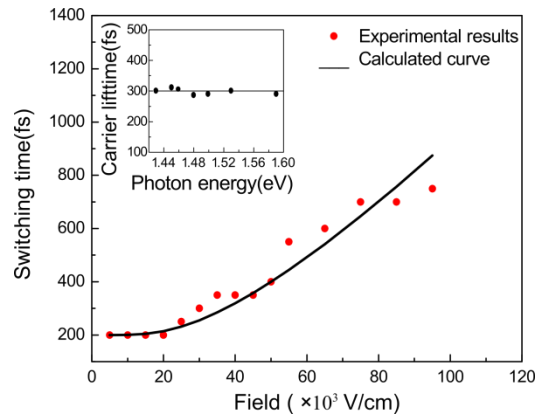


Figure 3.17: Bias voltage dependence of the switching times for LT-GaAs PC switches as calculated theoretically (solid line) and experimentally (scatter points) (taken from reference [177]).

Whilst photocurrent correlation measurements have proven useful for determining the photoconductive material properties, they also highlight a problematic effect when measuring the input pulse for systems with narrow centre conductors. The spot size of the focused optical beam has a finite diameter, which can cover both the switches for small values of the centre conductor width. As a result, both a convolution measurement and an input pulse measurement are effectively made simultaneously, resulting in a very narrow convolution pulse before the THz pulse as shown in Figure 3.18. This can be rectified by removing the pulse generated by the coherent interaction of the pump and probe beams, by changing the polarity of one of the beams using a half-wave-plate. The half-wave-plate rotates the polarity of the beam and in turn alters the amplitude of the convolution feature. The amplitude follows a sinusoidal fit to the relative angle of the half-wave-plate (see inset of Figure 3.18). For input measurements for the data shown in Figure 3.18, the half-wave-plate should be turned to 50° (with respect to the inset of Figure 3.18) to remove the convolution pulse.

It is interesting to note that the FWHM of the coherence feature is 110 fs wide and is only maintained during the time in which both the probe and pump beam strike the PC switch. The feature width would agree with the FWHM of the laser pulses. This has been attributed

by Jacobsen *et al* [178], to the “short carrier – carrier scattering time present at high carrier concentrations”.

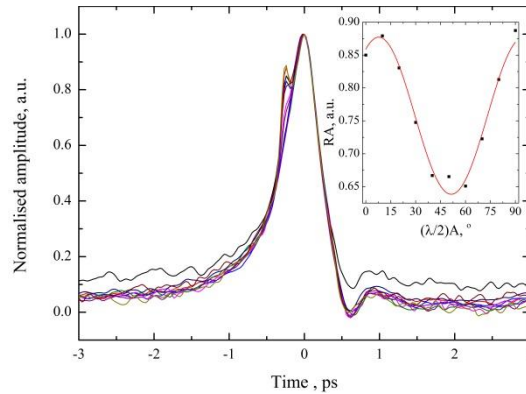


Figure 3.18: Normalised peak amplitude of input pulse measurements plotted for different positions of the half wave plate. Inset: Comparison of the relative amplitude (RA) as a function of the rotational angle of the half wave plate $((\lambda/2)A)$ fitted by sine function.

Further switch information could be extracted from the device by conducting a pump-probe reflection spectroscopy experiment [179, 180]. In this process, there is no electrical bias applied to the material under test. Instead, the pump beam creates free carriers, which are sampled by the probe beam, thus removing the electrical bias dependence of the earlier work. An optically delayed probe beam is reflected from the same focal spot as the pump beam. The amplitude of the reflected probe beam, modified by the conductivity (and therefore reflectivity) of the sample surface, is then monitored as a function of the time difference between the pump and probe beams. The resulting spectra is then analysed to determine a value for the carrier lifetime.

Using this process, it would be difficult to determine the carrier lifetimes for the LT-GaAs used in the PC switches, primarily due to the small size of the switches. The gold metallization would reflect most of the laser power, dominating the change in reflected probe amplitude due to the carrier concentration. The material could alternatively be analysed before the epitaxial lift off, but would then not be able to show any evidence of any changes in carrier lifetime caused by the material transfer or any of the other subsequent processes.

3.4.1.2. Input Pulse

The input pulse has a linear dependence on the both the laser power and the bias voltage (Figure 3.19). Within the -30 to 30 V and 0 – 10 mW bias ranges there is a clear

improvement in the amplitude of the signal, which can be used to compensate for signal attenuation in the transmission line. The insets of Figure 3.19 show the changes in peak amplitude as a function of the bias conditions, with a line of best fit applied to each; the input pulse amplitudes follow 0.35 nA/V and 1.04 nA/mW for the bias voltage and incident laser power respectively.

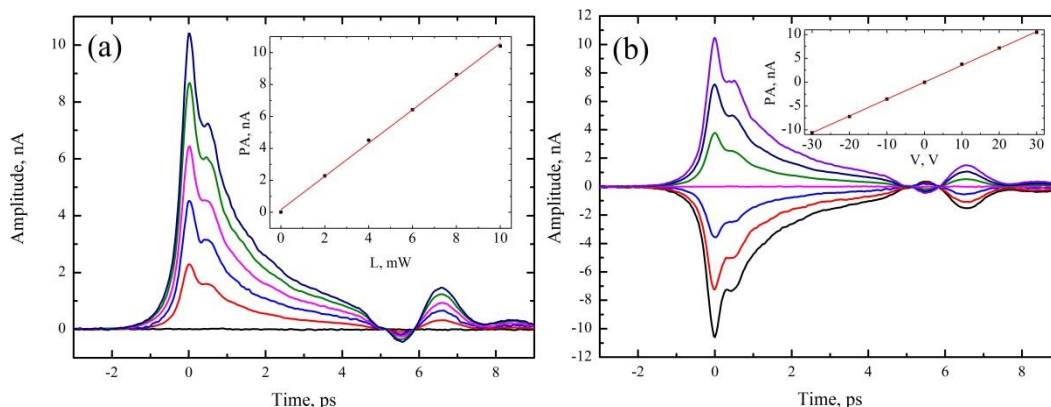


Figure 3.19: TDS spectra of the measured input pulse as a function of the (a) applied average laser power (5 mW increments from 0 mW (black) to 25 mW (indigo)) and (b) the applied voltage bias (10 V increments from -30 V (black) to 30 V (purple)). Insets: the respective peak amplitudes (PA) of the TDS spectra plotted against the bias conditions. A line of best fit is shown.

The input pulse has a FWHM of 1.13 ps when biased at 30 V for each of the laser powers, but as the bias voltage is reduced to 10 V for a fixed laser power (10 mW), the FWHM drops to 1.05 ps. This is in good agreement with the earlier photocurrent correlation measurements in section 3.4.1.1.2.

The input pulse also shows a negative reflection located 5.58 ps after the main transmitted pulse. This suggests that the transmission line has an impedance mismatch which is initially attributed to the CPW – PGL transition opposed to originating from impedance miss matching of the PC switches. This reflection proves to be problematic for noise-free frequency spectra and is ultimately truncated at a cost of lowering the frequency resolution of the spectra.

3.4.1.3. Output Pulse

The output pulse measured after propagation along the PGL can be generated by a single PC switch, or from both PC switches on either side of the CPW centre conductor. However, the input pulse cannot be measured using the two switch generation since a photocurrent

correlation measurement will be replicated (pump and probe beam would be focused onto the same PC switch). Therefore the comparison of amplitude dependence of the pulse generation and transmittance based on applied laser power and bias voltage is made using a single PC switch pulse generation.

The output pulse amplitude has a 0.17 nA/V bias voltage dependence and a 0.50 nA/mW laser power dependence. The output pulse also exhibits a larger FWHM of 1.68 ps, which is reduced to 1.63 ps as the bias voltage is dropped for a fixed laser power. The increase in the FWHM and the reduction in amplitude of the pulse in comparison to the input pulse are attributed respectively to dispersion and attenuation in the transmission line.

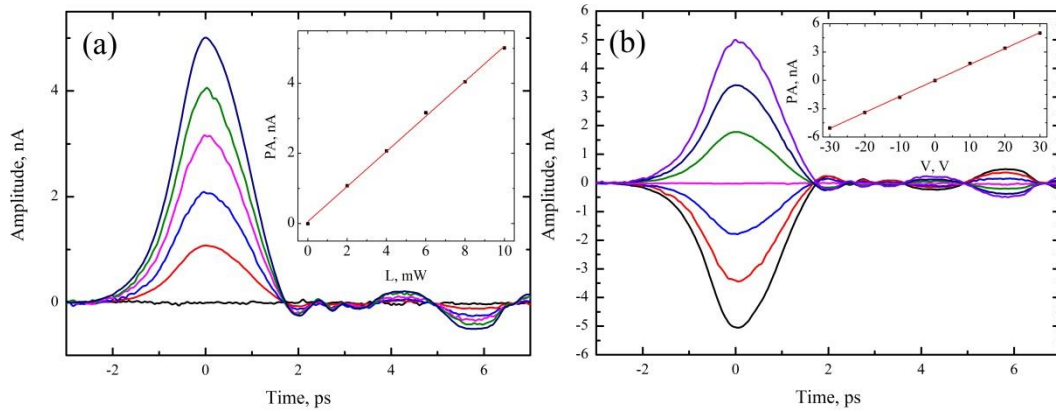


Figure 3.20: TDS spectra of the measured output pulse as a function of (a) the applied laser bias and (b) the applied voltage. Insets: the respective peak amplitudes (PA) of the TDS spectra plotted against the bias conditions. The line of best fit is shown.

Similarly to the input pulse measurements, there is a reflection observed 4.3 ps after the transmitted pulse maxima, but of positive amplitude. This is understandable if one considers that the device geometry is symmetrical; the generated pulse has transmitted along the transmission line, and is partially reflected at the PGL – CPW transition. The detector detects the positive pulse whilst the negative pulse propagates back along the transmission line to the initial PGL – CPW transition. The pulse is reflected back to the detecting side of the PGL as a positive pulse, which is detected in the output pulse TDS spectra.

3.4.1.3.1. Slotline Generation: Mode Testing

To investigate the mode of the detected transmitted signal, the signal is detected using both PC switches individually on either side of the CPW centre conductor. The detecting probe

beam is focused and aligned to a single detecting PC switch. The lock-in detector is then phase locked at the detected peak maxima obtained by moving the retro-reflector position. The lock-in detector phase lock function then remains untouched for the rest of the experiment, allowing any polarity differences between the PC switches to be detected as the probe beam and lock-in detector's electrical connection is moved between the two PC switches.

The pulse is generated using a slotline (Chapter 1) generation (10 mW laser, 30 V DC electrical bias) which is then detected using each PC switch in turn at the far end of the PGL. Figure 3.21 shows the resulting TDS spectra. Both detected pulses are of the same polarity suggesting a coplanar mode has been detected. This agrees well with theory for launching and detecting a PGL mode using the 2D horn antenna coupled CPW methodology (Chapter 1) [33]. The difference in the measured pulse amplitudes taken from each detection switch is attributed to differences in the PC switch quality.

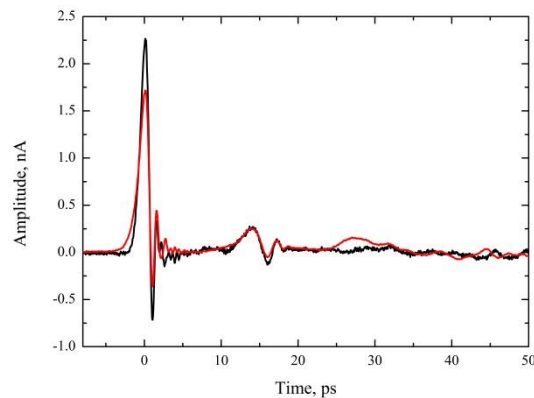


Figure 3.21: TDS spectra of the output pulse generated using slotline excitation, measured after propagation along a 1.5-mm-long featureless PGL. The pulse is measured from both sides of the CPW centre conductor.

3.4.1.3.2. Coplanar Generation: Mode Testing

Generation of the CPW mode (Chapter 1) can be “forced” into either a coplanar or slotline mode by using two PC switches to generate the pulse. A single pump laser beam was then used to excite both PC switches simultaneously, by increasing the focal spot size.

When aligning the single laser spot (10 mW) to both PC switches on either side of the CPW centre conductor, the focusing lens is moved towards the device, sending the focal spot behind the substrate. The spot size on the device surface is increased. Using two source-

meters, each powering a PC switch, the focus of the laser is altered to maximise and balance the recorded photocurrents. As a result, the photocurrent drawn (at 10 mW illumination power, 10 V DC bias) is reduced from 0.46 μA (0.16 μA dark current) for single PC switch generation to 0.25 μA on each PC switch. This is the reason that the relative amplitude of the transmitted pulse is reduced. This can be compensated for by either increasing the electrical bias or laser power.

By changing the relative polarities of the two electrical biases (both 30 V DC), either a pure coplanar mode or a slotline mode can be generated; to generate the symmetrical coplanar mode, the polarities must be the same, while to generate the asymmetrical slotline mode, the polarities are opposites. The resulting modes are measured using the same method as used for the slotline generation and the results are plotted for each of the bias conditions in Figure 3.22. The coplanar mode is detected when the pulses are of the same polarity and amplitude, and slotline mode is detected when the signal is “mirrored” in the x -axis with the same amplitudes, but opposite polarities.

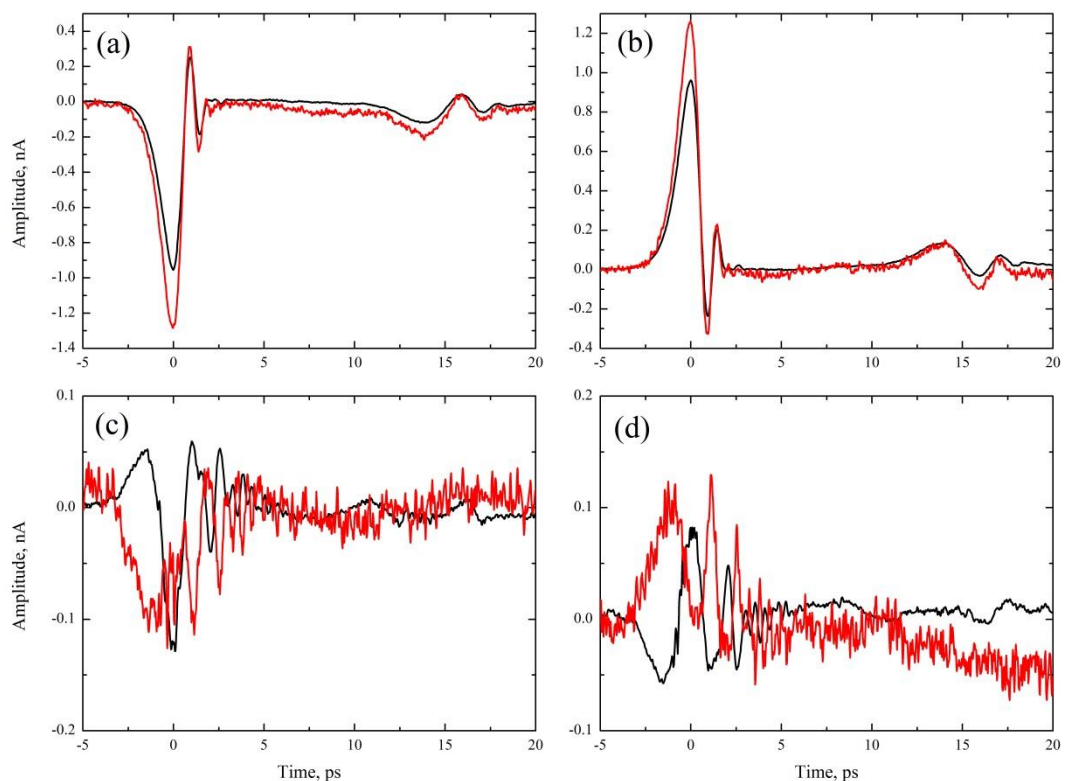


Figure 3.22: TDS spectra of the coplanar (a, b) and slotline (c, d) modes measured after propagation along a 1.5-mm-long featureless PGL. Each plot shows the measurements from both PC switches on either side of the CPW centre conductor.

When plotted for a single detection switch, Figure 3.23b, the amplitude differences between the different modes become clear; the slotline mode is more dispersive with more loss than the coplanar mode. This suggests that the PGL does not support the slotline mode. It can therefore be assumed that the PGL mode can only be excited by one mode; the coplanar mode.

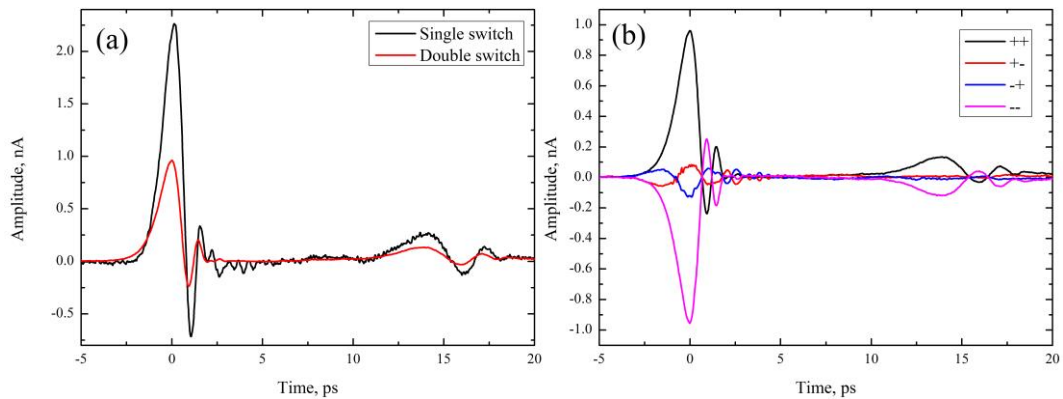


Figure 3.23: (a) Comparison of the transmitted pulse generated by double switch and single switch excitation. (b) Collated TDS spectra of the individual modes (legend highlights the polarities of 30 V DC biases) measured from the same switch plotted against each other.

Between single PC switch and double PC switch generation of the coplanar mode (Figure 3.23a), the single switch method is preferred. The single PC switch excitation signal has an improved signal amplitude (the position of the focal spot is not sacrificing half the laser power to illuminate a second PC switch), improved FWHM (single switch = 1.17 ps, double switch = 1.27 ps) and is directly comparable to input pulse measurements. As a result, single switch generation was found to be the preferred method for measuring the PGL devices.

3.4.2. Electrical Chopping of the PC Switch

In free space THz-TDS systems, the electrical DC bias applied to the PC emitter is “chopped”, as opposed to chopping the optical power. This allows for improved SNR of the resulting TDS spectra due to the improved stability of the reference signal applied to the lock-in detector. The electrical signal can also be chopped at higher frequencies than optical chopping allowing a wider range to find an optimal modulation frequency based on the detected SNR and signal amplitude. As a result, a square wave DC bias was applied to the generating PC switch of the PGL and the detected signal recorded.

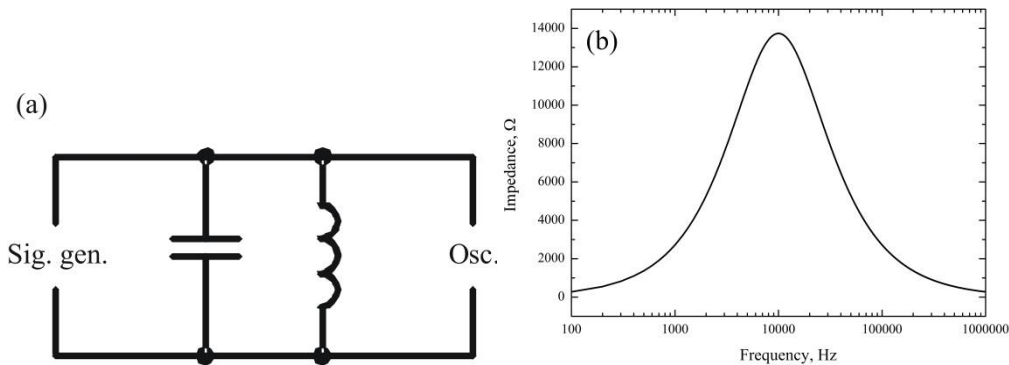


Figure 3.24: (a) Circuit diagram for testing the capacitance of the PC switch; the signal generator (sig. gen.), the PC switch (represented by the capacitor), the inductor and the oscilloscope (osc.) are all connected in parallel. (b) The impedance across the resonator against frequency (on a logarithmic scale).

The relative dark current is noted to increase as a function of the bias frequency (Figure 3.25d). This suggests that the PC switch has a small capacitance, which lowers the characteristic impedance of the switch with the increase in applied frequency. The capacitance of the PC switch was experimentally determined (Figure 3.24a) by connecting an inductor of a known value across the PC switch to form an electronic resonator. The resonant frequency was then found using a signal generator and oscilloscope connected in parallel with the resonator. The magnitude of the applied signal was maintained at 10 V peak to peak. The frequency of the applied signal was progressively increased from 100 Hz to the point where the magnitude of the signal seen in the oscilloscope is that of the signal generator; i.e. corresponding to the impedance reaching the maximum value (Figure 3.24b). The frequency was then further increased to observe a reduction in the magnitude of the signal to further confirm the maxima found. The frequency at this point was recorded and the capacitance of the PC switch calculated using Equation 3-4, giving 580 pF.

$$C = \frac{1}{4L(\pi f)^2} \quad 3-4$$

In terms of ps pulse generation, a 10 mW laser is applied to an electrically biased and chopped PC switch. The chopping bias used a square wave with peak to peak amplitude of 20 V, and a DC offset of 10 V. The square wave is from 0 – 20 V DC with varying frequency (225 – 2975 Hz, 250 Hz increments). The chopped signal is also used to trigger the lock-in amplifier with the lock in sensitivity reduced only when the signal is saturated. The lock-in amplifier's offset function was used for the initial scan (225 Hz), but not reset

for the other frequencies, allowing the relative increase in dark current to be recorded. The second PC switch was then used for detection. Figure 3.25a shows the resulting TDS spectra for different chopping frequencies. It is clear from the TDS data that the amplitude is significantly worse than that obtained using optical chopping. The relative amplitudes of the electrically chopped signals decrease to the point where no further change (~ 1 nA) was observed with increasing chopping frequency. The relative dark current was found to also increase with the chopping frequency, which suggests that there will be a maximum chopper frequency determined by the PC switch threshold current.

For the purpose of this thesis, the optical beam was chopped for lock-in detection with the DC biased PC switch. Whilst electrical chopping would be preferred due to its reputation of stability, the PC switch design would have to be modified to reduce the current due to an oscillating bias. This would be a design parameter to be considered when design PC switches in future generations of on-chip systems.

Further experimentation on the chopping frequency may include altering the pulse width modulation (PWM) of the chopper frequency. This may reduce the dark current as well as improve the signal to noise ratio, but would require a lock in amplifier with variable PWM reference signal (and these are usually specified to a fixed 50 % PWM).

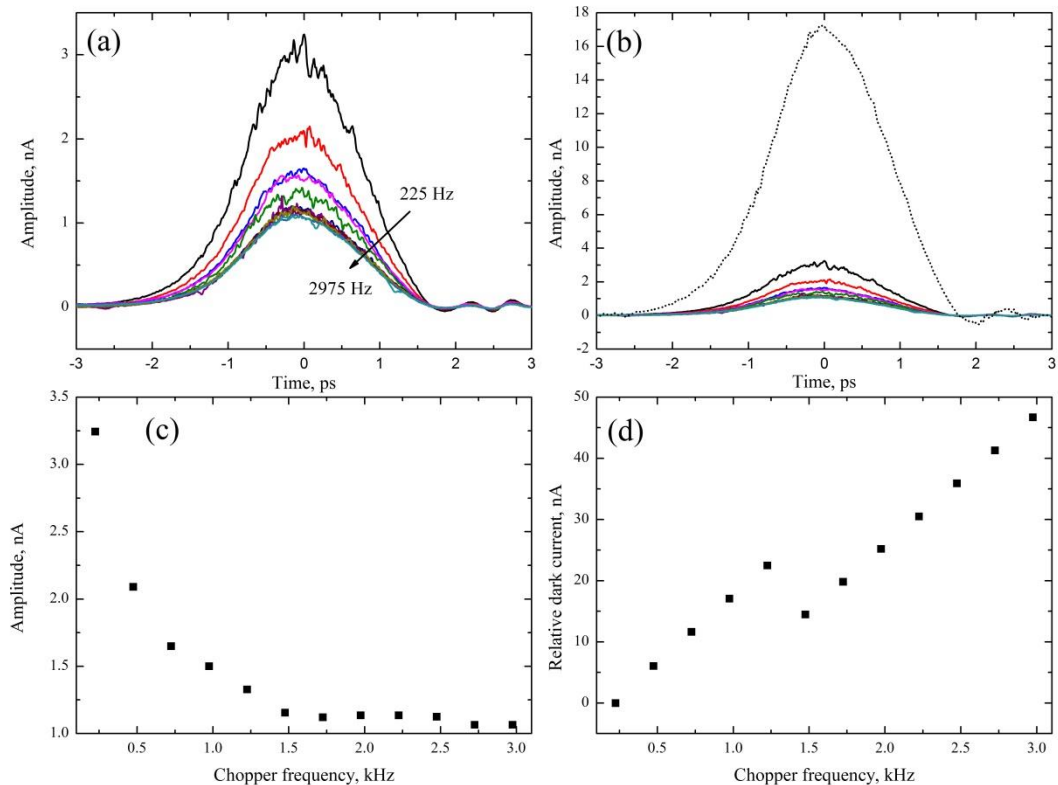


Figure 3.25: TDS spectra of an input pulse for different electrical chopping frequencies (a) without and (b) with the optical chop data (dotted line) for comparison. The amplitude of the (c) peak and (d) relative dark current of the TDS pulse are plotted as a function of the electrical chopping frequency. The inflection in the relative dark current measurement is the point where the sensitivity of the lock in amplifier is increased due to signal saturation.

3.4.3. Annealing Measurements

To optimize the annealing temperature for epitaxial transferred LT-GaAs PC switch THz generation, a method of stop-start annealing was investigated. In this process, the PC switch was fabricated using epitaxial transferred LT-GaAs on quartz, except the LT-GaAs is not annealed beforehand. The device was then tested and the switches characterized before removing the wire interconnects and cleaning the device. The device was then annealed in the rapid thermal annealer for 15 minutes, at the lowest of the chosen range of anneal temperatures. The device was then remounted and retested before annealing the device again at a greater temperature.

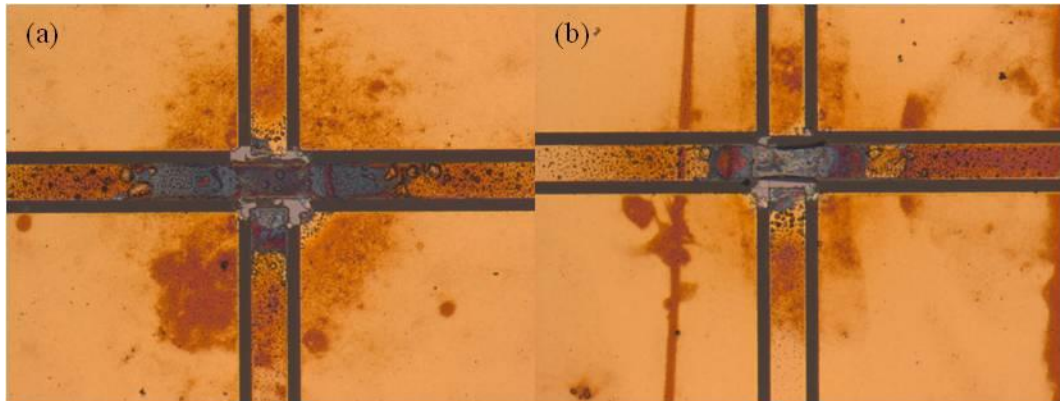


Figure 3.26: Micrographs of the PC switches following annealing at 500 °C. The LT-GaAs has been destroyed damaging the metallization surrounding the switches.

The results are presented for the un-annealed (though technically annealed at 250 °C during the fabrication in the post van der Waals vacuum oven step) and anneal temperatures 300 °C to 450 °C in 50 °C increments. Upon annealing at 500 °C, the device breaks down; Figure 3.26 shows the burnt out PC switches. It appears that the metal in contact with the LT-GaAs has burnt and some of the LT-GaAs has disappeared from between the switches. This may be attributed to the differences in thermal expansion of the metals, the quartz and the LT-GaAs. As a result, all LT-GaAs annealing at temperatures greater than 450 °C needs to be done before metallization, and the stop-start annealing methodology cannot be used beyond 450 °C.

For each anneal temperature, the device was characterized by measuring the input and output pulses (Figure 3.27) as well as recording the IV characteristics to find the dark and 10 mW resistance of the switches (Figure 3.28). There is no obvious change in the FWHM of the measured pulses however, nor are there any systematic changes to the signal to noise ratios. This may be due to the fact that the generating and detecting switches are both changing between each temperature measurement or the chosen switch geometries are not carrier lifetime limited. To measure the change in the generated signal due to annealing temperature, the same detector (not modified by annealing at each temperature) for each temperature is required as there may be different optimum anneal temperatures for THz generation compared with THz detection. This could be achieved by using a probe technique such as external EO detection [96] or external PC detection [43].

Further, this investigation assumes that annealing LT-GaAs (grown at the same temperature) at the same temperature will result in the same material parameters regardless of the samples thermal history (as long as it has not been heated beyond the anneal temperature).

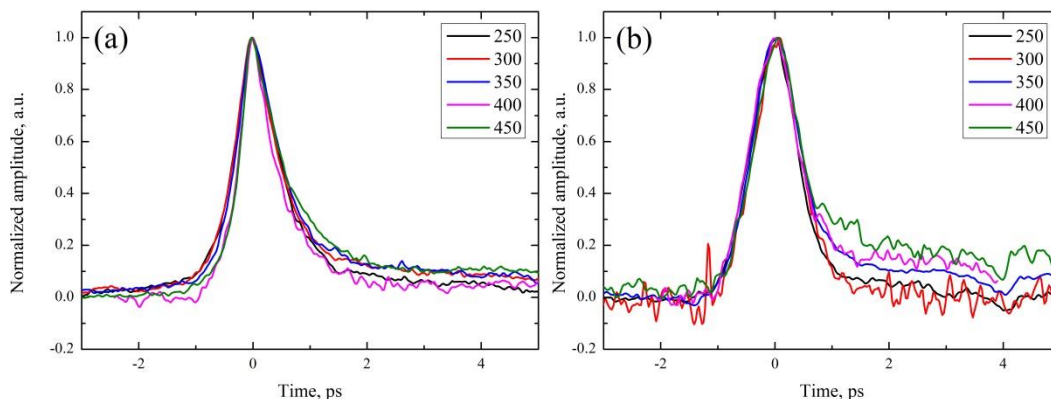


Figure 3.27: TDS spectra of (a) the input and (b) the output pulse at different annealing temperatures.

The IV characteristics can be assumed to be reasonably accurate, especially the dark current since the measurement is not dependant on any laser alignment issues. The trend shows a gradual rising of the dark resistance with the anneal temperature up to 400 °C. At 450 °C, there is a drastic change in the dark resistance. Figure 3.28 shows these results, compared to that of free space bowtie emitter testing by Gregory *et al* [133] showing an equal abrupt change in the resistance for anneal of 475 °C compared with 450 °C here which may be attributed to calibration error of the rapid thermal used in this work or that used in reference [133].

The higher anneal temperatures also demonstrated a greater difference in PC switch resistances for illuminated and non-illuminated biasing. This suggests that greater pulse amplitude can potentially be generated for the higher anneal temperatures as well as an improved detection SNR.

It should be noted that it is assumed there is no diffusion of the over laying metals (titanium and gold) into the LT-GaAs as the anneal temperatures are all well below the metal melting points.

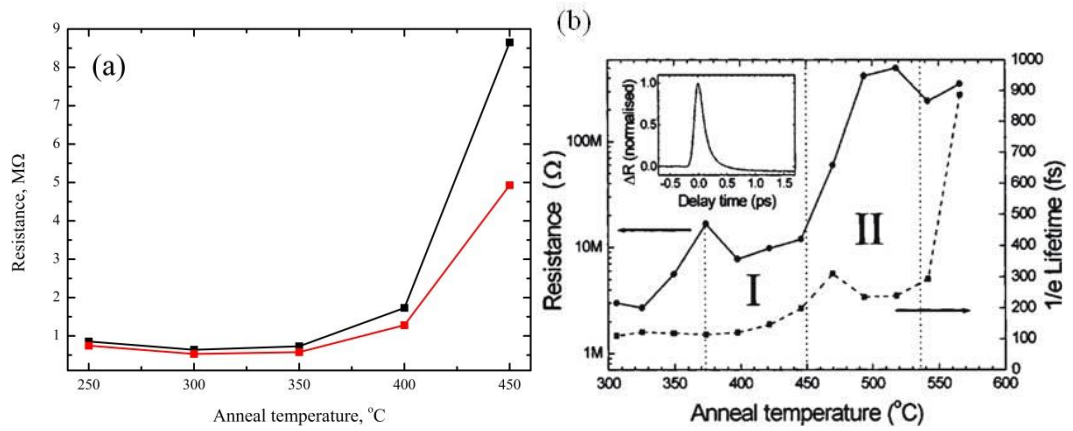


Figure 3.28: (a) Resistance of the PC switch for both dark (0 mW, black line) and illuminated (10 mW, red line) as a function of the anneal temperature. (b) Annealing temperature is against resistance and carrier lifetimes for free space emitters by Gregory *et al* [133]. I and II highlight the reported regions of the two stage increase in the resistivity of the LT-GaAs.

3.5. Wafer Thinning Theory

The initial formula for the effective permittivity of a PGL is given by [102]:

$$\epsilon_{eff} = \frac{\epsilon_r + 1}{2} \tag{3-5}$$

The formula assumes that the permittivity of the superstrate is 1 (i.e. air), and that the electric field is evenly distributed into the substrate and the superstrate. This analysis also assumes that the extent of the field into the substrate is far less than the substrate thickness. However, if the substrate is thinned, the substrate thickness will approach and eventually become thinner than the field extent, and this formula will therefore no longer be valid.

Therefore, a new formula needs to be derived to describe PGLs formed on substrates of thicknesses comparable to or less than the extent to the evanescent electric field. By making the following assumptions, the derivation of the formula is simplified.

- It is assumed that the field is circular around the centre conductor, similar to that of the Goubau and Sommerfeld lines. This assumption is further supported by HFSS simulations in (Chapter 2)
- The conductor has a negligible cross section, due to the relative cross section area in comparison to the electric field coverage.

- The field magnitude is evenly distributed within the circular area. Therefore the field is plotted as constant amplitude rather than as a decaying magnitude as function of the distance from the conductor.

With the assumptions made, a simple geometric model (Figure 3.29) is defined for the cross section view of the PGL with a substrate of thickness, h . The PGL metal is excluded from the model. The electric field is defined by a circle of radius, r , which is the effective extent of the evanescent field. The area of the substrate enclosed within the circle is calculated and multiplied by the relative permittivity of the substrate, ϵ_2 . The remaining area of the circle is calculated and multiplied by the permittivity of the superstrate, ϵ_1 . The total permittivity value within the circle is averaged by the circle's area to find the effective permittivity of the PGL. The formula can be broken down and simplified to:

$$\epsilon_{eff} = \frac{\epsilon_1[\pi + \theta - \text{Sin}\theta] + \epsilon_2[\pi - \theta + \text{Sin}\theta]}{2\pi} \tag{3-6}$$

Where,

$$\theta = 2\cos^{-1}\left[\frac{h}{r}\right] \tag{3-7}$$

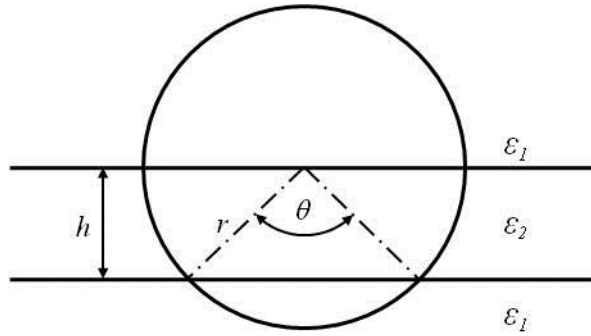


Figure 3.29: Geometric diagram of the cross section of the PGL on a substrate of permittivity, ϵ_2 , in a superstrate of permittivity, ϵ_1 . The substrate thickness is denoted by h and the extent of the evanescent field by r .

This formula is valid for all substrate thickness. In Figure 3.30a, the effective permittivity is plotted against substrate thickness for a range of substrate thicknesses from 20 μm to 160 μm , and is then compared with HFSS-computed values over the same range, (dotted line). The extent of the field is taken to be 100 μm (this is the effective extent of field measured by reference [95] for a 5 μm wide stub filter), the permittivity of the substrate to be

3.78 and the superstrate to be 1. The resulting figure shows an increase in permittivity from the initial substrate thickness to a point of saturation at $h = 100 \mu\text{m} = r$, the extent of the field. For substrate thicknesses greater than r , the effective permittivity is that calculated using the original Equation 3-5 for effective permittivity.

However, it is noted that there is an offset between the theoretical values obtained by HFSS and Equation 3-6. It is believed that this offset is due to the assumptions initially made in the derivation of the formula; the field is uniformly distributed within the circle, when in fact it is exponentially decaying. Nevertheless, it is still a reasonable guide for calculations and progressive trends.

In terms of transmission parameters, the HFSS results (Figure 3.30) show that there is a progressive increase in the bandwidth of the transmission line upon reduction in substrate thickness. In the 1 THz frequency window, the low frequency components ($< 300 \text{ GHz}$) remain unchanged whereas the high frequency loss is improved with the thinning of the substrate.

These results are a clear indication of the improved transmission line bandwidth which can be found from substrate thinning, and acted as a guide for experiments.

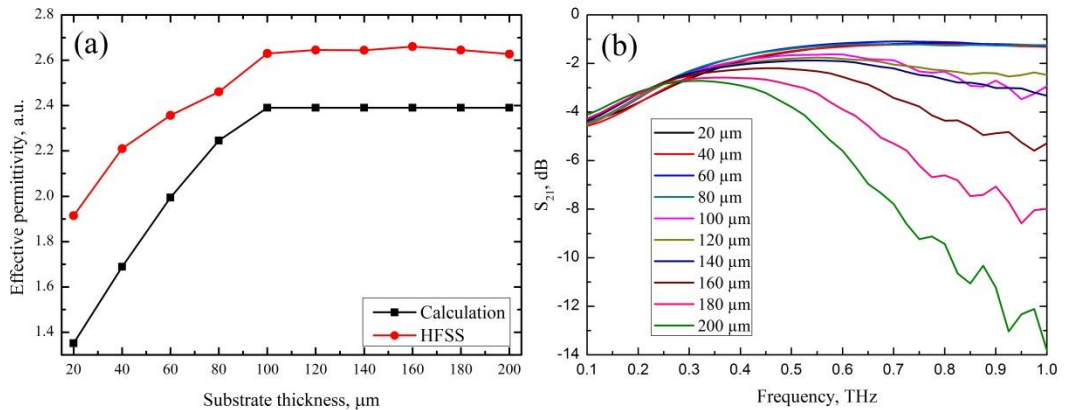


Figure 3.30: (a) Plot of theoretical values for effective permittivity, calculated using Ansoft HFSS at 500 GHz (black) and Matlab using the derived formula (red) for a range of substrate thicknesses. (b) HFSS results showing S_{21} parameters for an 800- μm -long, 5- μm -wide PGL on a quartz substrate with a varying thickness (20 – 200 μm , in 20 μm increments).

3.6. Chemical and Mechanical Thinning of Quartz Substrates

There are two main methods of reducing the thickness of substrates; mechanical or chemical. For quartz substrates, the choice of chemicals is limited to HF or buffered HF solutions, which have been demonstrated to be very efficient for defining microfluidic systems when the required etch depth is less than 100 μm . When attempting to etch 400 μm of the quartz used for PGL fabrication, however, the results were found to be poor owing to the non-uniformity of the etch. As shown in Figure 3.31, etching quartz with HF over these thicknesses reveals the grain structure of the quartz substrate. This was found to be unusable for thinned PGL lines as a constant substrate thickness was needed along the PGL, to remove permittivity mismatches which would result in problematic reflections.



Figure 3.31: Photograph of the quartz after substrate thinning using HF wet etching.

Therefore, mechanical lapping of the substrate was chosen as the preferred method. To test experimentally the concept of substrate thinning to enhance the bandwidth of PGL, the process was done by hand lapping, before investing in mechanical means.

3.6.1. Hand Lapping Process

The device side of the substrate was spin-coated (2000 rpm for 30 s) with a 2- μm -thick layer of S1813, before being hard baked (115 $^{\circ}\text{C}$ for 4 minutes). This acts as a surface protection for the device. The sample holder of the lapping chuck (Figure 3.32) was then heated on a hot plate at 120 $^{\circ}\text{C}$, and paraffin wax placed on to the holder which was allowed to melt. A thin glass slide was then placed onto the wax, and a second piece of paraffin wax then placed onto the slide. The device was then placed face down into the wax. The holder was removed from the hot plate and allowed to cool.

The holder was then placed into the lapping chuck, and positioned using the screws at the base of the device so that the difference in height (measured using a drop down micrometer) between the chuck edge and the device was equal to the depth of material to be removed. The sample holder was then secured into place by tightening the remaining screws and

placed top down onto sand paper (BuehlerMet@II Abrasive discs, SiC Grinding paper) and moved around the paper by hand. The sand paper was kept moist to trap any dust particles, as well as to improve the surface finish of the lap. A 200- μm -depth of thinning in quartz using silicon carbide sandpaper with an abrasive grit size of 127 μm , (P120) takes approximately 1 hour.

When the required thickness of the substrate was achieved, the holder was removed from the chuck and returned to the hot plate at 120 °C. The glass slide is removed from the holder, and the slide and device are placed into trichloroethylene to separate them. The device, when clear of wax, is placed into acetone and IPA to remove any remaining wax and the protective layer of resist.

The device is then remounted onto the PCB and the gold wire interconnects re-bonded.

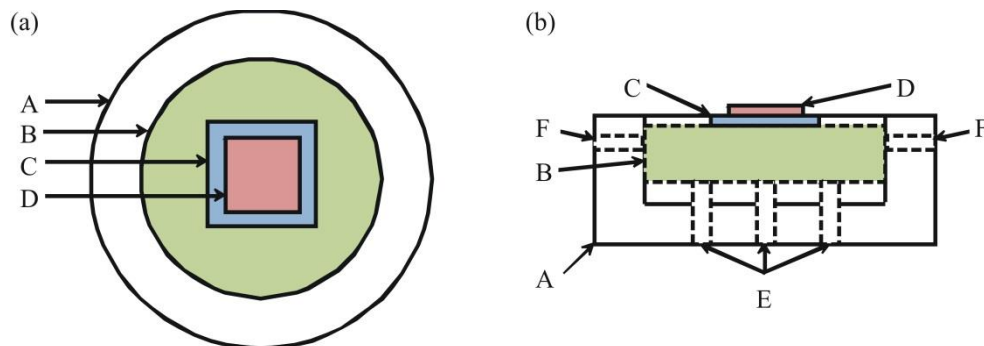


Figure 3.32: (a) Top view and (b) side view of the lapping chuck used. A = lapping chuck; B = sample holder; C = glass slide; D = sample to be thinned; E = sample holder levelling screws which alter the pitch of part B; F = sample holder securing screws. The difference between the top surface of A and the top surface of D is the distance to be removed by lapping.

3.6.2. Mechanical lapping – Logitech PM5 Precision Lapping & Polishing System

Whilst lapping by hand gave usable results for prototyping the fabrication process, it was still time consuming and gave a poor finish relative to automatic lapping machines. Deep scratches are caused by fragments of quartz from the edges of the device as well as the abrasive grit size being too large. The front and back surfaces of the finished sample was also found to be non-parallel due to uneven distribution of force on the lapping chuck when moving the chuck on the paper. A finer grit size would reduce both problems at a cost of increasing the production time.

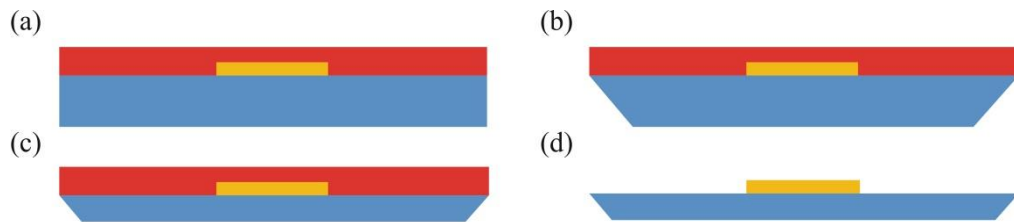


Figure 3.33: Simplified schematic of the step by step of the mechanical substrate thinning; (a) S1813 spun on and baked protecting the feature side of the device; (b) quartz edges are tapered for improved lapping; (steps not shown) device is mounted into the Logitech PP5 using the carrier disk and quartz wax; (c) quartz is removed by lapping; (d) wax is dissolved in trichloroethylene releasing the device, the S1813 is removed in acetone to reveal the device.

Using a Logitech PM5 Precision Lapping & Polishing System, the process was refined, made more controllable, and the production time reduced. The substrate was prepared for thinning by first tapering the edges to a 45° angle to reduce the chances of the edges of the substrate chipping. Chips off the edges of the substrate will scratch the substrate surface causing a weak spot.

The device side of the substrate was then coated with a $2\text{-}\mu\text{m}$ -thick layer of S1813, hard baked to protect the device. The device was then mounted onto the carrier disk using quartz wax (with stronger shear strength than paraffin wax) before being placed into a mounting jig (Logitech PP5). The sample was subjected to a 2.5 kg load on a flat cast iron plate, spinning at 70 rpm using $9\text{ }\mu\text{m}$ Al_2O_3 abrasive diluted to 10% in DI water suspension fluid. This resulted in a uniform surface roughness of ($R_a =$) 112 nm (mean value measured using a surface profiler) (micrograph shown in Figure 3.34b). The abrasive grit size was then reduced to $3\text{ }\mu\text{m}$ Al_2O_3 diluted to 15% in DI water reducing the surface roughness to ($R_a =$) 85 nm . The sample was then finished with a polish using a spinning (40 rpm) polishing cloth soaked in SF1 polishing fluid. This produced an optically flat finish on the quartz substrate.

The sample was finally removed by dissolving the wax in trichloroethylene and the resist removed using acetone. The sample was remounted onto the PCB and gold wire interconnects reconnected.

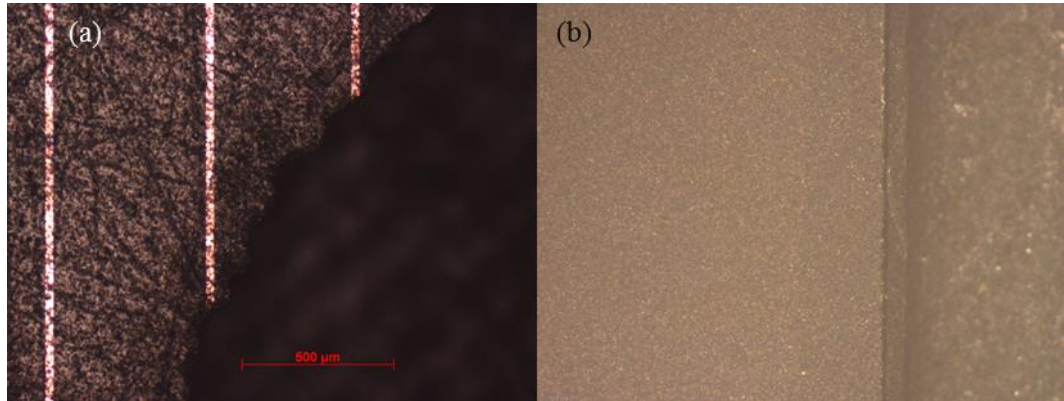


Figure 3.34: (a) Micrograph of the edge of a device substrate lapped by hand using BuehlerMet@II Abrasive discs, SiC grinding paper (P120). The micrograph shows the scratches (dark lines) caused by the rough grinding paper, which structurally weakens the substrate as well as the destroyed edge to the non-parallel mounting of the substrate to the chuck. (b) Micrograph of the edge of a device substrate (left hand side of image) lapped using the Logitech PM5 Precision Lapping & Polishing System with a consistent and even finish. The straight edges of the wafer have been maintained.

3.7. Experimental Results for Substrate thinning of PGLs

To test the theory of substrate thinning to enhance the bandwidth of the PGL, a 1.5 mm long PGL on quartz substrate was fabricated. The CPW regions of the device, as well as the PC switches were fabricated to have the same geometry as the devices discussed earlier. The device was initially tested for its operation characteristics before being successively removed from the PCB, modified (substrate thinned), remounted and retested.

3.7.1. Device characterization

It is evident from Figure 3.35 that the amplitude of the transmitted pulse can be increased without affecting the signal shape by either increasing either the bias laser power or bias voltage within their respective ranges. The pulse amplitude is well fitted with a linear dependence of 0.46 nA/mW with laser power (inset of Figure 3.35a) and 0.15 nA/V for the bias voltage (inset of Figure 3.35b). The PC switches are also able to detect and distinguish between the polarities of the biased signals. This was further emphasized by the IV sweeps (Figure 3.36) of the PC switches at different laser powers; all switches exhibit ohmic behaviour. The resistance values (obtained by linear fitting of the IV sweeps) are plotted against the laser bias to demonstrate the progressive reduction in resistance with an increase

in laser power (inset of Figure 3.36). The change in resistance with laser power shows an exponential dependence on the laser bias.

The time domain traces also show a reflection in the transmitted pulse seen at around 15 ps. It is believed that this originates from an impedance mismatch at the CPW – PGL transition. This reflection is problematic for achieving high resolution FFT data, but useful in calculating the propagation velocity, and therefore calculating the effective permittivity of the transmission line.

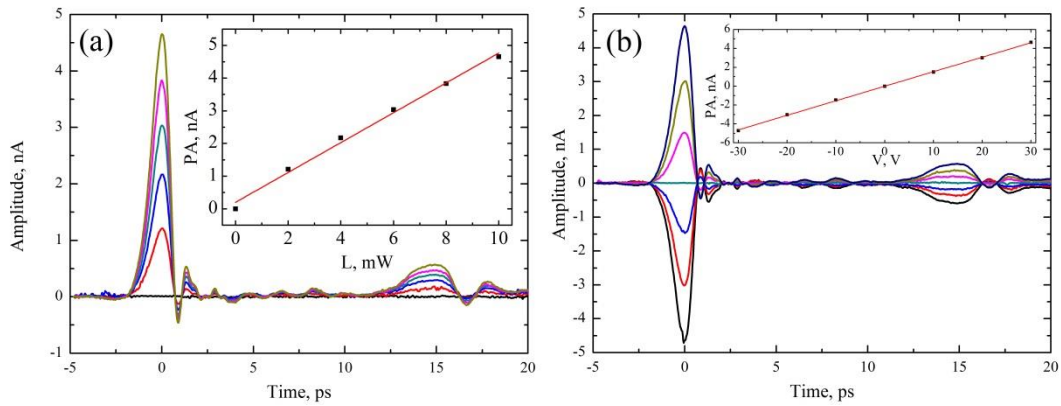


Figure 3.35: Time domain spectra of the transmitted pulse demonstrating the effect of increasing (a) the bias laser power for a fixed bias voltage and (b) the bias voltage for a fixed laser power (data taken from 85 μm substrate thickness device). The insets show their respective peak amplitudes (PA) with linear fits.

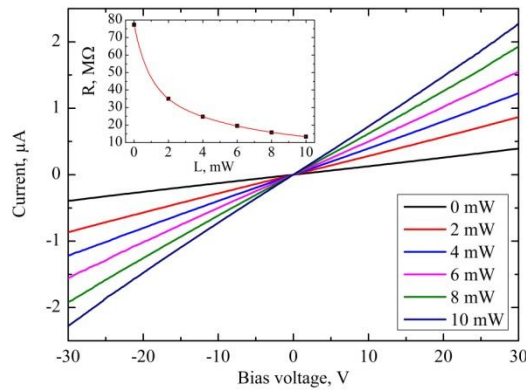


Figure 3.36: IV sweeps one of the four PC switches of the PGL varying laser powers. The insets show the laser power against the switch resistance (with an exponential decay fit) obtained using linear fitting of the main figures.

3.7.2. Effects of Substrate Thinning

Pulse measurements were taken for each of the substrate thicknesses under the same bias conditions; 30 V DC bias and 10 mW laser power. Both the input and output pulses were recorded using the same switch combinations. The results (Figure 3.37) show that as the substrate is thinned, there is negligible difference in the input pulse (main pulse) suggesting that the pulse generation is independent of the substrate thickness; however there is a progressive change in the transmitted pulse. As the substrate is thinned, the FWHM of the transmitted pulse is made progressively more narrow, suggesting a reduction in the dispersion of the transmission line (Figure 3.38). This means that the bandwidth of the device is also increasing (Figure 3.40). It should also be noted that a reflection seen between 14 and 17 ps in both the input and transmitted pulse plots occur earlier in time (Figure 3.38) and becomes more defined with substrate thinning. This suggests both an increase in propagation velocity and a reduction in attenuation of the signal. However, this reflection becomes problematic when the data undergoes FFT into the frequency domain and is usually the point in which the data is truncated. Although the bandwidth was improved, the effective resolution of the frequency spectra was reduced.

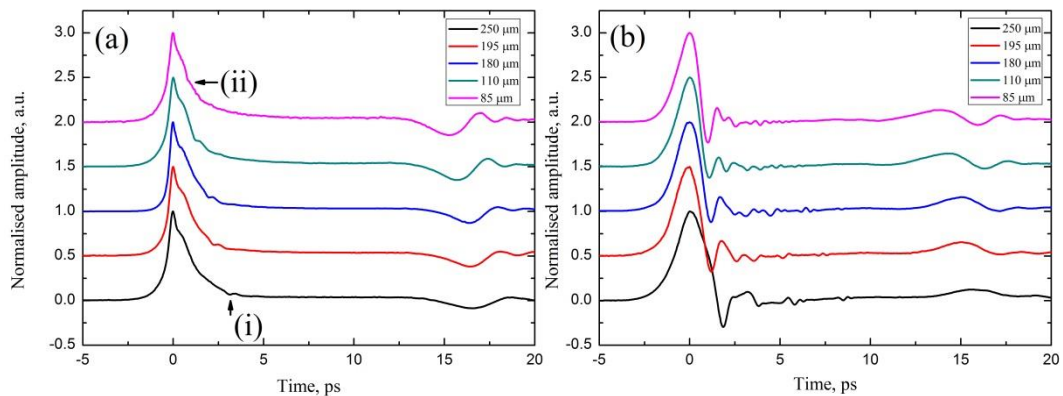


Figure 3.37: Normalised time domain spectra of (a) the input and (b) the transmitted pulses for five substrate thicknesses, vertically offset by 0.5 units for clarity. For (a), reflections of the input pulse off the back of the substrate have been marked on (i) 250 μm and (ii) 85 μm substrate thickness spectra.

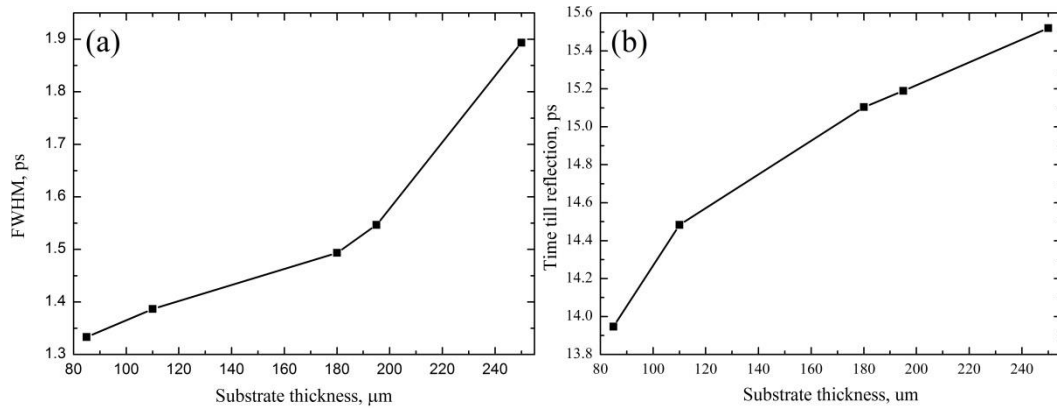


Figure 3.38: (a) FWHM of the transmitted pulse against substrate thickness. (b) The time difference between the maxima of the transmitted and the reflected pulse.

An interesting feature to note in the input pulse (not seen in the output) is a small reflection which occurs earlier in the time domain with substrate thinning moving from 3.12 ps (250 μm thick substrate, Figure 3.37a(i)) to 0.8 ps (85 μm thick substrate, Figure 3.37a(ii)). When the difference between the generated pulse and the small reflection is plotted against the substrate thickness (Figure 3.39a), the linear fit has a gradient of 7.55×10^7 m/s which corresponds reasonably well to the calculated value of 7.72×10^7 m/s (Equation 3-8, where $\epsilon_r = 3.78$). This is due to a reflection of the THz radiation from the emitter off the back surface of the substrate and has been observed by other groups (Figure 3.39b) [181]. Equation 3-8 calculates the group velocity as a function of the relative permittivity of the substrate. The relative amplitude of the reflection has negligible effect on the FFT of the input pulse data and can therefore be overlooked, but could be used in future to accurately determine the substrate thickness at the position of the PC switch. The reflection is not seen in the output pulse, suggesting that either it has not coupled itself back into the transmission line or that it has been attenuated to an undetectable magnitude at the output switch.

$$v = \frac{c}{2\sqrt{\epsilon_r}} \quad 3-8$$

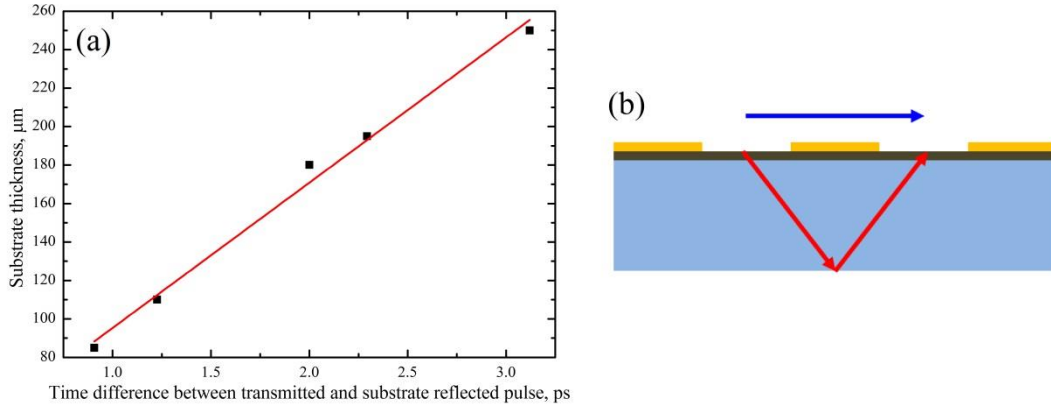


Figure 3.39: (a) Scatter plot showing the time to reflection due to the back of the substrate with a linear fit. (b) Cross section view of the PC switch showing the propagation of the (blue) main input pulse from generating to detection PC switch and the (red) reflection off the back of the substrate.

The effective permittivity of the transmission line can then be calculated using the time difference between the transmitted and reflected pulse using Equation 3-9.

$$\epsilon_{eff} = \left(\frac{ct}{2d}\right)^2 \quad 3-9$$

Here, d is the distance between the point of reflection (1.5 mm) and t is the time between the maxima of the transmitted and the reflected pulses. It can be seen from the plotted data (Figure 3.40) that, as the substrate is thinned, the effective permittivity of the transmission line is reduced in agreement with the calculation performed in section 3.5. However, there appears to be a less defined point of saturation of the effective permittivity in the measured device when compared to the theoretical and simulated predictions. This is attributed to the assumptions made in the theoretical work, but also to the fact that the calculation was done with continuous wave transmission at one frequency due the software limitations whereas the experimental work was performed using TDS pulse measurements which includes a spectrum of frequency elements.

Ultimately, there is also a progressive improvement in the bandwidth of the PGL. Figure 3.40b shows the bandwidth of the PGL for a range of substrate thicknesses; 250, 195, 180, 110 and 85 μm. The bandwidth of the device has increased to 1.5 THz for an 85-μm-thick

substrate, which is due to reduction in the dispersion of the transmission line, i.e. the group velocity mismatch seen by the signal above and below the PGL has been reduced.

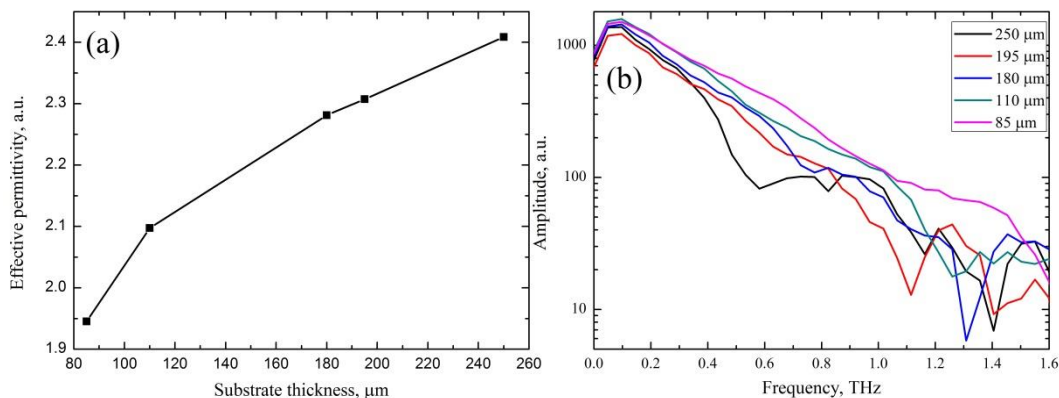


Figure 3.40: (a) Effective permittivity calculated using the time till reflection from the output data. (b) FFT of the normalised output pulse for varying substrate thickness.

3.8. Spectroscopy Application for PGLs

The enhanced bandwidth of the PGL is then used for spectroscopy of overlaid polycrystalline materials. 40 mg of lactose monohydrate (Fluka) was weighed out and pressed into a 0.55-mm-thick pellet with a diameter of 8 mm. The 0.55 mm thickness ensures that the full extent of the evanescent field from the PGL is utilised for spectroscopy. The pellet was then diced into 1 mm² pieces which were subsequently held over the PGL using tape. The 1 mm width ensured that the sample would fit comfortably onto the PGL without obstructing the optical path to the PC switches. The transmitted pulse was then recorded and Fourier transformed. With the inclusion of the reflection in the FFT, the spectrum is noisy with a resolution of ~ 30 GHz (limited by the finite time window recorded). Therefore a truncation of the reflection was applied to remove the oscillation and the data then zero padded to 2048 data points with a 26.67 fs time resolution (Figure 3.41). The resolution of the spectra is reduced to 60 GHz due to the smaller time window. Ultimately, there is a proof of principle that PGLs can be used for THz absorption spectroscopy of overlaid materials as two absorption peaks are measured in the lactose sample, at frequencies of 0.53 and 1.36 THz. These absorption peaks agree well with previously recorded data using both on-chip THz waveguides and free space TDS experiments [12, 22, 37, 182, 183].

The time difference between the transmitted and the reflected pulse has also increased from 13.94 ps to 14.73 ps corresponding to an increase in effective permittivity from 1.94 to 2.17, resulting directly from the presence of the overlaid lactose monohydrate sample. Using a series of formulae, an approximation for the refractive index of lactose monohydrate can be made.

$$\epsilon_{total} = \left(\frac{d-L}{d}\right)\epsilon_{ref} + \left(\frac{L}{d}\right)\epsilon_{load} \quad 3-10$$

$$\epsilon_{ref} = \frac{1 + \epsilon_{sub}}{2} \quad 3-11$$

$$\epsilon_{load} = \frac{\epsilon_{sample} + \epsilon_{sub}}{2} \quad 3-12$$

Where L is the sample length and d is the transmission line length. ϵ are the effective permittivity with their subscripts denoting which they represent; total loaded PGL measurement (*total*), unload PGL measurement (*ref*), the loaded partition of the PGL (*load*), the “substrate” (*sub*) and the sample under test (*sample*). Equations 3-11 and 3-12 can be equated to give a term for the permittivity of the sample, which in turn can be used to find the refractive index, n .

$$(n_{sample})^2 = \epsilon_{sample} = 2(\epsilon_{load} - \epsilon_{ref}) + 1 \quad 3-13$$

The refractive index for a 1 mm long sample of lactose monohydrate was found to be 1.636. This broadband refractive index value corresponds reasonably well to previous measurements (free space THz-TDS refractive index = 1.8 (averaged from 0.3 – 2 THz)) as an average value over a frequency spectrum, but cannot be considered to be an accurate measurement due to the margin of error of calculating the sample’s interaction length on the transmission line as well as the sample’s integrity; a sample with several air pockets will have a lower average refractive index per unit volume. For an accurate refractive index measurement, it is wiser to use a resonator [95], where the length of the interaction length between the sample under test and the PGL is less critical. For a load with a known permittivity, there is potential to measure the sample’s interaction length assuming that there is perfect contact between the sample under test and the PGL.

Conclusion

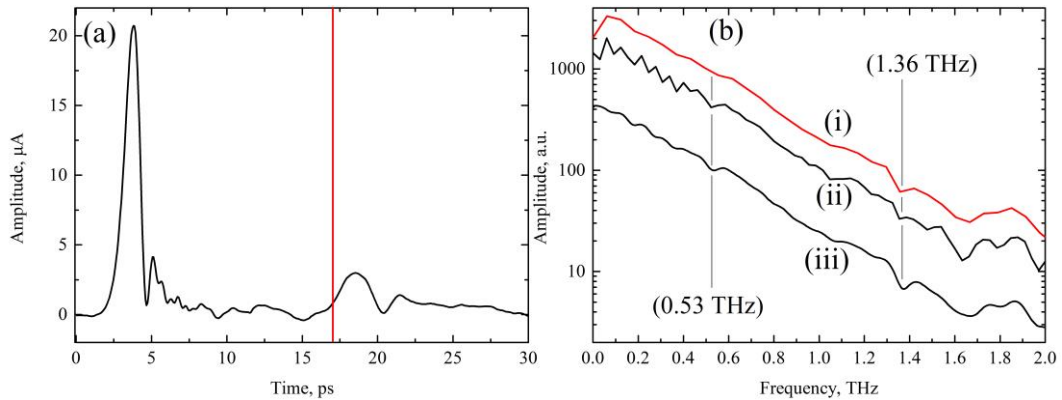


Figure 3.41: (a) Time domain spectra of the transmitted pulse of overlaid lactose monohydrate with the truncation point highlighted (red line). (b) The frequency spectra of the (ii) raw data, (i) truncated and (iii) zero padded TDS spectra with the two spectral features labeled.

3.9. Conclusion

In this chapter, a detailed description of the fabrication of on-chip devices using epitaxial transferred LT-GaAs on quartz has been presented. The methodology which was developed was used to fabricate all subsequent devices presented in this thesis. The experimental testing of the on-chip devices was also reviewed, with attention paid to the PC switches; the IV sweeps and the photocurrent correlation measurements highlight the change in the generated pulse shape due to the electrical bias and the laser power. Testing of the annealing temperature was proposed and tested, but for more informative results, individual devices should be fabricated and the LT-GaAs analyzed using optical pump – probe measurements to remove any influence due to the switch geometry and electrical biases.

Electrical chopping measurements highlight the difficulties of the said method; the capacitance of the PC switch causes a reduction in the impedance across the PC switches for increasing electrical chopping frequencies. Therefore the switch ideally needs to be redesigned for the ultimate optimisation, to reduce the capacitance, or optical chopping should be used. Due to time constraints of the project, the latter is chosen for the remaining experimental work.

The theory of substrate thinning aimed at increasing the system bandwidth was discussed through the derivation of a formula for the effective permittivity of PGLs and HFSS simulations. This was then experimentally confirmed with a thorough explanation of PGL fabrication techniques on quartz substrates and an explanation of the experimental setup

given. The basic understanding of the PC switch characteristics were explained with the tested PGL before reviewing the practical effects of substrate thinning. The expanded bandwidth was then used to demonstrate the potential of PGLs to be used for spectroscopy applications, but highlighted needed improvements.

The results presented in this chapter were presented as an invited talk at the IRMMW-THz 2011 conference in Houston, Texas and were published in the proceedings of the same conference [184].

It should be noted; in 2012, Treizebre *et al* published results for the effect of substrate thickness on transmission line properties [90]. The work used Pyrex ($\epsilon_r = 3.75$) substrate of two commercially available thicknesses; 500 μm and 350 μm . Using the S_{21} parameters obtained using VNA measurements, the 3 dB cut-off frequency is plotted against the substrate thickness. The two data points are then compared to the cut-off frequency for dielectric waveguides with good agreement suggesting the bandwidth is limited by the substrate modes. However, it is not clear from the data if the trend is continued for substrate thicknesses less than 350 μm to confirm these results or if the results are valid for pulsed propagation as well as the tested frequency propagation. Like all VNA work, the results are limited by the bandwidth of the VNA used.

Chapter 4. Variable Temperature THz-TDS Measurements of Polycrystalline Materials using Planar Goubau Lines

In the previous chapter, it was shown how substrate thinning can significantly enhance the bandwidth of PGLs, pushing further the range of applications for PGLs. The potential for PGLs to be used for absorption spectroscopy was introduced but suffered poor spectral resolution. In this chapter, several design modifications are presented to enhance the spectral resolution. The resulting designs are then utilised for variable temperature measurements of polycrystalline lactose monohydrate, a commonly used THz spectral standard, and the results compared with other spectroscopy systems.

4.1. Initial Design Improvements to Enhance the Frequency Resolution of PGL devices

The PGL designs are modified to enhance the spectral resolution by removing reflections in the system through impedance matching. At the same time, the designs are modified to improve the reliability of devices fabrication.

4.1.1. Sliding PC Switch Design

The spectral resolution of the PGL devices discussed in the previous chapter was limited by the reflections in the time domain spectra which originate from points of impedance mismatch which need to be located. Reviewing the CPW regions of the initial PGL devices, there were two noted points of impedance mismatching caused by the metal geometry. The first relates to the gap width to centre conductor width ratio, which is not maintained during the narrowing of the centre conductor, and is therefore responsible for a change in the transmission line impedance. The second is a break in the ground planes to accommodate the probe arms defining the PC switches, which causes a potential open circuit termination on the transmission line.

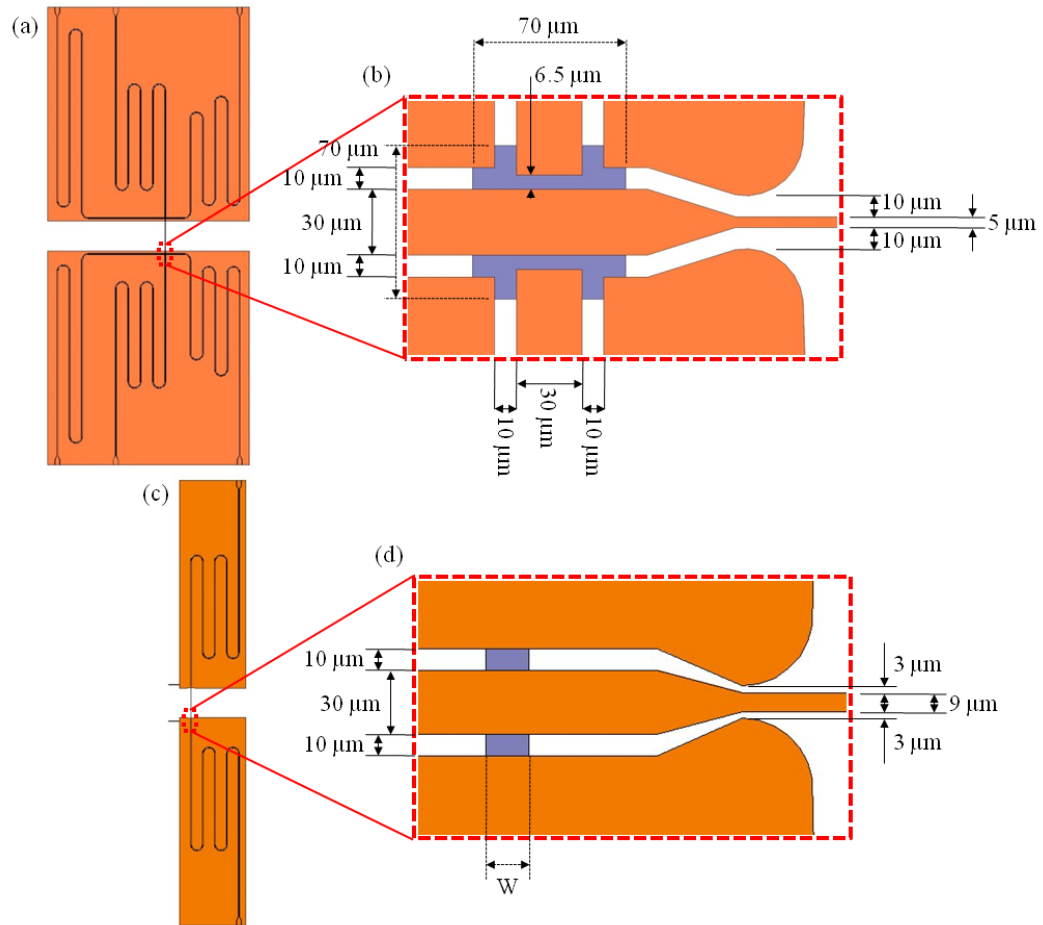


Figure 4.1: (a) A schematic of the second generation PGL device with the metallization shown in orange. (b) A magnified region of the switch regions shown for clarity (rotated 90° with respect to (a)). (c) A schematic of the third generation PGL device, highlighting the reduction in the device size. (d) A magnification of the switch regions of the design for clarity, with grey regions indicating LT-GaAs of width W (rotated 90° with respect to (c)).

The third generation PGL geometry in Figure 4.1c, d aims to combat both these issues as well as incorporating further fabrication advantages. The impedance mismatch due to the narrowing of the centre conductor has been rectified by reducing the gap widths at the PGL end of the CPW to maintain the geometry ratio and hence the impedance. To make the centre conductor $5 \mu\text{m}$ wide, the gaps on either side would have needed to be $1.33 \mu\text{m}$ wide, which would have proven difficult to define using optical lithography. Therefore the PGL width has been increased to $9 \mu\text{m}$ allowing the gap size to be increased to $3 \mu\text{m}$. This will also increase the extent of the evanescent field as a result (see simulation results in Chapter 2).

The PC switch itself was redesigned to remove the probe arms all together allowing a continuous ground plane to be defined. The PC switches were then defined by a “sliding

switch” geometry, where the PC switch size is determined by the width of the LT-GaAs in the CPW gaps. This method in turn offers several further advantages to previous device design with respect to the fabrication procedure. When selecting the regions of LT-GaAs to be used to define the base material of the PC switches, this decision needs to be made before the LT-GaAs etch when fabricating the generation I and II devices (two $70\ \mu\text{m} \times 70\ \mu\text{m}$ squares) [95, 170]. This limits the flexibility of the fabrication process. By defining two long “rails” of LT-GaAs, larger regions of LT-GaAs are available allowing selections of optimal LT-GaAs material for the PC switches just before the metallization (Figure 4.2a). The unused LT-GaAs are then covered by the ground planes, and so have no influence on the operating characteristics of the device.

This device geometry has further advantages which have been utilised for research into graphene characteristics. The rapidly growing research into graphene has expanded focus from the DC measurements to the higher electronic frequencies, but has so far been limited mostly to free-space THz characterisation (limited to absorption spectra). It was proposed that on-chip measurements of graphene, similar to CPW – 2DEG measurements, would give a more informative insight into the materials properties, specifically plasmons and magneto-plasmons [185].

It is worth mentioning that this new method of using sliding rails for defining the LT-GaAs for selectivity of better LT-GaAs has also subsequently proved beneficial for the fabrication of systems testing the ps response of graphene using PGL on-chip systems. One of the main difficulties in the fabrication of the PGLs is the transfer of relatively large areas of monolayer and bilayer graphene onto specific regions of the device. The solution is to fabricate the rails of LT-GaAs first, which allows more aggressive cleaning of the substrate between the PC rails accommodating the graphene transfer. A piece of graphene significantly larger than the area needed is bonded to the substrate. The quality of the graphene transfer is reviewed using Raman spectroscopy and AFM imaging allowing a more informed selection of graphene to be tested to be made [185]. The sliding of the metallization over the LT-GaAs allows this selection to be made, whereas earlier devices do not (Figure 4.2b).

The design was later modified to reduce the problematic coupling between the two PGLs; the PGLs were positioned 90° to one another. This reduced the coupling enabling any

detection of a transmitted pulse to be attributed to the graphene connecting the two PGLs. The sliding concept is still being used by the Leeds research group for graphene studies.

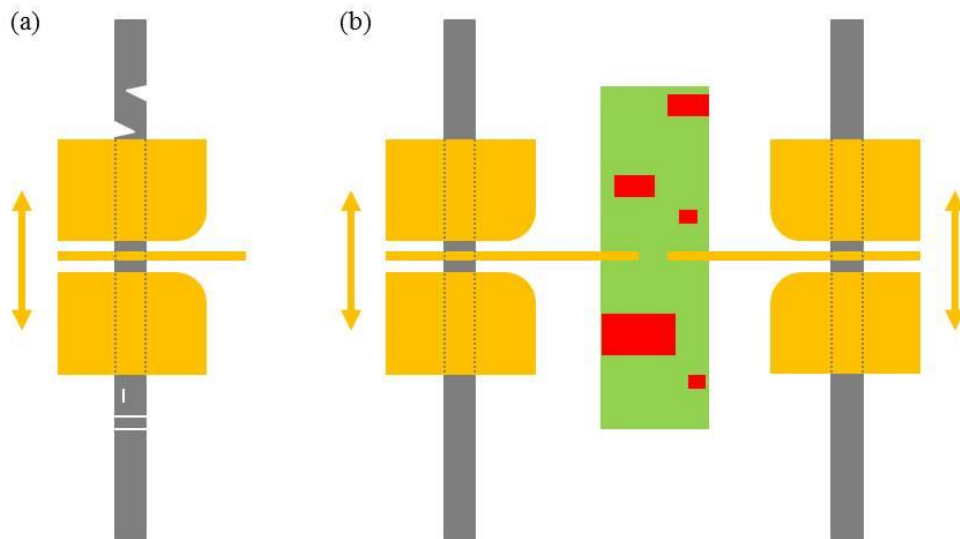


Figure 4.2: Simplified diagram demonstrating the use of LT-GaAs “rails” for defining the base material of the PC switches. The metallization position can be positioned anywhere along the LT-GaAs rails to select the best LT-GaAs (a) or the best graphene (green = good, red = bad) (b).

4.1.2. Experimental Results

In the earlier generation (I and II) of devices, the ground planes of the CPW regions were all connected to a common earth, whereas in these devices (generation III), the ground planes are used for the electrical bias and lock-in detection of the PC switches. Figure 4.3 shows the setups for measuring the input and output pulses of these devices.

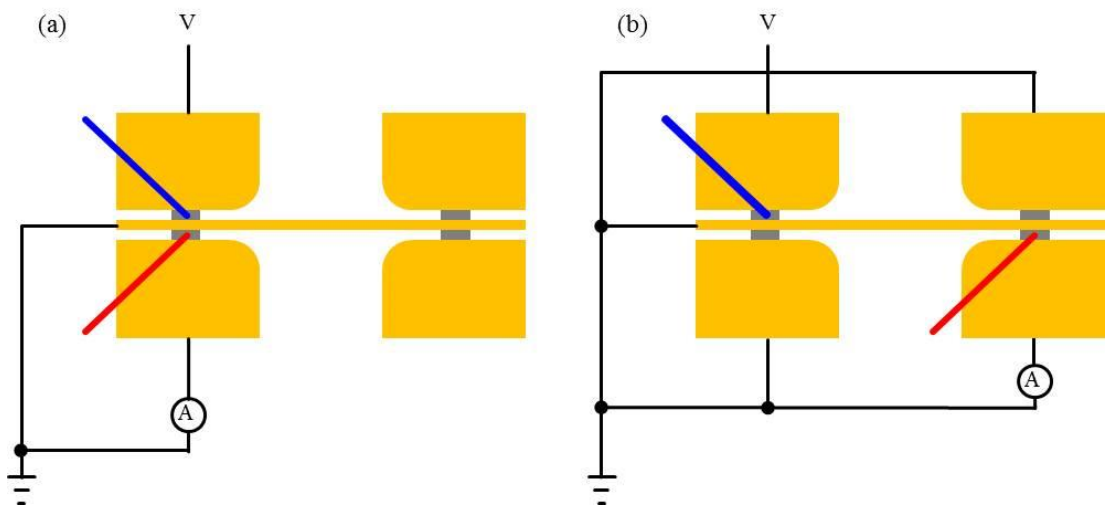


Figure 4.3: Simplified schematic diagram showing the electrical and optical bias conditions for generation and detection of an (a) input pulse and (b) an output pulse using the sliding switch geometry. The optical pump and probe beams are represented by the blue and red lines respectively.

The resulting input pulse FWHM is reduced in duration from 1.1 ps to 750 fs, and for a 500- μm -thick quartz substrate, the output pulse FWHM is 1.61 ps (Figure 4.4). Whilst there is a drastic reduction in the FWHM of the input pulse, an improvement which could potentially lead to a reduction in the output pulse width through substrate thinning, there is a new feature in the output time domain spectra, at 3.8 ps after the transmitted pulse a second pulse is recorded. The feature is too sharp and well defined to be a reflection which has propagated along the PGL (the broad positive reflection at 15 ps is more probable to be the reflection which has propagated along the PGL) therefore suggesting that it is a feature caused by the switch design.

The reflection seen in generation I and II devices cannot be attributed to the breaks in the ground planes used to define the probe arms since with these designs where the ground planes are continuous, reflections are still observed 15 ps after the transmitted pulse with the same polarities as observed in earlier work. Therefore the reflections are either due to the relative permittivity of LT-GaAs causing a change in the effective permittivity of the transmission line, and hence the impedance, or the mismatch at the CPW – PGL transition.

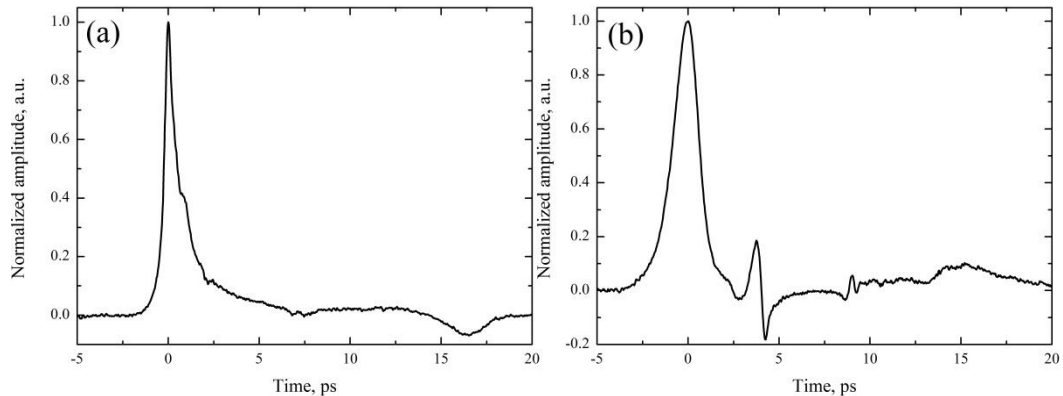


Figure 4.4: Normalized (a) input and (b) output pulse measured for device geometry shown in Figure 4.1.

4.2. Direct Excitation of the PGL Mode

It has been suggested that the reflections seen in the time domain spectra are a result of the CPW – PGL transition. Therefore a new design of PGLs was developed to remove the transition; an all-PGL geometry (Figure 4.10). The first PGLs designed by Treizebre were developed for VNA based measurements, which required ground planes for the electrical connections between the device under test and the VNA [89, 91]. This design was later developed to incorporate PC switching using LT-GaAs with little change to the lithographic design (defined in this thesis as generation II PGLs) [95, 96, 170]. Since VNAs were not used in this thesis or in any other high frequency studies of PGLs, the ground planes can be removed to reveal a device geometry similar to the microstrip with the exception of having no buried ground plane. This design modification highlights that for measurements systems which do not use VNAs, the ground planes are an unnecessary extra. The centre conductor has been made of a continuous width of 30 μm to remove impedance mismatches due to changing PGL widths and to give the evanescent field a greater extent than that of with a 5 μm width. The wider PGL also improves the fabrication yield by increasing the feature sizes and the therefore tolerances in the fabrication process.

The PGL was also designed to have all the electrical interconnects along the top edge of the substrate, with the PC switches at the other end (Figure 4.11). This allows the device to be mounted with ease into the microstat setup for cryogenic temperature measurements.

With the improvements to the surface roughness of the lapped and polished side of the substrate (due to the arrival of the Logitech lapping machine; refer to Chapter 3), the scattering of the pump and probe beam was reduced, therefore encouraging the method of

through-substrate excitation of the PC switches. This method has been used elsewhere for on-chip spectroscopy as it has the advantages of allowing the sample under test to cover the PC switches so removing restrictions on the size of the sample [57, 58].

4.2.1. Optimization of the PC Switch Designs for Direct Excitation of PGL Modes

With the new design of the PGL, the switch designs should also be optimised for a narrower pulse width. Therefore this section reviews the effect of the switch geometry on the shape of the input pulse.

4.2.1.1. LT-GaAs Width Dependence

The PC switch base material, LT-GaAs is applied to the substrate by van der Waals bonding, and then etched to a desired geometry. The size of the geometry has since been fixed to $70\ \mu\text{m} \times 70\ \mu\text{m}$ squares for earlier PGL devices (generation I and II). To test the effects of the LT-GaAs width, the PGL device was designed to compare different switch geometries along the same transmission line (1-mm-wide separation between switch pairs) (Figure 4.5). By placing all switches on the same transmission line, the conditions of the fabrication process (same LT-GaAs treatment resulting in the same carrier lifetimes and resistances; and metallization thickness) and testing (laser spot size) can be kept consistent. The probe arms were kept short (2 mm) for this work as only the pulse shapes were of interest, rather than the frequency resolution of the spectra, and the device size was also reduced improve the yield of the fabrication. The probe arm widths were also fixed at $30\ \mu\text{m}$ to ensure any differences could be attributed to the LT-GaAs width. The tested widths of LT-GaAs were 90, 70, 50, 30, 20, 10 and $5\ \mu\text{m}$. The substrate thickness is kept to $500\ \mu\text{m}$ since earlier work suggests that the substrate thickness has no effect on the pulse shape.

The resulting spectra shown in Figure 4.6 shows that there is a decrease in the FWHM of the input pulse as the width of the LT-GaAs was reduced. It is believed that this due to the change in the pulse fall time as the rise time remains unchanged for each of the LT-GaAs widths. This is attributed to one of two reasons; Firstly, the volume of LT-GaAs has been reduced, therefore lowering the potential amount of photocarriers to be excited using the laser pulse, which in turn will reduce the induced photocurrent caused by the applied electric bias, leading to a reduction in the pulse amplitude. Additionally, there are less photocarriers

to recombine when the illumination is removed, which would explain the faster decay time of the ps pulse.

The alternative explanation compares the length of the pulse along the transmission line. The increase in the LT-GaAs width could be compared with an integration of multiple emitters of negligible width being placed adjacent to one another along the same transmission line. As a result, there would be a sum of multiple pulses propagating along the transmission line, which would be observed as a broad peak.

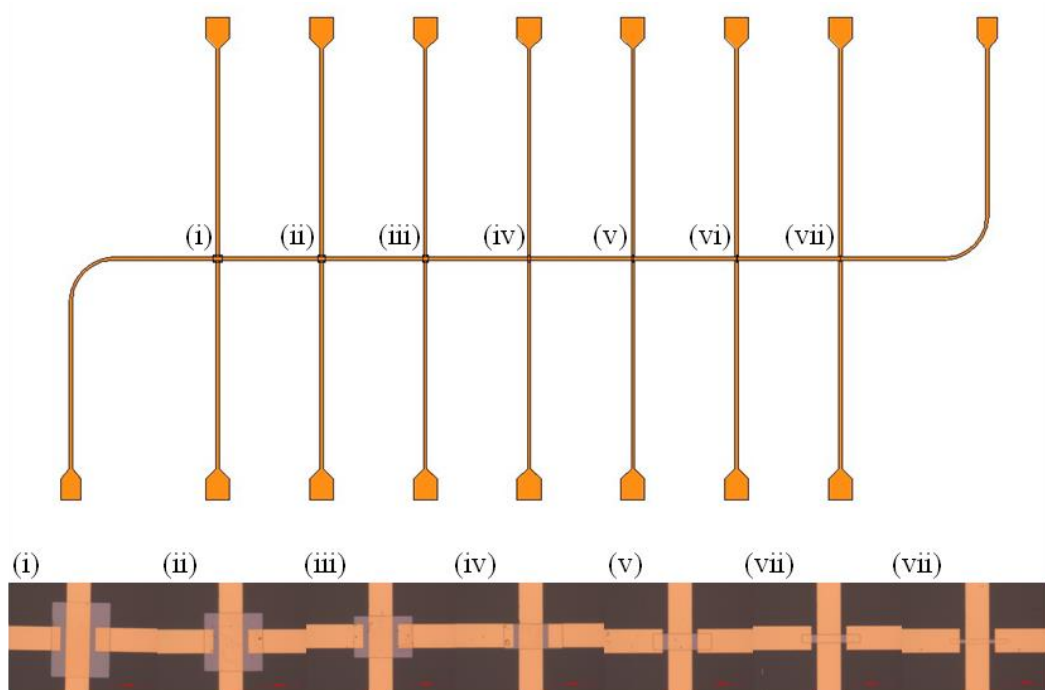


Figure 4.5: Schematic diagram of the overall LT-GaAs width, switch testing design with micrographs of the seven pairs of PC switches along the PGL for a range of LT-GaAs widths from $90\ \mu\text{m}$ (i) to $5\ \mu\text{m}$ (vii) (all rotated 90° with respect to the main figure).

This suggests that for a narrower input pulse, having a broader bandwidth, the width of the LT-GaAs needs to be $30\ \mu\text{m}$ or narrower as thinner LT-GaAs width show no improvement in the FWHM, whereas wider LT-GaAs widths have a broader FWHM. However, for LT-GaAs widths narrower than $20\ \mu\text{m}$ ($5\ \mu\text{m}$ and $10\ \mu\text{m}$ tested), whilst there was a photocurrent measured for a focused laser, there was no recorded pulse. This suggests that either the generated pulse has negligible amplitude, or the sensitivity of the switches to THz pulses was too poor. A study by Zhang *et al* uses a $10\text{-}\mu\text{m}$ -wide, 500-nm -thick GaAs emitter on a CPS with a sliding switch configuration can be used to generate a $310\ \text{fs}$ FWHM

transient pulse but was detected using external EO detection [186]. A similar study by Mikulics *et al* use 500-nm-wide, 500-nm-thick GaAs on CPS with EO detection to demonstrate a generated pulse with a 320 fs FWHM [187]. These studies would suggest that it is the sensitivity of the narrow LT-GaAs which is problematic for these designs.

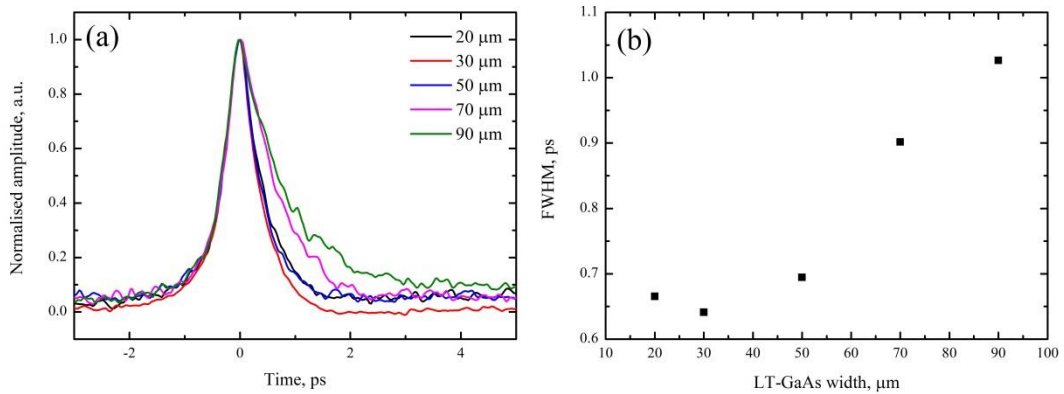


Figure 4.6: (a) TDS of the input pulse for different widths of LT-GaAs. (b) FWHM of the input pulse plotted against the LT-GaAs width

4.2.1.2. Probe Arm Width Dependence

Similarly to the LT-GaAs width measurements, the PC switches were fabricated along the same transmission line, from the same LT-GaAs, and on a 500-μm-thick quartz substrate. The only difference was that the width of the LT-GaAs was kept constant at 70 μm whilst the widths of the probe arms were progressively changed (Figure 4.7). Additionally, a 30-μm-wide probe is defined with a tapering of the tip to a width of 5 μm at the PC switch to improve the lithography and metallization on the PGL design whilst maintaining the potentially improved operating characteristics of a narrow probe arm.

Compared with the varying LT-GaAs width studies, the amount of available photocarriers is kept constant due to the unchanged focus and power of the laser (though narrower probe arms will have less optical screening of the excitation beam – see section 4.2.3.) as well as the width of the LT-GaAs being kept constant, but of the available generated photocarriers, only a fraction (for narrow probe arms) will be accelerated by an applied electric field. As a result, the narrower probe arm will have a narrowed effective PC switch geometry resulting in a shorter pulse being generated.

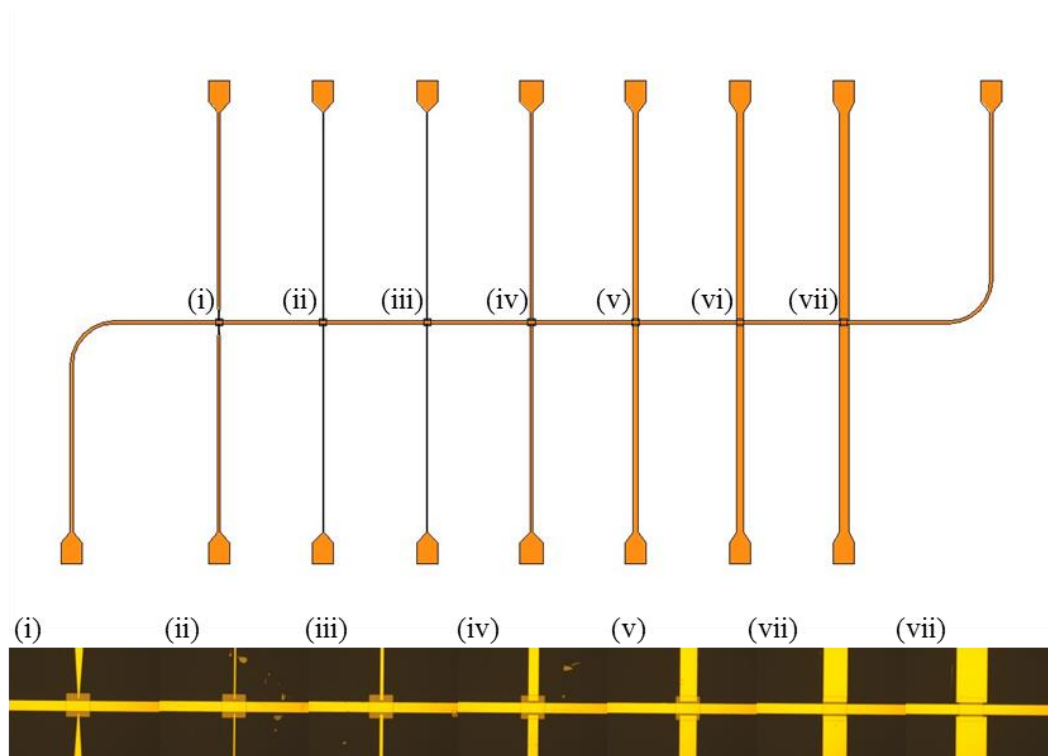


Figure 4.7: Schematic diagram of the overall metal width, switch testing design with micrographs of the seven pairs of PC switches along the PGL for the tapered tip (i) and a range of metal widths from 5 μm (ii) to 90 μm (vii).

The resulting normalised TDS spectra shown in Figure 4.8a shows a progressive reduction in the FWHM of the generated pulse as the width of the metallization was reduced from 90 μm to 5 μm wide. This extent of the change is shown in Figure 4.8b where the FWHM is plotted against the metallization width to show the 400 fs difference in FWHM between 90 μm and 10 μm wide probe arms. This is of similar order of improvement to the earlier work above where the LT-GaAs width was changing. However, the overall FWHM for the probe arm width variation work was not as short; there are identical switch geometries (30- μm -wide probe arms on the 70- μm -wide LT-GaAs) in both the experiments producing very different FWHMs. This has been attributed to the quality of the LT-GaAs, which has caused an offset in the FWHM which can be observed in Figure 4.8b.

The shortest FWHM was produced with the 5- μm -wide probe arm, but at a cost of low pulse amplitude. The tapered tip however has greater pulse amplitude, and a reduced FWHM of the ps pulse compared to the probe arm of the same width (30 μm). Therefore the tapered switch geometry was chosen for use in the generation IV PGL devices for the generation and detection of ps pulses on PGLs.

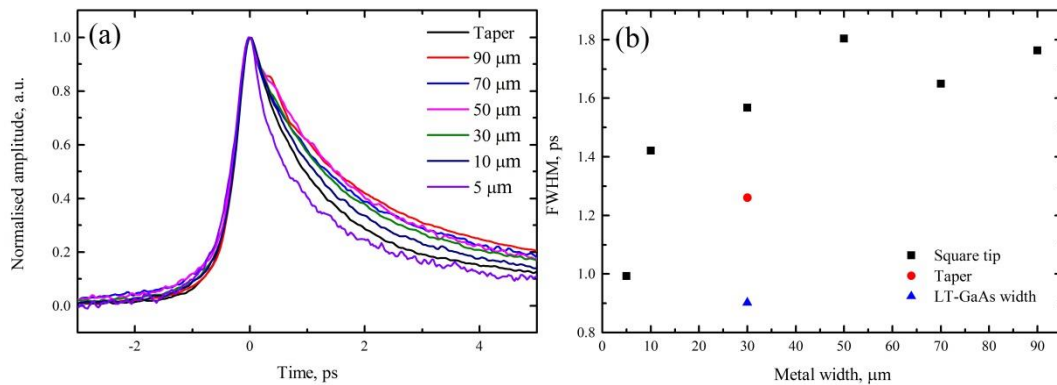


Figure 4.8: (a) TDS of the input pulse for different widths of metallization. (b) FWHM of the input pulse plotted against the metal width as well as the tapered metal (red circle) and FWHM of the data obtained from Figure 4.6 from the same geometry (blue triangle).

4.2.1.3. Ultra High DC Bias of the PC Switches

It is worth noting that in comparison to previously measured devices, the new PC switches have been tested to have a good operational resilience to extremely high biases. Previously, for generation I and II PGL devices fabricated epitaxial transferred PC switches have not been able to withstand high operating voltages and based on a “rule of thumb” approach, the bias voltages are rarely taken above 30 V DC. Figure 4.9 shows the TDS spectra of the PC switch biased to 150 V without breaking which still has good operating characteristic after the testing suggesting that there has been no immediate damage to the PC switch. However, for generating the narrowest pulse width with a pulse amplitude to overcome the attenuation of the transmission line, the optimum bias voltages will need to be found for the transmitted pulse. Extremely high electrical biasing of the PC switches will increase the noise amplitude as well as the FWHM of the pulse (the increase in FWHM with electrical bias is discussed in Chapter 3).

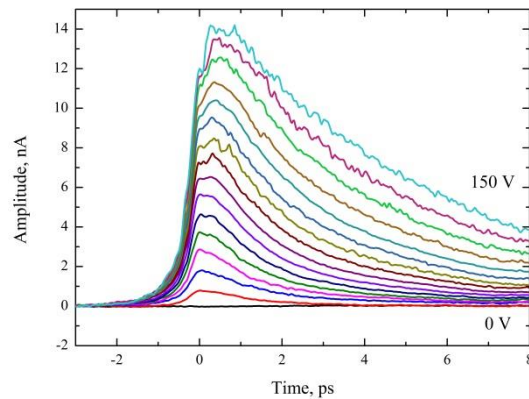


Figure 4.9: Input pulse measurements for varying bias voltages (0 – 150 V, 10 V increments)

4.2.2. PGL Device Design for use in a Microstat

The optimised design, shown in Figure 4.10 uses 70- μm -wide LT-GaAs squares with the tapered probe arm tips at either end of a 30- μm -wide, 1-mm-long PGL. The centre conductor is extended by 26 mm meandering lines (corner internal radius = 400 μm) to the bond pads to remove any potential reflections. The probe arms are 11.2 mm and 15.7 mm long from the probe tips to the bond pads. The bond pads were designed to lie along one edge of the device, away from the sensitive region, so the device could be tested using the microstat as the electrical connections of the microstat needed all to come from the same side of the device.

The quartz was lapped and polished to an optical finish with a thickness of 50 μm . This thickness was deemed mechanically strong enough to be handled during the fabrication stages and thin enough to give a sufficiently large bandwidth to the transmission line. The polished finish allows the device to be optically excited through the substrate.

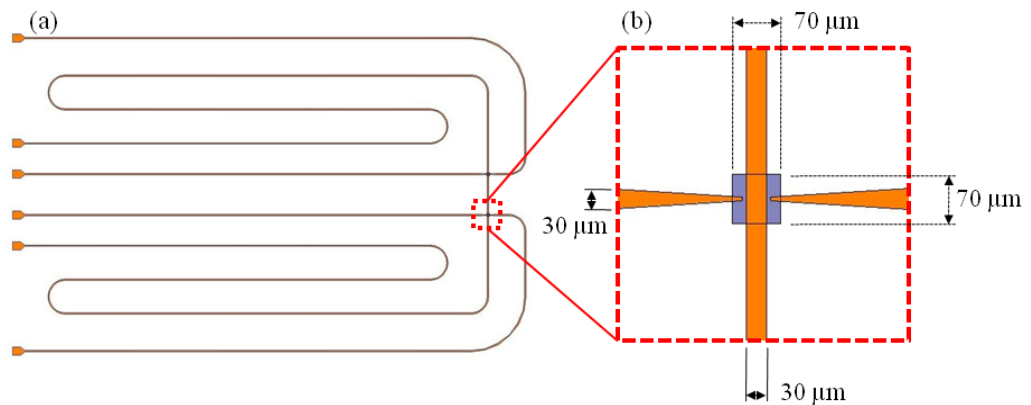


Figure 4.10: (a) A schematic of the device used for variable temperature spectroscopy measurements with the metallization in orange. (b) A magnification of one of the switch regions of the design for clarity with the grey LT-GaAs.

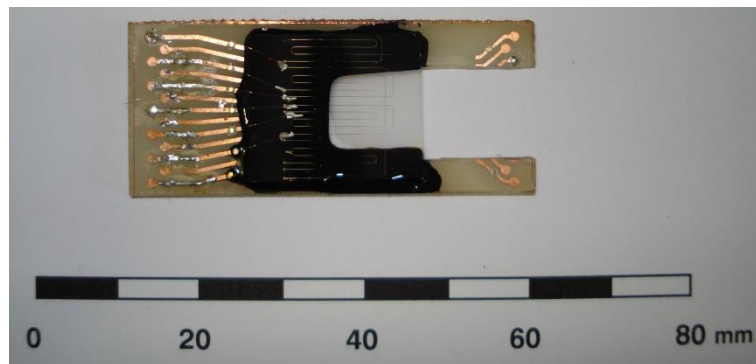


Figure 4.11: Image of the PGL mounted on the PCB used for microstat measurements.

4.2.3. Front Versus Backside Excitation of PC Switches

The PC switches at one end of the PGL were used to generate and detect an input pulse with both lasers first applied from the front of the substrate, and then from behind the substrate. Due to the thickness of the quartz being so small, the attenuation of the laser power due to the substrate is assumed to be negligible and is therefore ignored. The resulting data shown in Figure 4.12b shows that when normalized, the pulses are almost identical suggesting that the THz pulse shape has no dependence on the origin of the optical influence. But a clear difference is found regarding the amplitude of the pulses with the backside excitation having significantly larger amplitude. This difference in pulse amplitude is attributed to there being more LT-GaAs exposed on the backside of the substrate than on the frontside due to the metal masking some of the LT-GaAs; therefore more photocarriers are excited with each optical pulse (see Figure 4.13).

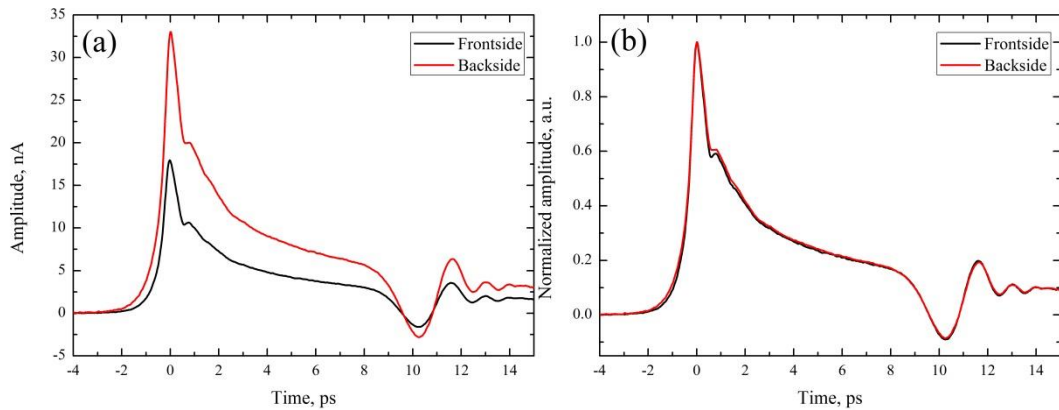


Figure 4.12: (a) Comparison of input pulses generated by frontside and through-substrate optical excitation of the PC switches. (b) Same data as (a) but normalized for comparison of the pulse shape.

The reflection, which was initially thought to be due to the PGL – CPW transition, has not been removed. Therefore it must be due to the LT-GaAs on quartz geometry or the switch metallization itself. However, the relative size of the reflection compared with the transmitted pulse in the transmitted pulse spectra has been reduced to a point where it has less effect on the FFT data.

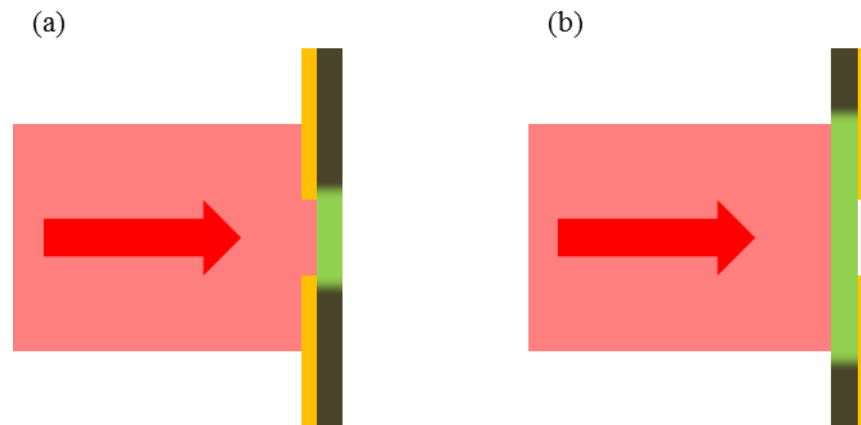


Figure 4.13: (a) Front and (b) through-substrate excitation of the PC switches. For (a) the gold metallization (yellow) screens the laser (red) from photo-generating carriers (green) in the LT-GaAs (grey). This screening is not observed in (b).

4.3. PGL Device Characterization

The generation IV PGL device was designed to be reflection free in order to achieve a high resolution THz-TDS. However, reviewing the transmitted pulse (Figure 4.14), there are several reflections which have been calculated based on converting the time domain into

distance using a propagation velocity of 1.77×10^8 ($= 0.59c$) found using the time between the main pulse and the first reflection.

The reflections at points (a) and (b) are attributed to reflections from the PC switches. Therefore changing the switch geometry has not removed the problematic reflections seen in generation I – III PGL devices, but has reduced the relative reflection amplitude per unit length of propagation along the PGL, from 4.56 %/mm to 2.35 %/mm. The broad feature at (c) is attributed to the corners in the centre conductor; this suggests that for time domain measurements using a 30- μm -wide PGL, a 400 μm internal radius is too sharp which has caused some of the signal to be reflected back along the transmission line. The reflection at position (d) is attributed to the wax support under the substrate; when mounting the quartz substrate to the PCB, some of the wax has spread along the transmission line so creating an impedance mismatch. The several reflections at position (e) are attributed to reflections from the bond pads of the probe arms.

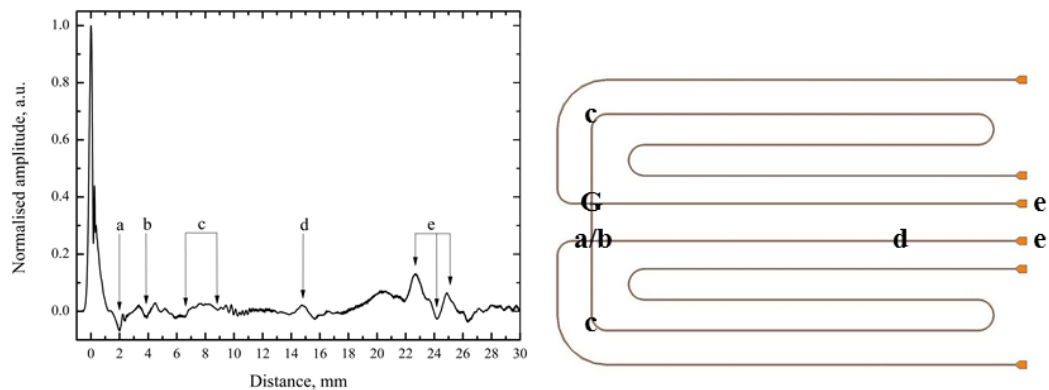


Figure 4.14: Time domain spectra of the transmitted pulse. The x -axis has been converted to distance in order to determine the origin of the reflections. Reflections are highlighted using arrows and lettering in both the spectra and schematic of the device (G represents the ps pulse generating PC switch).

From these conclusions, it is clear that the devices should ideally be designed with longer probe arms, bigger internal radius of turns and a lower permittivity PC material for the switches (which does not yet exist) or the whole device should be fabricated from the PC material (which would lose the low-loss advantage of using quartz). However the practicalities of resolving these problems are somewhat limited for designing PGL devices for microstat measurements. The limited space of the cold finger restricts the space keeping the internal radius to a minimum and probe arm lengths short.

Due to the relatively small amplitudes of the reflections, the device is used for the spectroscopy with the inclusion of the reflections in the FFT spectra.

4.4. Low-temperature Characterization of PGLs on Quartz

The device is mounted onto a cold finger using thermal conducting paste to enhance the thermal transfer between the PCB and the cold finger (Figure 4.15). The cold finger is then placed into the microstat (MicrostatHE, Oxford Instruments). The microstat has optical access to the front and back of the device via quartz windows. The microstat is pumped down, creating a vacuum around the sample before liquid helium is transferred to the cold finger. The temperature of the cold finger is controlled using a controller which can alter the heater accordingly to maintain a desired temperature (helium flow is controlled manually to reduce the helium consumption as the temperature is increased).

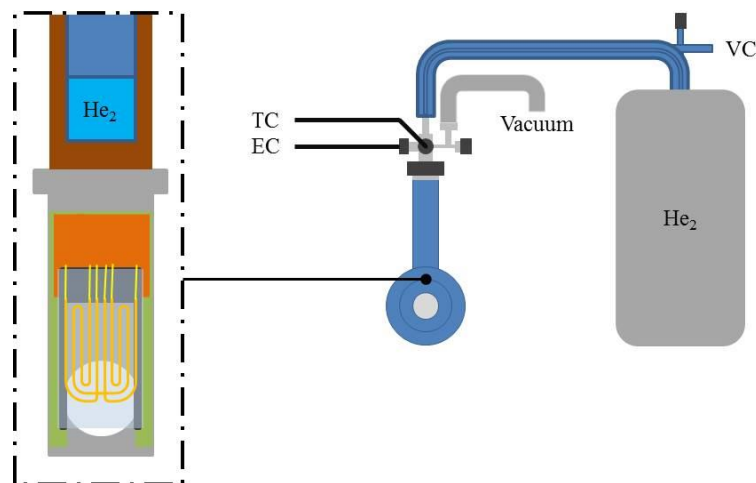


Figure 4.15: Schematic of the MicrostatHe showing the continuous helium transfer from the dewar to the microstat. The vacuum control (VC), electrical contacts (EC) and temperature controller (TC) are highlighted. The device end of the microstat is shown showing the PGL mounted on the PCB (light green) which is mounted onto the cold finger (grey). The cold finger is connected to the heat exchanger which holds the helium, the thermometer and the heating elements.

When conducting variable temperature measurements, the position of the laser spots on the device needs to be adjusted between each temperature in order to maintain the PC generation and detection of ps pulses. This is due to the cold finger contracting/expanding with the changes in temperature, which causes the position of the switches with respect to the laser to move. As a result, the variable temperature scans cannot be automated without introducing some form of control to the focusing and positioning of the lasers or using fibre optics.

Nevertheless, the changing position of the PC switch can be utilised as an indicator of when the device has stabilised at the desired temperature as there is a lag time between the cold finger reaching the target temperature (which the controller is sensing) and the PGL device reaching temperature. This is attributed to the differences in thermal conductivities between the thinned and suspended quartz substrate, the PCB and the cold finger.

The input and transmitted pulse for an unloaded PGL is measured at 10 K increments from 4 K to 100 K, and then in 25 K increments from 100 K to room temperature, 292 K. All the data is taken with a 30 V DC bias and 10 mW laser power applied from behind the device. The selected, resulting normalised TDS spectra are shown in Figure 4.16. It can be seen that, as the temperature is increased, there is no change in the TDS spectra with respect to the positioning of the reflections and the overall pulse shape. Between the input and transmitted pulses, there is a clear change in the shape of the main pulse; the transmitted pulse decays at a faster rate, and the second peak has become more defined as the temperature is reduced.

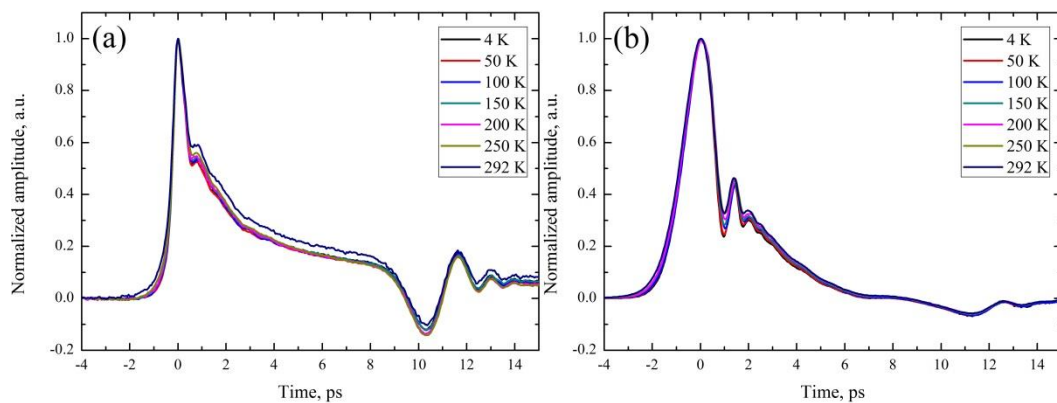


Figure 4.16: Normalised TDS spectra of input (a) and output (b) pulses measured at different temperatures.

When the FWHM of both the input and transmitted pulses are plotted against temperature (Figure 4.17), the pulse width was found to increase with temperature. This attributed to the increase in the carrier concentration with temperature which in turn will increase the recombination time. However, it is also worth noting that the trend for the FWHM of the input pulse and the output pulse are not the same, suggesting a changing dispersion with temperature. If dispersion in the transmission line was independent of temperature, the differences in FWHM for each temperature would be the same. As it is the input pulse FWHM which is changing with a greater rate at higher temperature, there may be an additional feature being excited during THz generation at high temperatures which is not supported by the PGL transmission line to be detected at the output PC switch. Further

research into the pulse generation through photocurrent correlation measurements and pump-probe reflection spectroscopy of the LT-GaAs across the measured temperature range may give further insight into the change in the FWHM observed in Figure 4.17.

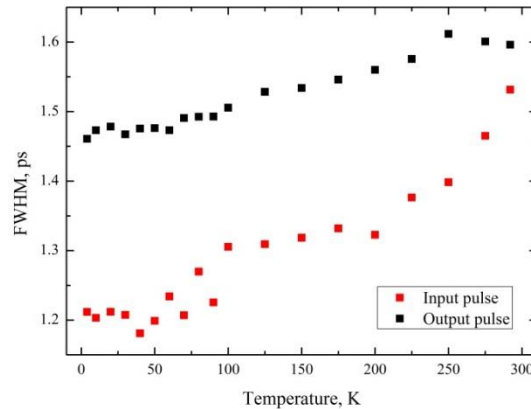


Figure 4.17: FWHM of the input pulse and output pulse plotted against temperature.

4.5. Spectroscopy of Polycrystalline Lactose Monohydrate using PGLs

Lactose monohydrate is a sugar found in milk (more commonly cow's milk) and is one of many crystalline forms of lactose. Lactose monohydrate has received a lot of attention in the THz band since it has a very narrow and low frequency spectral feature at 0.53 THz, as well as other features at higher frequencies. As a result of the lower frequency feature, lactose monohydrate has subsequently become an unofficial calibration standard for spectroscopy systems since it gives an indication of line width and the lower frequency limits of the spectroscopy system [12, 22, 37, 182, 183]. Lactose monohydrate was used during the initial testing of the PGL's spectroscopy potential (refer to Chapter 3) and is now used for the testing of new PGL designs. Lactose monohydrate, as with other organic crystalline structures, exhibits a THz spectral change as a function of temperature, which can be used to test the suitability of the system for variable temperature spectroscopy measurements.

4.5.1. Theoretical Modelling of the Origins of the Spectral Features in Lactose Monohydrate

To further understand the experimental results, the origins of the spectral features should be reviewed for lactose monohydrate. As previously stated, there has been a lot of research into

lactose monohydrate experimentally [12, 22, 37, 182, 183], and as a result there has also been several papers trying to predict the theoretical spectra [188-190].

Several groups have worked to resolve how lactose monohydrate gives rise to spectral features at THz frequencies using a simulation package, (VASP, Vienna *ab initio* simulation program), based on density functional theory. As a result, there have been different interpretations of the modes, but these correspond well with the experimentally reported frequencies.

Work by Saito *et al* [188] and Allis *et al* [189] attributes the peaks at 524 GHz and 1.41 THz to lactose molecular rotation. Whereas Jin *et al* [190] have attributed the 0.53 THz peak to a stretching mode and the 1.42 THz peak to a mixture of several inter- and intra-molecular modes. Both groups, however, do not report any calculated peak widths, making it difficult to determine which experimental result is “correct”.

4.5.2. HFSS Simulations to Model PGL Absorption Spectroscopy

In earlier work by Byrne [169], simulations of transmission line absorption spectroscopy using HFSS were demonstrated for MSLs to show the limited spectral amplitude of the MSL spectra for lactose monohydrate. In this method, the frequency dependant permittivity of the lactose monohydrate is extracted from the free space standard system TDS spectra (Figure 4.18a) by calculating the complex permittivity (Equation 4-1) from the absorption and refractive index spectra using Equations 4-2 and 4-3.

$$\varepsilon = \varepsilon' + j\varepsilon'' \quad 4-1$$

$$\varepsilon' = n^2 - \left(\frac{\alpha\lambda}{4\pi}\right)^2 \quad 4-2$$

$$\varepsilon'' = 2n\left(\frac{\alpha\lambda}{4\pi}\right) \quad 4-3$$

However, the HFSS material options do not allow complex numbers when defining the material parameters; as a result, the loss tangent of the materials is defined for the complex parts of the calculated permittivity using Equation 4-4 (Figure 4.18b). Conductivity, σ is assumed to be zero for lactose monohydrate, which simplifies the loss tangent to a ratio of

the real and imaginary parts of the permittivity. For modelling other crystalline compounds, the conductivity of the material may need to be defined.

$$\tan\delta = \frac{\omega\varepsilon'' + \sigma}{\omega\varepsilon'}$$

4-4

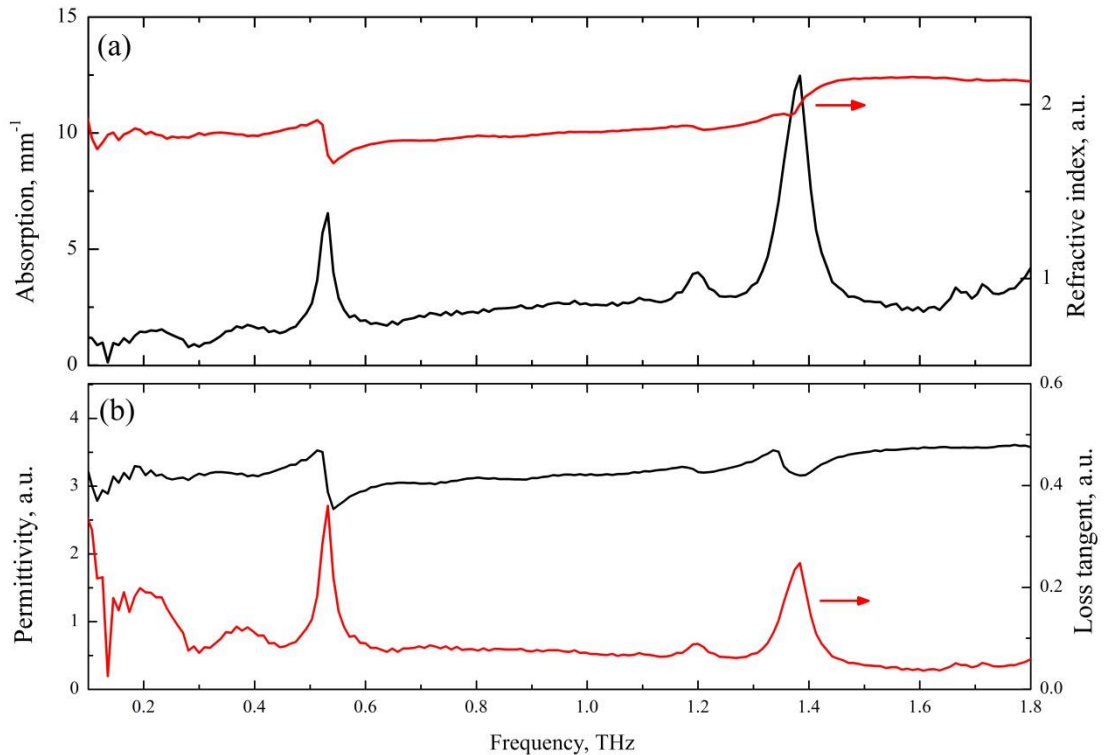


Figure 4.18: (a) The absorption and refractive index spectra of lactose monohydrate recorded using a free-space THz-TDS system (see Chapter 1). (b) The extracted permittivity and loss tangent of free space THz-TDS spectra of lactose monohydrate.

A volume was then defined over the transmission line, and the permittivity and loss tangent of the volume was made frequency dependant, to represent lactose monohydrate. It is accepted that the material parameters has been extracted from an experimental set up with a limited spectral resolution (10 GHz) and bandwidth (particularly below 300 GHz), but of the few simulated models available to represent lactose monohydrate, none of them offer a peak width for the spectral features, or a value for the refractive index. By using the free space THz-TDS spectra, it can be assumed within reason that all the THz has passed through the sample of known thickness to record the absorption spectra, and therefore there is a reduced discrepancy about what percentage of the transmitted radiation has interacted with the

sample; MSL spectroscopy has only partial THz interaction with the sample, which lowers the effective absorption coefficient recorded [169].

The purpose of the simulation is to test, theoretically, the effect of sample size and interaction length on the resulting spectra, which cannot be accurately achieved in the laboratory due to the fragility of the pellets, and therefore the experimental values for permittivity of lactose monohydrate were deemed to be acceptable for this application.

It should also be noted that the resolution of the spectra produced is limited to the resolution of the spectra produced by the standard THz-TDS system used (10 GHz). HFSS linearly interpolates data points between the specified data points allowing an alternative resolution to be simulated (5 GHz resolution recorded).

The resulting S_{21} parameters of the sample under test loaded PGL are plotted against the reference (*ref*) signal (unloaded PGL of the same geometry), as well as redefining the absorption spectra using Equation 4-5 which is derived from the S-parameters.

$$\alpha(f) = \frac{-2}{L} \ln \left[10^{(S_{21}^{SUT} - S_{21}^{ref})/20} \right] \quad 4-5$$

Where the L is the length of the sample and S_{21}^{SUT} and S_{21}^{ref} are the transmittance S-parameters for the loaded and unloaded transmission line, respectively.

4.5.2.1. Interaction Length between the Sample Under Test and the PGL

A volume of fixed width (400 μm) and height (200 μm) was defined in contact with the PGL. Using the parametric function in HFSS, the interaction length between the sample under test and the 800- μm -long PGL was increased from 100 μm (12.5 %) to 800 μm (100 %) in 100 μm (12.5 %) increments. The resulting S_{21} parameters and corresponding absorption spectra (Figure 4.19) show that the amplitude of the spectral features increases with the increase in interaction length. It is also interesting to note, that there is an increase in the background absorption of the spectra, which may be due to the scattering in the recorded free space THz-TDS spectra which can be numerically rectified [19, 191]. The relative peak amplitudes have changed with the two peaks having similar absorption opposed to the 1.4 THz peak being significantly stronger, as demonstrated in the free space spectra (Figure 4.18). However, the results are comparable to the permittivity of the free space spectra.

The absorption spectra also reveal oscillations in the frequency domain, which change as a function of the interaction length. The stronger oscillations occur for the 600- μm -long sample under test and are periodic by 110 GHz. This has been attributed to harmonics in the sample length on the PGL, which are removed when the entire length of the PGL is covered by the sample under test. The oscillations make it difficult to distinguish the lactose monohydrate spectral peak at 1.2 THz in the lower interaction lengths, as well as introducing a doublet peak from the single peak at 1.4 THz. The dip at 300 GHz is not a characteristic of the transmission line or the sample under test spectra, but a limit of the free space THz-TDS system use to acquire the raw spectra and can be ignored.

To maximise the sensitivity of the sensor as well as removing the oscillations, the entire length of the PGL needs to interact with the sample under test. This ensures that the smaller spectral features are recognised and the true nature of the sample under test is recorded. Interacting with the full length of the PGL also helps to further encourage the use of through-the-substrate excitation of the PC switches, to allow the sample under test to cover the entirety of the PGL length without dampening the PC switch operation. However, for measuring some samples in the higher frequency range, it may be advantageous to reduce the interaction length to reduce the attenuation of the transmission along the PGL.

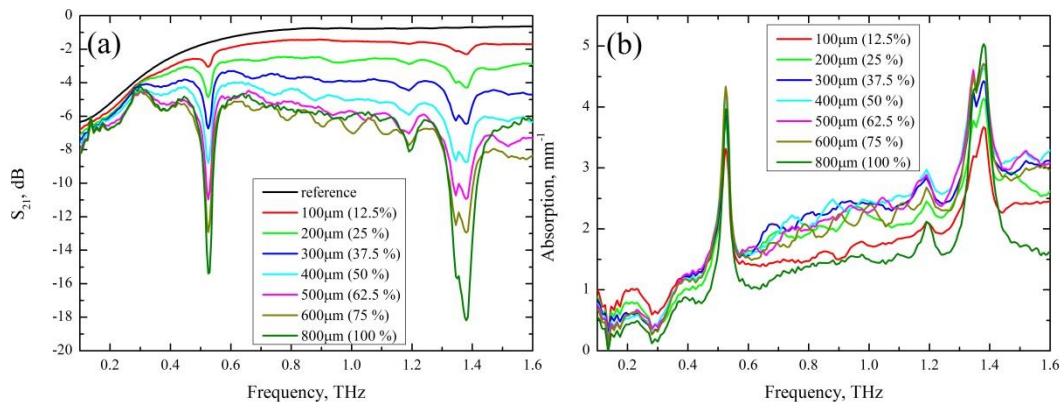


Figure 4.19: HFSS simulation determined (a) S_{21} parameters and (b) absorption spectra for a lactose monohydrate loaded PGL for varying interaction lengths.

4.5.2.2. Interaction Height between the Sample Under Test and the PGL

A volume of fixed width (400 μm) and length (800 μm – covering the entire length of the PGL to remove oscillations) was defined in contact with the 800- μm -long PGL. Using the parametric function, the thickness of the sample under test was increased from 50 μm to

250 μm in 50 μm increments. The resulting S_{21} parameters and corresponding absorption spectra (Figure 4.20) show the dependence of the absorption of spectral features within the THz range against the sample thickness. It is interesting to note that there is a saturation point, which is met at thinner samples for the 1.4 THz spectral feature whereas the saturation is found at thicker samples than for the 0.53 THz feature. This is attributed to the frequency dependence of the extent of the evanescent field (see Chapter 2).

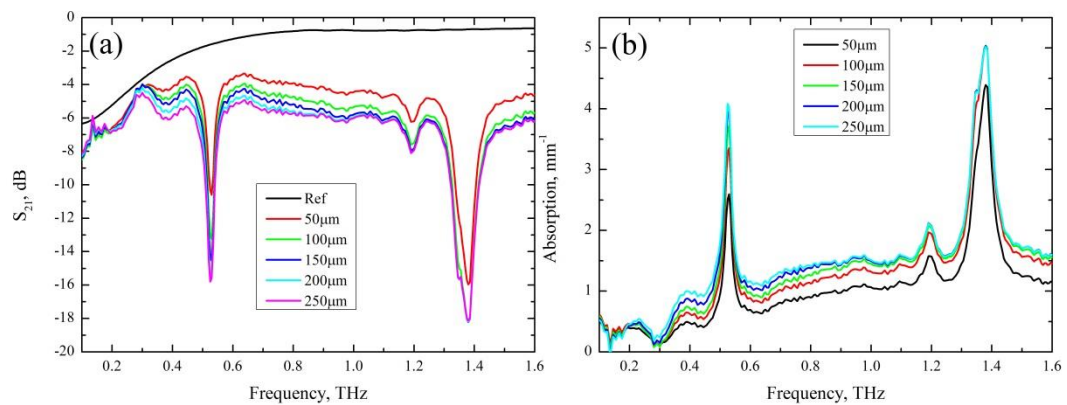


Figure 4.20: HFSS simulation determined (a) S_{21} parameters and (b) absorption spectra for a lactose monohydrate loaded PGL for varying interaction thicknesses.

The dependence of the sample under test sample thickness upon the recorded spectra could potentially be tested by fabricating pellets of different thicknesses during the sample preparation. However the fragility of the pellets may increase the minimum thickness of the sample.

4.5.2.3. Non-Contact Spectroscopy of the Sample Under Test using PGLs

The separation between the 800- μm -long PGL and the sample under test (800- μm -long, 400- μm -wide, and 200- μm -thick) was progressively increased in the simulation from being in contact to a 100 μm separation in 10 μm increments, and again from 100 μm to 200 μm separation in 50 μm increments. The model demonstrates the reach of the interacting evanescent electric field, showing how far away the sample under test has to be from the PGL in order to record absorption spectra. This will also determine the suitability of the PGL for measuring samples separated from the PGL by a boundary layer such as packaging or in the case of tablets, the coating.

The resulting S_{21} parameters and absorption spectra show that as the separation is increased, the spectral features become weaker; this is the same as the results seen for MSLs [12]. However, it is interesting to note the rate of change in the amplitude of the spectral features is not the same for the two frequencies; the 1.4 THz peak loses its amplitude faster than the 0.5 THz peak. This can be attributed to the change in the extent of the evanescent field with frequency (see Chapter 2). Therefore, for high frequency spectra of overlaid polycrystalline materials, it is critical that a good contact between the sample under test and the PGL is made to ensure any spectral features in higher frequency domain are detected.

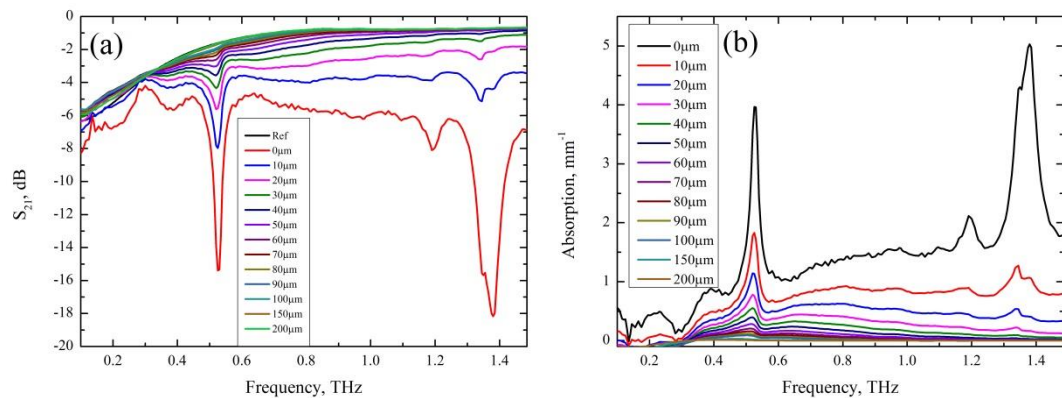


Figure 4.21: HFSS simulation determined (a) S_{21} parameters and (b) absorption spectra for a lactose monohydrate loaded PGL for varying interaction separation between the PGL and lactose surfaces.

Whilst this method can be experimentally tested using an x , y , z stage to mount and control the position of the sample under test over the PGL, it has been opted against in this project. The primary reason for doing so is due the fragility of the thinned substrate makes it unsuitable to use the method demonstrated by others, in which the sample is usually held onto the x , y , z stage using GE varnish and then pressed into the substrate [12, 95, 169, 170]. This ensures that the sample face is parallel to the substrate in order to achieve maximum interaction between the sample under test and the PGL. It is the initial pressing of the sample into the PGL which gives rise to concern; pressing too far into the substrate will be likely to cause the substrate (and lithographically defined waveguide) to break and potentially damage some of the conductor; if this is not performed then one cannot be certain that the sample under test and the substrate are plane parallel.

4.5.3. Sample Preparation

40 mg of lactose monohydrate (Fluka), finely ground using a pestle and mortar, was pressed into an 8-mm-diameter, 0.55-mm-thick pellet using a Specac hydraulic pellet press with an evacuable pellet die. In this process, a copper ring is placed into the die and 8 tons of force exerted onto the die. A vacuum is applied improving the integrity of the pellet, removing any residual air to ensure any etalons within the pellet are removed. After 10 minutes in the press, the copper ring with the pellet fixed into its centre is removed from the press and the lactose monohydrate pellet is removed from the copper ring.

The pellet was then diced into 1 mm² pieces using a scalpel blade, and then mounted onto the PGL between the PC switches. Room temperature measurements conducted using the generation II devices in Chapter 3, had held the sample under test over the PGL with sticky tape, but as the temperature was lowered, the tape contracts and forces the sample under test out of position. Therefore an alternative method was sought. A heat reduction of S1813 photoresist (80 °C, 48 hours), thicker and more manageable than the untreated resist, was tried as it was found to be controllable and easy to manipulate into place at either end of the sample under test using a wooden splinter (Figure 4.22). To remove the sample under test, the resist was dissolved in acetone and IPA.

However, it was difficult to ensure that the sample under test was in contact with the PGL when using the resist; especially when so little force could be applied to the sample while not risking the substrate breaking. During the initial testing, using this method, the resonances caused by the lactose monohydrate were therefore difficult to distinguish.

A third method was therefore adopted, in which lactose monohydrate was positioned over the PGL while a droplet of DI water was dropped over the sample. The DI water is soaked up by the lactose monohydrate. The sample under test was allowed to dry under ambient conditions, causing the lactose monohydrate to stick to the PGL. This method can control where a majority of the sample will lie with respect to the sensitive PGL, but suffers the drawback of losing the sample shape and integrity, and is limited to polycrystalline samples which crystallise into the desired form; polycrystalline materials crystallise into different forms (anhydrous, monohydrate, etc.) depending on the conditions of the surroundings as well as the solvent used. This method can be considered to be similar to drop casting used elsewhere, where the sample under test is dissolved into a solution and dropped onto the sensing surface [28]. There, the solvent is evaporated and the sample under test is left

behind, attached to the substrate. To remove the sample under test, a solvent is run over the surface, progressively dissolving the sample under test. The same method is applied for removing the lactose monohydrate; DI water is run over the PGL and quartz. The surface is then cleaned with an IPA wash.

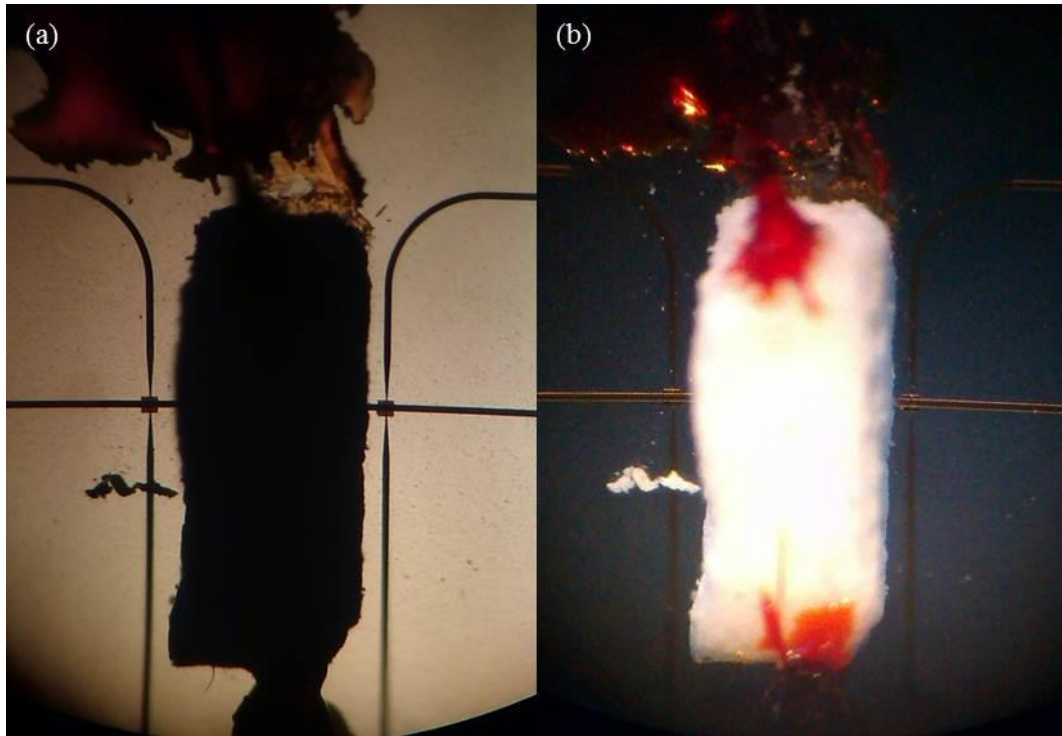


Figure 4.22: Images of the lactose monohydrate held against the PGL using a heat reduction of S1813. (a) is illuminated from behind the substrate to more clearly emphasize that the PC switches are not obstructed by the sample under test.

4.5.4. PC Switch Bias Conditions Effect on Recorded Spectral Features

The initial spectroscopy of lactose monohydrate was conducted at room temperature as a function of different switch voltage bias and applied laser powers. In theory, greater pulse amplitude will increase the electric field strength of the evanescent field, but should not affect the absorption spectra. However, changes in the TDS spectra signal to noise ratio may improve the cleanliness of the frequency spectra.

The spectra were taken using a 30 V, 60 V and 90 V DC bias with a pump beam power of 10 mW. Spectra were then taken using a 30 V bias with pump beam powers of 10 mW and 20 mW. The resulting truncated and zero padded data are shown in Figure 4.23, where it is

clear from the spectral results that there are no differences in the depth or width of the spectral peaks for the different bias conditions. Therefore the choice in bias conditions needs to be made based on the cleanliness of the resulting spectra and operating tolerances of the PC switches.

Additionally, it is interesting to note a similarity between the experimental (Figure 4.23) and theoretical results (Figure 4.19) for lactose monohydrate loaded PGLs; the frequency oscillation for a less-than-100 % interaction length has been reproduced. The experimental oscillations are of comparable magnitude to the 0.5 THz peak which is a problematic trait of the PGL when measuring unknown spectra of samples under test. Therefore it is critical to ensure a 100 % interaction length between the PGL and the sample under test.

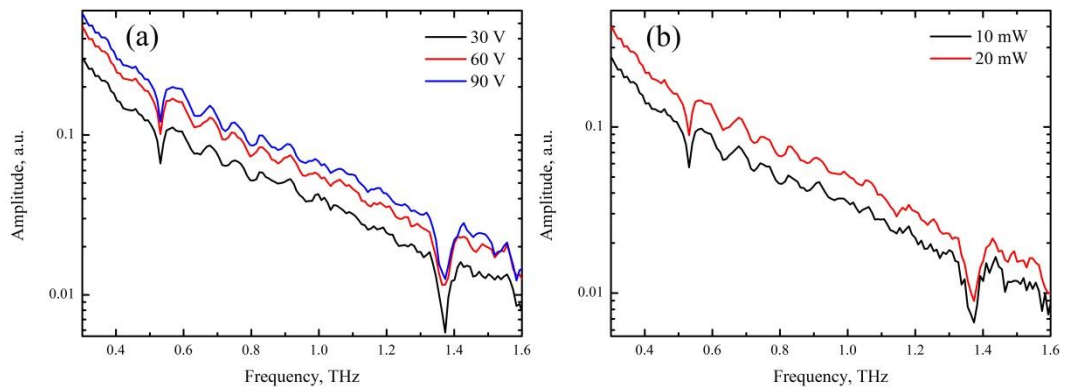


Figure 4.23: (a) THz spectra of lactose monohydrate for different bias voltages. (b) THz spectra of lactose monohydrate for different laser powers.

4.5.5. Variable Temperature Measurements using PGLs

The device was cooled initially to 4 K, and the experiment was given time (30 minutes – 1.5 hours) to stabilise at each subsequent temperature before measurements were recorded. The system was deemed stable when the photocurrent seen in the source-meter supplying the generating PC switch stabilised, which suggests that the position of the PC switch with respect to the focused laser spot was no longer moving.

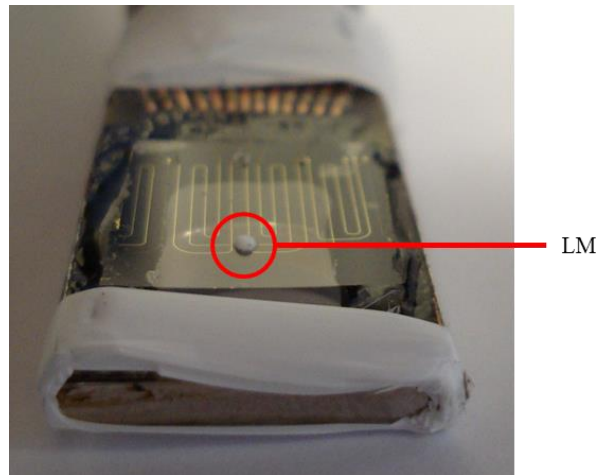


Figure 4.24: Image of the PGL on the cold finger. The PCB is held in place by the PTFE tape and the thermal grease between the PCB and the cold finger. The lactose monohydrate (LM) can be seen attached to the PGL.

Three scans (extending to 10 scans for the 4 and 292 K measurements) of the transmitted pulse for the lactose monohydrate loaded PGL were recorded for each temperature in the range 4 - 298 K (taking 10 – 100 K in 10 K increments, and 100 – 298 K in 25 K increments). An FFT was performed on the resulting time domain data and averaged to improve the SNR of the spectra. The standard deviation of the spectra is plotted as error bars to establish the bandwidth of the spectra, as well as helping to distinguish spectral features from the noise.

The noise can be reduced in spectra by truncating the problematic etalons from the analysed data. For the time domain spectra obtained using the latest PGL, the data was truncated 40 ps after the transmitted pulse, and then zero padded to 2^{14} data points.

The FFT spectra of lactose monohydrate (Figure 4.25) revealed two peaks; with the first peak at 0.53 THz, and the second at 1.4 THz. These positions agree well with free-space spectroscopy results and literature values from prior experimental [12, 22, 37, 182, 183] and theoretical papers [188-190]. The data plotted in Figure 4.25 shows the averaged FFT data from 10 scans with the error bars showing the standard deviation ($\times 3$) of the data points. From the size of the error bars, it can be assumed that the bandwidth of the spectral results is 2 THz, which is comparable to the bandwidth of CPW systems, and has exceeded any MSL system. It should be noted that the magnitude of the error has also been reduced with the reduction in temperature.

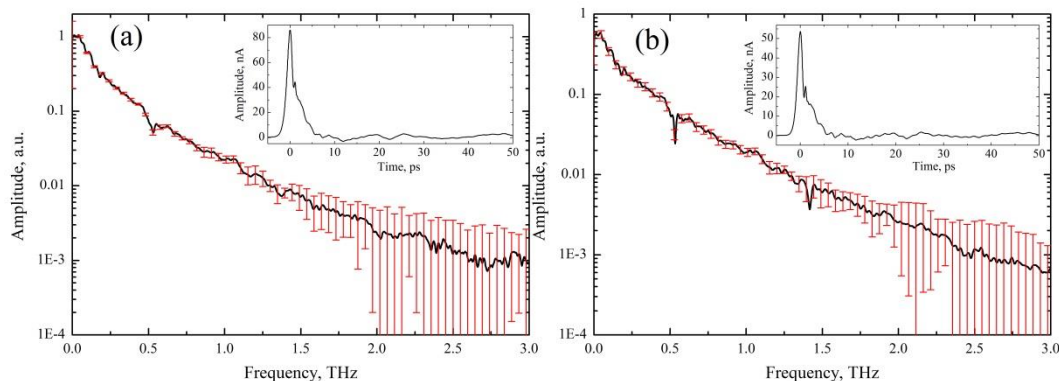


Figure 4.25: 292 K (a) and 4 K (b) FFT spectra of lactose monohydrate with standard deviation ($\times 3$) error bars (red) and TDS inset.

Whilst plotting the frequency spectra on a logarithmic scale has been the norm, the spectral features in the high frequency ranges are not really emphasized. Alternatively, the reciprocal of the amplitude can be used. The relative amplitude of the lower frequency peak, visually has been reduced in the spectra, Figure 4.26, but the peaks are cleaner and the noise floor is flatter, allowing for better visual judgement of a Gaussian fit to the peaks.

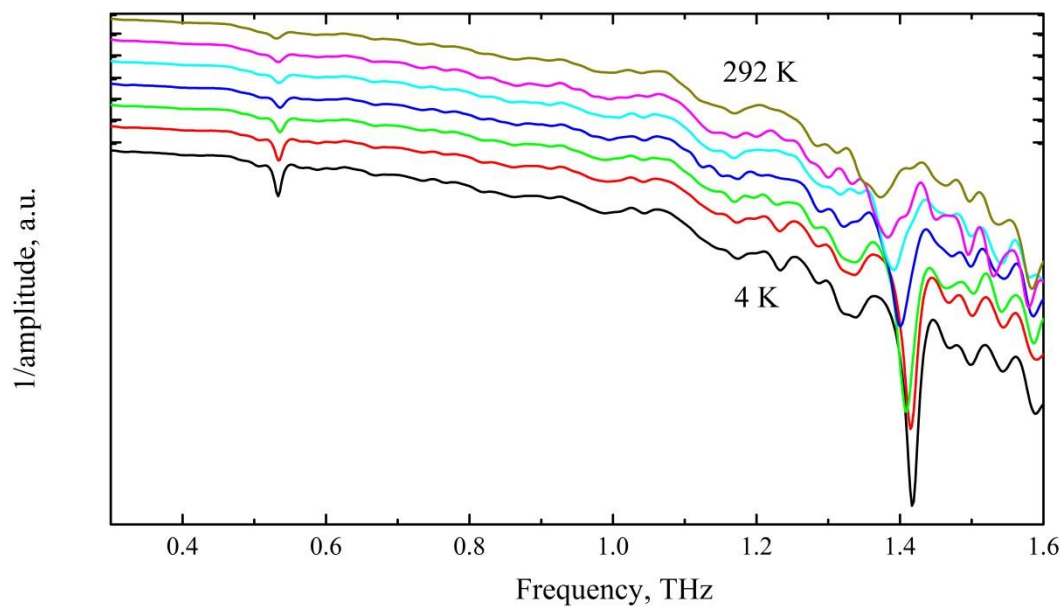


Figure 4.26: FFT spectra of lactose monohydrate for select temperatures (4, 50 – 250 (50 K increments) and 292 K). All spectra have been off-set vertically for clarity.

Due to the strong spectral absorption peaks of the lactose monohydrate in the frequency spectra, it is possible to review the peaks from the non-truncated and zero padded data amongst the low amplitude, high frequency noise. This ensures that fitting of Gaussians will be of the raw experimental data which has not been modified by the zero padding.

The inset of Figure 4.27 shows the spectra of the 0.53 THz peak of lactose monohydrate for a non-truncated and a truncated TDS data. The difference in floor amplitude is an artefact of the FFT, but it is interesting to note subtle differences in the peaks. The peak position of the Gaussian of the 533 GHz peak does not change, but the peak shape has broadened from a FWHM of 10 GHz to 14 GHz and the amplitude of the fit has been reduced from 0.064 to 0.031 as a result of truncating and zero padding the data. As a result, the truncated data does not resolve the narrow peak width of the 0.533 GHz peak.

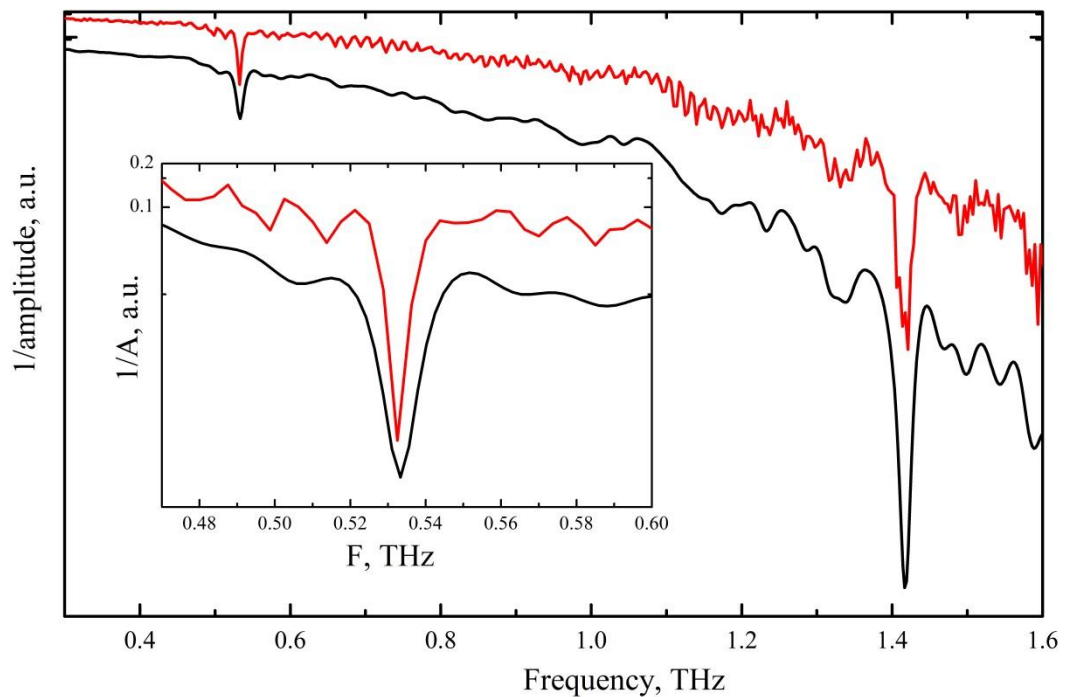


Figure 4.27: Frequency spectra of the truncated (black) and the non-truncated (red) TDS spectra for lactose monohydrate measured at 4 K. Spectra is off set for clarity. Inset: Same spectra with no offset.

The peak at 0.53 THz changes as a function of temperature, as there is a dependence of the FWHM of the peak. The peak becomes narrower with the reduction in temperature, following a linear fit of 0.059 GHz/K. The peak position, however, follows an unusual trend with both a red and blue shift in the same temperature sweep (Figure 4.28). This has been observed by Jin *et al* [190] and has been attributed through modelling to the increase in the unit cell length by thermal expansion, though no temperature scale was stated and therefore no direct quantitative comparison of the trend maxima can be made [190]. However, due to the limited spectral resolution of the PGL spectroscopy results being comparable to the size of the frequency shift, no definitive conclusion can be deduced until the system is

re-measured at a higher frequency resolution. Spectra of higher resolution would reduce the size of the error bars revealing the true nature of the peak shift.

This type of shift in a spectral feature has also been observed in protonated and deuterated sucrose, attributed to a different cause but mentioned here for completeness [192]; the strength of van der Waals forces within the crystalline sample is greater at lower temperatures causing an initial blue shift as the temperature rises. At higher temperature, the more dominant anharmonicity of the hydrogen bond causes the red shift. The resulting “peak” of the spectra of peak position against temperature was found to be different for different spectral features.

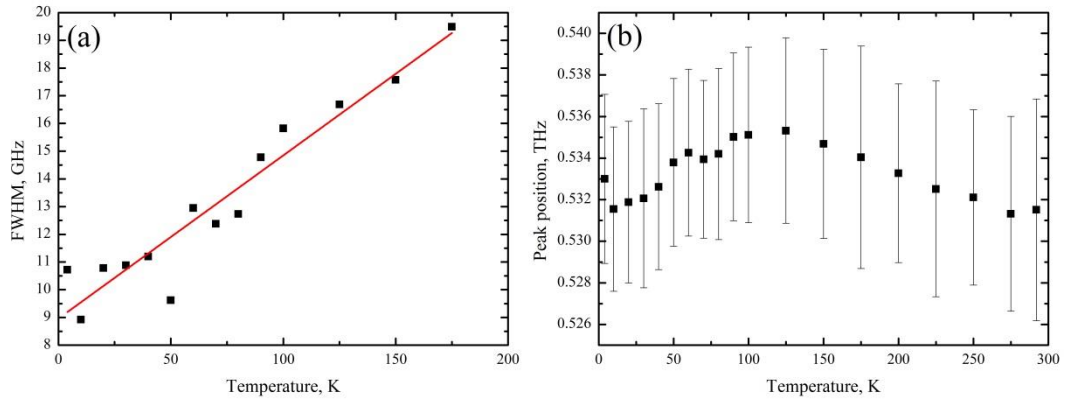


Figure 4.28: (a) FWHM of a Gaussian fit of the 0.53 THz peak of lactose monohydrate against temperature with a linear fit. (b) The 0.53 THz peak’s centre frequency as determined by Gaussian fit as a function of temperature.

The second peak at 1.4 THz (Figure 4.29) also shows a similar narrowing of the peak FWHM with a reduction in temperature (0.176 GHz/K) and has an overall wider peak. More interestingly, there is a spectral shift in the peak with temperature. This spectral shift has been observed in other polycrystalline materials (purine [193] and a range of nucleosides) with a trend fitting Equation 4-6 for calculating the centre frequency, $\nu(T)$, of the vibrational mode.

$$\nu(T) = \nu_0 - \frac{AT_C}{e^{T_C/T} - 1} \quad 4-6$$

Where ν_0 ($= 1.418$ THz) is the mode position at 0 K, A ($= 0.15$ GHz/K) is a constant, T is the temperature and T_C ($= 140$ K) is a characteristic temperature of the sample under test. Currently there are no recorded values for lactose monohydrate fitting using Equation 4-6,

but the fitting parameters are of a similar order of magnitude as previously tested samples, suggesting a degree of validity of the fit. The position of the peak at 4 K (1.417 THz) and 292 K (1.373 THz) appear to fit well with experimental values found elsewhere using free space TDS systems (Chapter 1).

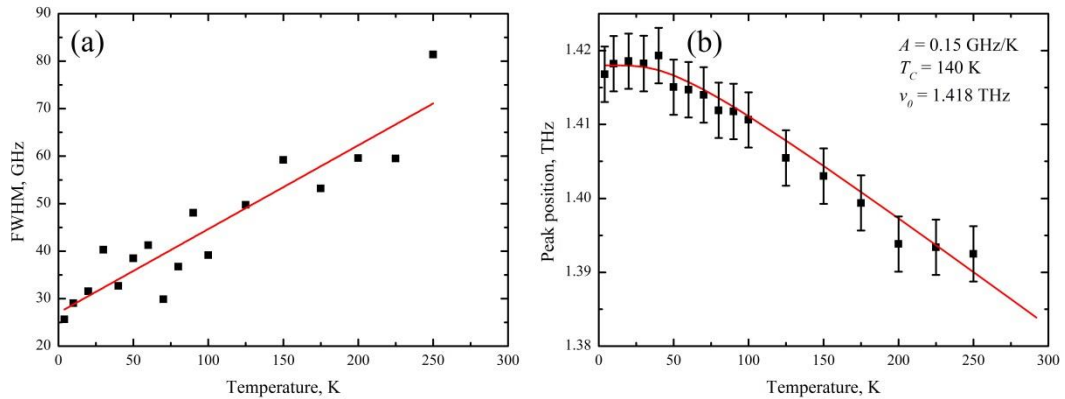


Figure 4.29: (a) FWHM Gaussian fit of the 1.4 THz peak of lactose monohydrate against temperature with a linear fit. (b) The 1.4 THz peak's centre frequency as determined by Gaussian fit against temperature. Figure also includes a fit determined by Equation 4-6.

To further test the validity of the variable temperature spectra of lactose monohydrate, a pellet (5 % by mass dilution with PTFE) was measured using the broadband TDS system from 4 K to 300 K in 10 K increments. The truncated and zero padded (to 4096 data points) is FFT to the frequency domain and analysed using Gaussian fitting of the spectral peaks.

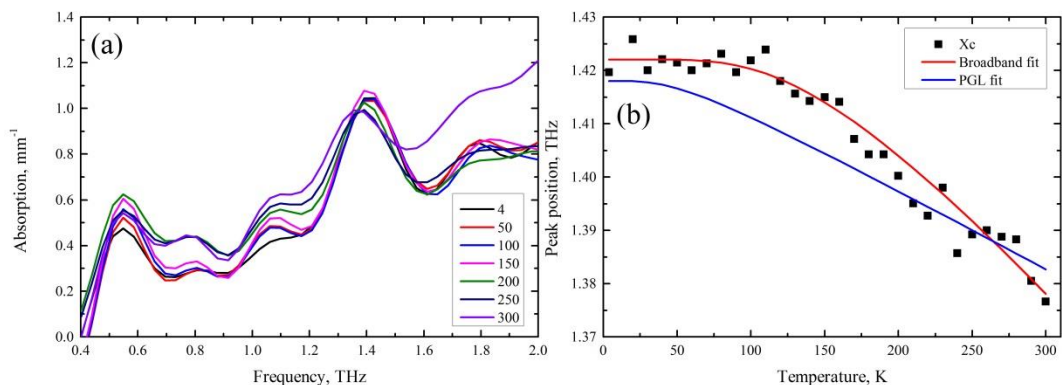


Figure 4.30: (a) Broadband THz-TDS absorption spectra of lactose monohydrate (5 % by mass dilution with PTFE) for 50 K increments from 4 K to 300 K. (b) The 1.4 THz peak's centre frequency as determined by Gaussian fit against temperature (error bars excluded for clarity as they exceed the limits of the figure). The figure also includes a fit determined by Equation 4-6 (red) as well as the fit for the PGL data for comparison (blue).

The 0.53 THz peak has been resolved very close to the low frequency cut-off of the spectra and shows no clear trend in the peak position as seen with the PGL spectra. However the spectra peak position of the 1.4 THz peak exhibits the same spectral shift observed in the PGL spectra with a fitting to Equation 4-6 ($\nu_0 = 1.422$ THz, $A = 0.34$ GHz/K, $T_C = 450$ K). The differences in the fits are clear (Figure 4.30b), which could be attributed to the dilution of the pellet or the limited resolution of the spectra. This can be clarified in future work by diluting the samples on the PGL system to see if there is a change in the peak position fit.

It should also be noted that even though the shift is less than the spectral resolution of the system, the Gaussian fitting of the peaks has produced peak positions following a trend seen in a higher resolution system. This further encourages the suggestion that the peak shift in the 0.53 THz peak in Figure 4.28 is real, despite strictly speaking being less than the resolution of the system.

Comparing the PGL TDS system to other methods (Table 4-1), we find PGLs to be a good compromise between bandwidth and resolution, as well as allowing reduction in sample preparation needs and volume. For the free space methods, the samples under test need to be diluted with a matrix material to reduce the overall absorption; recently, it has been found that the refractive index of the dilution matrix material has an influence on the resulting THz spectra. This would suggest that a non-dilute sample cannot be compared to a pure sample by amplitude scaling alone. Therefore methods which do not require such dilutions, such as the waveguide systems become more desirable, but still lack the bandwidth, which PGL demonstrate good progress to resolving. The volume of the sample under test which is required for the on-chip measurements is reduced, primarily due to the confinement of the electric field to a visible transmission line allowing ease of alignment, whereas the free space system use a large area sample to increase the tolerance of aligning the sample under test to the focus of the non-visible THz beam.

Whilst the PGL system is advantageous in several ways, there is still a preference for using alternative systems such as free space TDS where there is a broader bandwidth at a cost of frequency resolution or ATR where a force can be applied to the sample under test to increase the density of the sample. Thus, PGL is another choice of THz TDS system, not a replacement for all systems.

THz system	Resolution (GHz)	Bandwidth (THz)	FWHM (GHz)	
			0.53 THz	1.36 THz
FTIR (syncotron – high resolution scan) [15]	15	2.5	31	69
Free space TDS (standard setup) [this work]	10	0.3 – 2.8	25	56
Free space TDS (broadband) [this work]	182	0.4 – 8	112	255
ATR [22]	40	0.3 – 3.6	~ 73*	~ 84*
Tuneable photomixer [182, 183]	< 0.1	0.1 – 1.8	25	58
Tuneable multiplier [182]	Unrecorded	0.5 – 0.55	27	NR
Sommerfeld line [37]	~ 15*	~ 1	~ 33*	NR
Microstrip [12]	~ 2	~ 1.2	22	NR
Planar Goubau line [this work]	~ 3.75	~ 2	-	83
Planar Goubau line (zero padded) [this work]	~ 21	~ 2	19	33

Table 4-1: Table comparing the resolution (of the recorded data) and the bandwidth of systems used to investigate polycrystalline lactose monohydrate at room temperature. The table also specifies the recorded FWHM of the 0.53 and 1.36 THz peaks at room temperature where data is available. The values marked with “*”, represent values calculated from their respective publication figures using Origin image analysis tools and are indicative only of an approximation. Data which was not resolved due to bandwidth limits are marked as NR.

4.6. Conclusion

The design of the PGL device for spectroscopy applications was developed and optimised from earlier designs by the Leeds research group [170]. A sliding switch design resulted in several fabrication advantages over the generation II designs owing to the ability to create working PC switches with the metal having the option to be defined in different positions on the quartz. Though this method proved useful for graphene work, it still suffers reflections lowering the frequency resolution of resultant spectra. The design was later modified into an all PGL device by directly exciting the PGL mode. With the new waveguide design, the PC switch geometry was subsequently optimised to improve the FWHM of the generated THz pulse. Though reflections are still apparent in the TDS spectra, and attributed to the relative permittivity of the LT-GaAs causing an abrupt change in the effective permittivity resulting

in a sudden change in the characteristic impedance of the transmission line. This change in impedance gives rise to a reflection coefficient. However, the relative amplitude of the reflection is smaller than that observed in the generation II devices.

The improved PGL was mounted into the microstat, and the operating characteristics of the device tested from 4 K to 292 K. This setup was subsequently used for variable temperature measurements of polycrystalline lactose monohydrate. Peak analysis revealed a narrowing of spectral features as the temperature was reduced. The 1.4 THz spectral feature also exhibits a one-direction spectral shift with temperature verified using a direct comparison with measurements made using free space broadband THz-TDS. The 0.53 THz peak reveals a more interesting spectral shift; the peak shifts to a higher frequency and then back to its original position over the measured temperature range, in good agreement with prior theoretical work by other groups. However, since the size of the frequency shift is comparable to the frequency resolution of the spectra, the results can only be taken as tentative. To verify this finding, a higher resolution device would need to be made; using a 500- μm -thick quartz substrate device, with the same waveguide geometry, the temperature sweep needs to be repeated with longer time windows recorded. The thicker substrate will suppress the problematic reflections through attenuation and dispersion as well as reduce the bandwidth; the broad bandwidth of the thinned substrate devices is not needed to examine the 0.53 THz peak.

As a result of the theoretical modelling of the PGL interacting with the overlaid lactose monohydrate, the critical importance of maintaining the integrity of the sample under test (a poor integrity will reduce the interaction length between the PGL and the sample under test) over the PGL was noted during spectroscopy, as well as covering the entirety of the sensitive region of the PGL. Maximising the interaction length between the sample under test and the PGL will remove potential oscillations in the system which results in periodic oscillations in the resulting spectra with comparable amplitude to material specific spectral features.

The generation V PGL device (not yet fabricated and tested) with improved bandwidth will also need to have several modifications to the design in order to improve the resolution of the spectra; the probe arms need to be extended to remove the etalons generated by the external interconnects. The radius of the corners needs to be increased to remove broad etalons.

The results presented in this chapter were presented at a talk at the IRMMW-THz 2013 conference in Mainz, Germany and were published in the proceedings of the same conference. These results were also published in the Royal Society of Chemistry journal, Lab on a Chip (2013).

Chapter 5. PGL dielectric sensing

Whilst it is possible to obtain the frequency-dependant dielectric spectra of materials using THz-TDS measurements, the effect of loading the transmission line with the sample under test is to increase the effective permittivity, thereby causing attenuation and dispersion of the transmitted pulse (Chapter 2 and 3), reducing the device bandwidth. Therefore, with the introduction of filters, the sensing element of the system can be pushed away from the transmission line to reduce the dielectric loading of the PGL, recovering some of the bandwidth and signal amplitude of the transmitted pulse. However, the cost of this methodology is restriction of the dielectric sensing to predefined frequencies, determined by the filter design, which cannot practically be tuned to alternative frequencies. Nevertheless, these filters are more sensitive to loading by small quantities of material as well as materials with a small relative permittivity, both of which could be potential remain undetected by transmission line spectroscopy techniques. In this chapter, filter designs which have been used for dielectric sensing in the THz regime are reviewed before a new design is presented. Several design parameters are modified to optimize the response of the filter across a broad frequency band; 100 GHz – 2 THz. Furthermore, equations are developed for calculating the frequency response of the filters which are dependent on both the thicknesses and dielectric constants of the substrate and the dielectric load. Following the latest results in practical realization of PGLs on quartz substrates (Chapter 4), the parasitic regions of the devices are further modified to improve the etalon-free time window of the time-domain signal. These devices include the new filter designs, to allow measurements of their response to ps pulse operation, as opposed to the simulated continuous wave operation.

5.1. Filter Designs

The design of filters at microwave frequencies has been studied extensively, with several different geometries designed and demonstrated specifically for different frequency bands. The aim of this field of research is to produce sharper cut-off band response with a reduced geometric size. As the design frequencies are pushed into the THz regime, the geometries become smaller, reducing the number of fabrication methods available and hence the design options. As a result, filters presented in this chapter are defined using a single-step optical lithography, practically limiting the designs to 2D geometries as opposed to incorporating dielectric resonators [194].

5.1.1. Transmission Line and Series Filters

Transmission line filters turn the whole length of the PGL into a single dielectric sensor, removing the numerous advantages of the shunt stub and coupled filters; the spatial resolution of the dielectric sensor is reduced, and the ability to have multiple sensors on a single PGL is removed. Nevertheless, the PGL can be turned into a bandpass filter by introducing periodic changes in the width of the PGL (Figure 5.1a) [101]. This method of implementing a bandpass filter has been demonstrated previously at microwave frequencies for CPW structures, using corrugations of the centre conductor to create resonances in the waveguide [195]. Though these structures are suited to applications in which limiting the bandwidth to certain frequencies (removing higher and lower frequencies) is desired, particularly for communications, no practical application has yet been experimentally demonstrated.

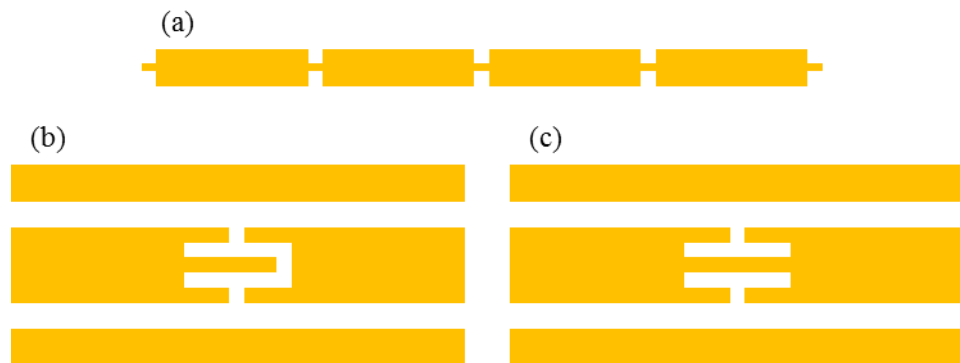


Figure 5.1: (a) Transmission line filter defined by corrugations in the PGL [101]. (b, c) Series filters defined in the centre conductor of CPWs used at microwave frequencies [196].

Since PGLs have adopted a modification of the CPW bandpass filter design, it is also worth discussing series bandstop filters which have been developed for the microwave frequency CPWs [196]. Here, a resonator is defined on the centre conductor (two examples are shown in Figure 5.1b and c), which resonates at a designed frequency. For resonances at frequencies at or near 30 GHz, the smallest feature size is 25 μm . Therefore scaling these dimensions to resonate at THz frequencies would require a more developed fabrication method, such as using electron beam lithography. Furthermore, it is not clear whether these designs would work for the TM mode supported by the PGL.

In this thesis, both the transmission line and series filters are opted against due to the loading of the transmission line when measuring dielectric constant of the sample under test. It is

preferable to move the sample under test away from the transmission line in order to maintain the bandwidth of the system to enable dielectric sensing at the higher frequencies.

5.1.2. Stub Filters

Stub filters are resonators which are electrically connected to the transmission line. They have been studied extensively for microwave frequencies and are well understood. For PGLs, there are two types of stub filter which have been demonstrated for THz dielectric sensing; the quarter wavelength stub and the spiral rejecter. This section will review both of these filters, and simulation results showing further modifications of the quarter wavelength stub into a dual impedance stub will be given.



Figure 5.2: Stub filters using (a) quarter wavelength stub, (b) dual impedance quarter wavelength stub and (c) spiral rejecters.

Quarter wavelength stub, QWS (Figure 5.2a) filters have been studied for both MSLs [51, 52, 169, 197] and PGLs [95, 170] at THz frequencies; a length of transmission line with an open circuit termination (corresponding to a positive total reflection – see Chapter 2). When the electrical length of the stub is equal to a quarter of the operating wavelength, the stub resonates at the first harmonic. The system will also exhibit additional harmonics when the electrical length matches the condition stated in Equation 5-1, where L is the QWS physical length and $n = 1, 3, 5, \dots$. As a result of the additional harmonics, there is a limit in the number of QWS of different lengths which can be incorporated into a single transmission line, before and overlap in the S parameters is observed. This makes it increasingly difficult to distinguish, with confidence, one harmonic from the next.

$$L = \frac{n\lambda}{4} \quad 5-1$$

QWSs have not been tested beyond 1.2 THz [197]; this partially due to the bandwidth of the tested transmission line, but also due to the change in the FWHM of the resonant peaks. To test the change in the FWHM as a function of changing the geometrical length of the QWS, the model is tested using HFSS (Figure 5.3). It is clear from Figure 5.3(a) that as the

resonant frequency is increased, the FWHM of the peak is progressively broadened suggesting the filter is not suited for higher frequencies on PGLs. This also reduces the number of filters which can be used on a single PGL without resonance overlap in the resultant spectra.

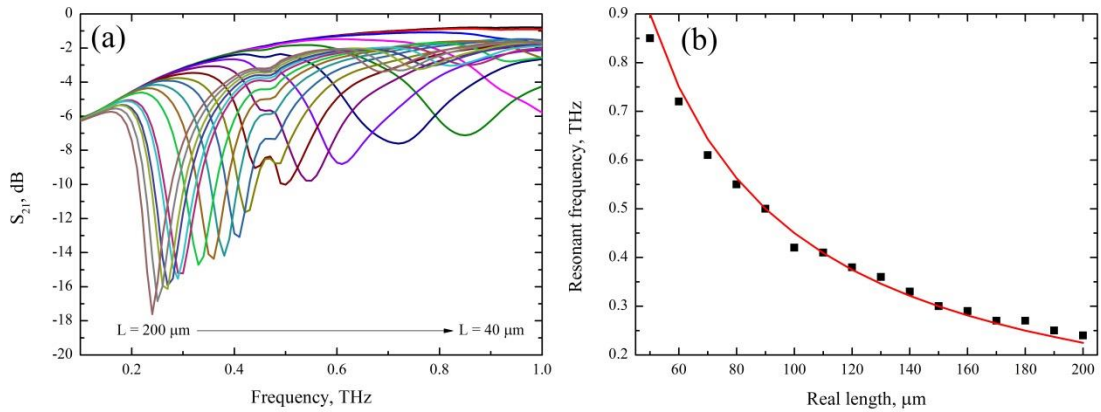


Figure 5.3: (a) S_{21} parameters for unloaded QWS filters of varying lengths (200 μm – 40 μm) on a 5- μm -wide PGL. (b) The corresponding resonant frequencies plotted against the filter length with a formula fit (Equation 5-2, $n = 1$).

Equation 5-1 can be further expanded upon to include the effective permittivity of the filter, as well as being rearranged to find the resonant frequency of the system (Equation 5-2). The effective permittivity of the filter is governed by the permittivity and thickness of the substrate (see Chapter 3) as well as the permittivity and thickness of the overlaid material.

$$f = \frac{nc}{4L\sqrt{\epsilon_{eff}}} \quad 5-2$$

As a result, the formulae developed in Chapter 3 for the effective permittivity of the PGL on thinned substrates need to be modified further for dielectric loading on top of the filter. Using Figure 5.4, the effective permittivity above (red) and below (blue) the substrate surface can be calculated. Above the substrate, the dielectric load (denoted by subscript L) has a finite thickness which is topped with either free space when measuring solid samples, or the fluidic channel material when measuring materials in fluidic systems (ϵ_F). Below the substrate surface, the substrate (denoted by subscript S) has a finite thickness suspended in free space (ϵ_I).

$$\varepsilon_{sub} = \frac{\varepsilon_{sub}(\pi - \theta_S + \sin\theta_S) + \varepsilon_1(\theta_S - \sin\theta_S)}{\pi} \quad 5-3$$

$$\varepsilon_{load} = \frac{\varepsilon_L(\pi - \theta_L + \sin\theta_L) + \varepsilon_F(\theta_L - \sin\theta_L)}{\pi} \quad 5-4$$

$$\theta_S = 2\cos^{-1}\left(\frac{h_S}{r}\right) \quad 5-5$$

$$\theta_L = 2\cos^{-1}\left(\frac{h_L}{r}\right) \quad 5-6$$

Using Equations 5-3 and 5-4, the effective permittivity for the filter can be calculated (Equation 5-7). As well as the dielectric load determining the resonant frequency, the substrate material and thickness have an influence. Therefore, when designing filters for PGLs, the metallization geometry needs to be determined for a substrate with a specified thickness and permittivity. Additionally, when using Equations 5-5 and 5-6, the extent of field, r , is frequency dependant (see Chapter 2) and therefore will have an influence on the resonant frequency with respect to Equation 5-2.

$$\varepsilon_{eff} = \frac{\varepsilon_{sub} + \varepsilon_{load}}{2} \quad 5-7$$

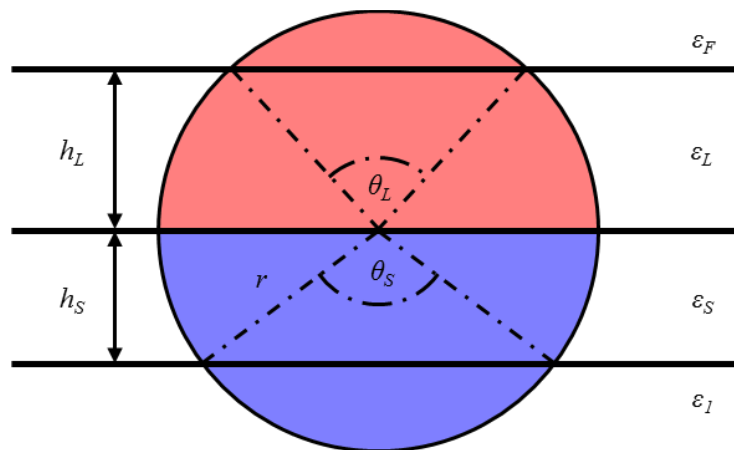


Figure 5.4: Cross section schematic for a loaded PGL. The load (red = ε_{load}), ε_L , has a finite thickness, h_L , with ε_F above the load determined by either free space or the permittivity of the fluidic material. The substrate (blue = ε_{sub}), ε_S , has a finite thickness, h_S , with ε_I below the substrate. The extent of the electric field is represented by r .

As well as being used to calculate the unknown permittivity of the overlaid material (with either a known thickness or a thickness significantly larger than the extent of the evanescent field), the filter and effective permittivity calculations could be utilised for calculating the thickness of dielectric films of a known relative permittivity on electrically insulating substrates of a known permittivity. This methodology would not be suited for calculating thickness of dielectric films on conducting surfaces owing to the changing of the field patterns from a PGL to a MSL field pattern.

Additionally, a more accurate calculation of the substrate thickness can be made for the substrate supporting the filter. Using an unloaded transmission line with a filter on substrate of known relative permittivity, the resonant frequency will be determined by the substrate thickness. This in turn would experimentally calibrate the fabrication of the PGLs on thinned substrates as the metallization geometry can be measured easily using microscope imaging.

A modification of the QWS filter is the dual impedance quarter wavelength stub, DI-QWS (Figure 5.2b) [197]. The single stub filter consists of two lengths of transmission line of different widths defining different impedances, Z_1 and Z_2 . The ratio of the impedance corresponds to the shift in the higher harmonics; a 3:1 ratio between Z_1 and Z_2 , shifts the second harmonic till it is observed at five times the fundamental frequency (as opposed to three times). Although theoretically the ratio can be increased to shift the second harmonic further away from the first harmonic, the ratio increase between the impedance causes the dimensions of the stub to become unreasonable; the width of the second section will become comparable to the length of the PGL, encouraging the desired PGL mode to resemble that of a CPS. Figure 5.5 compares the resulting S_{21} parameters for the single and dual impedance QWSs, demonstrating the shift of the second harmonic.

By increasing the feature-free frequency spectra between the first and second harmonics, more resonators can be incorporated into a single transmission line for simultaneous dielectric spectroscopy at more than one pre-selected frequency, without the problematic overlap of resonances. However, with the increased area of the filter, there is also a decrease in the spatial resolution of the sensor.

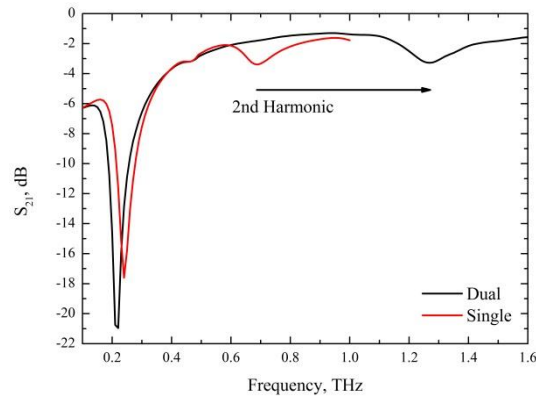


Figure 5.5: Comparison between dual (impedance ratio = 3:1) and single impedance filters, highlighting the shift of the second harmonic to the third harmonic position in dual impedance filters.

A variation of the QWS filters which have been studied on PGLs is the spiral rejecter (Figure 5.2c) [102, 104]. Developed for microfluidic sensing on a PGL using a VNA (up to 220 GHz), the design has been optimised by: varying the width of the wire defining the filter (widths greater than 20 μm for a filter on a 5- μm -wide PGL degrade the filter response); the bend corner geometry (which has very little influence), and the size of the gap between PGL conductors (this is the main influential parameter) [102]. The S_{21} response shows that introducing several filters of the same geometry along the same length of PGL increases the rejection strength; this also reduces the spatial resolution of the system by increasing the sensing area of the device.

5.1.3. Coupled Filters

Coupled filters have been demonstrated on PGLs through the use of ring resonators (Figure 5.6a, [103]), split ring resonators (Figure 5.6b, [103]) and metamaterial resonators (Figure 5.6c, [167]). Though only demonstrated theoretically, ring and split ring resonators can be coupled with the PGL to remove selected frequencies propagating along the PGL, but are usually demonstrated operating in pairs (one on either side of the PGL) to improve their response. The metamaterial resonators use a more complex structures developed from free-space systems, but provide a good rejection frequency. However, like the ring resonators, the design is usually developed in pairs on either side of the PGL to improve the response, reducing the spatial resolution of the dielectric spectrometer.

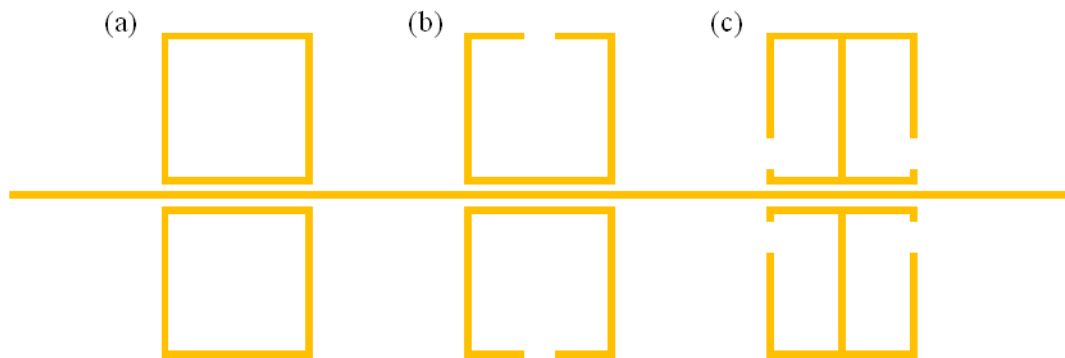


Figure 5.6: Examples of (a) ring, (b) split ring and (c) metamaterial resonators on either side of a PGL. Images are reproductions from respective references.

Figure 5.7 shows the design of a new resonator, defined using a “U” shaped filter coupled with the PGL. The filter is separated from the PGL by a $2\text{-}\mu\text{m}$ -wide gap ($= s$) and the total length of the filter is progressively varied whilst keeping the aspect ratio the same ($w = l$).

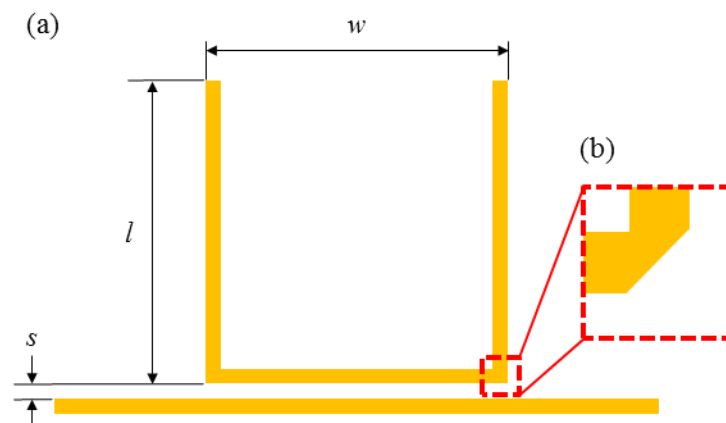


Figure 5.7: (a) Schematic of the coupled U filter on the PGL. The width and length of the U filter are labelled w and l respectively with the coupling separation between the PGL and filter labelled s . (b) The corners have been experimentally tested with right angle (a) to a chamfer (b).

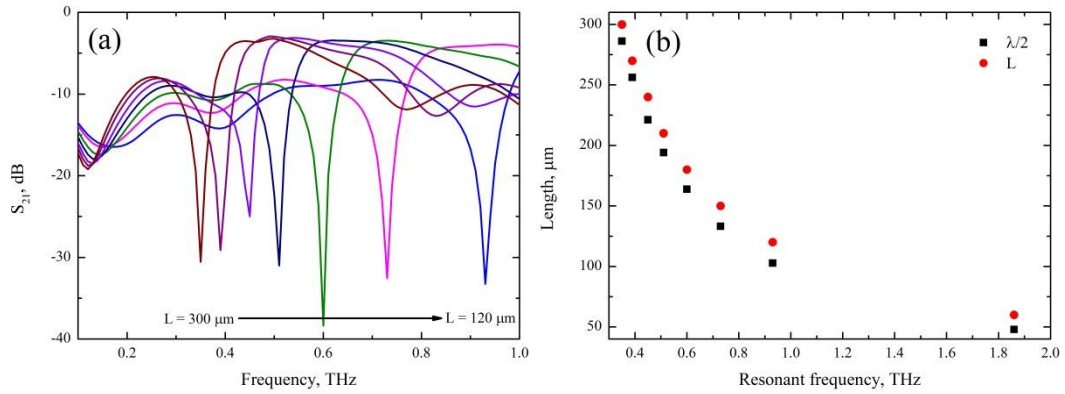


Figure 5.8: (a) S_{21} parameters for coupled U filters on PGL for varying total filter lengths, with the (b) corresponding plot highlighting the theoretical half wavelength and physical length values (Equation 5-8).

Figure 5.8 shows the resulting spectra exhibiting a half-wavelength filter-length resonance response. The slight offset between the simulated and calculated values for the resonances can be attributed to the length definition not taking into consideration the corners. Nevertheless, the results do confirm a half-wavelength characteristic as defined by Equation 5-8 where $n = 1, 2, 3, \dots$. The strength and width of the resonances are consistent over the measured frequency range making these filters an optimal design for dielectric sensing of overlaid material as well as accommodating multiple filters along the same transmission line.

$$L = \frac{n\lambda}{2} \quad 5-8$$

Similarly to QWSs, the “U” filter has additional harmonics to the fundamental frequency (see Figure 5.8a), but these are weak and less defined in comparison to the fundamental resonances of the filters at the same frequency. As a result, it is possible to incorporate additional resonators near the harmonics of existing resonators without a problematic overlap of spectra.

5.1.3.1. Filter Optimisation for an Improved Frequency Response

The “U” filter was chosen as the most appropriate design, based on the ability to maintain the FWHM across a broad frequency range, and the sharp discrete response of each fundamental resonance, enabling multiple filters to be applied to a single PGL without a significant spectral overlap. The design next, needs to be tested and optimised using Ansoft

HFSS. Using Figure 5.7 as a reference, the device geometry was altered systematically and the S_{21} parameters reviewed. The width of the filter is maintained to be the same as the 5- μm -wide PGL.

The aspect ratio of the filter is systematically varied whilst maintaining the length of the filter (180 μm). The results shown in Figure 5.9 show the depth of the resonance has a strong dependence on the coupling length between the filter and the PGL; the greatest depth of resonance is observed when the length and width of the filter are the same; an aspect ratio of one.

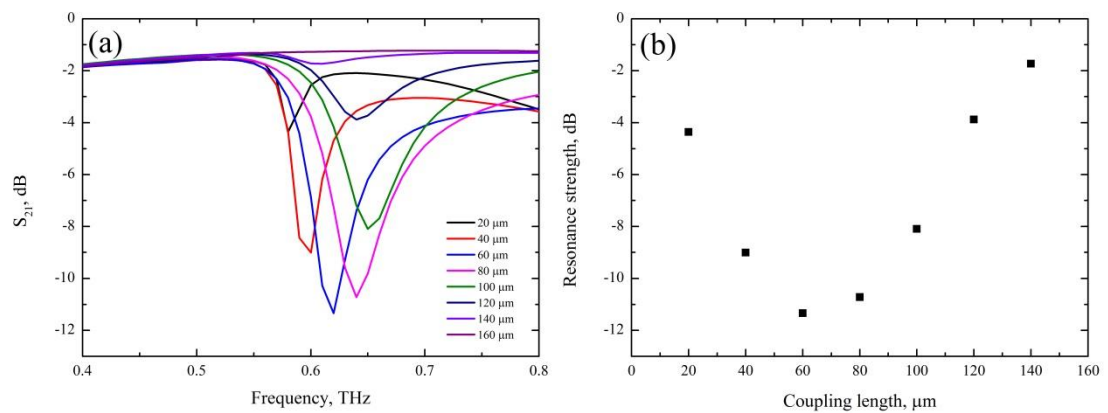


Figure 5.9: (a) S_{21} parameters for coupled U filters on PGL for varying coupling lengths, with (b) the corresponding scatter plot.

The separation between the filter and the PGL was progressively increased from 1 μm separation to a 50- μm -wide separation with no change in the response of the filter. This would suggest that the filter could be potentially positioned further away from the PGL allowing the loading effects of the transmission line to be minimised. However the separation between the filter and the PGL cannot be increased indefinitely due to the finite extent of the evanescent field. The effects of introducing corners (Figure 5.7b) were also negligible as seen in other PGL filter geometries [102]. Rotating the filter 90° to the side to make a “C” filter significantly reduces the strength of the filter whilst removing the weaker harmonics on either side of the main feature. The resonant frequency also shifts to lower frequencies (Figure 5.10).

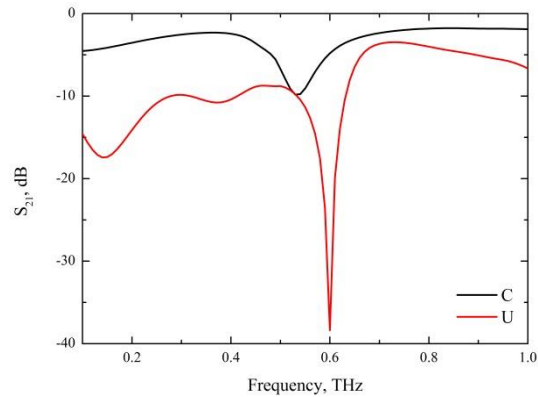


Figure 5.10: Comparison between the S_{21} parameters of a U filter and the same filter rotated 90° for a C filter.

The PGL is simulated with multiple filters along a single PGL, as would be necessary to allow overlaid dielectric material to be analysed at several defined frequencies within a single measurement. It is critical to ensure that the individual U filters do not interfere with one another, potentially causing spurious results. To ensure that a shift in any of the resonances is due to the individual filter and not several filters in a collective form, the separation between the filters needs to be greater than the extents of their respective evanescent fields. Therefore the filters were separated from one another by $400\ \mu\text{m}$ (a design condition maintained during practical realisation of the design).

The resulting simulated S-parameters for 3 filters in the $300\ \text{GHz} - 1\ \text{THz}$ range and $300\ \text{GHz} - 2\ \text{THz}$ frequency range are presented in Figure 5.11a and Figure 5.11b respectively. The results are very promising for practical realisation of multiple frequencies, dielectric sensing on PGLs. The fundamental resonance of the $180\text{-}\mu\text{m}$ -long filter ($n = 1$, $f = 600\ \text{GHz}$) remains distinguishable from the second harmonic of the $300\text{-}\mu\text{m}$ -long filter ($n = 2$, $f = 700\ \text{GHz}$).

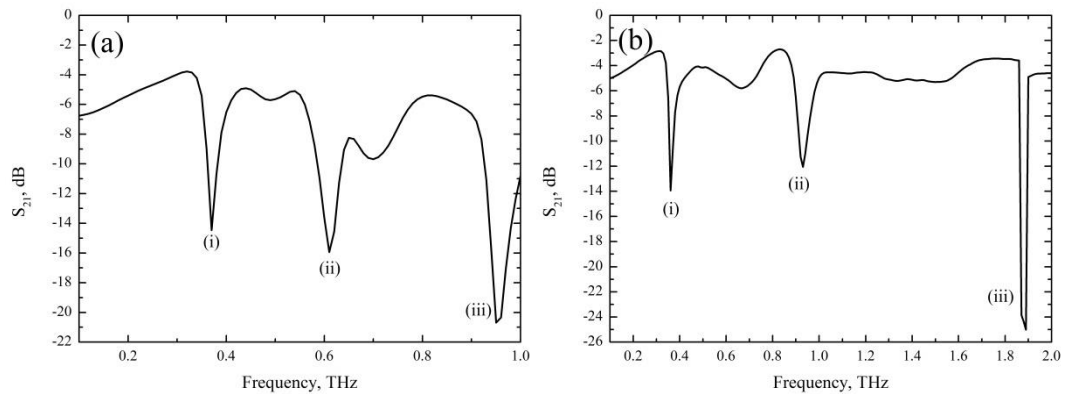


Figure 5.11: (a) S_{21} parameters of multiple U filters of lengths; (i) = 300 μm , (ii) = 180 μm and (iii) = 120 μm . (b) S_{21} parameters of multiple U filters of lengths; (i) = 300 μm , (ii) = 120 μm and (iii) = 60 μm .

Whilst Figure 5.11b shows the filter can be realised operating at 1.9 THz, the bandwidth of the generated and detected pulses only reached 2 THz for a 1-mm-long PGL. To ensure the third harmonic is measurable, in this project, the 60- μm -long U filter will be substituted for a 90- μm -long U filter which resonates at 1.3 THz.

5.1.3.2. Filter Sensitivity

To find the sensitive region of the U filter, a dielectric load is placed over the filter and moved from one position to the next (Figure 5.12b). The corresponding resonant frequency shifts with respect to the position of the load on the filter, with the greatest shift found at the tips of the filter; equivalent to the QWSs discussed previously. For an increased spectral sensitivity of the overlaid material, the filter should be loaded from the filter tip inwards towards the PGL. This has a second benefit of placing the load further away from the PGL to prevent the load reducing the bandwidth of the PGL.

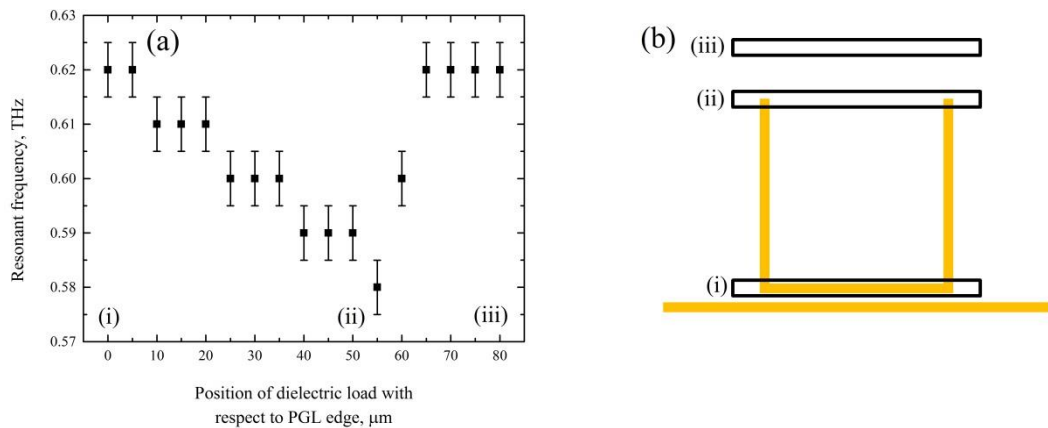


Figure 5.12: (a) S_{21} parameters (10 GHz resolution error bars) of a 180- μm -long "U" filter loaded at position (i), (ii) and (iii) marked on (b). (b) The schematic of the filter and the position of the dielectric load (black box).

To simulate the filter being used for a microfluidic application, a dielectric volume is defined covering the entirety of the filter. The permittivity of the dielectric volume is then varied from $\epsilon_L = 1$ (unloaded filter) to $\epsilon_L = 35$. The S_{21} parameters are recorded for each of the scans and the centre frequency of the resonance plotted in Figure 5.13a. The resonant frequencies, when plotted against the load permittivity, fit well to Equation 5-9, where the effective permittivity is determined by Equations 5-3 – 5-7. The fit's deviation from the simulated data points is attributed to the assumption of a fixed extent of the evanescent field used in the calculations, as well as the 5 GHz finite resolution of the S parameters.

$$f = \frac{nc}{2L\sqrt{\epsilon_{eff}}} \quad 5-9$$

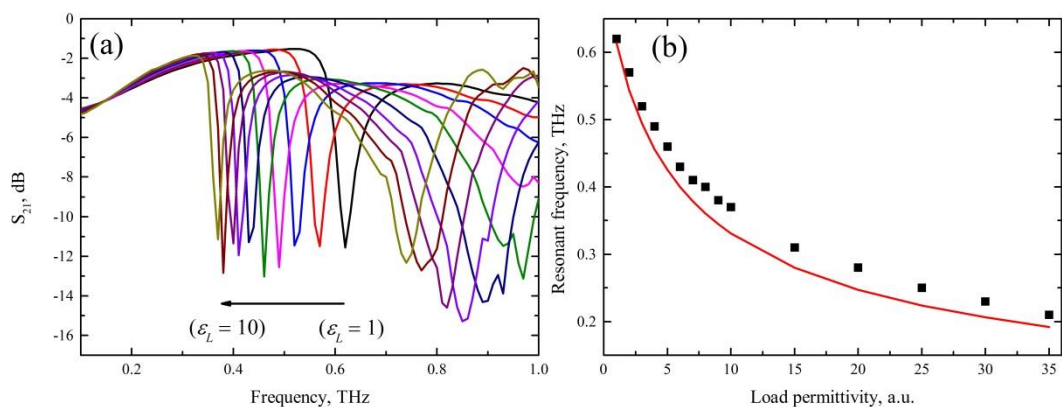


Figure 5.13: (a) S_{21} parameters for a loaded, 180- μm -long "U" filter coupled to a PGL for different load permittivity ($\epsilon_L = 1 - 10$, $\epsilon_L < 10$ omitted for clarity). (b) Resonant frequencies plotted against the load permittivity, fitted with Equation 5-9 ($n = 1$).

As well as observing a spectral shift in the first harmonic of the filter, the second harmonic has become stronger with an increased amplitude and FWHM. The rise of this feature will introduce complications in the design and operation of the coupled U filters for dielectric sensing with respect to the application and number of discrete frequencies which can be investigated within a single spectral scan.

This filter has a good response across a broad frequency range, from a single resonating element opposed to the multi-element filters used elsewhere. Therefore the spatial resolution is improved with the reduction in the finger print size. Additionally, due to the more sensitive area of the filter being found at ends of the U filter conductor, the sample under test can be applied only to the tips of the filter (providing a calibration of frequency response to dielectric load is established), pushing the dielectric loading of the transmission line further away from the transmission line in effort to maintain the high bandwidth of the system.

5.2. PGL Geometry Changes

Experimental testing of PGLs used in Chapter 4 highlighted further design specifications required for producing a broadband, high resolution PGL; the internal radius of the corners in the parasitic regions need to be large, and the length of the probe arms need to be long to remove the problematic etalons. The resulting design for testing the U filters, and ultimately for dielectric sensing, is shown in Figure 5.14. These devices are significantly larger than all previous devices in this project, to accommodate the long parasitic regions of the PGL; spacing between PGLs is increased to a minimum of 1 mm, and the internal radius of the corners has also been increased to 1 mm. The width of the PGL used for the transmission line is made 5- μ m-wide to tightly confine the THz radiation to the transmission line, to reduce the loading caused by the eventual microfluidic channel running alongside the PGL. The extent of the field along the probe arms are not of interest, and are therefore made 30 μ m wide and \sim 40 mm long. The PC switch tips are tapered to a 5- μ m-wide point. The length of the PGL between the two PC switches is 2 mm; this allows up to three U filters (300-, 180- and 90- μ m-long) to be placed along a single edge of the PGL without the cross talk (400- μ m-wide separation between filters and PC switches). It also ensures the devices can be compared with one another with a consistent PGL length and width; the only controllable variable will be the size of the U filter(s). Due to the increased size of the device, the latest design cannot be fitted in the microstat.

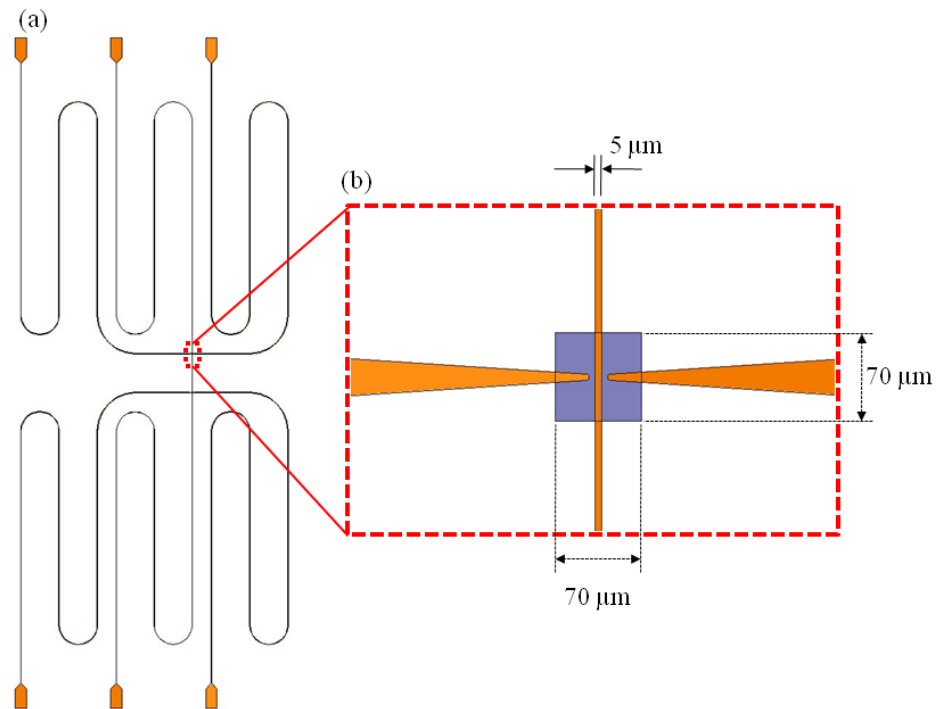


Figure 5.14: (a) schematic of the PGL used for high resolution THz dielectric sensing. (b) Schematic of one of PC switches highlighting the LT-GaAs dimensions and the metallization.

5.3. Experimental Results for Dielectric Sensors on PGLs

Due to complications with MBE growth and the failure of the Ti:sapphire laser used to excite the PC switches, the experimental results are limited for these device geometries. At the time of submission of this thesis, no experimental THz-TDS measurements have been obtained.

5.4. Conclusion

This chapter has covered a review of existing filters on PGLs, highlighting a need for a design of a filter which has a narrow FWHM of the fundamental harmonic across an extended bandwidth for dielectric sensing. As a result, a “U” shaped filter, capacitively coupled with the PGL, was designed and simulated, and produced a near constant FWHM of fundamental resonances between 300 GHz and 1 THz. Separated by a 2- μm -wide gap, the filter has a unity aspect ratio with the total length of the filter determining its resonant frequency. This resonant frequency has a further dependency on the effective permittivity of the filter, which itself is dependent on the substrate permittivity and thickness as well as the thickness and permittivity of the overlaid sample under test. Therefore, this filter can be used for dielectric sensing of overlaid material.

The design faults of the PGL devices tested in earlier chapters have since been rectified with an increase in the parasitic lengths and an increase in the radii of corners. These changes have been made in effort to remove problematic etalons from the time-domain signal, which will improve the resolution of the resultant spectra. However, as a result of these design changes, the size of the device has increased, reducing the yield of the fabrication of these PGL sensors; the handling of the wafer following the thinning of the substrate has become more troublesome. As a result of the heightened complexity of the fabrication of said devices, there have been no experimental results for this phase of work.

Whilst absorption spectroscopy can provide information across a broad bandwidth, it requires dielectric loading of the transmission line which reduces the bandwidth of the sensor. Therefore, the dielectric sensors discussed here provide an appealing alternative to transfer the loading effect of the sample under test away from the PGL and retain the system bandwidth. This trait is particularly desirable for the THz spectroscopy of the fluid-based samples. Additionally, the PGL is a single conductor system, removing the risk of electrically shorting the transmission line. However, information from the sample under test can only be determined for pre-set frequencies.

The results presented in this chapter were presented at the IRMMW-THz 2013 conference in Mainz, Germany and were published in the proceedings of the same conference.

Chapter 6. Conclusion

6.1. Project Overview

The project has greatly utilised the FEM simulation package, Ansoft HFSS for the theoretical characterization of the evanescent field of the PGL as well as investigating the field's dependence on the waveguide's geometry. Furthermore, the simulations have led to the development of a term for defining the effective permittivity based on the substrate material and thickness. These formulas have been successfully exploited for the understanding of the operation of and the harmonic frequency shift of resonators designed for dielectric sensing in the THz regime. As a result, using the design of the resonator, the dielectric constant of an overlaid material can be calculated based on the resonant frequency of the filter.

The PGL bandwidth has a strong dependence on the substrate thickness, which has been attributed to the substrate thickness influencing the effective permittivity of the transmission line. By thinning the substrate, the effective permittivity can be minimised to enhance the bandwidth of the transmission line. This has been demonstrated successful using both simulations and experimental THz-TDS measurements on fabricated PGLs working up to 2 THz. This enhanced bandwidth of the PGL has been exploited for the variable temperature measurements of lactose monohydrate, which has been proposed as a useful THz standard. By using lactose monohydrate, the resultant spectra were compared with other spectroscopy systems operating in the same frequency band. In doing so several advantages to the PGL system such as the enhanced frequency resolution and the resilience to the bulk absorption of the sample under test, removing the need to dilute and hence potentially change the recorded spectra has been demonstrated [15]. The temperature-dependant spectral shifts were observed and fitted with previously determined formulas, before being compared with previously recorded data.

It was previously recognised that the only methodology for exciting the PGL mode was with a CPW and 2D horn antenna. This has since been quashed for systems where VNAs are no longer used. This thesis has demonstrated PC switching can be used to directly excite the TM mode in the PGL, removing the need for CPWs in the parasitic regions and in doing so, the magnitude of the etalons due to the PC switches have been reduced, for enhancing the noise free frequency resolution.

The ability to enhance the bandwidth of PGLs has encouraged the development of a design of resonators with an improved Q factor across the bandwidth of the system. By keeping a near constant FWHM of the resonant features across the bandwidth of the system, the option of incorporating multiple filters along the PGL resonating at different frequencies is encouraged. This allows effective permittivity of a single sample under test to be probed at multiple predefined frequencies within a single THz-TDS measurement without the resonant feature overlapping on another in the resultant spectra. Furthermore, the electrical isolation of the resonator from the PGL is attractive for dielectric sensing applications where liquids are used.

6.2. Potential Improvements to Further PGL Research

Despite all the success of the project, there are several issues which have been highlighted during the project which need to be rectified to further on-chip THz-TDS systems but have not been achieved during this thesis due to time constraints. These have been highlighted with potential solutions below.

6.2.1. Device Design and Fabrication

Though the project has demonstrated the optimization of PC switch geometry by altering the width of the LT-GaAs and probe arms, there are still several design parameters to be investigated; PC material parameters (growth and anneal temperatures; material thickness), interdigitated electrodes and metal – semiconductor interface (Ohmic or Schottky contacts). However, this will be a time consuming process but will have benefits in the long term for on-chip systems in effort to increase the bandwidth of the input pulse to compete against free space systems. This would push the bandwidth limits of the system back to the transmission line properties.

For the material parameters, the 350-nm-thickness is arbitrary and other thicknesses could potentially be tested for epitaxial transferred PC switching, with thinner LT-GaAs having the benefit of reducing the permittivity mismatch from a waveguide perspective, but at a possible cost of reduced PC switching amplitude and sensitivity as well as an increased fragility during the epitaxial transfer process during fabrication. Thicker LT-GaAs would be more resilient to the stresses introduced by the epitaxial transfer process, with a potentially increased photocarrier population being excited by the laser (too thick of an LT-GaAs layer will exceed the optical penetration depth, preventing the geometrically deeper photocarriers

from being excited). Furthermore, the influence of the external electrical bias will be less for carriers LT-GaAs which are further away from the metal contacts. Both these effects suggest a greater pulse amplitude being created, but with a broader FWHM.

As well as the thickness of the LT-GaAs, the growth temperature and anneal was optimized based on free space emitters (which ultimately use EO detection schemes) [133], suggesting it could be possible to further improve the LT-GaAs for on-chip applications. This research would require several wafers to be grown individually using MBE as well as the epitaxial transfer process improved upon, to ensure differences in result can be directly attributed to the differences in the LT-GaAs.

The problematic epitaxial transfer process needs to be improved upon to improve the consistency of the PC switch characteristics on arbitrary substrates allowing S parameters to be found. This would be done with a more detailed investigation into the epitaxial transfer methods to which there are several that have been tried and tested using a range of different techniques [176, 198-200]. For the epitaxial lift off, there are several alternatives to the wax-support method used in this thesis [176]. One method is to etch the final LT-GaAs geometry whilst it is still attached to the host substrate, followed by the selective wet etch to release the LT-GaAs. This method reduces the area of the transferred material, which could reduce the micro-cracking, but does require an accurate control over the orientation and position on the host substrate [201, 202]. Furthermore, the sloped profile for the overlaid metal would be lost should the LT-GaAs be positioned upside down. An alternative method is to substitute the release layer for a phosphide based material such as InAlP, allowing a different selective etch to be used (HCl acid for selective etch of InAlP) [203]. Cheng *et al* had developed the lift-off methodology for reusing the growth substrate [203], analysing the cleanliness of the surface following the epitaxial lift off finding the solid by-products of the HF – AlAs etch forming on the surface increasing the surface roughness. The HCl – InAlP selective etch has more soluble by products, resulting in a smoother surface following the epitaxial lift off.

The handling of the epitaxial film is critical when considering the fragility of the 350-nm-thick LT-GaAs film; in this thesis, the wax support has been relied upon to provide a support medium to which the vacuum tool can hold onto. For the methods where the LT-GaAs has been patterned prior to lift off, the vacuum tool would be too aggressive, leading to an alternative method being used. One such method is to use a pipette to lift the LT-GaAs from the solution via a water droplet [202]. Another method is to use an electrostatically charged metallic tip [201]. However, both these methods are limited to areas

of LT-GaAs far less than that required by the project. Nevertheless, this does cast light on alternative methods which could be adopted and modified to improve the yield of the crack free transfer of thin crystal films.

The bonding of the LT-GaAs films to host substrates has predominately used van der Waals bonding, but there are alternative methods. For designs where an electrical connection is made to the LT-GaAs, AuSn solder can be used, but this would be unsuitable for the currently used PGL devices [54]. For an electrically isolated bond, a 50-nm-thick layer of water glass (sodium silicate) can be spin-coated onto the host substrate to be used as an adhesive, forming a bond between the GaAs and the host substrate which is four times stronger than that of van der Waals bonding [204]. The excess water glass is removed in a successive HF etch. For some host substrates, the surface chemistry can be modified for an improved adhesion with other materials; for silicon, surface treatment of selenium sulphide improves the bond between the silicon and the GaAs [205].

Despite the range of different methodologies, the sequence of the transfer process remains the same; an epitaxial lift-off, alignment and manipulation, followed by a bonding process. The process itself could in principle be redesigned (Figure 6.1) with the bonding of the PC material to the host substrate being done first, followed by the removal of the growth substrate using either lapping, selective top-down etching step or epitaxial lift off (though the selective etch must not affect the host substrate – thus HF is unusable for quartz); this process removes the wax which may be exerting strain on the thin LT-GaAs film (hence the micro-cracking) [175, 206, 207] as the wax is cooling during the initial preparation or as it is being lifted from the DI water by the vacuum tool.

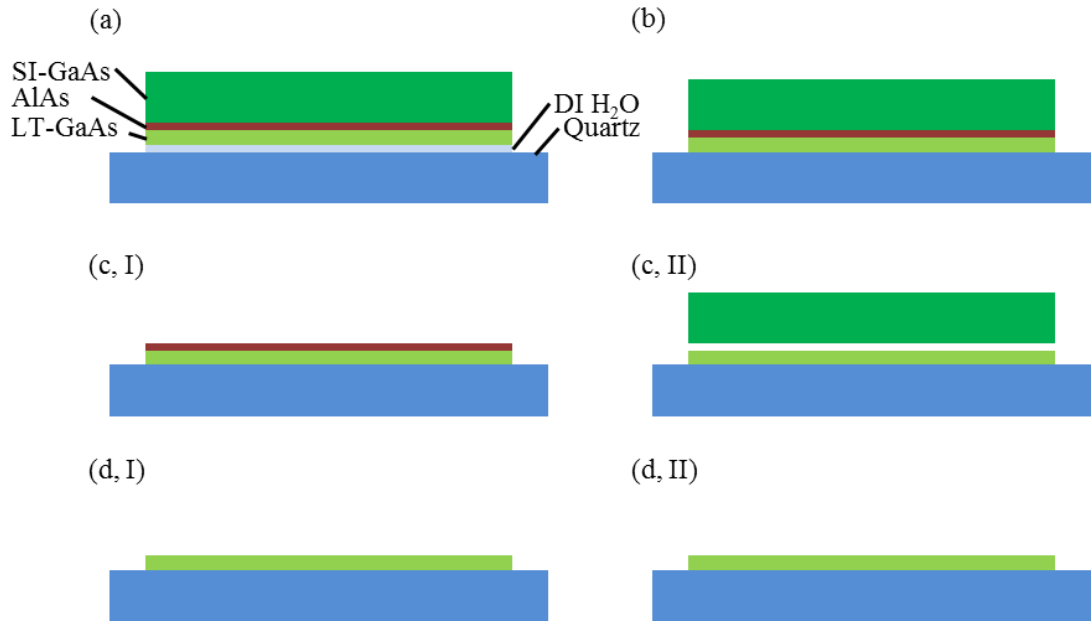


Figure 6.1: An alternative method for epitaxial transfer of LT-GaAs to arbitrary substrates (quartz used here). (a) The as-grown LT-GaAs wetted with DI water and placed onto the quartz. (b) The water evaporates under ambient conditions. The growth substrate is then removed using either process I or II; for I, (c) the bulk SI-GaAs is removed using a selective etch or lapping, (d) followed by the removal of the AlAs etch stop layer. For process II, (c) the substrate is placed into a selective etch, removing the AlAs layer, releasing the bulk SI-GaAs, (d) which is subsequently removed.

From the transmission line perspective, Ansoft HFSS (as well as other simulation packages used in other work) has been exploited for the optimization of the transmission line geometry; the practical realisation of these designs however remains challenging with respect to the substrate thickness. The 50- μm -thick quartz substrate is fragile, and as the device size increases to accommodate extended parasitic arms for high resolution spectroscopy, the yield of the fabrication reduces due to cracking in the substrate during the fabrication (more specifically when removing the thinned device from the carrier disk; see Chapter 3). As well as during fabrication, the device is vulnerable to breaking during the testing stages making it difficult to press the sample under test onto the PGLs. The post fabrication strength could be improved upon by introducing structural support to the back of the substrate using aerogel [82, 83]. Aerogel is a THz transparent material with $n \approx 1.06$ [82], but is very porous which could potentially be problematic when working with fluidic systems. Silica aerogel can be made either hydrophobic or hydrophilic by altering the conditions during its synthesis [83]. Aerogel has also been utilised as vessel for holding the water whilst it is analysed using a free space THz-TDS system [208], which could potentially be replicated for on-chip THz-TDS measurements of water.

Alternatively, other substrates can be tested, more specifically Kapton. Kapton is a polyimide film used as an insulated substrate for flexible electronics which has been recently applied to PGLs [162]. Commercially available in 25- μm -thick (or thicker) films, the fabrication process would need to be restructured with the epitaxial transfer being the most challenging. It is not yet known what the properties of Kapton are at $\lambda = 800 \text{ nm}$ which may prevent through-substrate excitation of the PC switch. If these issues are resolved there is great potential for a very robust and flexible spectroscopy system allowing a more vigorous handling of the sensor, though limited to a bandwidth of 4 THz due to spectral absorption features [209].

As the PGL on-chip system has evolved, the overall size of the device has increased in order to accommodate the large internal radii of the meandering long parasitic regions to postpone the problematic etalons. This is all very well for room temperature systems where space is not an issue, but for low temperature measurements conducted using a continuous flow microstat (Chapter 4) or dilution fridges, the available space for the on-chip system is limited. As a result, it would be beneficial for high resolution temperature dependant measurements to reduce the overall device size. To do this, the length of the parasitic regions of the probe arms and centre conductors need to be reduced, whilst maintaining an etalon free time window. One solution to the problem is to slow the pulse propagation with the introduction of corrugations into the transmission line [98]. However, with the transmission line being non-corrugated, corrugated parasitic regions may introduce a reflection at the interface. From the theoretical work presented here, wider PGLs have a weaker confinement of the electromagnetic field, suggesting a broadening of the PGL in the parasitic region could radiate, hence attenuate the pulses ultimately reducing the parasitic length and the chip's size.

6.2.2. Testing and Characterization of PGL

From a purely analytical point of view where only the material parameters and the geometrical dimensions are considered, the equations remain undefined. This is due to the complexities of analytically defining both electric and magnetic field based on the design of the waveguide itself due to its non-circular cross section [162]. There have been several comparisons to waveguides with similar electromagnetic field patterns, but each model misses a critical feature of the PGL. Therefore, it would be greatly beneficial to the PGL design community to derive some analytical terms such as the cutoff frequency and

characteristic impedance of the transmission line based on the material properties and the geometrical dimensions.

For the current fabrication process, it is unclear as to whether or not the LT-GaAs is good enough after being transferred to a host substrate to be used for ps pulse generation and detection. Therefore the device is fabricated to the finished geometry and tested. It would be preferable if the LT-GaAs could be characterized before the metallization; this could be achieved using the pump – probe beam spectroscopy discussed in Chapter 3. Furthermore, there is potential for a systematic study of the change in optoelectronic properties of the LT-GaAs due to the fabrication treatment by conducting measurements at intermitted points of the fabrication process; before epitaxial lift off, after van der Waals bonding, after the etching and after the metallization. This information would emphasize at which point the operating characteristics of the PC switch are degrading.

For investigations studying different waveguide geometries as well as different resonator designs, it would be better to use an external ps pulse generation and detection scheme [153-158]. This would remove the fabrication time associated with epitaxial transfer of the LT-GaAs as well as the etching steps. Furthermore, the results between different waveguides geometries would be directly comparable to one another since they have been measured with the same detector and source. Information of the evanescent field can also be found using a 2D mapping around the tested transmission line using the detecting external probe mounted on an x , y , z stage for direct comparison to field results found using simulation packages. However the external probes increase the experimental space size as well as introducing reflections due to the probe – transmission line interface, reducing the frequency resolution of the noise free spectra, therefore this technique is not a long term solution for the PGL on-chip THz-TDS systems but may be useful as a device characterization tool.

6.2.3. Further Spectroscopy Work

Whilst this project has successfully utilised the extended evanescent field of the PGL for spectroscopy of an overlaid polycrystalline sample, the sample had to be wetted with DI water to attach itself to the PGL ensuring optimal contact for maximum interaction with the PGL's electromagnetic field. As a result, the sample under test loses its integrity, losing both its shape and consistency, reducing the potential interaction with the PGL. An alternative method for accurately positioning and attaching the sample under test onto the transmission line without exerting a force onto the substrate should be sought. This thesis has

demonstrated gluing the sample with dissolvable “glue” (heat reduction of photoresist, S1813) but was unable to maintain a good contact with the transmission line. An alternative solution would be to drop cast the sample onto the transmission line as demonstrated for parallel plate waveguides [210-212]. Here, the sample under test is dissolved in a suitable solvent (or taken in the initial liquid form [212]) which is then pipetted onto the transmission line. The solvent is then evaporated, allowing the sample under test to crystallize onto the surface with the potential of forming a single crystal along the PGL. However, it should be noted that the crystallization of the sample under test is governed by many parameters such as the substrate material, the solvent used [210], and the temperature to name a few, with a potential to have a different crystal forming for different conditions. Whilst this would be an interesting field to study, for example, a possible change in THz spectra with the orientation of the crystal(s) of the sample under test as seen in free space THz-TDS of single crystals (Chapter 8 of reference [213]). However, it is very complicated to achieve repeatable control of the orientation of the crystallization of the samples and should only be considered for samples which have already have the crystallization conditions characterized which may or may not have a THz spectra.

However such a method would not be suitable for determining the spectra of the material before it is modified for drop casting spectroscopy. An alternative method could be to move the sensor opposed to moving the sample under test about the PGL. Here, the on-chip device would be positioned onto an x , y , z stage and the sample under test placed onto a surface, with the PGL being brought into contact. This would further encourage the introduction of fibre optics for the focusing of the laser power to the PC switches removing the need to realign and focus the optics associated with free space optics.

6.3. Direction of PGLs for Sensing Applications

This project has shown a lot of desirable properties for an on-chip spectroscopy system operating in the THz regime. The enhanced bandwidth of the PGL and the ability to mould the evanescent field to specific sensing applications enhances the range of applications PGLs could be applied to.

A field which PGLs have recently been entered into is the investigation of condensed matter systems (CMS) such as graphene and low dimensional semiconductor systems. Here, the PGLs are made narrow to confine the electric field to the conductor (to reduce cross talk across the gap) and a break made in the transmission line. The break in the transmission line

is then filled in with a CMS into which a transient pulse is injected and collected. The transmitted pulse, modified by the CMS, can be analysed to reveal spectral information. This work is currently being investigated for graphene at the University of Leeds [185].

Since the PGL is a single conductor transmission line, it is very attractive as a microfluidic sensor as the risks of electrically shorting the electrical conductors associated with transmission lines such as coplanar waveguides and coplanar striplines are removed. Microfluidic sensing is already established for PGL transmission lines and has been extensively studied up to 110 GHz, but has been hampered by the strong THz absorption of the water and bandwidth limited by the VNAs used to test the system [105-108]. The latter can be solved with the use of a higher bandwidth VNA; a 1.1 THz VNA is commercially available but only as a significant investment in comparison to the smaller bandwidth VNAs as well as being less flexible around design constraints of the system setup. As shown in this thesis and elsewhere [95, 96, 162, 170], the bandwidth can be extended beyond that of the VNA with the introduction of optoelectronic generation and detection for THz-TDS which would provide an attractive solution for microfluidic sensing.

To resolve the water's bulk absorption loading of the PGL, the water sample can be moved away from the PGL to maintain the transmission line bandwidth, with the introduction of electrically isolated resonators (Chapter 5). Here, the microfluidic channel would run parallel to the PGL, and over the sensitive regions of the filter, shifting the resonant frequency of the filter based on the dielectric constant of the fluidic sample. However, due to the resonators having a fixed sensing frequency, the permittivity of the fluidic sample can only be calculated for predefined frequencies.

For absorption spectra, the fluidic channel should overlay the featureless PGL. Therefore to reduce the bulk absorption of the water in effort to retain the bandwidth of the system, the liquid volume on the PGL needs to be minimised at a cost of potentially losing some of the weaker spectral information. This could be achieved by reducing the cross section of the fluidic channel, at a risk of requiring a higher pressure to force the liquid through the channels which may consequently break the substrate or separate the microfluidic defining material from the PGL substrate. This would be a case of trial and error fabrication and testing, investigating different materials and fabrication procedures, with a potential result of a very effective and sensitive microfluidic spectroscopy system operating at THz frequencies which would find applications in the both chemical and biological fields. In the biological field, there have been several proposals for using the PGLs for investigating individual cells

[97, 214]; here the cells are trapped over the PGL (and a pair of electrodes for low frequency analysis) by a narrowing of the fluidic channel [214].

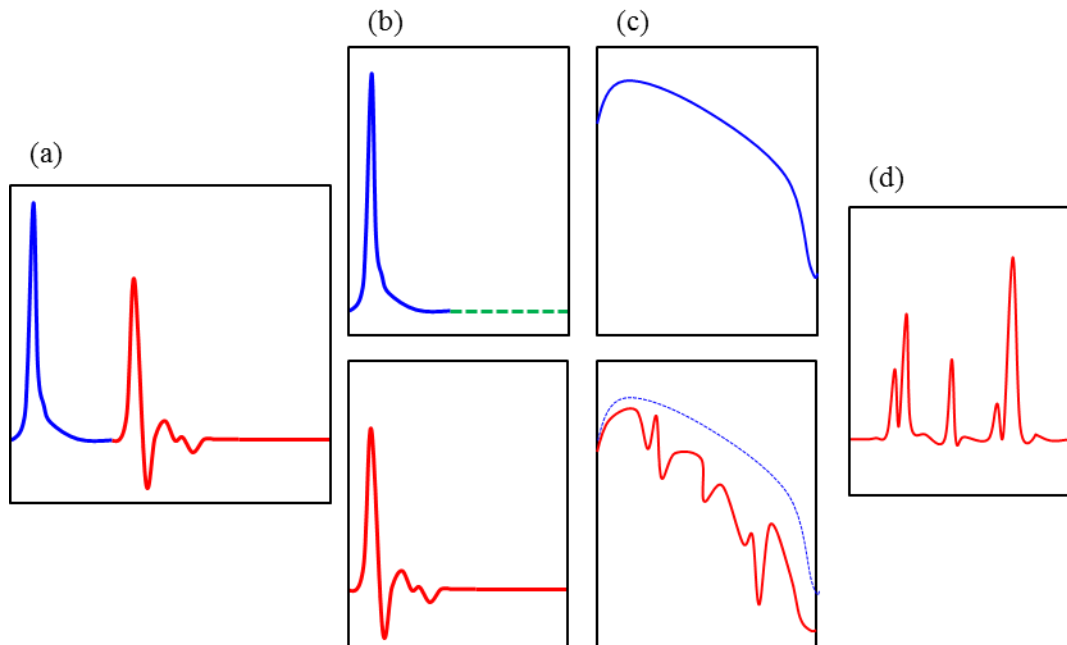


Figure 6.2: A theoretical projection of the one-scan method TDS analysis method; the recorded TDS spectrum (a) is split into (b) the reference signal (blue) and the sample signal (red). The reference signal is extended to the same time domain as the sample signal with zero padding (dashed green). Both TDS spectra undergo a (c) FFT and compared to give an absorption spectrum.

One of the main drawbacks observed for epitaxial transferred LT-GaAs on quartz for defining PC switches is the difficulty in defining PC switches with the same operating characteristics, which ultimately prevents the S parameters from being calculated. One method of overcoming this is to use a one-scan system which has been demonstrated for CPSs [215], where both the reference and information signal are recorded using the same scan window obtained from the same PC generation and detection scheme. Here, the input pulse is generated and detected using the methodology defined in Chapter 3, and the pulse coupled into a transmission line. The THz pulse propagates along the transmission line to an open circuit termination, causing a complete reflection of the transmitted pulse to the input pulse detecting PC switch. The pulse as a result has propagated along the transmission line twice, thus increasing the effective interaction length between the transmission line and the overlaid material in spectroscopy applications, twofold. Both the input and transmitted pulses are recorded using the same detector (Figure 6.2a). The transmitted pulse is then truncated from the TDS spectra and the input pulse is zero padded to provide the reference of

the same time length as the transmitted pulse's TDS spectra (Figure 6.2b). A FFT is performed on both signals (Figure 6.2c). From the frequency spectra, the S parameters and absorption spectra (Figure 6.2d) can be obtained, revealing spectral information for the overlaid material. However, this method requires that there are no etalons or additional features in the reference signal beyond the truncation point, allowing the reference signal to be accurately zero padded and that the transmitted signal does not contain features originating from the reference signal. Furthermore, the input pulse must have decayed before the arrival of the reflected transmitted pulse; this design condition will increase the minimum length of the transmission line to increase the separation between the input and transmitted pulses, further reducing the bandwidth of the transmitted signal.

The reflection due to the PC switch may also cause the terminated transmission line to be perceived as an antenna and resonate. This will cause resonant features in the spectra limiting the applications of the setup, or alternatively can be utilised for a single frequency THz dielectric spectroscopy sensor.

Should the problems associated with epitaxial transfer of LT-GaAs onto quartz be resolved to produce PC switches with the same operating characteristics, a multiport THz-TDS system could be devised. PGLs operated using VNAs up to 325 GHz have been used in a multiport system where the PGL is split from a single transmission line into two or more transmission lines (Figure 6.3b) [90]. As stated earlier, the bandwidth can be enhanced with the introduction of PC switches and THz-TDS methodology. The individual signals would be detected by two separate detectors equidistant from the generating switch; the system would have to be symmetrical to ensure the same signal is recorded for both detectors, for both transmission lines in the same state. Such a system would allow two or more signals to be recorded separately and simultaneously using two (or more) probe beams and lock-in amplifiers (one setup for each of the multiport transmission lines). One transmission line would represent an unloaded reference signal whilst the other transmission line, loaded with a sample under test would record the spectral information of the sample. The two spectra would be compared with one another to reveal absorption spectra. Whilst this method removes the assumption of featureless spectra of the reference signal used in the one-scan method, it requires repeatable fabrication of the devices; the methods used currently do not have repeatable operating characteristics of the PC switches. Additionally, the power of the generated THz pulse is divided for each of the multiport transmission lines, reducing the strength of the pulse used to record absorption spectra of the overlaid samples under test.

This would reduce the sensitivity to the smaller features as well as reduce the overall SNR of the transmitted pulse.

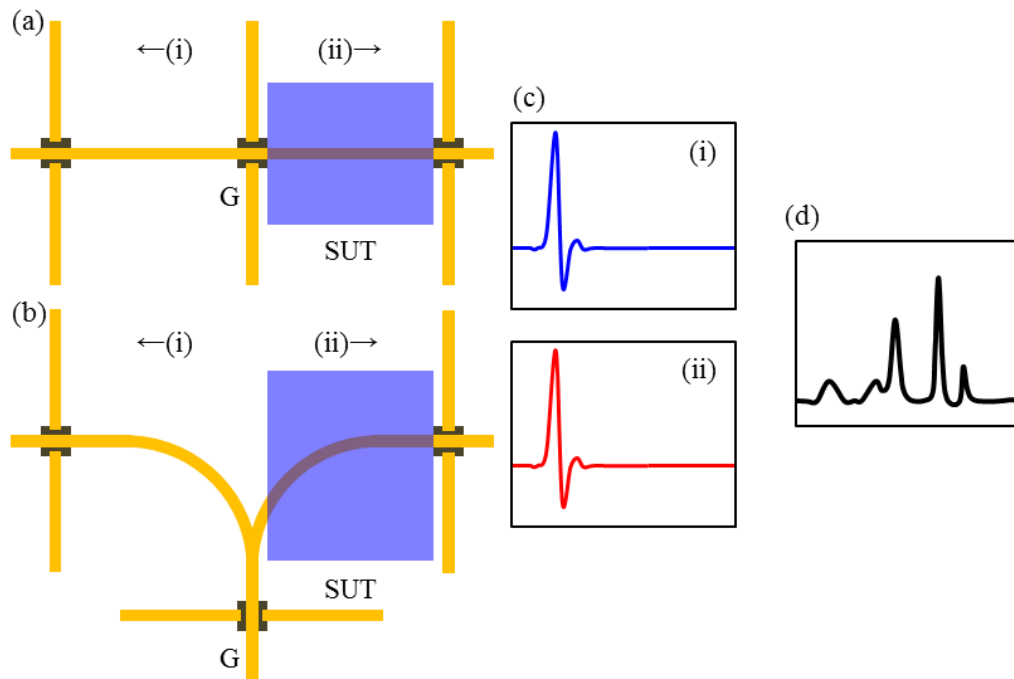


Figure 6.3: Schematics of a multiport system using a straight length of PGL (a) and a split PGL (b) for simultaneous measurements of an unloaded transmission line and loaded (sample under test (SUT)). The pulse generated by the PC switch at G is recorded (c) after propagation in both directions (i and ii). The TDS spectra undergo a FFT (not shown) and compared with one another to reveal absorption spectra.

In summary, the PGL has shown itself to be an attractive alternative to other transmission lines such as CPW and MSLs due to the ability to design the extended evanescent field for specific applications such as absorption spectroscopy. However, there still remains more development to be done to push the bandwidth of these on-chip systems to higher frequencies in order to compete against the well-established free-space systems. This thesis has highlighted and investigated some areas which would address these frequency limitations with potential solutions.

6.4. Publications

The work presented in this thesis has been presented and published in conference proceedings as well as peer reviewed publications.

6.4.1. Conference Proceedings

C. Russell, C. D. Wood, L. Dazhang, A. D. Burnett, L. H. Li, E. H. Linfield, A. G. Davies, J. E. Cunningham, "Increasing the bandwidth of planar on-chip THz devices for spectroscopic applications," in *Infrared, Millimeter and Terahertz Waves (IRMMW-THz), 2011 36th International Conference on*, 2011, pp. 1-3 (Invited talk, Student competition runner up)

C. Russell, C. D. Wood, A. D. Burnett, L. Li, E. H. Linfield, A. G. Davies, J. E. Cunningham, "Optimization and application of on-chip terahertz Goubau lines," in *Infrared, Millimeter and Terahertz Waves (IRMMW-THz), 2013 38th International Conference on*, 2013, pp. 1-2 (accepted)

6.4.2. Publication

C. Russell, C. D. Wood, A. D. Burnett, L. Li, E. H. Linfield, A. G. Davies, J. E. Cunningham, "Spectroscopy of polycrystalline materials using thinned-substrate planar Goubau line at cryogenic temperatures," Royal Society of Chemistry, Lab on a Chip, 2013 (accepted)

References

- [1] J. Federici, and L. Moeller, "Review of terahertz and subterahertz wireless communications," *Journal of Applied Physics*, vol. 107, no. 11, pp. 111101, 2010.
- [2] S. Ho-Jin, and T. Nagatsuma, "Present and Future of Terahertz Communications," *Terahertz Science and Technology, IEEE Transactions on*, vol. 1, no. 1, pp. 256-263, 2011.
- [3] P. H. Siegel, "Terahertz technology," *Microwave Theory and Techniques, IEEE Transactions on*, vol. 50, no. 3, pp. 910-928, 2002.
- [4] P. H. Siegel, "Terahertz technology in biology and medicine," *Microwave Theory and Techniques, IEEE Transactions on*, vol. 52, no. 10, pp. 2438-2447, 2004.
- [5] J. A. Zeitler, P. F. Taday, D. A. Newnham, M. Pepper, K. C. Gordon, and T. Rades, "Terahertz pulsed spectroscopy and imaging in the pharmaceutical setting - a review," *Journal of Pharmacy and Pharmacology*, vol. 59, no. 2, pp. 209-223, 2007.
- [6] P. U. Jepsen, D. G. Cooke, and M. Koch, "Terahertz spectroscopy and imaging – Modern techniques and applications," *Laser & Photonics Reviews*, vol. 5, no. 1, pp. 124-166, 2010.
- [7] M. Tonouchi, "Cutting-edge terahertz technology," *Nat Photon*, vol. 1, no. 2, pp. 97-105, 2007.
- [8] A. G. Davies, A. D. Burnett, F. Wenhui, E. H. Linfield, and J. E. Cunningham, "Terahertz spectroscopy of explosives and drugs," *Materials Today*, vol. 11, no. 3, pp. 18-26, 2008.
- [9] B. B. Hu, and M. C. Nuss, "Imaging with terahertz waves," *Opt. Lett.*, vol. 20, no. 16, pp. 1716-1718, 1995.
- [10] X. Wang, D. J. Hilton, L. Ren, D. M. Mittleman, J. Kono, and J. L. Reno, "Terahertz time-domain magnetospectroscopy of a high-mobility two-dimensional electron gas," *Opt. Lett.*, vol. 32, no. 13, pp. 1845-1847, 2007.
- [11] M. van Exter, C. Fattinger, and D. Grischkowsky, "Terahertz time-domain spectroscopy of water vapor," *Optics Letters*, vol. 14, no. 20, pp. 1128-30, 1989.
- [12] M. B. Byrne, J. Cunningham, K. Tych, A. D. Burnett, M. R. Stringer, C. D. Wood, L. Dazhang, M. Lachab, E. H. Linfield, and A. G. Davies, "Terahertz vibrational absorption spectroscopy using microstrip-line waveguides," *Applied Physics Letters*, vol. 93, no. 18, pp. 182904, 2008.
- [13] H. W. Hubers, M. F. Kimmitt, N. Hiromoto, and E. Brundermann, "Terahertz Spectroscopy: System and Sensitivity Considerations," *Terahertz Science and Technology, IEEE Transactions on*, vol. 1, no. 1, pp. 321-331, 2011.
- [14] I. P. S. Martin, G. Cinque, G. Rehm, C. A. Thomas, and R. Bartolini, "Operating the Diamond Light Source in Low Alpha Mode for Users," *International Particle Accelerator Conference 2013*, 2013.
- [15] A. D. Burnett, "Private communication," 2013.
- [16] Y. C. Shen, P. C. Upadhyaya, H. E. Beere, E. H. Linfield, A. G. Davies, I. S. Gregory, C. Baker, W. R. Tribe, and M. J. Evans, "Generation and detection of ultrabroadband terahertz radiation using photoconductive emitters and receivers," *Applied Physics Letters*, vol. 85, no. 2, pp. 164-166, 2004.
- [17] M. Naftaly, and R. E. Miles, "A method for removing etalon oscillations from THz time-domain spectra," *Optics Communications*, vol. 280, no. 2, pp. 291-295, 2007.

- [18] W. Linghui, L. Yuanyan, W. Yingxin, and Z. Ziran, "A method for removing echoes in the terahertz time-domain spectroscopy system." pp. 1-4, 2012.
- [19] M. Kaushik, B. W. H. Ng, B. M. Fischer, and D. Abbott, "Reduction of Scattering Effects in THz-TDS Signals," *Photonics Technology Letters, IEEE*, vol. 24, no. 2, pp. 155-157, 2012.
- [20] C. J. Strachan, T. Rades, D. A. Newnham, K. C. Gordon, M. Pepper, and P. F. Taday, "Using terahertz pulsed spectroscopy to study crystallinity of pharmaceutical materials," *Chemical Physics Letters*, vol. 390, no. 1-3, pp. 20-24, 2004.
- [21] U. Schade, K. Holldack, P. Kuske, G. Wustefeld, and H.-W. Hubers, "THz near-field imaging employing synchrotron radiation," *Applied Physics Letters*, vol. 84, no. 8, pp. 1422-1424, 2004.
- [22] D. A. Newnham, and P. F. Taday, "Pulsed Terahertz Attenuated Total Reflection Spectroscopy," *Appl. Spectrosc.*, vol. 62, no. 4, pp. 394-398, 2008.
- [23] A. Wojdyla, and G. Gallot, "Attenuated internal reflection terahertz imaging," *Optics Letters*, vol. 38, no. 2, pp. 112-114, 2013.
- [24] R. Mendis, and D. Grischkowsky, "Undistorted guided-wave propagation of subpicosecond terahertz pulses," *Optics Letters*, vol. 26, no. 11, pp. 846-848, 2001.
- [25] S.-H. Kim, E. S. Lee, Y. B. Ji, and T.-I. Jeon, "Improvement of THz coupling using a tapered parallel-plate waveguide," *Optics Express*, vol. 18, no. 2, pp. 1289-1295, 2010.
- [26] J. S. Melinger, S. S. Harsha, N. Laman, and D. Grischkowsky, "Guided-wave terahertz spectroscopy of molecular solids [Invited]," *J. Opt. Soc. Am. B*, vol. 26, no. 9, pp. A79-A89, 2009.
- [27] V. Astley, B. McCracken, R. Mendis, and D. M. Mittleman, "Analysis of rectangular resonant cavities in terahertz parallel-plate waveguides," *Opt. Lett.*, vol. 36, no. 8, pp. 1452-1454, 2011.
- [28] N. Laman, S. Sree Harsha, and D. Grischkowsky, "Narrow-line waveguide terahertz time-domain spectroscopy of aspirin and aspirin precursors," *Applied Spectroscopy*, vol. 62, no. 3, pp. 319-326, 2008.
- [29] R. Mendis, V. Astley, J. Liu, and D. M. Mittleman, "Terahertz microfluidic sensor based on a parallel-plate waveguide resonant cavity," *Applied Physics Letters*, vol. 95, no. 17, pp. 171113, 2009.
- [30] D. Pozar, *Microwave engineering*: John Wiley & Sons Inc, 1998.
- [31] J. S. Melinger, N. Laman, S. S. Harsha, and D. Grischkowsky, "High resolution terahertz spectroscopy of organic polycrystalline thin films using a parallel metal plate waveguide," *CLEO '07. 2007 Conference on Lasers and Electro-Optics*. pp. 223-224, 2007.
- [32] G. Goubau, "Surface waves and their application to transmission lines," *Journal of Applied Physics*, vol. 21, pp. 1119-1128, 1950.
- [33] G. Goubau, "Single-conductor surface-wave transmission lines," *Proceedings of the Institute of Radio Engineers*, vol. 39, pp. 619-624, 1951.
- [34] G. Goubau, "Open wire lines," *Institute of Radio Engineers Transactions on Microwave Theory and Techniques*, vol. MTT-4, no. 4, pp. 197-200, 1956.
- [35] T. I. Jeon, J. Zhang, and D. Grischkowsky, "THz Sommerfeld wave propagation on a single metal wire," *Applied Physics Letters*, vol. 86, no. 16, pp. 1-3, 2005.
- [36] H. M. Barlow, and A. L. Cullen, "Surface waves," *Proceedings of the IEE - Part III: Radio and Communication Engineering*, vol. 100, no. 68, pp. 329-341, 1953.
- [37] M. Walther, M. R. Freeman, and F. A. Hegmann, "Metal-wire terahertz time-domain spectroscopy," *Applied Physics Letters*, vol. 87, no. 26, pp. 261107, 2005.

- [38] J. A. Deibel, K. Wang, M. Escarra, N. Berndsen, and D. M. Mittleman, "The excitation and emission of terahertz surface plasmon polaritons on metal wire waveguides," *Comptes Rendus Physique*, vol. 9, no. 2, pp. 215-231, 2008.
- [39] H. Cao, and A. Nahata, "Coupling of terahertz pulses onto a single metal wire waveguide using milled grooves," *Optics Express*, vol. 13, no. 18, pp. 7028-7034, 2005.
- [40] M. Wächter, M. Nagel, and H. Kurz, "Frequency-dependent characterization of THz Sommerfeld wave propagation on single-wires," *Optics Express*, vol. 13, no. 26, pp. 10815-10822, 2005.
- [41] M. Wächter, M. Nagel, and H. Kurz, "Sommerfeld wires at terahertz frequencies," *IEEE MTT-S International Microwave Symposium Digest*, pp. 1299-1302, 2006.
- [42] J. C. Wiltse, "Low-loss surface-wave propagation on coated or uncoated cylindrical conductor from 0.1 to 1 THz," *2007 IEEE Antennas and Propagation Society International Symposium*, pp. 4657-4660, 2008.
- [43] M. Wächter, M. Nagel, and H. Kurz, "Frequency-dependent characterization of THz Sommerfeld wave propagation on single-wires," *Opt. Express*, vol. 13, no. 26, pp. 10815-10822, 2005.
- [44] Y. B. Ji, E. S. Lee, J. S. Jang, and T. I. Jeon, "Enhancement of the detection of THz Sommerfeld wave using a conical wire waveguide," *Optics Express*, vol. 16, no. 1, pp. 271-278, 2008.
- [45] K. Wang, and D. M. Mittleman, "Guided propagation of terahertz pulses on metal wires," *Journal of the Optical Society of America B: Optical Physics*, vol. 22, no. 9, pp. 2001-2008, 2005.
- [46] J. F. O'Hara, R. D. Averitt, and A. J. Taylor, "Prism coupling to terahertz surface plasmon polaritons," *Optics Express*, vol. 13, no. 16, pp. 6117-6126, 2005.
- [47] M. Gong, T. I. Jeon, and D. Grischkowsky, "THz surface wave collapse on coated metal surfaces," *Optics Express*, vol. 17, no. 19, pp. 17088-17101, 2009.
- [48] T. I. Jeon, and D. Grischkowsky, "THz Zenneck surface wave (THz surface plasmon) propagation on a metal sheet," *Applied Physics Letters*, vol. 88, no. 6, pp. 061113, 2006.
- [49] J. F. Bulzacchelli, H.-S. Lee, K. G. Stawiasz, S. Alexandrou, and M. B. Ketchen, "Picosecond optoelectronic study of superconducting microstrip transmission lines," *IEEE Transactions on Applied Superconductivity*, vol. 5, no. 2 pt 3, pp. 2839-2843, 1995.
- [50] F. Stewing, T. Kleine-Ostmann, and M. Koch, "A new class of improved-efficiency THz filters for on-chip detection of biomaterials," *Microwave and Optical Technology Letters*, vol. 41, no. 2, pp. 79-82, 2004.
- [51] J. Cunningham, C. Wood, A. G. Davies, I. Hunter, E. H. Linfield, and H. E. Beere, "Terahertz frequency range band-stop filters," *Applied Physics Letters*, vol. 86, no. 21, pp. 1-3, 2005.
- [52] J. Cunningham, C. Wood, A. G. Davies, C. K. Tiang, P. Tosch, D. A. Evans, E. H. Linfield, I. C. Hunter, and M. Missous, "Multiple-frequency terahertz pulsed sensing of dielectric films," *Applied Physics Letters*, vol. 88, no. 7, 2006.
- [53] C. Wood, J. Cunningham, P. C. Upadhyaya, E. H. Linfield, I. C. Hunter, A. G. Davies, and M. Missous, "On-chip photoconductive excitation and detection of pulsed terahertz radiation at cryogenic temperatures," *Applied Physics Letters*, vol. 88, no. 14, pp. 142103, 2006.
- [54] S. Kasai, A. Tanabashi, K. Kajiki, T. Itsuji, R. Kurosaka, H. Yoneyama, M. Yamashita, H. Ito, and T. Ouchi, "Micro strip line-based on-chip terahertz integrated devices for high sensitivity biosensors," *Applied Physics Express*, vol. 2, no. 6, 2009.

- [55] M. Nagel, P. H. Bolivar, M. Brucherseifer, H. Kurz, A. Bosserhoff, and R. Buttner, "Integrated THz technology for label-free genetic diagnostics," *Applied Physics Letters*, vol. 80, no. 1, pp. 154-156, 2002.
- [56] M. Nagel, P. H. Bolivar, M. Brucherseifer, H. Kurz, A. Bosserhoff, and R. Buttner, "Integrated planar terahertz resonators for femtomolar sensitivity label-free detection of DNA hybridization," *Applied Optics*, vol. 41, no. 10, pp. 2074-2078, 2002.
- [57] T. Ohkubo, M. Onuma, J. Kitagawa, and Y. Kadoya, "Micro-strip-line-based sensing chips for characterization of polar liquids in terahertz regime," *Applied Physics Letters*, vol. 88, no. 21, pp. 212511, 2006.
- [58] J. Kitagawa, Y. Akiyama, M. Onuma, and Y. Kadoya, "Fiber-coupled sensor chip based on micro-strip-line working in THz regime," *IRMMW-THz2007 - Conference Digest of the Joint 32nd International Conference on Infrared and Millimetre Waves, and 15th International Conference on Terahertz Electronics*. pp. 857-858, 2007.
- [59] H.-M. Heiliger, M. Nagel, H. G. Roskos, H. Kurz, F. Schnieder, W. Heinrich, R. Hey, and K. Ploog, "Low-dispersion thin-film microstrip lines with cyclotene (benzocyclobutene) as dielectric medium," *Applied Physics Letters*, vol. 70, no. 17, pp. 2233-2235, 1997.
- [60] M. Nagel, T. Dekorsy, M. Brucherseifer, P. Haring Bolivar, and H. Kurz, "Characterization of polypropylene thin-film microstrip lines at millimeter and submillimeter wavelengths," *Microwave and Optical Technology Letters*, vol. 29, no. 2, pp. 97-100, 2001.
- [61] E. Peytavit, C. Donche, S. Lepilliet, G. Ducournau, and J. F. Lampin, "Thin-film transmission lines using cyclic olefin copolymer for millimetre-wave and terahertz integrated circuits," *Electronics Letters*, vol. 47, no. 7, pp. 453-454, 2011.
- [62] K. Takase, T. Ohkubo, F. Sawada, D. Nagayama, J. Kitagawa, and Y. Kadoya, "Propagation characteristics of terahertz electrical signals on micro-strip lines made of optically transparent conductors," *Japanese Journal of Applied Physics, Part 2: Letters*, vol. 44, no. 28-32, pp. L1011-L1014, 2005.
- [63] J. Kitagawa, T. Ohkubo, M. Onuma, and Y. Kadoya, "THz spectroscopic characterization of biomolecule/water systems by compact sensor chips," *Applied Physics Letters*, vol. 89, no. 4, pp. 041114, 2006.
- [64] Y. Kadoya, M. Onuma, S. Yanagi, T. Ohkubo, N. Sato, and J. Kitagawa, "THz wave propagation on strip lines: Devices, properties, and applications," *Radioengineering*, vol. 17, no. 2, pp. 48-55, 2008.
- [65] M. Nagel, F. Richter, P. Haring-Bolivar, and H. Kurz, "A functionalized THz sensor for marker-free DNA analysis," *Physics in Medicine and Biology*, vol. 48, no. 22, pp. 3625-3636, 2003.
- [66] J. Cunningham, M. Byrne, P. Upadhyaya, M. Lachab, E. H. Linfield, and A. G. Davies, "Terahertz evanescent field microscopy of dielectric materials using on-chip waveguides," *Applied Physics Letters*, vol. 92, no. 3, pp. 032903, 2008.
- [67] N. Sato, J. Kitagawa, and Y. Kadoya, "Propagation of THz pulses on microstrip discontinuities," *Infrared, Millimeter, and Terahertz Waves, 2009. IRMMW-THz 2009. 34th International Conference on*. pp. 1-2, 2009.
- [68] S. Gupta, J. F. Whitaker, and G. A. Mourou, "Subpicosecond pulse propagation on coplanar waveguides: Experiment and simulation," *IEEE Microwave and Guided Wave Letters*, vol. 1, no. 7, pp. 161-163, 1991.
- [69] J. Lee, H. Lee, W. Kim, J. Lee, and J. Kim, "Suppression of coupled-slotline mode on CPW using air-bridges measured by picosecond photoconductive sampling," *IEEE Microwave and Guided Wave Letters*, vol. 9, no. 7, pp. 265-267, 1999.
- [70] M. Griebel, J. H. Smet, J. Kuhl, K. von Klitzing, D. C. Driscoll, C. Kadow, and A. C. Gossard, "Picosecond sampling with fiber-illuminated ErAs:GaAs photoconductive switches

- in a strong magnetic field and a cryogenic environment," *Applied Physics Letters*, vol. 82, no. 19, pp. 3179-3181, 2003.
- [71] R. W. McGowan, D. Grischkowsky, and J. A. Misewich, "Demonstrated low radiative loss of a quadrupole ultrashort electrical pulse propagated on a three strip coplanar transmission line," *Applied Physics Letters*, vol. 71, no. 19, pp. 2842-2844, 1997.
- [72] R. Sprik, I. N. Duling, III, C. C. Chi, and D. Grischkowsky, "Far infrared spectroscopy with subpicosecond electrical pulses on transmission lines," *Applied Physics Letters*, vol. 51, no. 7, pp. 548-550, 1987.
- [73] D. Grischkowsky, I. N. Duling, III, J. C. Chen, and C. C. Chi, "Electromagnetic shock waves from transmission lines," *Physical Review Letters*, vol. 59, no. 15, pp. 1663-1666, 1987.
- [74] H. Cheng, J. F. Whitaker, T. M. Weller, and L. P. B. Katehi, "Terahertz-bandwidth characterization of coplanar waveguide on dielectric membrane via time-domain electro-optic sampling," *IEEE MTT-S International Microwave Symposium Digest*, pp. 477-480, 1994.
- [75] M. Y. Frankel, S. Gupta, J. A. Valdmanis, and G. A. Mourou, "Terahertz attenuation and dispersion characteristics of coplanar transmission lines," *IEEE Transactions on Microwave Theory and Techniques*, vol. 39, no. 6, pp. 910-916, 1991.
- [76] S. Alexandrou, R. Sobolewski, and T. Y. Hsiang, "Time-domain characterization of bent coplanar waveguides," *IEEE Journal of Quantum Electronics*, vol. 28, no. 10, pp. 2325-2332, 1992.
- [77] J. Kitagawa, S. Yanagi, M. Onuma, and Y. Kadoya, "THz fingerprint spectra detected by sensor chips based on coplanar strip-lines made on low-permittivity plastic substrate," *IRMMW-THz2007 - Conference Digest of the Joint 32nd International Conference on Infrared and Millimetre Waves, and 15th International Conference on Terahertz Electronics*, pp. 283-284, 2007.
- [78] S. Yanagi, M. Onuma, J. Kitagawa, and Y. Kadoya, "Propagation of terahertz pulses on coplanar strip-lines on low permittivity substrates and a spectroscopy application," *Applied Physics Express*, vol. 1, no. 1, pp. 012009, 2008.
- [79] L. L. W. Leung, H. Wai-Cheong, and K. J. Chen, "Low-loss coplanar waveguides interconnects on low-resistivity silicon substrate," *Components and Packaging Technologies, IEEE Transactions on*, vol. 27, no. 3, pp. 507-512, 2004.
- [80] W. H. Knox, J. E. Henry, K. W. Goossen, K. D. Li, B. Tell, D. A. B. Miller, D. S. Chemla, A. C. Gossard, J. English, and S. Schmitt-Rink, "Femtosecond excitonic optoelectronics," *IEEE Journal of Quantum Electronics*, vol. 25, no. 12, pp. 2586-2595, 1989.
- [81] H. Cheng, J. F. Whitaker, T. M. Weller, and L. P. B. Katehi, "Terahertz-bandwidth pulse propagation on a coplanar stripline fabricated on a thin membrane," *IEEE Microwave and Guided Wave Letters*, vol. 4, no. 3, pp. 89-91, 1994.
- [82] M. Y. Frankel, R. H. Voelker, and J. N. Hilfiker, "Coplanar transmission lines on thin substrates for high-speed low-loss propagation," *IEEE Transactions on Microwave Theory and Techniques*, vol. 42, no. 3, pp. 396-402, 1994.
- [83] A. Soleimani Dorcheh, and M. H. Abbasi, "Silica aerogel; synthesis, properties and characterization," *Journal of Materials Processing Technology*, vol. 199, no. 1-3, pp. 10-26, 2008.
- [84] D. R. Dykaar, A. F. J. Levi, and M. Anzlowar, "Ultrafast coplanar air-transmission lines," *Applied Physics Letters*, vol. 57, no. 11, pp. 1123-1125, 1990.
- [85] U. D. Keil, D. R. Dykaar, A. F. J. Levi, R. F. Kopf, L. N. Pfeiffer, S. B. Darack, and K. W. West, "High speed normal and superconducting coplanar transmission lines," *IEEE Transactions on Applied Superconductivity*, vol. 3, no. 1 pt 4, pp. 2812-2815, 1993.

- [86] C. D. Wood, D. Mistry, L. H. Li, J. E. Cunningham, E. H. Linfield, and A. G. Davies, "On-chip THz generation and detection at milli-Kelvin temperatures for the study of ultrafast phenomena in confined semiconductor systems." pp. 1-3.
- [87] C. D. Wood, D. Mistry, L. H. Li, J. E. Cunningham, E. H. Linfield, and A. G. Davies, "On-chip terahertz spectroscopic techniques for measuring mesoscopic quantum systems," *Review of Scientific Instruments*, vol. 84, no. 8, pp. 085101, 2013.
- [88] D. Debuissou, A. Treizebre, T. Houssin, E. Leclerc, D. Bartes-Biesel, D. Legrand, J. Mazurier, S. Arscott, B. Bocquet, and V. Senez, "Nanoscale devices for online dielectric spectroscopy of biological cells," *Physiological Measurement*, vol. 29, no. 6, pp. 213-225, 2008.
- [89] A. Treizebre, T. Akalin, and B. Bocquet, "Planar excitation of Goubau Transmission Lines for THz BioMEMS," *IEEE Microwave and Wireless Components Letters*, vol. 15, no. 12, pp. 886-888, 2005.
- [90] A. Treizebre, S. Laurette, Y. Xu, R. G. Bosisio, and B. Bocquet, "THz power divider circuits on Planar Goubau Lines (PGLs)," *Progress In Electromagnetics Research C*, vol. 26, pp. 219-228, 2012.
- [91] T. Akalin, A. Treizebre, and B. Bocquet, "Single-wire transmission lines at terahertz frequencies," *IEEE Transactions on Microwave Theory and Techniques*, vol. 54, no. 6, pp. 2762-2767, 2006.
- [92] A. Treizebre, B. Bocquet, X. Yansheng, and R. G. Bosisio, "New THz excitation of planar Goubau line," *Microwave and Optical Technology Letters*, vol. 50, no. 11, pp. 2998-3001, 2008.
- [93] I. Türer, A. Chahadih, Y. Zappart, J.-F. Lampin, and T. Akalin, "Terahertz Plasmonic Y-Splitters with Planar Goubau Lines," *International Workshop on Optical Terahertz Science and Technology 2013*, 2013.
- [94] M. Horibe, and R. Kishikawa, "Metrological Traceability in Waveguide S-parameter Measurements at 1.0 THz Band," *Instrumentation and Measurement, IEEE Transactions on*, vol. 62, no. 6, pp. 1814-1820, 2013.
- [95] L. Dazhang, J. Cunningham, M. B. Byrne, S. Khanna, C. D. Wood, A. D. Burnett, S. M. Ershad, E. H. Linfield, and A. G. Davies, "On-chip terahertz Goubau-line waveguides with integrated photoconductive emitters and mode-discriminating detectors," *Applied Physics Letters*, vol. 95, no. 9, pp. 092903, 2009.
- [96] D. Gacemi, J. Mangeney, T. Laurant, J. F. Lampin, T. Akalin, K. Blary, A. Degiron, P. Crozat, and F. Meng, "THz surface plasmon modes on planar Goubau lines," *Opt. Express*, vol. 20, no. 8, pp. 8466-8471, 2012.
- [97] A. Treizebre, and B. Bocquet, "Investigation on living cells with a THz BioMEMS," *2007 Joint 32nd International Conference on Infrared and Millimeter Waves and the 15th International Conference on Terahertz Electronics (IRMMW-THz)*. pp. 82-83, 2007.
- [98] S. Laurette, A. Treizebre, and B. Bocquet, "Corrugated goubau lines to slow down and confine THz waves," *IEEE Transactions on Terahertz Science and Technology*, vol. 2, no. 3, pp. 340-344, 2012.
- [99] W. Rotman, "A Study of Single-Surface Corrugated Guides," *Proceedings of the IRE*, vol. 39, no. 8, pp. 952-959, 1951.
- [100] S. A. Maier, S. R. Andrews, L. Martín-Moreno, and F. J. García-Vidal, "Terahertz Surface Plasmon-Polariton Propagation and Focusing on Periodically Corrugated Metal Wires," *Physical Review Letters*, vol. 97, no. 17, pp. 176805, 2006.
- [101] T. Akalin, E. Peytavit, and J. F. Lampin, "Bendings and filters with single strip THz plasmonic waveguides," *2007 Joint 32nd International Conference on Infrared and*

- Millimeter Waves and the 15th International Conference on Terahertz Electronics (IRMMW-THz)*. pp. 75-76, 2007.
- [102] A. Treizebre, M. Hofman, and B. Bocquet, "Terahertz spiral Planar Goubau line rejectors for biological characterization," *Progress In Electromagnetics Research M*, vol. 14, pp. 163-176, 2010.
- [103] T. Akalin, E. Peytavit, and J. F. Lampin, "THz long range plasmonic waveguide in membrane topology," *2008 33rd International Conference on Infrared, Millimeter and Terahertz Waves (IRMMW-THz 2008)*, 2008.
- [104] S. Laurette, A. Treizebre, and B. Bocquet, "Co-integrated microfluidic and THz functions for biochip devices," *Journal of Micromechanics and Microengineering*, vol. 21, no. 6, pp. 065029, 2011.
- [105] A. Abbas, A. Treizebre, P. Supiot, N.-E. Bourzgui, D. Guillochon, D. Vercaigne-Marko, and B. Bocquet, "Cold plasma functionalized TeraHertz BioMEMS for enzyme reaction analysis," *Biosensors and Bioelectronics*, vol. 25, no. 1, pp. 154-160, 2009.
- [106] A. Abbas, A. Treizebre, N. Bourzgui, D. Guillochon, D. Vercaigne-Marko, P. Supiot, and B. Bocquet, "Terahertz Biomems for Enzymatic Catalysis Monitoring," *5th International Conference on Microtechnologies in Medicine and Biology*, 2009.
- [107] S. Laurette, A. Treizebre, F. Affouard, and B. Bocquet, "Subterahertz characterization of ethanol hydration layers by microfluidic system," *Applied Physics Letters*, vol. 97, no. 11, pp. 111904, 2010.
- [108] S. Laurette, A. Treizebre, A. Elaghi, B. Hatirnaz, R. Froidevaux, F. Affouard, L. Duponchel, and B. Bocquet, "Highly sensitive terahertz spectroscopy in microsystem," *RSC Advances*, vol. 2, no. 26, pp. 10064-10071, 2012.
- [109] S. Laurette, A. Treizebre, N. E. Bourzgui, and B. Bocquet, "Terahertz interferometer for integrated goubau-line waveguides," *Progress in Electromagnetics Research Letters*, vol. 30, pp. 49-58, 2012.
- [110] Y. Xu, and R. G. Bosisio, "A study of planar goubau lines (PGLs) for millimeter- And submillimeter-wave integrated circuits (ICs)," *Microwave and Optical Technology Letters*, vol. 43, no. 4, pp. 290-293, 2004.
- [111] S. Kasap, *Principles of electronic materials and devices*, 3 ed.: McGraw-Hill, 2006.
- [112] S. Kasap, *Optoelectronics and photonics principles and practices*: Prentice Hall, Inc., 2001.
- [113] W. Qi, and X.-C. Zhang, "Design and characterization of traveling-wave electrooptic terahertz sensors," *Selected Topics in Quantum Electronics, IEEE Journal of*, vol. 2, no. 3, pp. 693-700, 1996.
- [114] Q. Wu, and X.-C. Zhang, "7 terahertz broadband GaP electro-optic sensor," *Applied Physics Letters*, vol. 70, no. 14, pp. 1784-1786, 1997.
- [115] K. Tsuzuki, T. Ishibashi, H. Yasaka, and Y. Tohmori, "InP-based n-i-n Mach-Zehnder optical modulator," *Electronics and Communications in Japan (Part II: Electronics)*, vol. 88, no. 8, pp. 1-9, 2005.
- [116] H. J. Bakker, S. Hunsche, and H. Kurz, "Time-resolved study of phonon polaritons in LiTaO₃," *Physical Review B*, vol. 48, no. 18, pp. 13524-13537, 1993.
- [117] H. J. Bakker, S. Hunsche, and H. Kurz, "Investigation of anharmonic lattice vibrations with coherent phonon polaritons," *Physical Review B*, vol. 50, no. 2, pp. 914-920, 1994.
- [118] T. Taniuchi, S. Okada, and H. Nakanishi, "Widely-tunable THz-wave generation in 2-20 THz range from DAST crystal by nonlinear difference frequency mixing," *Electronics Letters*, vol. 40, no. 1, pp. 60-62, 2004.
- [119] Q. Wu, and X.-C. Zhang, "Ultrafast electro-optic field sensors," *Applied Physics Letters*, vol. 68, no. 12, pp. 1604-1606, 1996.

- [120] L. Meignien, J. Mangeney, P. Crozat, L. Duvillaret, and M. Hanna, "Two-port vectorial terahertz electro-optic sampling system," *Applied Physics Letters*, vol. 92, no. 13, pp. 131103, 2008.
- [121] L. Desplanque, J. F. Lampin, and F. Mollot, "Generation and detection of terahertz pulses using post-process bonding of low-temperature-grown GaAs and AlGaAs," *Applied Physics Letters*, vol. 84, no. 12, pp. 2049-2051, 2004.
- [122] X. Zheng, S. Wu, R. Sobolewski, R. Adam, M. Mikulics, P. Kordos, and M. Siegel, "Electro-optic sampling system with a single-crystal 4-N,N-dimethylamino-4[prime]-N[prime]-methyl-4-stilbazolium tosylate sensor," *Applied Physics Letters*, vol. 82, no. 15, pp. 2383-2385, 2003.
- [123] G. A. Mourou, and K. E. Meyer, "Subpicosecond electro-optic sampling using coplanar strip transmission lines," *Applied Physics Letters*, vol. 45, no. 5, pp. 492-494, 1984.
- [124] S. Seitz, M. Bieler, G. Hein, K. Pierz, U. Siegner, F. J. Schmuckle, and W. Heinrich, "Characterization of an external electro-optic sampling probe: Influence of probe height on distortion of measured voltage pulses," *Journal of Applied Physics*, vol. 100, no. 11, pp. 113124, 2006.
- [125] M. Bieler, K. Pierz, and U. Siegner, "Simultaneous generation and detection of ultrashort voltage pulses in low-temperature grown GaAs with below-bandgap laser pulses," *Applied Physics Letters*, vol. 94, no. 5, pp. 051108, 2009.
- [126] J. L. Freeman, S. K. Diamond, H. Fong, and D. M. Bloom, "Electro-optic sampling of planar digital GaAs integrated circuits," *Applied Physics Letters*, vol. 47, no. 10, pp. 1083-1084, 1985.
- [127] J. F. Lampin, L. Desplanque, and F. Mollot, "Detection of picosecond electrical pulses using the intrinsic Franz-Keldysh effect," *Applied Physics Letters*, vol. 78, no. 26, pp. 4103-4105, 2001.
- [128] S. Verghese, K. A. McIntosh, and E. R. Brown, "Highly tunable fiber-coupled photomixers with coherent terahertz output power," *Microwave Theory and Techniques, IEEE Transactions on*, vol. 45, no. 8, pp. 1301-1309, 1997.
- [129] A. Nahata, "Nonlinear optical generation and detection of ultrashort electrical pulses in transmission lines," *Opt. Lett.*, vol. 26, no. 6, pp. 385-387, 2001.
- [130] A. Nahata, and T. F. Heinz, "Generation of subpicosecond electrical pulses by optical rectification," *Opt. Lett.*, vol. 23, no. 11, pp. 867-869, 1998.
- [131] D. Dragoman, and M. Dragoman, "Terahertz fields and applications," *Progress in Quantum Electronics*, vol. 28, no. 1, pp. 1-66, 2004.
- [132] P. C. Upadhyya, F. Wenhui, A. Burnett, J. Cunningham, A. G. Davies, E. H. Linfield, J. Lloyd-Hughes, E. Castro-Camus, M. B. Johnston, and H. Beere, "Excitation-density-dependent generation of broadband terahertz radiation in an asymmetrically excited photoconductive antenna," *Optics Letters*, vol. 32, no. 16, pp. 2297-2299, 2007.
- [133] I. S. Gregory, C. Baker, W. R. Tribe, M. J. Evans, H. E. Beere, E. H. Linfield, A. G. Davies, and M. Missous, "High resistivity annealed low-temperature GaAs with 100 fs lifetimes," *Applied Physics Letters*, vol. 83, no. 20, pp. 4199-4201, 2003.
- [134] S. Gupta, J. F. Whitaker, and G. A. Mourou, "Ultrafast carrier dynamics in III-V semiconductors grown by molecular-beam epitaxy at very low substrate temperatures," *IEEE Journal of Quantum Electronics*, vol. 28, no. 10, pp. 2464-2472, 1992.
- [135] L. Prechtel, L. Song, D. Schuh, P. Ajayan, W. Wegscheider, and A. W. Holleitner, "Time-resolved ultrafast photocurrents and terahertz generation in freely suspended graphene," *Nature Communications*, vol. 3, 2012.
- [136] A. C. Warren, N. Katzenellenbogen, D. Grischkowsky, J. M. Woodall, M. R. Melloch, and N. Otsuka, "Subpicosecond freely propagating electromagnetic pulse generation and

- detection using GaAs:As epilayers,” *Applied Physics Letters*, vol. 58, no. 14, pp. 1512-1514, 1991.
- [137] D. F. Blossey, “Wannier Exciton in an Electric Field. II. Electroabsorption in Direct-Band-Gap Solids,” *Physical Review B*, vol. 3, no. 4, pp. 1382-1391, 1971.
- [138] D. E. Carlson, and C. R. Wronski, “Amorphous silicon solar cell,” *Applied Physics Letters*, vol. 28, no. 11, pp. 671-673, 1976.
- [139] M. Schall, M. Walther, and P. Uhd Jepsen, “Fundamental and second-order phonon processes in CdTe and ZnTe,” *Physical Review B - Condensed Matter and Materials Physics*, vol. 64, no. 9, pp. 943011-943018, 2001.
- [140] D. K. Gaskill, N. Bottka, L. Aina, and M. Mattingly, “Band-gap determination by photoreflectance of InGaAs and InAlAs lattice matched to InP,” *Applied Physics Letters*, vol. 56, no. 13, pp. 1269-1271, 1990.
- [141] N. Chimot, J. Mangeney, L. Joulaud, P. Crozat, H. Bernas, K. Blary, and J. F. Lampin, “Terahertz radiation from heavy-ion-irradiated In_{0.53}Ga_{0.47}As photoconductive antenna excited at 1.55 μm ,” *Applied Physics Letters*, vol. 87, no. 19, pp. 193510, 2005.
- [142] J. Lloyd-Hughes, E. Castro-Camus, and M. B. Johnston, “Simulation and optimisation of terahertz emission from InGaAs and InP photoconductive switches,” *Solid State Communications*, vol. 136, no. 11–12, pp. 595-600, 2005.
- [143] M. B. Ketchen, D. Grischkowsky, T. C. Chen, C. C. Chi, I. N. Duling, III, N. J. Halas, J. M. Halbout, J. A. Kash, and G. P. Li, “Generation of subpicosecond electrical pulses on coplanar transmission lines,” *Applied Physics Letters*, vol. 48, no. 12, pp. 751-753, 1986.
- [144] Z. Xuemei, X. Ying, R. Sobolewski, R. Adam, M. Mikulics, M. Siegel, and P. Kordos, “Femtosecond response of a free-standing LT-GaAs photoconductive switch,” *Applied Optics*, vol. 42, no. 9, pp. 1726-1731, 2003.
- [145] S. Alexandrou, W. Chia-Chi, R. Sobolewski, and T. Y. Hsiang, “Generation of subpicosecond electrical pulses by nonuniform illumination of GaAs transmission-line gaps,” *IEEE Journal of Quantum Electronics*, vol. 30, no. 5, pp. 1332-1338, 1994.
- [146] B. Tissafi, A. S. Grimault-Jacquin, and F. Aniel, "Optimization of THz pulses emitted by an InGaAs photoconductive switch," *IRMMW-THz 2010 - 35th International Conference on Infrared, Millimeter, and Terahertz Waves, Conference Guide*, 2010.
- [147] S. Verghese, N. Zamdmer, H. Qing, and A. Forster, “Cryogenic picosecond sampling using fiber-coupled photoconductive switches,” *Applied Physics Letters*, vol. 70, no. 20, pp. 2644-2646, 1997.
- [148] B. Tissafi, A. S. Grimault, and F. Aniel, "Effect of InGaAs surface states and interfaces on the photo-generated THz pulse shape," *2008 33rd International Conference on Infrared, Millimeter and Terahertz Waves (IRMMW-THz 2008)*, 2008.
- [149] J. F. Holzman, F. E. Vermeulen, and A. Y. Elezzabi, “Ultrafast photoconductive self-switching of subpicosecond electrical pulses,” *IEEE Journal of Quantum Electronics*, vol. 36, no. 2, pp. 130-136, 2000.
- [150] M. Mikulics, S. Wu, M. Marso, R. Adam, A. Forster, A. van der Hart, P. Kordos, H. Luth, and R. Sobolewski, “Ultrafast and highly sensitive photodetectors with recessed electrodes fabricated on low-temperature-grown GaAs,” *IEEE Photonics Technology Letters*, vol. 18, no. 7, pp. 820-822, 2006.
- [151] N. Vieweg, M. Mikulics, M. Scheller, K. Ezdi, R. Wilk, H. W. Hubers, and M. Koch, "Enhanced emission from THz antennas made of low-temperature-grown GaAs with annealed ohmic contacts," *2008 33rd International Conference on Infrared, Millimeter and Terahertz Waves (IRMMW-THz 2008)*, 2008.

- [152] M. Sirbu, S. B. P. Lepaul, and F. Aniel, "Coupling 3-D maxwell's and boltzmann's equations for analyzing a terahertz photoconductive switch," *IEEE Transactions on Microwave Theory and Techniques*, pp. 2991-2997, 2005.
- [153] J. Kim, S. Williamson, J. Nees, S.-i. Wakana, and J. Whitaker, "Photoconductive sampling probe with 2.3-ps temporal resolution and 4- μ V sensitivity," *Applied Physics Letters*, vol. 62, no. 18, pp. 2268-2270, 1993.
- [154] T. Pfeifer, H.-M. Heiliger, H. G. Roskos, and H. Kurz, "Generation and detection of picosecond electric pulses with freely positionable photoconductive probes," *IEEE Transactions on Microwave Theory and Techniques*, vol. 43, no. 12 pt 2, pp. 2856-2861, 1995.
- [155] T. Pfeifer, H. M. Heiliger, E. S. von Kamienski, H. G. Roskos, and H. Kurz, "Fabrication and characterization of freely positionable silicon-on-sapphire photoconductive probes," *J. Opt. Soc. Am. B*, vol. 11, no. 12, pp. 2547-2552, 1994.
- [156] M. Wachter, M. Nagel, and H. Kurz, "Tapered photoconductive terahertz field probe tip with subwavelength spatial resolution," *Applied Physics Letters*, vol. 95, no. 4, pp. 041112, 2009.
- [157] J. Lee, H. Lee, S. Yu, and J. Kim, "A micromachined photoconductive near-field probe for picosecond pulse propagation measurement on coplanar transmission lines," *IEEE Journal on Selected Topics in Quantum Electronics*, vol. 7, no. 4, pp. 674-682, 2001.
- [158] M. Nagel, A. Michalski, T. Botzem, and H. Kurz, "Near-field investigation of THz surface-wave emission from optically excited graphite flakes," *Optics Express*, vol. 19, no. 5, pp. 4667-4672, 2011.
- [159] M. Nagel, A. Michalski, and H. Kurz, "Contact-free fault location and imaging with on-chip terahertz time-domain reflectometry," *Optics Express*, vol. 19, no. 13, pp. 12509-12514, 2011.
- [160] M. M. Hasan, "An Expression for Group Velocity in a Transmission Line," *Electromagnetic Compatibility, IEEE Transactions on*, vol. 53, no. 1, pp. 261-262, 2011.
- [161] M. J. Hagmann, "Isolated carbon nanotubes as high-impedance transmission lines for microwave through terahertz frequencies," *Nanotechnology, IEEE Transactions on*, vol. 4, no. 2, pp. 289-296, 2005.
- [162] D. Gacemi, J. Mangeney, R. Colombelli, and A. Degiron, "Subwavelength metallic waveguides as a tool for extreme confinement of THz surface waves," *Sci. Rep.*, vol. 3, 2013.
- [163] M. King, and J. C. Wiltse, "Surface-wave propagation on coated or uncoated metal wires at millimeter wavelengths," *Antennas and Propagation, IRE Transactions on*, vol. 10, no. 3, pp. 246-254, 1962.
- [164] U. Paoletti, T. Suga, and H. Osaka, "Equivalent circuit for Sommerfeld wave," *IEICE Electronics Express*, vol. 8, no. 19, pp. 1590-1595, 2011.
- [165] Y. Xu, and R. G. Bosisio, "A comprehensive study on the planar type of goubau line for millimetre and submillimetre wave integrated circuits," *Microwaves, Antennas & Propagation, IET*, vol. 1, no. 3, pp. 681-687, 2007.
- [166] T. Akalin, A. Treizebre, and B. Bocquet, "High resolution biosensor based on surface wave transmission lines at THz frequencies," *2005 European Microwave Conference*, 2006.
- [167] W. C. Chen, J. J. Mock, D. R. Smith, T. Akalin, and W. J. Padilla, "Controlling Gigahertz and Terahertz Surface Electromagnetic Waves with Metamaterial Resonators," *Physical Review X*, vol. 1, no. 2, pp. 021016, 2011.
- [168] J. Emond, M. Grzeskowiak, G. Lissorgues, S. Protat, F. Deshours, E. Richalot, and O. Picon, "A low-loss planar goubau line and a coplanar-PGL transition on high-resistivity silicon substrate in the 57–64 GHz band," *Microwave and Optical Technology Letters*, vol. 54, no. 1, pp. 164-168, 2012.

- [169] M. B. Byrne, "Thesis: Pulsed imaging and spectroscopy using on-chip THz waveguides," *University of Leeds*, 2008.
- [170] L. Dazhang, "Thesis: On-chip terahertz pulsed systems," *University of Leeds*, 2010.
- [171] A. McIntosh, K. B. Nichols, S. Verghese, and E. R. Brown, "Investigation of ultrashort photocarrier relaxation times in low-temperature-grown GaAs," *Applied Physics Letters*, vol. 70, no. 3, pp. 354-356, 1997.
- [172] A. Claverie, and Z. Liliental-Weber, "Extended defects and precipitates in LT-GaAs, LT-InAlAs and LT-InP," *Mater. Sci. Eng. B, Solid-State Mater. Adv. Technol.* pp. 45-54, 1993.
- [173] J. F. Whitaker, "Optoelectronic applications of LTMBE III-V materials," *Mater. Sci. Eng. B, Solid-State Mater. Adv. Technol.* pp. 61-7, 1993.
- [174] J. K. Luo, H. Thomas, D. V. Morgan, and D. Westwood, "Thermal annealing effect on low temperature molecular beam epitaxy grown GaAs: arsenic precipitation and the change of resistivity," *Applied Physics Letters*, vol. 64, no. 26, pp. 3614-3616, 1994.
- [175] P. Demeester, I. Pollentier, P. D. Dobbelaere, C. Brys, and P. V. Daele, "Epitaxial lift-off and its applications," *Semiconductor Science and Technology*, vol. 8, no. 6, pp. 1124, 1993.
- [176] E. Yablonovitch, D. M. Hwang, T. J. Gmitter, L. T. Florez, and J. P. Harbison, "Van der Waals bonding of GaAs epitaxial liftoff films onto arbitrary substrates," *Applied Physics Letters*, vol. 56, no. 24, pp. 2419-2421, 1990.
- [177] L. Deng, W. Z. Lin, Z. R. Sun, and Z. G. Wang, "Response characteristic of femtosecond LT-GaAs photoconductive switches at different voltage biases," *Journal of Physics D: Applied Physics*, vol. 42, no. 24, 2009.
- [178] R. H. Jacobsen, K. Birkelund, T. Holst, P. Uhd Jepsen, and S. R. Keiding, "Interpretation of photocurrent correlation measurements used for ultrafast photoconductive switch characterization," *Journal of Applied Physics*, vol. 79, no. 5, pp. 2649-2657, 1996.
- [179] E. S. Harmon, M. R. Melloch, J. M. Woodall, D. D. Nolte, N. Otsuka, and C. L. Chang, "Carrier lifetime versus anneal in low temperature growth GaAs," *Applied Physics Letters*, vol. 63, no. 16, pp. 2248-2250, 1993.
- [180] S. Gupta, M. Y. Frankel, J. A. Valdmanis, J. F. Whitaker, G. A. Mourou, F. W. Smith, and A. R. Calawa, "Subpicosecond carrier lifetime in GaAs grown by molecular beam epitaxy at low temperatures," *Applied Physics Letters*, vol. 59, no. 25, pp. 3276-3278, 1991.
- [181] N. G. Paulter, D. N. Sinha, A. J. Gibbs, and W. R. Eisenstadt, "Optoelectronic measurements of picosecond electrical pulse propagation in coplanar waveguide transmission lines," *Microwave Theory and Techniques, IEEE Transactions on*, vol. 37, no. 10, pp. 1612-1619, 1989.
- [182] E. R. Brown, J. E. Bjarnason, A. M. Fedor, and T. M. Korter, "On the strong and narrow absorption signature in lactose at 0.53 THz," *Applied Physics Letters*, vol. 90, no. 6, pp. 061908, 2007.
- [183] A. Roggenbuck, H. Schmitz, A. Deninger, I. C. Mayorga, J. Hemberger, R. Güsten, and M. Grüninger, "Coherent broadband continuous-wave terahertz spectroscopy on solid-state samples," *New Journal of Physics*, vol. 12, no. 4, pp. 043017, 2010.
- [184] C. Russell, C. D. Wood, L. Dazhang, A. D. Burnett, L. H. Li, E. H. Linfield, A. G. Davies, and J. E. Cunningham, "Increasing the bandwidth of planar on-chip THz devices for spectroscopic applications," *Infrared, Millimeter and Terahertz Waves (IRMMW-THz), 2011 36th International Conference on*. pp. 1-3, 2011.
- [185] V. Miseikis, "Thesis: The Interaction of Graphene with High-Frequency Acoustic and Electromagnetic Waves," *University of Leeds*, 2012.

- [186] J. Zhang, M. Mikulics, R. Adam, D. Grützmacher, and R. Sobolewski, "Generation of THz transients by photoexcited single-crystal GaAs meso-structures," *Applied Physics B*, pp. 1-6, 2013.
- [187] M. Mikulics, J. Zhang, J. Serafini, R. Adam, D. Grutzmacher, and R. Sobolewski, "Subpicosecond electron-hole recombination time and terahertz-bandwidth photoresponse in freestanding GaAs epitaxial mesoscopic structures," *Applied Physics Letters*, vol. 101, no. 3, pp. 031111, 2012.
- [188] S. Saito, T. M. Inerbaev, H. Mizuseki, N. Igarashi, R. Note, and Y. Kawazoe, "First Principles Calculation of Terahertz Vibrational Modes of a Disaccharide Monohydrate Crystal of Lactose" *Japanese Journal of Applied Physics* vol. 45, no. 43, pp. L1156-L1158, 2006.
- [189] D. G. Allis, A. M. Fedor, T. M. Korter, J. E. Bjarnason, and E. R. Brown, "Assignment of the lowest-lying THz absorption signatures in biotin and lactose monohydrate by solid-state density functional theory," *Chemical Physics Letters*, vol. 440, no. 4-6, pp. 203-209, 2007.
- [190] B. B. Jin, Z. X. Chen, Z. Li, J. L. Ma, R. Fu, C. H. Zhang, J. Chen, and P. H. Wu, "Mode assignment of terahertz spectrum of α -lactose monohydrate," *Infrared, Millimeter, and Terahertz Waves, 2009. IRMMW-THz 2009. 34th International Conference on*. pp. 1-2, 2009.
- [191] M. Franz, B. M. Fischer, and M. Walther, "The Christiansen effect in terahertz time-domain spectra of coarse-grained powders," *Applied Physics Letters*, vol. 92, no. 2, pp. 021107, 2008.
- [192] M. Walther, B. M. Fischer, and P. Uhd Jepsen, "Noncovalent intermolecular forces in polycrystalline and amorphous saccharides in the far infrared," *Chemical Physics*, vol. 288, no. 2-3, pp. 261-268, 2003.
- [193] Y. C. Shen, P. C. Upadhyaya, E. H. Linfield, and A. G. Davies, "Temperature-dependent low-frequency vibrational spectra of purine and adenine," *Applied Physics Letters*, vol. 82, no. 14, pp. 2350-2352, 2003.
- [194] R. N. Simons, *Coplanar Waveguide Circuits, Components, and Systems*: John Wiley & Sons, Inc., 2001.
- [195] D. F. Williams, and S. E. Schwarz, "Design and Performance of Coplanar Waveguide Bandpass Filters," *Microwave Theory and Techniques, IEEE Transactions on*, vol. 31, no. 7, pp. 558-566, 1983.
- [196] K. Hettak, N. Dib, A. F. Sheta, and S. Toutain, "A class of novel uniplanar series resonators and their implementation in original applications," *Microwave Theory and Techniques, IEEE Transactions on*, vol. 46, no. 9, pp. 1270-1276, 1998.
- [197] C. D. Wood, "Thesis: On-chip THz Systems," *University of Leeds*, 2006.
- [198] J. J. Schermer, G. J. Bauhuis, P. Mulder, W. J. Meulemeesters, E. Haverkamp, M. M. A. J. Voncken, and P. K. Larsen, "High rate epitaxial lift-off of InGaP films from GaAs substrates," *Applied Physics Letters*, vol. 76, no. 15, pp. 2131-2133, 2000.
- [199] M. M. A. J. Voncken, J. J. Schermer, G. Maduro, G. J. Bauhuis, P. Mulder, and P. K. Larsen, "Influence of radius of curvature on the lateral etch rate of the weight induced epitaxial lift-off process," *Materials Science and Engineering: B*, vol. 95, no. 3, pp. 242-248, 2002.
- [200] J. J. Schermer, P. Mulder, G. J. Bauhuis, M. M. A. J. Voncken, J. van Deelen, E. Haverkamp, and P. K. Larsen, "Epitaxial Lift-Off for large area thin film III/V devices," *physica status solidi (a)*, vol. 202, no. 4, pp. 501-508, 2005.
- [201] M. Mikulics, R. Adam, M. Marso, A. Forster, P. Kordos, H. Luth, S. Wu, X. Zheng, and R. Sobolewski, "Ultrafast low-temperature-grown epitaxial GaAs photodetectors transferred on flexible plastic substrates," *Photonics Technology Letters, IEEE*, vol. 17, no. 8, pp. 1725-1727, 2005.

- [202] A. Steve, P. Emilien, V. Duong, C. H. R. Alistair, and P. Daniel, "Fluidic assembly of hybrid MEMS: a GaAs-based microcantilever spin injector," *Journal of Micromechanics and Microengineering*, vol. 20, no. 2, pp. 025023, 2010.
- [203] C. W. Cheng, K. T. Shiu, N. Li, S. J. Han, L. Shi, and D. K. Sadana, "Epitaxial lift-off process for gallium arsenide substrate reuse and flexible electronics," *Nature Communications*, vol. 4, 2013.
- [204] K. Koh, T. Deguchi, S. Okamoto, Y. Aoki, C. Kanashiro, and K. Hohkawa, "Study of semiconductor film bonding technology on piezoelectric substrate using water glass," *Japanese Journal of Applied Physics, Part 1: Regular Papers and Short Notes and Review Papers*, vol. 42, no. 9 A, pp. 5613-5618, 2003.
- [205] J. Arokiaraj, H. Okui, H. Taguchi, T. Soga, T. Jimbo, and M. Umeno, "Electrical characteristics of GaAs bonded to Si using SeS₂ technique," *Japanese Journal of Applied Physics, Part 2: Letters*, vol. 39, no. 9 A/B, pp. L911-L913, 2000.
- [206] Y. Sasaki, T. Katayama, T. Koishi, K. Shibahara, S. Yokoyama, S. Miyazaki, and M. Hirose, "High-Speed GaAs Epitaxial Lift-Off and Bonding with High Alignment Accuracy Using a Sapphire Plate," *Journal of the Electrochemical Society*, vol. 146, no. 2, pp. 710-712, 1999.
- [207] J. I. Maeda, Y. Sasaki, N. Dietz, K. Shibahara, S. Yokoyama, S. Miyazaki, and M. Hirose, "High-rate GaAs epitaxial lift-off technique for optoelectronic integrated circuits," *Japanese Journal of Applied Physics, Part 1: Regular Papers and Short Notes and Review Papers*, vol. 36, no. 3 SUPPL. B, pp. 1554-1557, 1997.
- [208] Z. Jiangquan, and D. Grischkowsky, "Terahertz time-domain spectroscopy of submonolayer adsorption in hydrophilic silica aerogel," *Optics Letters*, vol. 29, no. 9, pp. 1031-1033, 2004.
- [209] P. D. Cunningham, N. N. Valdes, F. A. Vallejo, L. M. Hayden, B. Polishak, X.-H. Zhou, J. Luo, A. K.-Y. Jen, J. C. Williams, and R. J. Twieg, "Broadband terahertz characterization of the refractive index and absorption of some important polymeric and organic electro-optic materials," *Journal of Applied Physics*, vol. 109, no. 4, pp. 043505, 2011.
- [210] N. Laman, S. S. Harsha, D. Grischkowsky, and J. S. Melinger, "High-Resolution Waveguide THz Spectroscopy of Biological Molecules," *Biophysical Journal*, vol. 94, no. 3, pp. 1010-1020, 2008.
- [211] J. S. Melinger, N. Laman, S. S. Harsha, and D. Grischkowsky, "Line narrowing of terahertz vibrational modes for organic thin polycrystalline films within a parallel plate waveguide," *Applied Physics Letters*, vol. 89, no. 25, pp. 251110, 2006.
- [212] J. S. Melinger, N. Laman, and D. Grischkowsky, "The underlying terahertz vibrational spectrum of explosives solids," *Applied Physics Letters*, vol. 93, no. 1, pp. 011102, 2008.
- [213] K.-E. Peiponen, A. Zeitler, and M. Kuwata-Gonokami, *Terahertz Spectroscopy and Imaging*: Springer, 2013.
- [214] H. Chetouani, A. Treizebre, B. Bocquet, D. Legrand, and V. Senez, "Integration of electrodes and Goubau transmission lines into a BioMEMS for wideband spectroscopy characterization (Hz–THz)," 2008.
- [215] N. Ohta, S. Yanagi, M. Onuma, J. Kitagawa, and Y. Kadoya, "Propagation of terahertz pulses on polymer-based coplanar striplines," *Proceedings of 2008 Asia Pacific Microwave Conference, APMC 2008*.